DGK Ausschuss Geodäsie (DGK)
der Bayerischen Akademie der Wissenschaften

Reihe C | Dissertationen | Heft Nr. 983

Andreas Maximilian Piter

Monitoring Transport Infrastructure using Sentinel-1 InSAR Time Series

München 2026

Verlag der Bayerischen Akademie der Wissenschaften, München

ISSN 0065-5325 ISBN 978 3 7696 5395 3

DGK Ausschuss Geodäsie (DGK)
der Bayerischen Akademie der Wissenschaften

Reihe C Dissertationen Heft Nr. 983

Monitoring Transport Infrastructure using Sentinel-1 InSAR Time Series Analysis

Von der Fakultät für Bauingenieurwesen und Geodäsie
der Gottfried Wilhelm Leibniz Universität Hannover
zur Erlangung des akademischen Grades
Doktor-Ingenieur (Dr.-Ing.)
genehmigte Dissertation

von

Andreas Maximilian Piter, M. Sc.

München 2026

Verlag der Bayerischen Akademie der Wissenschaften, München

ISSN 0065-5325 ISBN 978 3 7696 5395 3

Adresse des Ausschusses Geodäsie (DGK)
der Bayerischen Akademie der Wissenschaften:

Ausschuss Geodäsie (DGK) der Bayerischen Akademie der Wissenschaften
Alfons-Goppel-Straße 11 ● D – 80 539 München
Telefon +49 – 89 – 23 031 1113 ● Telefax +49 – 89 – 23 031 - 1283 / - 1100
e-mail post@dgk.badw.de ● http://www.dgk.badw.de

Prüfungskommission:
Vorsitzender: Prof. Dr.-Ing. habil. Christian Heipke
Referent: Prof. Dr.-Ing. Mahdi Motagh
Korreferenten: Prof. Dr.-Ing. Hamza Alkhatib
Prof. Dr. Andrew Hooper

Tag der mündlichen Prüfung: 11.05.2026

:

Diese Dissertation ist auf dem Server des Ausschusses Geodäsie (DGK)
der Bayerischen Akademie der Wissenschaften, München unter <http://dgk.badw.de/>
sowie unter Wissenschaftliche Arbeiten der Fachrichtung Geodäsie und Geoinformatik
der Leibniz Universität Hannover (ISSN 0174-1454), Nr. 423,
<https://repo.uni-hannover.de/handle/123456789/22686>, Hannover 2026, elektronisch publiziert

© 2026 Ausschuss Geodäsie (DGK) der Bayerischen Akademie der Wissenschaften, München

Alle Rechte vorbehalten. Ohne Genehmigung der Herausgeber ist es auch nicht gestattet,
die Veröffentlichung oder Teile daraus zu vervielfältigen.

ISSN 0065-5325 ISBN 978 3 7696 5395 3

Abstract

Geodetic monitoring of transport infrastructure including railway and highway networks is essential to assess risks resulting from natural and anthropogenic influences and to provide early warning to mitigate hazards. Since the launch of the European Space Agencies' Sentinel-1 satellites, Interferometric Synthetic Aperture Radar (InSAR) time series analysis provides a large potential for cost-effective and long-term displacement monitoring of infrastructure. However, the medium spatial resolution of the Sentinel-1 sensor, approximately 5 m×20 m, poses challenges for transport infrastructure monitoring. The potential of Sentinel-1 for this task has not yet been understood, and tailored InSAR time series methods are lacking. Moreover, with conventional InSAR time series approaches, infrastructure remain unobservable if they were constructed or demolished during the study period, which is more likely to occur the longer the observation period provided by the Sentinel-1 mission.

This thesis introduces a new InSAR time series analysis method tailored to the characteristics of transport infrastructure depicted in Sentinel-1 images. It assumes a spatially correlated displacement signal, selects both Point Scatterer (PS) and Distributed Scatterer (DS) pixels, and operates on single-look resolution to preserve the highest spatial resolution of the small baseline interferograms. Moreover, the method targets potential changes of the transport infrastructure during their operational lifetime by estimating the displacement time series for each pixel within the period in which the scatterer exhibits a coherent signal, which is referred to as coherent lifetime. The method identifies changes in the scattering through one of three change detection methods based on either the amplitude time series, or the structure of the coherence matrix or the phase noise in the interferograms. The performance and characteristics of the three methods are compared through experiments. These methods can be used as modules, while a phase unwrapping approach is employed to jointly address Continuously Coherent Scatterer (CCS) and Temporarily Coherent Scatterer (TCS) pixels.

In the experiments, the role of PS and DS pixels at transport infrastructure is assessed in two study areas yielding mostly DS pixels at railway tracks and predominantly PS pixels at bridges, while highways provide the least coherent pixels. The efficacy of the method is demonstrated by the observation of local displacements directly at transport infrastructure, despite the coarse spatial resolution of the sensor. The results suggest that vegetation in the surrounding of the transport infrastructure significantly reduces the monitoring potential with Sentinel-1 images because neighbouring decorrelated pixels negatively affect the phase filtering and coherence of DS pixels.

Furthermore, long study periods of more than 9 years were analysed in three study areas to demonstrate the method's capability to derive displacement time series for infrastructure present

only during part of the study period by exploiting TCS pixels. The analysis of two study areas focused on transport infrastructure, while the third one was used to study the transferability of the method to high-rise buildings in an urban environment yielding good agreement of the displacement time series with results from the literature. The validation of three change detection methods revealed that the coherent lifetime of TCS pixels estimated from coherent change detection methods is more closely aligned with the infrastructure's lifetime compared to the change detection results based on the amplitude time series, which is an incoherent change detection method. The two coherent methods performed similarly, but only the change detection based on the phase noise preserved spatial detail, whereas the method based on the coherence matrix was substantially more computationally demanding than the other two. Overall, the method based on the phase noise appears most suitable for practical application. However, achieving robust change detection results remains challenging. In summary, the experiments reveal the potential and the limitations of Sentinel-1 images for transport infrastructure monitoring.

Keywords: Transport Infrastructure, InSAR Time Series Analysis, Sentinel-1, Temporarily Coherent Scatterers

Kurzfassung

Die geodätische Überwachung von Verkehrsinfrastruktur, einschließlich Schienen- und Autobahnnetzen, ist für die Bewertung von Risiken aufgrund von natürlichen und anthropogenen Einflüssen, sowie für die frühzeitige Warnung vor Gefahren wichtig. Seit dem Start der Sentinel-1 Satelliten der Europäischen Weltraumorganisation (ESA) bietet die Interferometric Synthetic Aperture Radar (InSAR)-Zeitreihenanalyse ein großes Potenzial für eine kosteneffiziente und langfristige Überwachung von Oberflächenverschiebungen an Infrastrukturen. Die mittlere räumliche Auflösung des Sentinel-1 Sensors von etwa 5 m×20 m stellt jedoch eine Herausforderung für die Überwachung von Verkehrsinfrastrukturen dar. Das Potenzial von Sentinel-1 für diese Aufgabe ist bislang nicht hinreichend untersucht, und angepasste InSAR-Zeitreihenmethoden fehlen. Zudem lassen sich Infrastrukturen mit konventionellen InSAR-Zeitreihenansätzen nicht beobachten, wenn sie im Untersuchungszeitraum gebaut oder abgerissen wurden, was jedoch mit zunehmender Beobachtungsdauer durch die Sentinel-1 Mission wahrscheinlicher wird.

Diese Arbeit stellt eine neue InSAR-Zeitreihenmethode vor, die auf die Eigenschaften von Verkehrsinfrastruktur in Sentinel-1 Aufnahmen zugeschnitten ist. Sie setzt ein räumlich korreliertes Verschiebungssignal voraus, wählt sowohl Punktstreuer als auch verteilte Streuer aus und arbeitet in Single-Look Auflösung, um die höchste räumliche Auflösung der Interferogramme mit kleinen Basislinien zu erhalten. Darüber hinaus adressiert die Methode mögliche Veränderungen der Infrastruktur über ihre Nutzungsdauer, indem für jedes Pixel die Verschiebungszeitreihe innerhalb des Zeitraums geschätzt wird, in dem der Streuer ein kohärentes Signal aufweist, der sogenannten kohärenten Lebensdauer. Änderungen des Streuverhaltens werden mit einer von drei Veränderungsdetektionsmethoden identifiziert, die entweder auf der Amplitudenzeitreihe, auf der Struktur der Kohärenzmatrix oder auf dem Phasenrauschen der Interferogramme beruhen. Die Methoden sind modular einsetzbar und ihre Wirksamkeit und Effizienz werden experimentell miteinander verglichen. Die interferometrischen Phasen von kontinuierlich kohärenten und temporär kohärenten Streuern werden in einem gemeinsamen Ansatz abgewickelt.

In den Experimenten wird die Bedeutung von Punktstreuern und verteilten Streuern für die Überwachung von Verkehrsinfrastrukturen in zwei Untersuchungsgebieten untersucht. An Bahnstrecken überwiegen verteilte Streuer, an Brücken Punktstreuer, während Autobahnen die geringste Zahl kohärenter Pixel liefern. Es wird gezeigt, dass mit der vorgestellten Methode die Beobachtung lokaler Verschiebungen trotz der groben räumlichen Auflösung des Sensors direkt an Verkehrsinfrastrukturen möglich ist. Die Ergebnisse deuten zudem darauf hin, dass Vegetation in der Umgebung der Verkehrsinfrastruktur das Überwachungspotenzial mit Sentinel-1 Aufnahmen deutlich verringert.

Darüber hinaus wurden lange Untersuchungszeiträume von mehr als 9 Jahren in drei Gebieten analysiert in denen Infrastrukturen nur während eines Teils des Zeitraumes vorhanden waren. Es wird gezeigt, dass die Methode dennoch Verschiebungszeitreihen für diese Infrastrukturen ableiten kann. In zwei Gebieten werden Verkehrsinfrastrukturen untersucht, während im dritten Gebiet die Übertragbarkeit der Methodik auf Hochhäuser in einer urbanen Umgebung geprüft wird. Die resultierenden Verschiebungszeitreihen stimmen gut mit Ergebnissen aus der Literatur überein. Die Validierung der drei Methoden für die Veränderungsdetektion zeigt, dass die kohärente Lebensdauer von temporär kohärenten Streuern besser mit der Lebensdauer der Infrastruktur übereinstimmt, wenn kohärente Veränderungsdetektionsmethoden verwendet wurden, d.h. basierend auf der Kohärenzmatrix oder dem Phasenrauschen. Die beiden kohärenten Methoden liefern ähnliche Ergebnisse, jedoch bewahrte nur die auf Phasenrauschen basierende Methode räumliche Details, während die auf der Kohärenzmatrix basierende Methode erheblich rechenaufwendiger war als die beiden anderen. Insgesamt erscheint die auf Phasenrauschen basierende Methode für die praktische Anwendung am geeignetsten. Die Erzielung robuster Veränderungsdetektionsergebnisse bleibt jedoch eine Herausforderung. Die Experimente verdeutlichen sowohl das Potenzial als auch die Grenzen von Sentinel-1 Aufnahmen bei der Überwachung von Verkehrsinfrastrukturen.

Nomenclature

Acronyms

ADI	Amplitude Dispersion Index
ALOS	Advanced Land Observing Satellite
CCS	Continuously Coherent Scatterer
CODE-DE	COpernicus Data and Exploitation platform – DEutschland
CPL	Combined Eigenvalue maximum likelihood Phase Linking
DEM	Digital Elevation Model
DePSI	Delft Persistent Scatterer Interferometry
DInSAR	Differential Interferometric Synthetic Aperture Radar
DS	Distributed Scatterer
DSI	Distributed Scatterer Interferometry
EMI	Eigenvalue decomposition-based Maximum likelihood of Interferometric phase
ERS	European Remote Sensing Satellite
GIS	Geographic Information System
GNSS	Global Navigation Satellite System
IDR	Interval Deviation Rate
InSAR	Interferometric Synthetic Aperture Radar
ISCE	InSAR Scientific Computing Environment
KS	Kolmogorov-Smirnov
LOS	Line-Of-Sight
LRT	Likelihood Ratio Test
MACD	Mean Absolute Coherence Difference
MATD	Mean Absolute Temporal Difference
MiaplPy	MIAmi Phase Linking in PYthon
MintPy	Miami INsar Time-series software in PYthon
MSBAS	Multi-stack Small Baseline Subset
OSM	OpenStreetMap
PDF	Probability Density Function
PLC	Phase Linking Coherence
PNOA	National Air Orthophotography Plan
PS	Point Scatterer
PSI	Persistent Scatterer Interferometry
PUMA	Phase Unwrapping MAx-flow

SAR	Synthetic Aperture Radar
SBAS	Small BAseline Subset
SCR	Signal-to-Clutter Ratio
SLC	Single-Look Complex
SNAPHU	Statistical-cost, Network-flow Algorithm for PHase Unwrapping
SNR	Signal-to-Noise Ratio
SpaTZ	SPAtioTemporal Selection of Scatterers
SRTM	Shuttle Radar Topography Mission
StaMPS	Stanford Method for Persistent Scatterers
TCS	Temporarily Coherent Scatterer
TPC	Temporal Phase Coherence

Symbols

General

μ	Mean
σ	Standard-deviation
j	Imaginary unit
$\boldsymbol{\nu}, \lambda$	Eigenvector and corresponding Eigenvalue
H_0, H_A	Null- and alternative hypothesis
α	Significance level of a hypothesis test
$R(k)$	Autocorrelation function at time-lag k

Mathematical Operators

$\mathbb{E}[\cdot]$	Expectation operator
$\text{argmin}(\cdot)$	Argument of minimum value
$\text{argmax}(\cdot)$	Argument of maximum value
^{T}	Transposition
$\circ$	Hadamard product of two matrices
^{H}	Hermitian transposition of a matrix
*	Complex conjugate
$\lvert \cdot \rvert$	Matrix determinant
$Tr(\cdot)$	Trace operator
$\angle(\cdot)$	Phase of a complex number
$\mathcal{W}(\cdot)$	Wrapping operator

SAR Observations

y	Complex valued observations
A	Amplitude
ψ	Phase
$\bar{\psi}$	Filtered phase after Phase Linking
N	Number of SAR images
λ	Wavelength
r	Slant range distance between the sensor and the pixel
θ	Local incidence angle

SAR Interferometry

ϕ	Ambiguous interferometric phase wrapped into $[-\pi, \pi)$
φ	Unambiguous interferometric phase
φ_{disp}	Phase contribution from displacement
φ_{topo}	Phase contribution from topography
φ_{atmo}	Phase contribution from atmosphere
φ_{noise}	Phase noise
ϑ	Inverted phase
$\tilde{\vartheta}$	Residual inverted phase
d	Displacement
M	Number of interferograms
$B_\perp$	Perpendicular baseline
B_t	Temporal baseline
v	Displacement velocity
Δh	DEM error
γ	Theoretical coherence
γ_{arc}	Ensemble coherence for an arc
γ_{TPC}	Temporal phase coherence
γ_{PLC}	Phase linking coherence
$\boldsymbol{C}$	Covariance matrix
$\boldsymbol{\Gamma}$	Coherence matrix

Change Detection

n	Index of the image after which a change has happened
l_k	Set of indices of the SAR images for the whole image stack or the two subsets
M_k	Number of interferograms created from the whole image stack or the two subsets
p_k	Likelihood that the phase noise follows the marginal distribution of the interferometric phase
$k = 0, 1, 2$	Index indicating the whole image stack or one of the two subsets
$\Lambda(\cdot)$, $L(\cdot)$	Test score and normalised test score of the Likelihood Ratio Test (change detection based on the phase noise)
$D(\cdot)$	Test score of the Likelihood Ratio Test (change detection based on the coherence matrix)
$K(\cdot)$	Test value of F test (change detection based on the amplitude)
σ^2	Scale parameter of Rayleigh distribution

Contents

1 Introduction **1**
1.1 Motivation 1
1.2 Problem Statement 3
1.3 Contributions and Scientific Goals 6
1.4 Thesis Outline 8

2 Basics **9**
2.1 Synthetic Aperture Radar Observations 9
2.2 Interferometric and Differential Interferometric Synthetic Aperture Radar 10
2.3 Interferometric Synthetic Aperture Radar Time Series Analysis 13
2.3.1 Estimation of the Phase Contributions 13
2.3.2 Pixel Selection 15
2.3.3 Interferogram Network 19
2.3.4 Spatial Phase Unwrapping 19
2.3.5 Time Series Strategies 21

3 Literature Review **25**
3.1 Monitoring Transport Infrastructure with Continuously Coherent Scatterers 25
3.1.1 Sensors 27
3.1.2 Scattering 28
3.1.3 Bridges 29
3.1.4 Railway Tracks 31
3.1.5 Highways 31
3.1.6 Regional and Local Displacements 32
3.1.7 Discussion 32
3.2 Analysis of Temporarily Coherent Scatterers 34
3.2.1 Adjustment of the Study Period 34
3.2.2 Approaches Based on Change Detection 34
3.2.3 Integration into Time Series Analysis 35
3.2.4 Exploitation of the Signal Characteristics 39
3.2.5 Discussion 40

4 A New Approach for Monitoring of Temporarily Coherent Transport Infrastructure **43**
4.1 Overview 43
4.2 Prerequisites and Assumptions 44

4.3 Coherent Lifetime Estimation . . . 45
4.3.1 Change Detection . . . 46
4.3.1.1 Changes in Phase Noise . . . 47
4.3.1.2 Changes in Coherence Matrix Structure . . . 49
4.3.1.3 Changes in Amplitude Time Series . . . 50
4.3.2 Pixel Selection . . . 51
4.3.2.1 Temporal Phase Coherence . . . 51
4.3.2.2 Phase Linking Coherence . . . 51
4.4 Time Series Analysis . . . 52
4.4.1 Atmospheric Filtering . . . 54
4.4.1.1 First-Order Points . . . 54
4.4.1.2 Outlier Removal . . . 54
4.4.1.3 Phase Unwrapping . . . 55
4.4.1.4 Estimation of Atmospheric Effects . . . 56
4.4.2 Densification . . . 56
4.4.2.1 Second-Order Points . . . 56
4.4.2.2 Phase Unwrapping . . . 57
4.5 Discussion . . . 57
4.5.1 Discussion on the Coherent Lifetime Estimation . . . 58
4.5.2 Discussion on the Time Series Analysis . . . 60

5 Experimental Setup . . . 63
5.1 Objectives . . . 63
5.2 Study Areas and Datasets . . . 66
5.3 Processing Parameters . . . 69
5.4 Evaluation Strategy . . . 73
5.4.1 Masking of Infrastructure . . . 73
5.4.2 Plausibility Metrics for the Coherent Lifetime . . . 73

6 Results and Discussion . . . 77
6.1 Experiment 1: Pixel Selection at Transport Infrastructure . . . 77
6.2 Experiment 2: Observability of Local and Regional Displacements . . . 85
6.3 Experiment 3: Coherent Lifetime Estimation at Transport Infrastructure . . . 93
6.4 Experiment 4: Displacement Analysis of Temporarily Coherent Pixels . . . 101
6.5 Experiment 5: Transferability to Urban Infrastructure . . . 104

7 Conclusions and Outlook . . . 111

A Appendix . . . 115
A.1 Literature Overview on Transport Infrastructure Monitoring . . . 115
A.2 Coherent Lifetime Plots for Figuera . . . 118
A.3 Implementation in Open-Source Software . . . 119

Acknowledgements . . . 123

Bibliography **125**

1 Introduction

1.1 Motivation

Railway and highway networks are critical transport infrastructure that are susceptible to various hazards in their surroundings, such as land subsidence, ground motion due to mining activities, landslides, and instability of the infrastructure itself. Railway and highway bridges are particularly vulnerable infrastructure which might deform over time due to the ageing process of the material, leading to degradation. Three examples from the past eight years highlight the vulnerability of transport infrastructure in Germany (Figure 1.1). In autumn 2017, the highway A20 close to Tribsees, subsided over a length of about 90 m at both driving directions due to unstable foundations in a marshland area (Die Autobahn GmbH des Bundes, 2025). In spring 2023, the Rahmedetal bridge close to Lüdenscheid, was demolished as a precaution due to instability and danger of collapse (Zacher, 2025). Most recently, in autumn 2024, the Carola bridge over the Elbe river in Dresden, collapsed due to cracks in the reinforced concrete (Kelch, 2024). All three examples led to high repair costs and increased traffic loads on surrounding streets and bridges. Traffic was redirected through cities instead of bypassing them, which also increased the load on smaller transport infrastructure not designed for heavier loads. Geodetic monitoring is required to ensure the safety and reliability of these critical infrastructure.

Although ground- and satellite-based geodetic measurements such as levelling or GNSS measurements provide valuable data, conducting regular monitoring using these methods is challenging due to the extensive area covered by transport infrastructure and the associated high costs. InSAR time series analysis can complement ground-based measurements by providing displacement data over wide areas on regular temporal intervals. The technique has emerged as an invaluable tool for infrastructure monitoring, offering high-precision displacement measurements essential for assessing



Figure 1.1: Examples of vulnerable transport infrastructure in Germany. a) Subsidence at the A20, Tribsees (Photo ©Stefan Tretropp). b) Demolition of the Rahmedetal-bridge, Lüdenscheid (Photo ©Daniel Schröder). c) Partial collapse of the Carola-bridge in Dresden (Photo ©picture alliance/dpa, Robert Michael).

structural health (Emadali et al., 2017; Haghighi and Motagh, 2021; Aziz Zanjani et al., 2024). Therefore, a transport infrastructure monitoring service based on InSAR time series analysis shall be developed for Germany to provide regular displacement measurements to decision makers.

Despite its potential, InSAR time series analysis is subject to several challenges and limitations. One of the main constraints is the availability of Synthetic Aperture Radar (SAR) images for a specific study area. Effective InSAR time series analysis requires SAR data with both spatial and temporal resolutions high enough to ensure that the displacement signal is sampled without aliasing. Satellite missions like TerraSAR-X and COSMO-SkyMed provide high spatial resolution X-band SAR images ideal for infrastructure observations (Wang et al., 2019; Farneti et al., 2023; Tonelli et al., 2023). Nevertheless, their relatively narrow swath and limited global coverage constrain their usability for large-scale infrastructure monitoring.

The Sentinel-1 SAR mission has significantly advanced InSAR time series analysis by offering wide spatial coverage, a free data policy, and a moderate temporal resolution of 6 to 12 days. This has enabled the development of continuous monitoring systems and fostered ground motion services (Kalia et al., 2017; Raspini et al., 2018; Crosetto et al., 2020). However, while the medium spatial resolution of Sentinel-1 of approximately 5 m by 20 m (Torres et al., 2012) is sufficient for capturing displacements at a broader scale, it may not adequately sample highly localised displacements directly at transport infrastructure, potentially missing fine-scale displacement signals due to the inherent resolution limitations. Nevertheless, Sentinel-1 images have been used in various studies to derive displacements at transport infrastructure such as highways (Fárová et al., 2019; Shi et al., 2022; Hussain et al., 2023), railway tracks (Huang et al., 2017; Chang et al., 2020; Luo et al., 2022) and bridges (Qin et al., 2021; Schlögl et al., 2021, 2022; Nettis et al., 2023; Lasri et al., 2023). In these studies, standard InSAR time series methods have been used which were originally designed for applications different from transport infrastructure monitoring. Existing methods have not been tailored for the task of transport infrastructure monitoring and, in particular, the suitability of Sentinel-1 for this task has not yet been assessed.

A major limitation of InSAR time series analysis is signal decorrelation across multiple acquisitions, preventing displacement measurement across all individual pixels. Only pixels that maintain a coherent signal over at least several images can be exploited for displacement analysis. When InSAR time series methods were initially developed, only few image acquisitions from SAR sensors like ERS or Envisat were available. Consequently, only pixels were selected that maintain a coherent signal over the whole study period. Nowadays, a temporal sampling of every 6 or 12 days and temporal coverage of more than 10 years allow to also analyse objects that are constructed or demolished during the study period (Hu et al., 2019b; Dörr et al., 2022). As selecting coherent pixels in the area of interest is vital for retrieving reliable displacement results, the focus of this thesis is the selection of coherent pixels at transport infrastructure.

1.2 Problem Statement

The overall goal of this thesis is to develop a new InSAR time series analysis method for Sentinel-1 images tailored to transport infrastructure monitoring. To *monitor* is defined by the Oxford English Dictionary (2025) as follows:

> *To observe, supervise, or keep under review; to keep under observation; to measure or test at intervals, especially for the purpose of regulation or control.*

In that sense, the focus of this thesis is to observe and measure the local Line-Of-Sight (LOS) displacements at transport infrastructure with respect to their immediate surrounding, which can be provided to decision makers for regulation and control. This excludes assessing risks and actual damages, as well as the interpretation of displacements which are all important aspects, but not part of this thesis.

Three types of transport infrastructure are differentiated in this thesis: Railway tracks, highways and associated bridges. The proposed methodology is tailored to linearly-shaped transport infrastructure, such as railway tracks and highways. Thus, only bridges that are considered part of this linear infrastructure are analysed. These include small bridges that, for instance, lead a highway over railway tracks or over a small river, or are part of a highway junction. Other small bridges may be bridges over highways for pedestrians or side roads. In contrast, long spanning bridges are not considered in this thesis because a different methodology is required to precisely locate the scatterers on the bridge to correctly interpret the measured displacements, due to the height of a bridge and the side-looking SAR imaging geometry. These bridges can be several kilometres long and more than hundred metres high, e.g. crossing valleys or large rivers and have been studied extensively (e.g. Selvakumaran et al., 2020; Song et al., 2023; Zhou et al., 2025; Giordano et al., 2025) often analysing the thermal expansion of the bridge to detect anomalous behaviour.

While InSAR time series methods have been tailored to e.g. urban infrastructure (Kampes, 2006; Van Leijen, 2014) or rural areas (Hooper et al., 2007; Ferretti et al., 2011), a method suitable for transport infrastructure needs to address the infrastructure's characteristics in terms of shape and size, expected displacements, as well as backscattering properties including challenges arising from construction and demolition. Each of these characteristics and challenges will be discussed in the following.

Shape and Size

The shape and size of the infrastructure influence the observability in SAR images and hence are important characteristics. Railway tracks and highways are called linear-infrastructure due to their elongated shape. With a width between 10 m and 40 m, the linear-infrastructure are narrow but have a length that can span hundreds of kilometres. In comparison, one frame of Sentinel-1 has a ground range coverage of 251 km in interferometric wide swath imaging mode (Torres et al., 2012). The spatial resolution is approximately 5 m×20 m in range×azimuth, respectively, depending on the look angle and the local topography. This means that although the transport infrastructure may

be depicted in length in one or more Sentinel-1 image frames, the spatial resolution of the sensor is only sufficient to capture the infrastructure width in a few pixels.

The number of pixels which cover the transport infrastructure in width depends on the orientation of the sensor w.r.t. the direction of the infrastructure. This is highlighted by the following example. The width of two neighbouring railway tracks, might cover about 10 m in total. A highway might cover around 30 to 40 m in width depending on the number of lanes. Consequently, the railway and highway are covered by two and six to eight Sentinel-1 pixels, respectively, if the satellite's flight direction is parallel to the direction of the infrastructure (Figure 1.2a). In contrast, if the satellite's flight direction is perpendicular (Figure 1.2b), only half a pixel or two pixels would cover the railway track and highway in width, respectively. Only few pixels are available to assess the displacement at the transport infrastructure itself. However, among the pixels covering the transport infrastructure, not all show a coherent SAR signal over time as required for InSAR time series analysis. Consequently, an InSAR time series method tailored to transport infrastructure monitoring needs to carefully select the coherent scatterers among the pixels covering the infrastructure.

The shape and size of the linear-infrastructure has also implications for the estimation of the phase contributions at the scatterers. While only few pixels in the image correspond to the transport infrastructure, the majority of the pixels in the image are not of interest for the monitoring task. Nevertheless, those pixels cannot be discarded as they contain relevant information about the surrounding of the transport infrastructure such as regional displacements (see discussion on displacements) or the atmospheric phase contribution. It is not possible to estimate the atmospheric phase contribution, which is the largest error source, from pixels on the transport infrastructure only. For a reliable estimation of the atmospheric effect, a representative sampling is required.

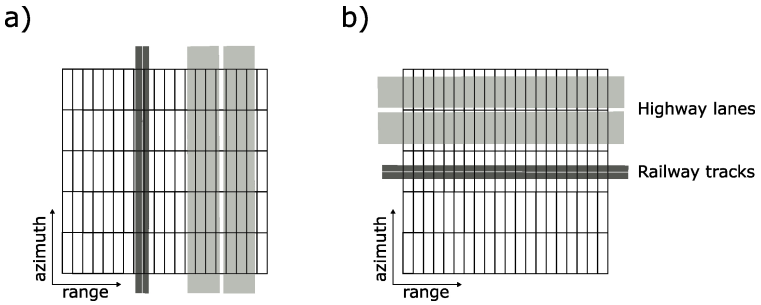


Figure 1.2: Pixel coverage at a highway and a railway track for the spatial resolution of Sentinel-1 with 5 m×20 m pixel size in range and azimuth, respectively, depending on the direction of the transport infrastructure: a) Transport infrastructure is parallel to, and b) perpendicular to the flight direction of the satellite (azimuth direction).

Displacements

Displacements[1] at transport infrastructure can occur for reasons either related to the infrastructure itself, like the ageing process of the material leading to structural instability (Nettis et al., 2023), or due to ground motion which deforms or displaces the infrastructure (Haghighi and Motagh, 2021;

[1]Notably, the term *displacement* is used in this thesis to describe the change along the LOS of the sensor measured with InSAR time series analysis. In contrast, the term *deformation* refers to deforming of an object.

Hussain et al., 2023; Fárová et al., 2019). While the former is observed as local displacements at the transport infrastructure, the latter corresponds to a displacement signal at a regional scale.

Local displacements can be captured by a few pixels in a medium spatial resolution Sentinel-1 image. Several pixels are expected to show a similar displacement signal related to the same phenomenon at the infrastructure, i.e. a spatially correlated displacement can be assumed. In order to reliably assess the hazard of a localised displacement signal, multiple scatterers showing the same displacement signal are required. Observing the displacement at a single pixel, however, is not sufficient to perform a reliable hazard assessment due to the ambiguous phase of the SAR signal and its error-prone phase unwrapping which degrades the trustworthiness of a single pixel's displacement result (Selvakumaran et al., 2018). Consequently, individual pixels with a displacement behaviour distinct from its neighbourhood are not targeted in this thesis although their displacement time series can be retrieved with dedicated methods (Van Leijen, 2014; Schenk, 2015).

Transport infrastructure can also be threatened by ground motion at or in the vicinity of the infrastructure. In mountainous regions for instance, monitoring slow-moving landslides is essential to mitigate damage before the landslide is triggered (Wang et al., 2021b; Hussain et al., 2023). Although landslides can also affect transport infrastructure, monitoring of landslides is not part of this thesis. Mining activities were shown to cause ground motion impacting larger spatial scales (Carnec and Delacourt, 2000; Kircher et al., 2003; Wegmüller et al., 2004; Tang et al., 2020), hence, also potentially affecting transport infrastructure. Further sources for displacements include the local geology (Niu et al., 2024) and ground water level changes (Amelung et al., 1999; Haghighi and Motagh, 2024). These sources all appear as spatially correlated displacements during the InSAR time series analysis.

To conclude, displacements at the transport infrastructure can be caused by various sources appearing as local or regional displacement signals. The displacement signals relevant for the task of transport infrastructure monitoring are argued to be spatially correlated instead of being a local and distinctive displacement signal which is present in single pixels only. Differentiating the causes based on the observed displacements is, however, outside the scope of this thesis.

Backscattering Properties

The quality of the observed SAR signal is important for the observability of transport infrastructure with InSAR time series analysis. Two factors need to be considered: The Signal-to-Noise Ratio (SNR) and the temporal evolution of the signal.

A high SNR often corresponds to a high backscattering intensity, while a low backscattering yields a low SNR (Hanssen, 2001). The scattering properties are different for railway tracks, highways and their bridges. However, the properties are similar in X-band and C-band images as depicted by the temporally averaged amplitude images of TerraSAR-X and Sentinel-1 in Figure 1.3. The highest SNR is expected at bridges and railway tracks and the lowest at highways which have a smooth surface relative to the cm-range wavelength of the SAR sensors. Nevertheless, filtering techniques can increase the SNR of low backscattering pixels from the time series of the pixel and

its neighbourhood (Ferretti et al., 2011). The filtering success depends on the backscattering in the surrounding of the infrastructure which, e.g., in Germany, often is covered by vegetation. Vegetation, however, is not suitable for InSAR time series analysis due to its decorrelation of the signal from one image acquisition to another. Vegetation also impacts the backscattering at transport infrastructure due to shadow effects resulting from the height of a tree and the side-looking SAR imaging geometry such that parts of the infrastructure could be occluded.

The phase of the SAR signal is exploited in InSAR time series analysis which requires that the SAR signal of two image acquisitions are coherent in order to retrieve the displacement from the phase difference of the two acquisitions. In case of newly constructed or demolished infrastructure, the backscattering properties change and the signal becomes incoherent during the monitoring period. The period in which the signal of a scatterer is coherent is called the coherent lifetime. In order to observe transport infrastructure, the coherent lifetime has to be identified and the InSAR time series analysis has to be restricted to that period. As each transport infrastructure and even each pixel covering the transport infrastructure can be coherent during an individual time span, the InSAR time series analysis should treat each pixel according to its coherent lifetime.

1.3 Contributions and Scientific Goals

This thesis contains the following contributions:

1. **Tailored InSAR time series method**
   The main contribution of this thesis is a new InSAR time series analysis method tailored to transport infrastructure monitoring with Sentinel-1 images. The method addresses the aforementioned characteristics of the transport infrastructure. The shape and extent within the Sentinel-1 images is dealt with through a two-step approach which removes the atmospheric effect to facilitate phase unwrapping. The displacements at the infrastructure are assumed to be spatially correlated which affects the choice of the pixel selection method and the phase unwrapping approach. The backscattering properties at the transport infrastructure are thoroughly analysed and targeted with suitable pixel selection methods because the availability of coherent pixels strongly affects the potential of the Sentinel-1 images for transport infrastructure monitoring.

2. **Analysis of temporarily coherent scatterer pixels at transport infrastructure**
   The proposed InSAR time series method retrieves the displacement time series of each pixel according to its coherent lifetime. This facilitates incorporating Temporarily Coherent Scatterer (TCS) pixels in addition to the Continuously Coherent Scatterer (CCS) pixels that are generally employed. Two improvements are made to the InSAR time series methodology to incorporate TCS pixels. First, a coherent lifetime estimation approach is proposed which identifies pixels exhibiting a change of the scattering mechanism during the study period. Then, CCS and TCS pixels are selected according to their coherent lifetime. Second, a phase unwrapping approach is proposed which allows to retrieve the displacement time series of the coherent pixels within their individual coherent lifetime.

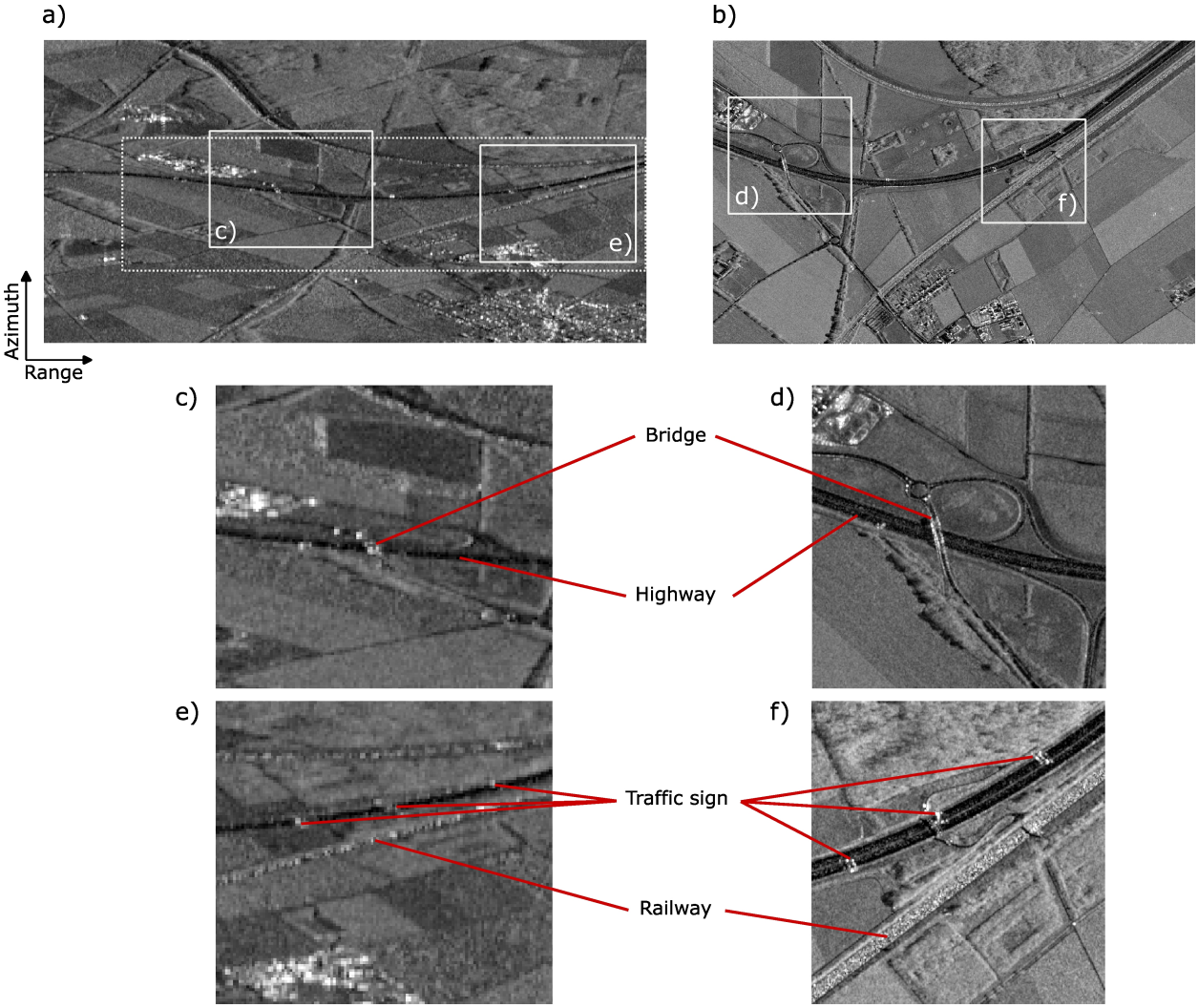


Figure 1.3: Mean amplitude images of transport infrastructure from a) Sentinel-1 and b) TerraSAR-X Stripmap with a spatial resolution of 5 m×20 m and 3 m×3 m, respectively. The images show a part of the highway A4 and of the railway tracks between Aachen and Cologne, located south of the Hambach open-pit mine in Germany. The amplitude images are averaged temporally to reduce the effect of speckle, hence, smoothing the image. Moreover, image normalisation is applied to improve the contrast of the images. The white box with a dotted outline in a) corresponds to the extent of the TerraSAR-X amplitude image shown in b). Notably, the areas appear differently due to the non-quadratic shape of the Sentinel-1 pixels. The white boxes in a) are shown in more detail in c) and e), while the white boxes in b), corresponding to approximately the same areas, are depicted in d) and f). The backscattering at the transport infrastructure is similar in TerraSAR-X and Sentinel-1 images. The highway appears dark in images of both sensors, indicating a low backscattering. However, due to the differences in the spatial resolution, the highway lanes can only be differentiated in the TerraSAR-X image. The backscattering is higher at railway tracks compared to highways, as a consequence these appear brighter in the mean amplitude images.

3. **Comparison of change detection methods for the coherent lifetime estimation**
   The identification of pixels exhibiting a change in the scattering mechanism is achieved through change detection. Within the proposed framework for coherent lifetime estimation, the suitability of the three change detection methods for transport infrastructure monitoring is investigated through experiments. A validation scheme is proposed for quantifying the plausibility of the estimated coherent lifetime based on a reference period derived from optical images with sparse and irregular temporal sampling.

The contributions are achieved by investigating the following main research questions to improve the understanding of transport infrastructure monitoring with Sentinel-1 images using the proposed InSAR time series analysis method.

- *How is the scattering at transport infrastructure characterized and what is the potential of the proposed pixel selection methods for transport infrastructure depicted in Sentinel-1 images?*
- *To which degree can local and regional displacements be observed and differentiated at transport infrastructure using Sentinel-1 images?*
- *How plausible is the coherent lifetime estimated from the three change detection methods?*
- *What is the contribution of the identified TCS pixels to the observation of displacements at infrastructure in long time series?*
- *To which degree can the proposed InSAR time series method be transferred to urban infrastructure monitoring?*

Five experiments are carried out to answer these scientific questions. The thesis is complemented by two developed software packages allowing to reproduce the results and to compare different methods for coherent lifetime estimation within one InSAR time series analysis framework (see Section A.3). The first package implements the change detection methods, while the second provides the InSAR time series method. Moreover, the InSAR time series analysis package is an integral part of the operational transport infrastructure monitoring service for the German federal state of Schleswig-Holstein[2].

1.4 Thesis Outline

The remainder of the thesis starts with an overview of the basics of InSAR time series analysis in Chapter 2. It is followed by a review of the literature relevant to both, transport infrastructure monitoring with InSAR time series analysis and analysis of TCS pixels in Chapter 3. The new methodology tailored to transport infrastructure monitoring is presented in Chapter 4. To answer the research questions, five experiments are conducted which are described in the experimental setup in Chapter 5, while the respective results are discussed in Chapter 6. Finally, the thesis is concluded in Chapter 7 together with an outlook to future research.

[2]The service was developed during the project SAR4Infra (2020-2024) financed by the German Federal Ministry of Digital and Transport.

2 Basics

In this chapter, the basics of InSAR time series analysis relevant to the thesis are discussed. Section 2.1 presents the observations in SAR images. Then, starting from InSAR, the problem of measuring surface displacements using Differential Interferometric Synthetic Aperture Radar (DInSAR) is formulated in Section 2.2. The theory in Section 2.1 and 2.2 follows the description of the fundamentals by Hanssen (2001). Finally, the concepts, assumptions and main processing steps for InSAR time series analysis are discussed in Section 2.3.

2.1 Synthetic Aperture Radar Observations

The complex SAR observation y of a target consists of the amplitude A and the phase ψ

$$y = Ae^{j\psi} \tag{2.1}$$

with the imaginary unit j. While the amplitude describes the strength of the backscattered signal, the phase is a function of the distance between the sensor and the scatterer. The phase measurement is ambiguous and is wrapped into the interval $[-\pi, \pi)$. The received signal for a pixel in the SAR image consists of the sum of multiple individual scatterers which cannot be resolved from each other. On a pixel level, two types of scattering are differentiated: distributed and point scattering (Hanssen, 2001). While the phase is uniformly distributed independent of the scattering type, the amplitude signal differs.

For point scattering, there is a dominating scatterer which exhibits a strong backscattering, while all other scatterers in the pixel are assumed to be clutter. The amplitude for point scattering follows a Rice distribution

$$f(A \mid \nu, \sigma) = \frac{A}{\sigma^2} \exp\left(\frac{-(A^2+\nu^2)}{2\sigma^2}\right) I_0\left(\frac{A\nu}{\sigma^2}\right) \tag{2.2}$$

with the non-centrality parameter $\nu \geq 0$, the scale parameter σ and the modified Bessel function $I_0(\cdot)$ of first kind and order zero (Figure 2.3b). The phase is uniformly distributed.

For distributed scattering, it is assumed that the phase of the individual scatterers is uniformly distributed and uncorrelated, and that none of the scatterers is dominating the others. In this case, the distributed scattering is described by a complex circular Gaussian random variable whose amplitude is Rayleigh distributed

$$f(A \mid \sigma) = \frac{A}{\sigma^2} \exp\left(-\frac{A^2}{2\sigma^2}\right), \tag{2.3}$$

which is a special case of the Rice distribution for $\nu = 0$ (Figure 2.3a).

SAR images are acquired with a side-looking sensor to resolve the backscattered signal from the surface along the slant-range distance, i.e. points on the surface are mapped into the SAR image along the slant-range distance and not along the ground-range distance. This causes three types of geometric distortions (Figure 2.1) which complicate the interpretation of SAR images: shadow, layover, and foreshortening (Hanssen, 2001). Shadows occur in the SAR images for parts which are not visible along LOS due to objects with a higher elevation, e.g. shadows are present in the image at the non-illuminated side of a building. Elevation on the surface can also lead to foreshortening of a slope facing the sensor. The slope appears shorter in slant-range than in ground-range. Layover occurs if an elevated object is closer to the SAR sensor than a point on the surface, the latter having a smaller ground-range distance. In case of a building, it means that multiple scatterers from different heights are imaged at the same slant-range distance.

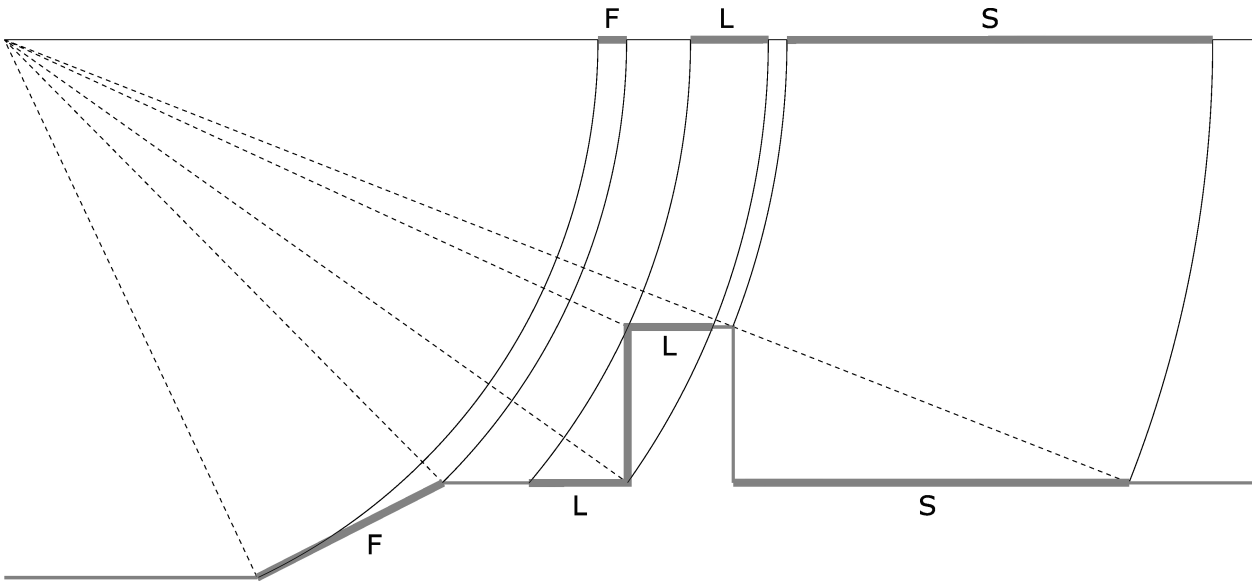


Figure 2.1: Simplified scheme of the SAR imaging geometry with the side-looking sensor located in the top left corner. The slope oriented towards the sensor appears foreshortened (F) in the SAR image. The building yields layover (L) at the roof, the wall and the ground in front of the building. The area behind the building is not illuminated which results in shadow (S).

2.2 Interferometric and Differential Interferometric Synthetic Aperture Radar

With InSAR, the phase difference is measured between two coregistered SAR images of the same target on the earth surface acquired at similar positions in orbit. The distance between the two positions of the satellite during image acquisition measured perpendicular to the look direction is called the perpendicular baseline $B_\perp$, while the difference in time is called the temporal baseline B_t (see Figure 2.2). The complex multiplication of two SAR observations of the same target forms an interferogram

$$y_1 y_2^* = A_1 A_2 e^{j(\psi_1 - \psi_2)} \tag{2.4}$$

with the complex conjugate denoted by *. The spatial resolution of the interferogram is either single-look if derived from the original Single-Look Complex (SLC) images, or multilook. Multilooking of

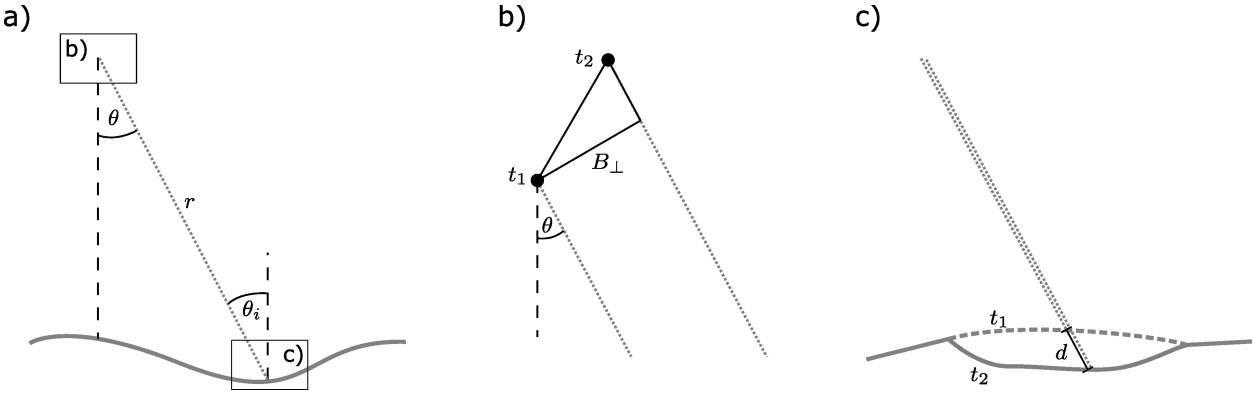


Figure 2.2: Imaging geometry for repeat-pass interferometry with image acquisitions at time t_1 and t_2, the distance between the sensor and the target r, the look angle of the sensor θ, the local incidence angle of the target θ_i, the perpendicular baseline between the two satellite positions $B_\perp$, and the displacement d at the target due to surface changes. The rectangles in a) are shown in more detail in b) and c).

an interferogram is performed by averaging the complex values of an interferogram within a spatial window around each pixel followed by subsampling which leads to a reduced spatial resolution.

An interferogram formed by two images acquired at the same time (single-pass interferometry) contains the phase from topography, while an interferogram computed from two images at different epochs (repeat-pass interferometry) additionally contains the phase related to changes in the topography. In order to only measure the latter, also referred to as surface deformation or displacement, the topography phase has to be removed. This is achieved with DInSAR for which the topographic phase, derived from an external Digital Elevation Model (DEM), is subtracted from the interferogram resulting in a differential interferogram. Moreover, the phase resulting from a reference surface, the so-called flat-earth phase component has to be removed using precise ephemerides. The ambiguous interferometric phase ϕ of a differential interferogram, from here-on called interferogram for simplicity, contains four major phase contributions

$$\phi = \mathcal{W}\left(\varphi_{\text{disp}} + \varphi_{\text{topo}} + \varphi_{\text{atmo}} + \varphi_{\text{noise}}\right) \tag{2.5}$$

and is wrapped into the interval $[-\pi, \pi)$, with $\mathcal{W}$ being the wrapping operator. The unambiguous phase can be obtained through phase unwrapping which is discussed in Section 2.3.4. The first phase contribution is the phase related to the displacement which shall be inferred from the interferometric phase. Notably, the displacement can only be observed along the LOS of the sensor. The second phase contribution results from an inaccurate DEM which was used to remove the topography-related phase. The third phase contribution results from the atmospheric phase delays during the two image acquisitions. The last phase contribution is related to the noise, e.g. from the sensor or other decorrelation sources. In order to obtain a reliable estimate of the displacement, the other phase contributions need to be estimated and removed. However, there is only one observation for each pixel in the interferogram from which three phase contributions and the noise shall be inferred. As a consequence, the phase contributions cannot be distinguished from each other in one interferogram because the problem is under-determined. InSAR time series methods are designed to distinguish the phase contributions from each other based on multiple interferograms from a

co-registered SAR image stack. The differentiation of the phase contribution will be discussed in the following section.

The noise in the interferometric phase depends on the correlation of the SAR signals in the two images forming the interferogram. The phase correlation is described by the coherence γ

$$\gamma = \frac{|\mathbb{E}[y_1 y_2^*]|}{\sqrt{\mathbb{E}[y_1 y_1^*]\mathbb{E}[y_2 y_2^*]}} \tag{2.6}$$

with the expectation operator $\mathbb{E}[\cdot]$. However, only one observation is available for each pixel in each image, so a different approach is required to approximate the phase noise which is discussed in the following section in the context of InSAR time series analysis.

The coherence can be expressed as the product of separate decorrelation mechanisms affecting the signal's correlation (Zebker and Villasenor, 1992)

$$\gamma = \gamma_{geometrical} \cdot \gamma_{temporal} \cdot \gamma_{other}. \tag{2.7}$$

The geometrical decorrelation accounts for different incidence angles under which the target is observed in two images due to the baseline between the satellites' positions. A complete decorrelation is observed beyond the critical baseline (Hanssen, 2001) which is not reached in interferograms from Sentinel-1 images due to the satellite's narrow orbital tube which limits the range of the baselines. Temporal decorrelation results from changes of the scatterers within a pixel over time leading to a different sum of the backscattered signal of the scatterers. While in the case of point scattering, the dominant scatterer has a deterministic signal is assumed to not change over time, distributed scattering often exhibits temporal decorrelation as e.g. the location of the individual scatterers changes. Often, the temporal decorrelation for distributed scattering is modelled with an exponential decay function (Rocca, 2007)

$$\gamma_{temporal}(t) = (\gamma_0 - \gamma_\infty)e^{t-\tau} + \gamma_\infty \tag{2.8}$$

with the initial coherence γ_0, the long-term coherence γ_∞, and the decorrelation time τ. However, temporal decorrelation can be caused by various changes on the surface which do not fit the given model. For instances, vegetation growth or snow cover can lead to seasonally changing correlation of the signal, while construction work would lead to an abrupt decorrelation.
Other sources of decorrelation include sensor-related thermal or system noise, processing induced decorrelation, and volume decorrelation occurring e.g. at vegetation. With modern sensors, such as Sentinel-1, the sensor induced decorrelation is considered to be negligible. Surface changes cannot be observed at vegetation due to volume and temporal decorrelation in combination with the satellite's revisit time of multiple days in which the signal has already decorrelated. Therefore, decorrelated pixels are masked and pixels with a coherent signal are selected (see Section 2.3.2).

While the phase in a SAR image is uniformly distributed, the Probability Density Function (PDF) of the interferometric phase ϕ in single-look interferograms is given by $f(\phi \mid \gamma)$ (Just and Bamler, 1994)

$$f(\phi \mid \gamma, \phi^0) = \frac{(1-|\gamma|^2)}{2\pi} \frac{1}{1-|\gamma|^2\cos^2(\phi-\phi^0)} \cdot \left(1 + \frac{|\gamma|\cos(\phi-\phi^0)\arccos(-|\gamma|\cos(\phi-\phi^0))}{\sqrt{1-|\gamma|^2\cos^2(\phi-\phi^0)}}\right) \tag{2.9}$$

given the coherence γ and the expected phase value ϕ^0 around which the distribution is centred (Figure 2.3c).

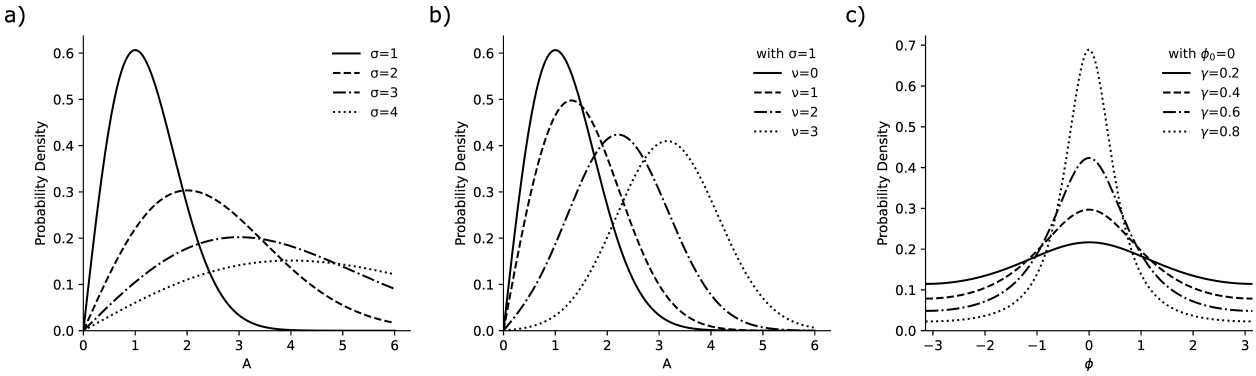


Figure 2.3: The amplitude of the SAR signal follows either a) the Rayleigh or b) the Rice distribution. Notably, the two distributions are the same for $\nu = 0$. The PDF of the interferometric phase for single-look resolution interferograms is shown in c) for different coherence values.

2.3 Interferometric Synthetic Aperture Radar Time Series Analysis

InSAR time series analysis extends DInSAR to multiple images from which a network of interferograms is created. This allows to separate the phase contributions based on assumptions on their temporal and spatial correlations. InSAR time series analysis requires a stack of co-registered SLC images (Hanssen, 2001; Fattahi et al., 2017) as input and yields the displacement time series for pixels which show a coherent signal in the interferograms as output. As with DInSAR, the topographic phase and the flat-earth phase are removed from each interferogram at the beginning of the InSAR time series analysis.

In the following, the principle of InSAR time series analysis is discussed. First, the estimation of the phase contributions from a stack of interferograms is presented. Second, as the phase contributions can only be estimated for pixels with a coherent signal, pixel selection approaches are explained for different scattering mechanisms. Third, commonly used interferogram networks are described which are used to estimate the phase contributions. Moreover, the choice of the interferogram network, depending on the requirements of the application, is presented. Fourth, the issue of spatial phase unwrapping and the approach selected for its resolution in this thesis are discussed. Finally, an overview on the variety of strategies for InSAR time series analysis is given together with a proposed categorisation of the strategies based on their main characteristics.

2.3.1 Estimation of the Phase Contributions

The phase contributions (see Equation 2.5) come with different correlation characteristics. The phase signals from displacement are correlated in time and often also correlated in space, while the phase due to the DEM error is correlated with the perpendicular baseline. The atmospheric phase delays are correlated spatially. To be precise, the atmospheric signal is also correlated in time, but for periods shorter than the revisit time of, e.g., the satellites of the Sentinel-1 mission. The noise is assumed to be uncorrelated in both, space and time.

Displacement and DEM Error

The phase contribution resulting from displacement d (see Figure 2.2)

$$\varphi_{\text{disp}} = -\frac{4\pi}{\lambda} d, \tag{2.10}$$

with the sensor's wavelength λ, can be estimated from the interferogram network with a temporal displacement model. The most common assumption is a mean displacement velocity v leading to the phase change

$$\varphi_{\text{disp}} = -\frac{4\pi}{\lambda} B_t \cdot v \tag{2.11}$$

which is correlated with the temporal baseline B_t.
The phase contribution from topography resulting from the DEM error Δh

$$\varphi_{\text{topo}} = -\frac{4\pi}{\lambda} \frac{B_\perp}{r \sin\theta_i} \cdot \Delta h \tag{2.12}$$

is correlated with the perpendicular baseline $B_\perp$, with the distance r between sensor and target, and the local incidence angle θ_i (see Figure 2.2).

The mean velocity and DEM error can be estimated for each coherent pixel from the unwrapped phases of the interferograms using least-squares if the atmospheric effect was removed beforehand. The unwrapped interferometric phases can be retrieved, e.g. with spatial phase unwrapping for each interferogram separately (see Section 2.3.4). However, it is not possible to estimate the two parameters, mean velocity and DEM error, from the wrapped interferometric phases. In this case, the interferometric phase difference between two coherent pixels can be exploited, the so-called arc phase. If the two pixels are close to each other, both pixels show a similar atmospheric effect. Consequently, the arc phase contains a reduced atmospheric effect which eases the estimation of the mean velocity difference and DEM error difference between the two coherent pixels from the wrapped interferometric phases. The solution is given by the parameters $v, \Delta h$ that minimise the phase residuals ϕ_{noise}, i.e. maximise the ensemble coherence $\hat{\gamma}$ (Ferretti et al., 2001)

$$\underset{v,\Delta h}{\operatorname{argmax}}\ \hat{\gamma}_{\text{arc}} = \frac{1}{M} \cdot \left| \sum_{i=1}^{M} e^{j \cdot \phi^i_{\text{noise}}(v,\Delta h)} \right| \tag{2.13}$$

from M interferograms. The parameters can be found e.g. using grid-search (Van Leijen, 2014; Esch, 2020) or based on the periodogram (Ferretti et al., 2001; Schenk, 2015). This approach could also be used for temporal phase unwrapping to estimate the float or integer ambiguities of the interferometric arc phases to reconstruct the phase time series corresponding to an anticipated displacement model (Kampes, 2006; Van Leijen, 2014).

Atmosphere

The phase contribution from the atmosphere is caused by different signal propagation distortions in the ionosphere and troposphere during the two image acquisitions related to the interferogram (Hanssen, 2001). The ionospheric phase advance depends on the wavelength, being more pronounced in longer wavelengths, and on the latitude, with larger effects in high latitudes and equatorial regions (Meyer, 2010). However, for C-band SAR images acquired in mid-latitudes, the ionospheric effect

is considered to be negligible. Hence, the atmospheric phase contribution is attributed to the tropospheric phase delay and results either from vertical stratification or turbulent processes in the troposphere (Hanssen, 2001). The vertical stratification of the troposphere leads to a height-dependent phase delay often occurring in mountainous regions. The effect can be modelled and removed from an interferogram by correlating the interferometric phase with the topographic height (Bekaert et al., 2015a; Fattahi and Amelung, 2015). The turbulent processes are described by the wet and hydrostatic refractivity along the LOS signal propagation path through the troposphere (Jolivet et al., 2011; Bekaert et al., 2015b). The refractivity is impacted by the atmospheric pressure, the water vapour pressure, and the temperature. The atmospheric phase contribution can be removed from the interferograms through auxiliary information, e.g. corrections derived from weather models (Jolivet et al., 2011; Fattahi and Amelung, 2015; Yu et al., 2018; Cao et al., 2021), Global Navigation Satellite System (GNSS) (Shamshiri et al., 2020), or multi-spectral images (Fattahi and Amelung, 2015). Alternatively, the atmospheric effect can be considered directly in the InSAR time series analysis. It can be modelled as part of the stochastic model (Kampes, 2006), or can be estimated from the interferometric phase by exploiting the spatial correlation of the signal (e.g. Ferretti et al., 2001; Van Leijen, 2014; Crosetto et al., 2018). As stated above, both the atmospheric and displacement signal are correlated in space, while the displacement signal is additionally correlated in time. Once the phase contributions from displacement and DEM error are removed from the unwrapped interferometric phase, the phase due to atmosphere and noise remain in the residual phases. The atmospheric phase can be estimated from the residual phases of the coherent pixels using Kriging (Wackernagel, 2003) to differentiate the spatially correlated atmosphere from the spatially uncorrelated phase noise.

2.3.2 Pixel Selection

InSAR time series analysis is applied to coherent pixels which can be categorised based on two criteria. On the one hand, pixels with a coherent signal are either called Point Scatterer (PS) or Distributed Scatterer (DS) pixels based on their scattering mechanism (see Section 2.1 and Figure 2.4). On the other hand, the coherent pixels can also be differentiated based on their coherent lifetime independent of the scattering mechanism: Pixels which have a coherent signal over the whole study period are called Continuously Coherent Scatterer (CCS) pixels, while pixels with a coherent signal over part of the study period only are called Temporarily Coherent Scatterer (TCS) pixels. TCS pixels result from a change in the scattering mechanism over time. The selection and handling of TCS pixels is an ongoing field of research. Therefore, it is discussed in detail during the literature review in Chapter 3, while the selection of CCS pixels is discussed here.

The displacement signal can only be derived for pixels with a coherent signal, i.e. with a low phase noise. In order to assess the phase noise, the phase contributions have to be separated. However, the separation is not straightforward and requires phase unwrapping as the observed interferometric phase is wrapped. Phase unwrapping is relative to a spatial and temporal reference, for which again a set of coherent pixels has to be known. This results in a circular process when attempting to select coherent pixels from the wrapped phases in the interferograms. To solve the pixel selection problem, approximations of the phase noise are employed. Another challenge arises from the non-redundant

SAR observations which yield one observation per epoch for each pixel. Often, either temporal or spatial stationarity are assumed such that multiple observations over time or from neighbouring pixels can be exploited to improve the phase noise approximation.

The pixel selection methods are either tailored to Point Scatterer (PS) or Distributed Scatterer (DS) pixels addressing the different scattering mechanisms. Temporal stationarity is often assumed for PS pixels, while the signal of DS pixels is considered to be stationary in space. Spatial stationarity assumption is often avoided for PS pixels because PS pixels can exhibit a distinct backscattering signal compared to its neighbouring pixels.

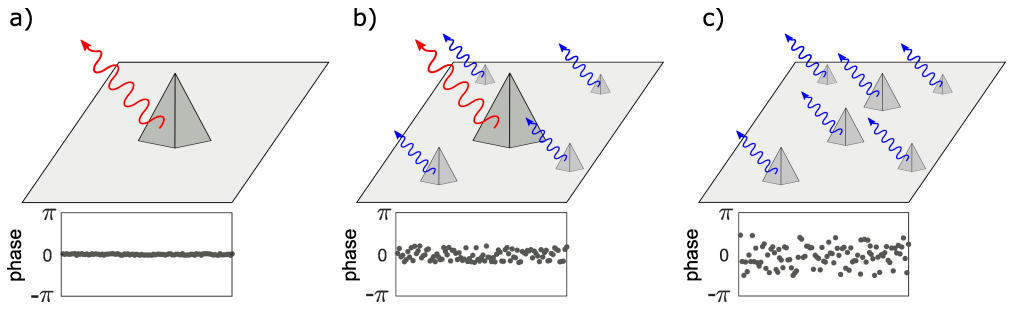


Figure 2.4: Scattering mechanisms in a pixel with its expected phase variations over time for a) an ideal single scatterer, b) a point scatterer with clutter from other weaker scatterers, and c) multiple weak scatterers forming a distributed scatterer pixel (adapted from Hooper et al. (2007) and Haghighi (2019)).

Selection of Point Scatterer Pixels

A PS pixel exhibits a strong backscattering from the dominant scatterer in the pixel and clutter from other scatterers (Hanssen, 2001). Two categories of pixel selection methods exist for PS pixels, either based on the amplitude signal or based on phase analysis.

A stable amplitude signal over time serves as an indicator for a low phase noise of a PS pixel. This relation is described by the Amplitude Dispersion Index (ADI)

$$\mathrm{ADI} = \frac{\sigma_A}{\mu_A} \simeq \sigma_\psi. \tag{2.14}$$

with the amplitude mean μ_A and standard deviation σ_A over time (Ferretti et al., 2001). The ADI assesses the pixel's suitability in a computationally rapid manner on the level of individual pixels, but the approximation holds only for low ADI values as shown by simulations (Ferretti et al., 2001; Hooper et al., 2007). Therefore, the set of pixels selected with ADI has to be refined and a posteriori pixel selection methods should be applied, e.g. phase-based outlier tests to estimate the phase noise level (Van Leijen, 2014).
Another pixel selection approach based on the amplitude is the Signal-to-Clutter Ratio (SCR) which exploits both, the time invariant dominant signal of the PS pixel and its time-variant clutter (Kampes, 2006; Czikhardt et al., 2022). While the signal is computed over time from an individual pixel, it is assumed that the neighbouring pixels represent the clutter which requires using a spatial estimation window.

The second category of pixel selection methods for PS pixels builds on phase analysis. The goal is to approximate the phase contributions in Equation (2.5) to obtain an approximation of the phase noise. This phase analysis requires a displacement model and a set of coherent pixels from which all phase contributions can be estimated. The approach taken by Hooper et al. (2007) starts with a set of candidate pixels obtained using a relaxed threshold on the ADI and then estimates the phase contributions by assuming that the displacement is spatially correlated. The resulting phase noise estimation for all candidate pixels is biased due to incoherent pixels among the candidates. Therefore, the set of candidates must be iteratively refined until a reliable estimation of the phase is obtained. A similar approach is proposed by Zhao and Mallorqui (2019) which also assumes a spatial displacement model. Unlike the previous approach, iterations are not required because the set of candidates is taken from the spatial neighbourhood of a PS pixel. This approach provides a computationally efficient approximation of the phase noise (for details on the method see Section 4.3.2.1).

Selection of Distributed Scatterer Pixels

A DS pixel exhibits a weaker backscattering compared to PS pixels. The signal is composed of the sum of multiple scatterers without a dominant scatterer (Hanssen, 2001). Moreover, DS pixels are more prone to decorrelation leading to a lower SNR compared to PS pixels. Therefore, the interferograms are filtered to increase the SNR for DS analysis before parameter estimation and phase unwrapping (Hanssen, 2001; Guarnieri and Tebaldini, 2008).

Phase filtering requires samples from the spatial neighbourhood and for this purpose, the signal of the DS pixel is assumed to be stationary in space. In practice, the spatial neighbourhood is defined with an adaptive or non-adaptive window covering neighbouring pixels (see Figure 2.5). While the non-adaptive window is computationally efficient because it is the same for each pixel, it loses spatial details due to the high correlation of the signal of neighbouring pixels after phase filtering (Lee et al., 1994). Moreover, the filtered phase is likely to be biased because pixels with a different scattering behaviour, e.g. PS pixels, could be included in the estimation window. For an adaptive window, a set of pixels that show a similar scattering behaviour and fulfil the stationarity assumption must be identified in the neighbourhood of the DS pixel. (Ferretti et al., 2011; Parizzi and Brcic, 2011; Goel and Adam, 2012; Spaans and Hooper, 2016). A biased phase due to pixels in the neighbourhood is less likely to occur when an adaptive window is used. Adaptive windows facilitate the preservation of spatial details in the interferograms. However, the adaptive window comes with increased computational costs because it has to be determined for each individual DS pixel separately.

Phase filtering in each interferogram can be achieved by multilook processing (Berardino et al., 2002). Afterwards, the spatial coherence of the interferometric phase (Equation 2.6) is evaluated from samples over the same spatial neighbourhood and DS pixels are selected based on the spatial coherence in the interferograms (e.g. Berardino et al., 2002; Mora et al., 2003).

Phase linking is another phase filtering approach for DS pixels (Guarnieri and Tebaldini, 2008; Ferretti et al., 2011). Its goal is to optimise the phase time series based on all possible interfero-

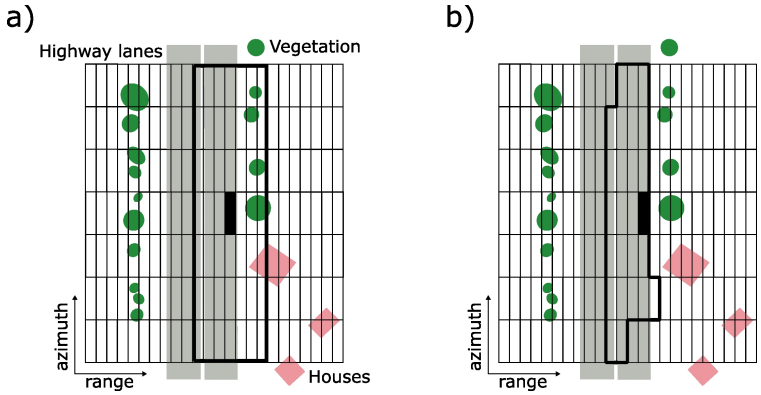


Figure 2.5: Example for the neighbourhood definition with a) a non-adaptive and b) an adaptive window for a pixel on the highway (marked in black) and a 7×7 pixels^2 window size (thick black outline). The size of the non-quadratic pixels corresponds to the spatial resolution of $5\,\mathrm{m}\times20\,\mathrm{m}$ in Sentinel-1 images. The non-adaptive window contains highway pixels, as well as pixels depicting vegetation and a building. In contrast, the adaptive window excludes pixels with a different scattering behaviour. Thus, in this example, the vegetated pixels, which are most likely decorrelated, and the building pixels, which presumably exhibit a stronger backscattering, are not part of the window.

grams derived from the SAR stack in order to minimise the decorrelation of DS pixels. For the signal of a DS pixel, a complex circular Gaussian distribution is assumed (see Section 2.1) which is fully described by the complex covariance matrix or, if normalised, the coherence matrix. The coherence matrix represents the coherent behaviour of the pixel over time. Its estimation requires the complex-valued time series of the neighbouring pixels with a similar scattering behaviour, so-called sibling pixels. Thus, phase linking requires an adaptive spatial window to correctly retrieve the optimised phases. Thereby the spatial resolution of the interferograms is maintained which allows to analyse DS pixels in single-look resolution interferograms. The adaptive spatial window is commonly determined using amplitude statistics to measure the similarity between the time series of the DS pixel and its neighbours (Parizzi and Brcic, 2011; Shamshiri et al., 2018).

Several phase linking approaches have been proposed (e.g. Ferretti et al., 2011; Fornaro et al., 2014; Samiei-Esfahany et al., 2016; Ansari et al., 2018) which follow similar steps including the selection of sibling pixels to compute the coherence matrix and phase optimisation based on the coherence matrix. The main difference between the proposed phase linking methods lies in their different weighting of the interferograms to retrieve the filtered phases (Ferretti et al., 2011; Fornaro et al., 2014; Ansari et al., 2018; Mirzaee et al., 2023). Finally, DS pixels are selected using the Phase Linking Coherence (PLC) which is a measure of fit for the phase filtering result and the phase noise level of the DS pixel (Ferretti et al., 2011).

A drawback of phase linking is the high computational demand caused by the optimisation of large coherence matrices. To reduce the computational time without compromising the estimation precision, Ansari et al. (2017) proposed a sequential phase linking approach. It reduces the computational complexity by splitting the coherence matrix into several mini-stacks. Phase linking is applied on each of the ministacks and the results are finally stacked to retrieve the full phase time series.

A Posteriori Pixel Selection

The discussed pixel selection methods for PS and DS pixels are applied before phase unwrapping to reduce the impact of incoherent pixels on the final displacement results. The set of selected pixels can be further refined after phase unwrapping using a posteriori pixel selection criteria. These include for instance the assessment of the precision derived from the covariance matrix of the phase observations, or the standard deviation of the displacement time series with respect to a pre-defined displacement model, or the spatio-temporal consistency of the displacement time series (Van Leijen, 2014). Alternatively, metrics sensitive to the quality of the phase unwrapping result could be assessed (Pepe and Lanari, 2006; Manunta et al., 2019).

2.3.3 Interferogram Network

A network of interferograms is created from the co-registered SAR stack. While a maximum of $\frac{N(N-1)}{2}$ different interferograms can be computed from N SAR images, only $N-1$ interferograms are independent. The interferograms are characterised by their temporal and perpendicular baselines leading to variations in the phase contributions (Equation 2.5). Different sets of interferograms are exploited depending on the displacement magnitude and the type of scattering in the study area.

The magnitude of the displacement signal impacts the choice of the interferograms. Small displacement rates are obscured by the phase noise level of a scatterer in interferograms with short temporal baselines, while this displacement signal exceeds the noise level in interferogams with long temporal baselines. In contrast, high displacement rates can be aliased in long temporal baseline interferograms, while the displacement signal might be retrievable in short temporal baseline interferograms (Emadali et al., 2017).

The interferogram network type can be chosen to match the prevalent scattering mechanisms. The temporal decorrelation is negligible for an ideal PS pixel due to its long-term coherence and only perpendicular baselines beyond the critical baseline lead to loss of coherence. This allows the usage of long baselines such as in a single-reference network (Figure 2.6a). For DS pixels, interferograms with short temporal and perpendicular baselines are favourable to minimise the temporal and geometrical decorrelation of the target, such as in a small baseline network (Figure 2.6b). The narrow orbital tube of Sentinel-1 limits the perpendicular baselines and thus the geometrical decorrelation is limited for both, PS and DS pixels.

The most common interferogram networks include a single-reference, a small baseline, and a fully connected network (Figure 2.6). The usage of these three interferogram networks within existing strategies for InSAR time series analysis is discussed in Section 2.3.5.

2.3.4 Spatial Phase Unwrapping

In order to retrieve the displacement signal, the absolute phases, or unwrapped phases, have to be found from the wrapped interferometric phases. For each interferogram the phases shall be unwrapped spatially under the assumption that the phase is smooth in space. To be precise, it is assumed that the absolute phases of two neighbouring points do not differ more than π. Several

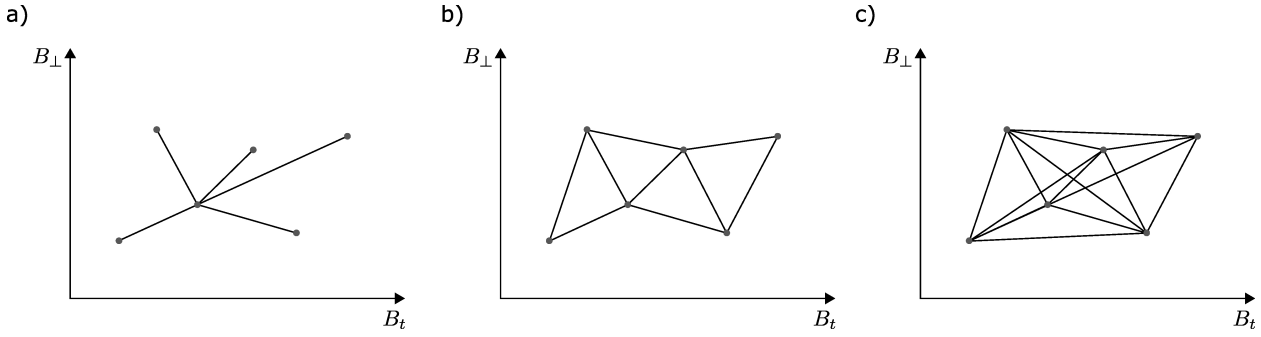


Figure 2.6: Examples of interferogram network types: a) single-reference network, b) small baseline network, c) full network. Each dot denotes an image, while an arc between two images represents an interferogram.

methods were proposed to unwrap the phase (e.g. Costantini, 1998; Chen, 2001; Bioucas-Dias and Valadao, 2007).

The problem can be formulated to find the integer multiple of 2π, given by the integer wrap count vector $\boldsymbol{k}$, which resolves the absolute phase $\boldsymbol{\varphi}$ from the wrapped phase $\boldsymbol{\phi}$

$$\boldsymbol{\varphi} = \boldsymbol{\phi} + 2\pi\boldsymbol{k} \tag{2.15}$$

where the size of all three vectors is given by the number of points whose phases shall be unwrapped. The Phase Unwrapping MAx-flow (PUMA) method used in this thesis, solves the problem by global optimisation using energy minimisation within the point network (Bioucas-Dias and Valadao, 2007). The point network is represented with a graph and each two neighbouring points form a clique for which an energy function is defined, a so-called clique potential V. The clique potential depends on the phase difference $\Delta\varphi_{pq}$ between the neighbouring points indexed by p, q. The resulting energy is low in case of similar phase values and high for large phase differences. The total energy E to be minimized is given by the sum over all clique potentials in the graph $\mathbb{G}$

$$E(\boldsymbol{k}|\boldsymbol{\phi}) = \sum_{pq\in\mathbb{G}} V(\Delta\varphi_{pq}) = \sum_{pq\in\mathbb{G}} V(2\pi(k_p - k_q) - (\phi_p - \phi_q)). \tag{2.16}$$

PUMA solves this energy minimisation problem with graph-cuts (Boykov and Kolmogorov, 2004). The solution is achieved through a sequence of binary classifications, increasing the wrap count for one set of points that are separated from another set by the graph cut. The optimisation problem converges after a finite number of iterations if the clique potential is convex. Finally, Equation (2.15) is evaluated using the wrap count vector derived with PUMA yielding the absolute phase value for each point in the network.

Phase discontinuities violate the spatial phase smoothness assumption and pose challenges for phase unwrapping as the location of the discontinuities is not known beforehand. Convex clique potentials result in a smoothing of the phase at phase discontinuities in the graph. In contrast, non-convex clique potentials are preferable as they preserve the discontinuities. To ensure convergence of the PUMA method also for non-convex clique potentials, an approximate solution is proposed by Bioucas-Dias and Valadao (2007) which regularises the energy function.

PUMA is of L^p-norm with p depending on the clique potential, e.g. L^1-norm for non-convex clique potential. While other phase unwrapping methods like e.g. Statistical-cost, Network-flow Algorithm for PHase Unwrapping (SNAPHU) (Chen, 2001) require the points to be located in a regular grid, for PUMA, the graph can be constructed from any neighbourhood including a sparse irregular network, or regular grid. For a sparse irregular network, the edges of the graph have to be defined, e.g. using a Delaunay network.

2.3.5 Time Series Strategies

Over the past 25 years, several time series strategies have been developed for different applications to estimate the phase contributions from a stack of interferograms and to derive the displacement time series. Typically, InSAR time series methods consist of similar steps: Creating an interferogram network, selecting coherent scatterers, estimating the phase contributions, unwrapping the interferometric phases, and filtering the phase contribution due to atmosphere. Extensive reviews on InSAR time series analysis are given by Osmanoğlu et al. (2016); Crosetto et al. (2016); Minh et al. (2020).

In the following, an overview is given on the most common strategies based on three categories which have been established over the years: Persistent Scatterer Interferometry (PSI), Small BAseline Subset (SBAS) and Distributed Scatterer Interferometry (DSI). The three categories are, however, insufficient to describe the strategies as evidenced by the variety of methods and modifications of these strategies presented in the literature. Therefore, a set of parameters is presented that provide a more comprehensive characterisation of InSAR time series strategies. Those parameters are listed in Table 2.1 together with possible options which were found in the literature.

Table 2.1: Descriptive parameters for InSAR time series strategies with possible options. The specifications of the method proposed in this thesis are written in bold letters.

Parameter	Options		
Scattering:			
Type	**PS**	**DS**	
Coherent	**continuously**	**temporarily**	
Interferograms:			
Resolution	**single-look**	multilook	
Network	single-reference	**redundant**	
Processing:			
Strategy	refinement	**densification**	
Pixel selection	**a priori**	a posteriori	
Displacement model	temporal	**spatial**	
Phase unwrapping	temporal (1D)	**spatial (2D)**	spatio-temporal (3D)
Atmospheric filtering	**phase-based**	auxiliary data	

Persistent Scatterer Interferometry

PSI methods focus on the exploitation of PS pixels in single-look resolution interferograms (Ferretti et al., 2001) and are used in a variety of engineering (Schenk, 2015; Emadali et al., 2017; Aziz Zanjani et al., 2024), geophysical (Hooper et al., 2007; Spaans and Hooper, 2016) and geological applications (Raspini et al., 2019; Wang et al., 2023b). Most PSI methods utilise a single-reference interferogram network (e.g. Ferretti et al., 2001; Werner et al., 2003; Kampes, 2006; Van Leijen, 2014) because PS pixels exhibit minimal temporal and geometrical decorrelation. The single-reference interferogram network has the advantage, that the interferometric phases can be directly interpreted as a time series. This simplifies the estimation of a temporal displacement model from the correlation of the interferometric phases with the temporal baseline.
The main steps of PSI with a single-reference interferogram network are as follows. PS pixels are selected a priori, e.g. based on the ADI. Two sets of PS pixels with different phase noise levels are selected. The set of high-quality PS pixels is used to estimate the atmospheric phase contribution, while the other set is included afterwards to densify the set of points. The phase contributions are estimated from the wrapped phases for which a spatial network is created to connect PS pixels and to compute the interferometric arc phases. Temporal unwrapping is applied to estimate the parameters from the displacement model and the DEM error for each arc. The parameters for each arc are integrated using least-squares with respect to a reference point whose displacement and DEM error are assumed to be zero. The integration yields the parameters for each PS pixel in the network. To retrieve the displacement time series, the known phase contributions are removed from the interferograms and the residual phases are unwrapped in space. The atmospheric effects are filtered and removed from the unwrapped phase time series. The final set of PS pixels is obtained by including and unwrapping the phases of more PS pixels. The PSI approach based on the single-reference network allows each PS pixel to follow a displacement behaviour distinct from its neighbourhood. However, the temporal displacement model has to be anticipated based on prior knowledge on the study area.

Beside a single-reference interferogram network also other interferogram networks can be applied for processing PS pixels, e.g. a small baseline network (Hooper, 2008; Zhang et al., 2010, 2011; Goel and Adam, 2012; Devanthéry et al., 2014; Spaans and Hooper, 2016), a minimum spanning tree (Blanco-Sánchez et al., 2008; Perissin and Wang, 2012), or multiple small baseline interferograms (Schenk, 2015). Small baseline interferogram networks, or more generally, redundant interferogram networks can be used with both, a temporal or a spatial displacement model (Mora et al., 2003; Crosetto et al., 2011; Devanthéry et al., 2014). The estimation of a temporal displacement model from wrapped small baseline interferograms is challenging due to the limited bandwidth of the baselines. The single-reference interferogram network provides a larger baseline bandwidth which is favourable for correlation analysis with the interferometric phase. However, stacking of the periodograms through multiple sets of small baseline interferograms increases the SNR for the estimation of the phase contributions (Goel and Adam, 2012; Schenk, 2015). If a redundant interferogram network is utilised, phase unwrapping errors can be detected and corrected in the interferogram network for each PS pixel (Monserrat et al., 2009; Crosetto et al., 2011).

PSI methods can also rely on a spatial displacement model (Hooper et al., 2004, 2007; Hooper, 2008; Goel and Adam, 2012; Spaans and Hooper, 2016) instead of a temporal displacement model, or combine both (Caro Cuenca et al., 2011; Chang et al., 2019). The PSI method proposed by Hooper et al. (2007) builds upon a spatial displacement model and differs significantly from the methods based on a temporal displacement model. It combines a single-reference network, or a small baseline network (Hooper, 2008), with a spatial displacement model. In contrast to the densification approach, an initial set of PS candidates is iteratively refined to obtain the coherent PS pixels (see Section 2.3.2). The spatially correlated phase contributions, i.e. displacement and atmospheric signal, are removed during the refinement through spatial filtering. The spatially uncorrelated DEM error is estimated and removed from the phase residuals to retrieve the phase noise level of the PS pixels. In this approach, pixels with a displacement signal distinct from their neighbourhood are discarded as opposed to the PSI methods built upon a temporal displacement model discussed in the beginning of this section.
An alternative approach to the aforementioned PSI with a spatial displacement model is to estimate the phase contributions from small baseline interferograms after the phases are unwrapped spatially (Goel and Adam, 2012). This differs from the approach with a temporal displacement model as discussed above, in which the modelled displacement signal is removed from the interferograms before spatial phase unwrapping of the residual phases and restored afterwards. The inversion of the interferogram network allows to retrieve non-linear displacement signals without anticipating a temporal displacement model if the interferograms are unwrapped spatially.

Small Baseline Subset

SBAS focuses on DS pixels in multilooked interferograms (Berardino et al., 2002; Mora et al., 2003; Lanari et al., 2004). As the name suggests, SBAS uses a network of small temporal and perpendicular baselines to reduce the effect of temporal and geometrical decorrelation, respectively. Moreover, the phases of the DS pixels are filtered through multilooking of each interferogram. Thereby, the number of pixels in the interferograms is reduced significantly which reduces the computational effort for large-scale displacement analysis (Manunta et al., 2019). DS pixels are selected based on the spatial coherence in the interferograms. Afterwards, the interferograms are unwrapped in space assuming spatial correlation of the displacement signal. The phase contributions from DEM error can be estimated from the unwrapped phases (Fattahi and Amelung, 2013) and the atmospheric effects filtered based on phase correlations or auxiliary data. Finally, the displacement time series is retrieved through inversion of the interferogram network benefitting from the redundancy and connectivity in the network. A variety of modifications to SBAS have been proposed, for instance the multi-scale analysis of small baseline interferograms in both, single- and multilook resolution (Lanari et al., 2004), or the explicit consideration of spatial correlations between observations of neighbouring pixels (Jolivet and Simons, 2018). SBAS is often used for geophysical and geological applications (Sandwell et al., 2011; Yunjun et al., 2019; Dalaison and Jolivet, 2020; Morishita et al., 2020), but is not ideal for infrastructure monitoring due to the reduced spatial resolution of the DS pixels which presents challenges when assessing small and localised displacements.

Distributed Scatterer Interferometry

DSI, or also called PSDS, can be considered as an extension of PSI to include DS pixels in single-look resolution analysis. Phase linking is applied to improve the phase quality of DS pixels (Guarnieri and Tebaldini, 2008; Ferretti et al., 2011; Samiei-Esfahany et al., 2016; Ansari et al., 2018). Afterwards, DS pixels are selected using the PLC (Ferretti et al., 2011). The full network of interferograms is used during phase linking to optimise the phases. However, the strategy for estimating the displacement time series is not specific to DSI. Instead, existing PSI methods can be used and displacements are retrieved jointly for DS and PS pixels (Ferretti et al., 2011; Fornaro et al., 2014; Shamshiri et al., 2018; Mirzaee et al., 2023).

3 Literature Review

This chapter provides an overview of the relevant literature and is subdivided into two parts. The first part, Section 3.1, reviews existing approaches for transport infrastructure monitoring using InSAR time series analysis with CCS pixels and concludes with a discussion on the existing research gaps. The second part, Section 3.2, reviews existing approaches for the analysis of TCS pixels and highlights remaining challenges for TCS analysis both, in general and in particular for transport infrastructure monitoring.

3.1 Monitoring Transport Infrastructure with Continuously Coherent Scatterers

The challenges and trends of InSAR for monitoring displacements at transport infrastructure were discussed in detail in the review by Macchiarulo et al. (2022b). Many of the challenges discussed by the authors of the review are general to InSAR time series analysis and, hence, apply also to transport infrastructure. These limitations include geometrical distortions of the side-looking sensor and the sensitivity of the sensor to displacements along LOS. Further, the authors mentioned challenges during the decomposition of LOS measurements from different orbits, phase unwrapping errors and the need for quality estimators which are independent of the anticipated displacement model. Another challenge arises from the unknown location of a scatterer. The interpretation of the displacement products, however, require an accurate geolocation of the scatterers which can be aided by the use of laser scanning data. The authors of the review highlighted that the location and distribution of PS pixels is unknown prior to the analysis. Hence, it is not clear whether an infrastructure actually is observable with InSAR time series before starting the analysis. The availability of PS pixels was stated to be a major limitation in monitoring transport infrastructure. However, the authors of the review did not discuss the type of scattering prevalent at transport infrastructure and so the selection of DS pixels was not addressed. Instead, it was suggested to focus on the usage of quasi-PS pixels or installing artificial corner reflectors to the infrastructure. The density of coherent pixels depends on the selection of a coherence threshold for PS pixels, which, according to Macchiarulo et al. (2022b), was not well studied. The authors further highlighted the importance of the choice of a reasonable displacement model for the study area to be able to extract pixels at the infrastructure.

The availability of Sentinel-1 images with a wide-area coverage, short revisit times and free data policy has fostered the implementation of various ground motion services on a country-scale, e.g. for Germany (Kalia et al., 2017), Norway (Dehls et al., 2019), Italy (Manunta et al., 2019), Greece (Papoutsis et al., 2020), and Japan (Morishita, 2021). Also services on a federal-state-level, e.g. for

landslide monitoring in Tuscany (Bianchini et al., 2018) or even on the European-level (Crosetto et al., 2020) have been established. Even though these ground motion monitoring services were not tailored to the characteristics of transport infrastructure, they often offer a first impression of the displacement signal present in the surrounding or even at the transport infrastructure. The displacement products of the ground motion services combined with geodata such as OpenStreetMap (OSM), can further be post-processed to assess hazards at infrastructure (Barra et al., 2022). For instance, the ground motion service for Tuscany was used to detect anomalies in the spatial and temporal displacement patterns (Raspini et al., 2018). Talledo and Saetta (2025) used the final displacement products from the European ground motion service to mask pixels on bridges and assessed the hazard associated to displacement. Similarly, Giordano et al. (2025) studied a particular bridge in detail based on the final displacement products from the European ground motion service. They clustered the points on the bridge, decomposed the LOS signal from two ascending and two descending orbits and studied the relation between displacement and temperature variation. Haghighi and Motagh (2021) studied the hazard resulting from land subsidence in Iran on a national scale using Sentinel-1 images. The displacement maps indicated significant subsidence on a regional scale which also affected transport infrastructure. The intersection of the displacement map with the location of the transport infrastructure allowed to assess the subsidence along railway tracks, highways and road networks. Chang et al. (2016) focused particularly on monitoring of railway tracks on a national scale for the Netherlands and contributed an approach to align the displacement products from multiple satellite orbits. Further, the authors proposed to assess local gradients between neighbouring PS pixels along the railway tracks and to classify the local gradients based on the temporal displacement behaviour. In contrast to the previously discussed studies, Chang et al. (2016) did not use Sentinel-1 but Radarsat-2 images which have a higher spatial resolution but are not freely available.

A quantitative literature review is conducted as part of this thesis. A total of 67 studies are analysed which were published between 2012 and 2026 and deal with InSAR time series analysis for monitoring bridges, railway tracks or highways. The results of the literature review are shown in Figure 3.1 and all analysed studies are listed in Table A.1 in the Appendix. Figure 3.1a shows the total number of studies divided by bridges, railway tracks and highways. The majority of the studies focused on bridge monitoring (40 studies), while a comparable number of studies reported on monitoring of railway tracks (17 studies) and highways (16 studies). The primary focus on bridges can possibly be attributed to the bridges' larger vulnerability compared to railway tracks and highways as shown by studies dealing with bridge failures (see Section 3.1.3). In the following, the sensors used for transport infrastructure monitoring and the targeted scattering types are investigated based on the quantitative literature review. Subsequently, the contributions of the studies are discussed separately for each transport infrastructure type.

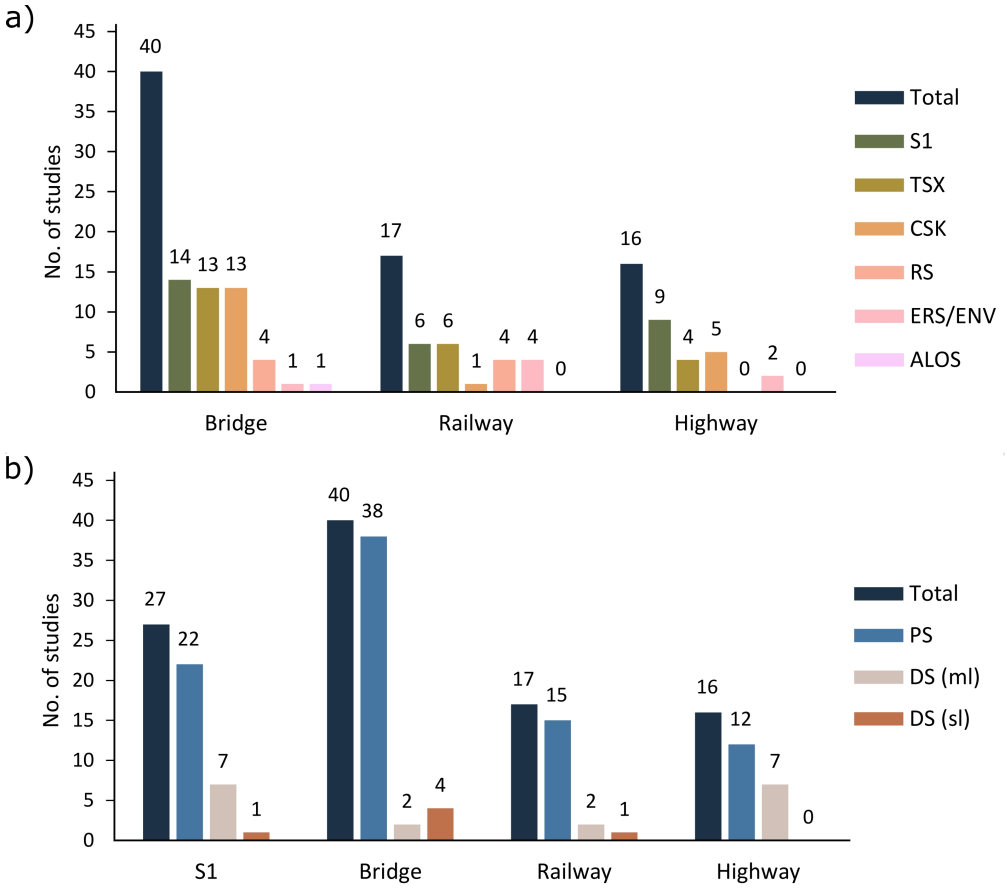


Figure 3.1: Quantitative literature review categorised by the type of infrastructure in combination with a) the utilised SAR satellite mission, and b) the type of addressed scattering including PS pixels, DS pixels in multilook (ml), or in single-look (sl) resolution interferograms. In b), the type of scattering is additionally listed for studies in which Sentinel-1 images are used. In some studies, datasets from more than one satellite mission are used or more than one scattering is addressed. In consequence, the total number of studies is not equal to the sum of the sub-categories (satellite mission or scattering type). The corresponding studies analysed in the quantitative literature review are listed in Table A.1 in the Appendix. Abbreviations: Sentinel-1 (S1), TerraSAR-X (TSX), COSMO-SkyMed (CSK), Radarsat (RS), European Remote Sensing Satellite or Environmental Satellite (ERS/ENV), Advanced Land Observing Satellite (ALOS). Details about these satellite missions are listed in Table A.2 in the Appendix.

3.1.1 Sensors

The total number of studies is subdivided by the SAR satellite missions used (details on the satellite missions are listed in Table A.2 in the Appendix). For bridge monitoring, sensors with either C-band (Sentinel-1, Radarsat, ERS/Envisat; used in 20 studies) or X-band (TerraSAR-X, COSMO-SkyMed; used in 26 studies) were used. Images from ALOS with L-band SAR was used only in one study. The wavelength seems not decisive for bridge monitoring, but instead a higher spatial resolution turns out to be beneficial. Images with a high spatial resolution, i.e. less than 5 m (TerraSAR-X, COSMO-SkyMed, Radarsat; used in 30 studies), were used more frequently than medium resolution images (Sentinel-1, ERS/Envisat, ALOS; used in 16 studies). For monitoring railway tracks, images with high (11 studies) and medium (10 studies) spatial resolution were used with an equal amount.

For highways, it is apparent that Sentinel-1 was used in more than half of the studies. However, images from Sentinel-1 are among the most used in the displacement analysis of all three transport infrastructure types. The reason can be the free-data policy and wide-area coverage of the satellite mission which fostered studies on the suitability of the sensor for transport infrastructure monitoring.

The role of the sensor's spatial resolution for the analysis of transport infrastructure was studied by Wang et al. (2021a) for a railway segment in Beijing, China. The authors compared the displacement results from medium resolution images from Sentinel-1 (5 m×20 m) with very high resolution TerraSAR-X Spotlight images (1 m×1 m) and high resolution TerraSAR-X Stripmap images (3 m×3 m). The displacement maps and time series were found to agree well between the different sensors. Strong scatterers corresponding to PS pixels were found at railway tracks, highway fences and buildings. At the railway tracks, the strong scattering resulted from the rails, sleepers and fasteners. As expected, the authors found that the spatial resolution of the sensor determined the number of PS pixels. From TerraSAR-X spotlight images, about 65 times more PS pixels were found compared to the pixels detected in Sentinel-1 images in a buffer zone of 50 m along the railway track. The differences in the spatial resolution were particularly visible in the mean amplitude image of the three sensors (see also Figure 1.3 for a comparison of TerraSAR-X Stripmap and Sentinel-1 images). In TerraSAR-X Spotlight images, the steel rails, rail fasteners, sleepers, and railway contact net pillars were all visible. In TerraSAR-X Stripmap images, merely the railway contact net pillars were recognisable. In contrast, distinguishing the railway tracks from its surroundings was not possible in Sentinel-1 images. Also, only TerraSAR-X Spotlight images allowed to estimate the differential displacement between two neighbouring railway tracks.

3.1.2 Scattering

The quantitative literature review gives insights on the type of scattering addressed in studies about transport infrastructure monitoring as shown in Figure 3.1b. The majority of the 67 evaluated studies targeted PS pixels with 95 %, 88 % and 75 % of the studies on bridges, railway tracks and highways, respectively. In contrast, DS pixels, either in multilook or single-look resolution, were studied in less than 20 % of the studies for both bridges and railway tracks. For highways, DS pixels in multilook resolution interferograms were used in 44 % of the studies, perhaps due to the wide areas covered by highways and the reduced resolution in multilooked interferograms which decreases the computational demand. While DS pixels in single-look resolution were used in four studies on bridges, they were not used for highway and only once for railway monitoring.
The majority of the studies, in which Sentinel-1 images were used, targeted PS instead of DS pixels. If DS pixels were used in a study, they were addressed in multilooked interferograms. However, multilooking comes at the cost of further reducing the medium spatial resolution of Sentinel-1 images. Consequently, the signal from the transport infrastructure was mixed with the signal from its surrounding which can lead to loss of coherence if the neighbourhood is vegetated. Interestingly, DS pixels in single-look resolution interferograms from Sentinel-1 images were only addressed in one study. This clear preference towards PS pixels suggests that only PS pixels are suitable for analysing the transport infrastructure, while DS pixels are absent. However, the limited availability

of software for single-look DS analysis could have prevented authors from exploiting DS pixels for transport infrastructure monitoring.

Among the studies included in the quantitative literature review, only one explicitly addressed the role of PS and DS pixels. Ma et al. (2019) aimed to achieve sub-millimetre accuracy from InSAR time series analysis with COSMO-SkyMed images for monitoring highspeed railway tracks in China. The railway track is located on a viaduct on which the authors found both PS and DS pixels in single-look resolution interferograms. PS pixels were associated with double bounce at the railway structure itself, i.e. rails and sleepers, as the PS pixels were found along two parallel lines corresponding to the railway tracks. In contrast, DS pixels seemed to stem from single-bounce at the concrete surface of the viaduct. The results indicated a significantly higher DS pixel density compared to PS pixel density. However, insights from this study using COSMO-SkyMed images cannot be directly transferred to Sentinel-1 images due to differences in the sensor's wavelength and spatial resolution.

3.1.3 Bridges

Bridge monitoring received considerable attention as shown by the number of studies in the quantitative literature review. Many studies focussed on methodological improvements which are reviewed in the following.

The deflection of a bridge was estimated by Qin et al. (2017a) from InSAR time series results to assess the structural health. The assessment of the deflection required to estimate and remove the thermally induced displacement signal, which resulted from thermal expansion of the bridge. In several studies, the thermal expansion was estimated by correlating the phase observations with the air temperature using either C-band (Huang et al., 2017; Cusson and Stewart, 2024; Giordano et al., 2025) or X-band images (Fornaro et al., 2012; Lazecky et al., 2017; Tonelli et al., 2023; Long et al., 2025). The thermal expansion of the bridges derived from InSAR time series analysis were further incorporated into numerical models to assess bridge stability (Cusson et al., 2018; Lorenz et al., 2024).

One focus of previous studies on bridge monitoring was on assessing the structural health of the infrastructure (Huang et al., 2018) and providing early warning to decision makers (Talledo and Saetta, 2025). Cusson et al. (2021) proposed early warning thresholds based on the thermal sensitivity estimation to detect anomalous behaviour. Peduto et al. (2018) developed fragility curves that describe the probability of a damage at various bridges in the city of Amsterdam depending on the differential settlement derived from InSAR time series. To derive the fragility curves, the authors complemented the InSAR time series observations with in situ damage assessment and knowledge on the bridge structure. Nettis et al. (2023) suggested a prioritisation scheme for in situ assessment of the bridges' structural health based on the displacement information from InSAR time series analysis combined with the expected losses caused by the collapse of a bridge. Calò et al. (2024b) developed an early warning approach which was implemented in a bridge analysis tool for QGIS (Calò et al., 2024a). It operates on the displacement signal of a bridge decomposed into its longitudinal and vertical displacement. Miano et al. (2024) built an early warning system for

bridges on the hazard assessment at a local and regional level based on statistical measures of the displacement signal.

Studying bridge failure was another focus of previous studies. The goal was to identify precursor displacements and to understand the capabilities of InSAR time series analysis for detection of precursory signals. Sousa and Bastos (2013) detected a precursor displacement from medium spatial resolution European Remote Sensing Satellite (ERS) images at the Hintze Ribeiro Bridge in Portugal which collapsed in 2001. The InSAR time series analysis revealed a maximum precursor LOS mean velocity of 20 mm/year away from the satellite at three out of five pixels at the bridge. Selvakumaran et al. (2018) analysed the precursor to the Tadcaster Bridge failure in England in 2015 using high resolution TerraSAR-X images. Due to a lack of PS pixels, the interferograms were multilooked to exploit DS pixels. Among eight DS pixels on the bridge, only one DS pixel showed an accelerated displacement. The location of that pixel corresponded to the part of the bridge that collapsed. The collapse of the Morandi Bridge in 2018 in Italy, provoked a discussion on the observability of displacements at this particular bridge. While Milillo et al. (2019) postulated that combining images from two COSMO-SkyMed and one Sentinel-1 orbit in a new probabilistic approach allows to observe a precursor displacement, Lanari et al. (2020) disagreed and presented displacement results from both single-look SBAS and SAR tomography which did not show any precursor. Farneti et al. (2023) modelled the uncertainty during displacement estimation for bridges accounting for random and systematic errors. The authors applied the methodology to the Albiano-Magra Bridge in Italy which collapsed in 2020 to analyse the precursor displacement. Although displacements were found at the bridge itself, the authors supposed that the nearby activated slow moving landslide might have caused the bridge failure. All cases of bridge failure analysis were demonstrated after the collapse of the bridges happened. This type of analysis is prone to confirmation bias as precursor displacement is expected to be visible in the displacement results. Moreover, for most of the cases, a potential precursor displacement was visible at a few pixels only. This highlights the need of pixel selection criteria suitable for transport infrastructure monitoring.

Phase unwrapping poses challenges during bridge monitoring, particularly for monitoring of long-span bridges. Modifications in the point network for spatial phase unwrapping were proposed to avoid violating the spatial phase continuity assumption (Zhang et al., 2018; Wang et al., 2023a). For instance, as Song et al. (2023) demonstrated, phase jumps at the expansion joints of a long-span bridge, arising from thermal expansion, can be overcome through phase unwrapping per segment and a local reference point selection for each of the segments.

Other methodological improvements for bridge monitoring include an object-based estimation of the displacement parameters (Kang et al., 2017), an improved localisation of the coherent scatterers through ray-tracing (Sadeghi et al., 2024), the distinction of multiple scattering due to reflections on the water and at the bridge (Qin et al., 2021) and the combination of InSAR time series results with in situ measurements from e.g. a total station (Selvakumaran et al., 2020). Moreover, the displacement time series were clustered based on the temporal characteristics to reveal spatial displacement patterns (Schlögl et al., 2021, 2022; Caspani et al., 2026).

3.1.4 Railway Tracks

The sensitivity of InSAR time series results to displacements at railway tracks was investigated by Chang et al. (2018). To ease the interpretation of the displacement results, the authors proposed to transform the LOS displacement signal into a rail-aligned coordinate system. Further, quality and sensitivity metrics were proposed which consider the relation between the LOS direction of the sensor and the direction of the rail. The authors studied the impact of combining LOS observations from ascending and descending orbit tracks of multiple satellite missions on the quality metrics. All sensitivity analyses were conducted under the assumption that the railway tracks are covered sufficiently with coherent pixels.

Attempts were made to link or replace in situ measurements at railway tracks with displacement results from InSAR time series analysis (Bernhard et al., 2024). Koohmishi et al. (2024) provided a review on the combination of InSAR time series analysis with ground penetrating radar and machine learning for railway monitoring. In this context, the authors identified four main limitations of InSAR time series analysis: The availability of PS pixels at railway tracks, the inability to measure subsurface conditions, limited spatial resolution and the processing of big datasets.

The interpretation of displacements at transport infrastructure requires a precise geolocation of the scatterers in order to assign the displacement to the infrastructure or to the neighbourhood. Hu et al. (2019a) proposed a method to link the position of PS pixels from Radarsat-2 images to corresponding points in a laser scanning point cloud. The method intersects the error ellipsoid of the estimated position of the PS pixels with the laser scanning points. Chang et al. (2020) extended this approach by classifying the PS pixels after the geolocation improvement. Three classes were proposed: PS on railway tracks, on embankments, and in the surrounding. The combination of the InSAR time series results with laser scanning data was shown to improve the geolocation of the scatterers in the medium spatial resolution images from Sentinel-1. However, this approach requires the availability of laser scanning data.

In addition to studies on methodological improvements, there are also studies that aimed to understand the causes of displacement at railway tracks. North et al. (2017) studied the relation of subsidence of both, railway and highway, to the soil type and identified the highest subsidence at railway tracks on peat soils. Similarly, Jia et al. (2021) analysed the relation between displacement and ground water level, while Qin et al. (2017b) studied the thermal dilation of railway tracks.

3.1.5 Highways

In previous publications, the displacement at highways was studied to determine the related hazard. Niu et al. (2024) applied a large buffer around the highways and clustered the displacement time series in space and time to infer a geological hazard susceptibility map. Similarly, Macchiarulo et al. (2022a) analysed the PS density and mean displacement velocity per regularly spaced segment along the highways. Wang et al. (2019) studied the driving factors for displacements at highways and categorised the displaced pixels into ground subsidence in the highway's neighbourhood, dynamic load due to traffic, or post-construction settlement. Monti et al. (2025) focused on hazards in the surrounding of highways by assessing the landslide susceptibility.

The relation between highway displacements and the type of soil was analysed in several studies. Delgado Blasco et al. (2019) studied displacements in a region covering the city of Rome and its surrounding and found the maximum displacement at unconsolidated deposits such as gravel, sands and clay. The same authors repeated their observation in consecutive studies (Orellana et al., 2020, 2023). The hypothesis that displacements are associated to the underlying soil type at the highway inspired other researchers to incorporate a tailored temporal displacement model into InSAR time series analysis. These displacement models address the consolidation process of the soil (Zhu et al., 2021; Xing et al., 2022), or use the precipitation as a driving factor for displacement (Long et al., 2025). These displacement models have in common that their parameters are estimated after the small baseline interferograms were spatially unwrapped.

3.1.6 Regional and Local Displacements

It can be assumed that measuring local displacements, which only occur at the transport infrastructure, is challenging when using Sentinel-1 images due to the medium spatial resolution of the sensor. Here, studies are reviewed in which Sentinel-1 images have been used for transport infrastructure monitoring. Regional displacement signals can result from seasonally frozen ground (Shi et al., 2022), geological hazards (Niu et al., 2024), landslides (Monti et al., 2025), or large-scale land subsidence (Haghighi and Motagh, 2021; Shami et al., 2022; Xue et al., 2024). The local displacement signal can be targeted by analysing the scatterers within a buffer around the transport infrastructure (North et al., 2017; Macchiarulo et al., 2022a). However, it may not be clear from the scatterers within the buffer alone whether the displacement affects only the infrastructure or also a larger area. Although Wang et al. (2021a) targeted local displacement signals, merely regional displacements were present in the study area observed in Sentinel-1 images. This was also shown by the displacement map from TerraSAR-X images of the same area.
Local displacements were explicitly targeted by Chang et al. (2020) through the geolocation improvement with laser scanning data which was used to decide whether the PS pixels belonged to the railway track. Delgado Blasco et al. (2019) and Orellana et al. (2020) showed several examples of both regional and local displacements at the highway network around the city of Rome derived from Sentinel-1 images. The literature shows that the use of Sentinel-1 images for transport infrastructure monitoring is not limited to displacements on a regional scale but also localised displacements can be detected if enough coherent pixels are identified.

3.1.7 Discussion

The literature review revealed a variety of studies investigating the capabilities of InSAR time series analysis for transport infrastructure monitoring. Although national scale monitoring is particularly useful for railway tracks and highways which cover large areas, the employed methods are not tailored to the task. Products from national ground motion services have, nevertheless, been used for hazard assessment at transport infrastructure. The review showed that methodological improvements were mostly presented for bridge monitoring including tailored phase unwrapping and analysis of thermal expansion of the bridge. Early warning systems were developed to prevent bridge failure. The studies on railway tracks targeted improvement of the geolocation of the scatterers, combination with in situ

measurements and investigating the sources for displacement signals. For highways, studies focused on assessing hazards and modelling the relation between displacement and soil characteristics.

The literature review suggests that transport infrastructure monitoring is possible on a national scale. However, while most studies on railway and highway monitoring discussed the use of final displacement products, none focussed on the requirements for the InSAR time series method for deriving realistic displacement results. Although several InSAR time series methods might be suitable to derive the displacement products, the assumptions underlying the methodology need to fit to the type of displacement present at the transport infrastructure. In this thesis, the requirements for an InSAR time series method are discussed and a method is proposed accordingly.

The quantitative literature review shows that high-resolution sensors were preferably used for bridge monitoring, but displacements were also derived from medium spatial resolution Sentinel-1 images. In general, Sentinel-1 images were often used, particularly for highways, despite the sensor's coarse resolution. As expected, the spatial resolution of Sentinel-1 is a limiting factor as shown by the comparison with high resolution images from TerraSAR-X. The review also shows that InSAR time series analysis with Sentinel-1 images is not limited to regional displacements, but also localised displacement signals can be observed. The availability of coherent pixels at transport infrastructure is a frequently mentioned challenge. Consequently, the selection of coherent pixels is even more important in Sentinel-1 images. The analysis of the targeted scattering types in the quantitative literature review reveals that predominantly PS pixels were used, while DS pixels in full resolution have rarely been exploited. The analysis of PS and DS pixels in COSMO-SkyMed images of railway tracks suggested, although not being directly transferable, that also DS pixels can be present at transport infrastructure in Sentinel-1 images.

In conclusion, the selection of coherent pixels is essential for the success of transport infrastructure monitoring, especially for medium spatial resolution Sentinel-1 images, to enable the observation also of localised displacement signals. In this thesis, the characteristics of both, PS and DS pixels, at transport infrastructure are investigated.

3.2 Analysis of Temporarily Coherent Scatterers

The analysis of TCS pixels is, as opposed to the selection of CCS pixels, subject to ongoing research and, hence, the relevant literature about TCS analysis for InSAR time series analysis is reviewed in this section. Analysing TCS pixels in InSAR time series methods allowed to also observe displacements during the lifetime of individual infrastructure which have been built or demolished during the monitoring period (Hu et al., 2019b; Dörr et al., 2022). As a consequence, higher pixel densities were achieved compared to CCS pixels only.

3.2.1 Adjustment of the Study Period

In order to incorporate TCS pixels in the time series analysis, TCS pixels need to be identified and distinguished from CCS pixels. While the signal of a CCS pixel is coherent over the entire study period, the signal of TCS pixels is coherent only during their coherent lifetime. Therefore, the displacement time series should be derived for TCS pixels merely during their coherent lifetime to avoid error propagation from the incoherent signal during phase unwrapping. One way of handling TCS pixels is to shorten the time series so that TCS pixels appear as CCS pixels. Aziz Zanjani et al. (2024) followed this approach in order to study high-rise buildings along the coastline of Miami, United States. While some of the buildings were constructed, others were demolished during the overall study period. However, these changes happened at different times. The authors created multiple subsets of the time series according to the lifetime of the individual buildings to estimate the displacement time series. Another example is the approach taken by Izumi et al. (2022) which targets the displacement at peatlands in Indonesia. The signal at the peatlands gradually decorrelated over time and, additionally, lost coherence abruptly due to fire events. The authors subdivided the three-year study period into three one-year study periods and estimated the displacement time series with the SBAS method for each of the study periods independently. This approach led to a higher point density and allowed to study displacement in subsets of the time. Manually adapting the study period, as shown in these two studies, is a workaround for the displacement estimation of TCS pixels, but it is not optimal. The individual coherent lifetime of each TCS pixel was not considered, and relevant displacement information was thereby discarded. Moreover, prior knowledge about the coherent lifetime of the targeted pixels was required. To overcome these limitations, the coherent lifetime needs to be identified from the SAR stack for each TCS pixel.

3.2.2 Approaches Based on Change Detection

The identification of TCS pixels was often approached via change detection (Ferretti et al., 2004; Brcic and Adam, 2013; Ansari et al., 2014; Hu et al., 2019b; Dörr et al., 2022). This approach was motivated by the idea that a change of the scattering mechanism due to surface changes leads to the start or end of the signal's coherent period, e.g. construction or demolition of a building.

The first change detection approach was introduced by Ferretti et al. (2004) who observed that the change in the phase noise of a PS pixel was connected to a significant change of the pixel's amplitude. As a solution, changes were detected in the amplitude time series assuming a normal

distribution for the amplitude. However, the amplitude is not normal distributed, but follows a Rice distribution for PS pixels with a strong backscattering and a Rayleigh distribution for low-backscattering such as DS pixels. The study did not provide any quality assessment nor did the authors discuss how TCS pixels were included into the InSAR time series analysis.

Brcic and Adam (2013) followed up on the change detection on the amplitude time series and compared different Likelihood Ratio Tests (LRTs) based on Gaussian, Rice and Rayleigh distributions. Based on simulations, the authors concluded that the Gaussian change detection worked best considering performance and speed, although all methods performed equally well on a stack of ERS SAR images. The authors mentioned the incorporation of TCS pixels into the InSAR time series analysis as an open topic for future research.

The method presented by Ansari et al. (2014) focuses on the transition between scattering with Rayleigh distributed and Rice distributed amplitudes which represents incoherent and coherent signals, respectively. The most appropriate model was selected among a set of hypotheses using a bayesian estimation framework. Three hypotheses were formulated: Firstly, the pixel is not a TCS pixel if the amplitude follows a Rice distribution. Secondly, the pixel is a fading TCS pixel if the amplitude transitions from the Rice to the Rayleigh distribution. Thirdly, the pixel is an appearing TCS pixel if the amplitude transitions from the Rayleigh to the Rice distribution. The method was shown to be robust based on simulated data. Also, a case study with TerraSAR-X images of Berlin proved that a newly constructed building can be detected. The TCS detection was validated spatially based on the location of the constructed building. However, a temporal validation to ensure the plausibility of the change dates in the real data is missing. Also in this study, incorporating TCS pixels into InSAR time series analysis was outside of the scope of the study.

3.2.3 Integration into Time Series Analysis

Hu et al. (2019b) proposed an extension for the InSAR time series method implemented in the software Delft Persistent Scatterer Interferometry (DePSI) (Van Leijen, 2014) to include the analysis of TCS pixels. The extension of the method consists of three main steps: Identification of TCS candidates, change detection and displacement retrieval for CCS and TCS pixels. Similar to previous studies, the authors identified TCS pixels based on the amplitude distribution. A TCS candidate was assumed to have a high amplitude dispersion compared to PS or DS pixels. Therefore, two amplitude dispersion thresholds were applied, a lower threshold to select PS pixels and a higher threshold to identify TCS candidates. According to the authors, TCS pixels were mistaken for incoherent DS pixels when amplitude dispersion was used as the sole criterion. Incoherent DS pixels were detected and removed with a hypothesis test that identifies pixels whose amplitude follows a Rayleigh distribution over the entire time span. For the TCS pixels, changes were detected in the time series with a hierarchical estimation that splits the time series into two subsets and identifies the most likely change date. The basis of the hypothesis test for the change detection was the assumption that each of the two tested subsets follows a different Rayleigh distribution (for details about the method see Section 4.3.1.3).
Once all change dates were detected for each TCS pixel, the displacement time series were esti-

mated. The InSAR time series method of DePSI was modified for this step. A first-order network was created consisting of CCS pixels only. Afterwards, the network was densified with CCS and TCS pixels. For each TCS pixel, arcs to the closest first-order points were created and the displacement and height error parameters were estimated for the interferometric arc-phases in a single-reference interferogram network. The coherent lifetime of a TCS candidate was determined based on the quality of the parameter estimation.
Two case studies were shown by Hu et al. (2019b) to demonstrate the method. The first one analysed Sentinel-1 images of the city of Delft, Netherlands, in which construction work was present. The plausibility of the change detection result was reasoned from an increase of the amplitude signal at approximately the same time for the pixels associated with a building. However, the authors reported that the initially selected TCS pixels based on the amplitude analysis were "extremely noisy". Therefore, TCS pixels were further removed based on the uncertainty of the parameter estimation for the arcs between the TCS candidates and the closest first-order points. The second case study with TerraSAR-X images of the airport in Shanghai, China, showed construction work during the whole study period. The amount of scatterers was doubled by using TCS compared to the conventional CCS-only analysis. Besides the displacement analysis, the change dates estimated for the TCS pixels were used to identify the constructed or demolished infrastructure on the airport site.
Compared to the previously discussed studies, Hu et al. (2019b) provided a methodology that additionally estimates the displacement time series of TCS pixels. However, the proposed methodology requires anticipating a temporal displacement model for phase unwrapping, which is common to most PSI methods that utilise a single-reference interferogram network. The authors did not discuss the implications of the selected single-reference interferogram network. However, for TCS pixels, whose coherent lifetime does not cover the reference image, the phase of the reference image is expected to add noise to the interferograms within the coherent lifetime. This problem is inherent to a single-reference interferogram network, but can be solved using a redundant interferogram network. A major limitation of the study was the noisy change detection result. The results of the method showed an increased point density, but the resulting displacement maps gave the impression of added salt-and-pepper noise resulting from TCS pixels. As PS pixels were targeted with the amplitude based analysis, the TCS pixels should appear at infrastructure such as buildings and not in presumably vegetated areas as apparent in the displacement map.

Hu et al. (2019a) applied the amplitude-based TCS identification and change detection approach proposed by Hu et al. (2019b) in the context of transport infrastructure monitoring. However, the goal of the study was to improve the geolocation of the scatterers along railway tracks by combining the InSAR time series results with laser scanning measurements. TCS pixels were selected during the time series analysis but the authors did not evaluate the suitability of the method for transport infrastructure. The authors stated a significant improvement of the point density but did not analyse whether the detected TCS corresponded to changes at the railway tracks, or whether TCS improved the observability of the railway tracks.

An extension of the TCS method by Hu et al. (2019b) was proposed by Hu et al. (2024) which reduces the high number of false positive detections. The amplitude images were spatially low-pass filtered before identifying TCS candidates to reduce the effect of speckle in the SAR images. The

amplitude based change detection method remained unchanged. A mathematical relation between the phase standard deviation and amplitude dispersion was derived from simulations for varying time series lengths to improve the selection of TCS pixels using an amplitude dispersion threshold. A change date refinement procedure was proposed because the authors reported that the initial change date can be incorrect. In the refinement, the temporal and spatial phase unwrapping results are analysed to remove incoherent images and adjust the estimated coherent lifetime of the TCS pixels. However, for a refinement strategy to work correctly, a good first approximation of the coherent lifetime is required. The authors applied the same case study at Shanghai airport as Hu et al. (2019b), employing both TerraSAR-X and COSMO-SkyMed images. The displacement maps appeared less noisy compared to the results of Hu et al. (2019b). A validation of the change dates was not provided.

Another time series approach for TCS analysis was proposed by Dörr et al. (2022) which incorporates TCS pixels into the Multi-stack Small Baseline Subset (MSBAS) approach (Schenk, 2015) and uses single-look resolution interferograms for the analysis of urban infrastructure. For the identification of TCS candidates, the hypothesis test from Hu et al. (2019b) was applied. However, Dörr et al. (2022) found that, even though the phase change was related to an amplitude change, the change date estimated from the amplitude did not reflect the onset of the coherent lifetime. There were a significant time delays between the amplitude change dates and the coherent lifetime of the scatterers in built environments. This observation led the authors to enhance the change detection by a phase-based change date refinement. TCS pixels were assumed to have a different phase noise level before and after the change (Figure 4.5a and b). However, the phase noise cannot be directly assessed as the phase is wrapped and the noise is superimposed by phase contributions from displacement, DEM error and atmospheric phase delay. Using the interferometric phase noise as an indicator for a change in the scattering mechanism requires to estimate and remove the phase contributions. The change date from the amplitude change detection was used by Dörr et al. (2022) as initialisation to estimate and remove the phase contributions from the interferograms within each subset of the time series given by the initial change date. Afterwards, the most likely change date was searched with a proposed LRT based on the marginal distribution of the interferometric phase (for details see Section 4.3.1.1). For this purpose, the phase contributions were estimated in each subset. The final change dates were the ones for which a higher coherence level was achieved, either from amplitude change detection or phase-based refinement. Only TCS pixels exceeding a given coherence threshold were selected for the time series retrieval. An adaptive threshold for the coherence was proposed to adjust for the different lengths of the coherent lifetime of each TCS pixel. In the next step, Dörr et al. (2022) included the TCS pixels into the InSAR time series method of MSBAS. Reliable CCS pixels in a small area were averaged to form a reference point that reduces the atmospheric effect in a small area. Then, the interferometric arc phases between the reference point and each CCS and each TCS pixel were computed. The phase contributions were estimated for the arcs. The phase contributions from displacement and DEM error were removed from the interferograms in a small baseline network and the residual phases in the interferograms were spatially unwrapped using the grid-based phase unwrapping approach implemented in the Stanford Method for Persistent Scatterers (StaMPS) (Hooper and Zebker, 2007). The phases of TCS pixels were only unwrapped during their coherent lifetime. Finally, the phase contributions were restored and

the interferogram network was inverted to retrieve the displacement time series. While CCS pixels were temporally referenced to a common first acquisition, the TCS pixels were aligned with the displacement time series of neighbouring CCS pixels that exhibited a similar temporal displacement pattern.
Dörr et al. (2022) presented a case study with Sentinel-1 images of the city of Ca Mau, Vietnam. The study area is characterised by high construction activity. The authors reported an increase in the point density due to TCS pixels. Moreover, there was a slight increase in average coherence of all coherent pixels through the phase-based change point refinement compared to amplitude-based change detection only. The TCS pixels were validated spatially by comparison with the location of constructed buildings in optical images.
The applicability of the method from Dörr et al. (2022) is limited by the assumptions taken for the phase-based refinement. The proposed method requires a temporal displacement model during the phase-based refinement to retrieve the phase noise in the interferograms and to correctly estimate the change date. Consequently, only TCS pixels which follow the predefined temporal displacement model are selected. Furthermore, the initial change point from the amplitude change detection must be close to the true change date to facilitate convergence of the change point refinement. Since the phase noise is not available prior to the phase-based refinement, it has to be estimated for each change point candidate. As a result, the estimated phase noise depends on how the time series is divided into subsets, because different interferograms are available for the estimation in each subset. For a reliable estimation of the phase contributions during the phase-based refinement, a set of reliable pixels is required in the neighbourhood to form a spatial reference point. The distance to the reference point impacts the estimation quality for both, the change detection and the displacement retrieval. An extension of this change detection approach is proposed in this thesis to overcome the discussed limitations.

In a recent study by Li et al. (2025), the usage of TCS pixels was motivated by observing excavations related height changes of the scatterers due to mining activities. Pixels exhibiting a coherent signal before and after a height change were targeted and interferograms connecting the two periods were supposed to be incoherent. In contrast to the previous studies, DS pixels in unwrapped and multilooked interferograms in a small baseline interferogram network were used instead of PS pixels in wrapped single-look interferograms. The authors proposed a functional model for the interferometric phase which incorporates a different DEM error and mean displacement velocity for the periods before and after the change. The parameters were estimated from the unwrapped interferograms for all change date candidates. Finally, the change dates were selected which minimised the sum of squared phase residuals. Hence, this approach is similar to the phase-based approach proposed by Dörr et al. (2022) as both methods assess the phase noise level to identify the change date. The method from Li et al. (2025) assumes a height change for each pixel, but areas with a significant height change are classified with a threshold on the difference of the estimated DEM errors. The provided simulations showed the improvement of the proposed method compared to the conventional SBAS method. The proposed method was further demonstrated with Sentinel-1 images of a mining region.
The method assumes that the height of each pixel changes directly from one value to another. Thereby, it is also assumed that the pixel's signal is coherent before and after the change. While

this might be suitable for excavations, it limits the method's suitability for other applications in which TCS pixels exhibit an incoherent signal at least over part of the time series.

3.2.4 Exploitation of the Signal Characteristics

State-of-the-art InSAR time series methods for TCS analysis included change detection as discussed in the previous section. A variety of methods particularly suited for detecting changes in SAR stacks were proposed in the literature and were demonstrated for various applications, for instance damage mapping after an earthquake (Monti-Guarnieri et al., 2018), detection of construction work in urban areas (Villamil Lopez and Stilla, 2022), mapping volcanic ashes (Jung et al., 2016) or volcano lava flow (Costa et al., 2025b), and identifying changes in open-pit mines (Costa et al., 2025a). For TCS analysis, methods that map spatial changes are unsuitable, e.g. damage mapping by comparing pre- and post event images (earthquake, volcanic ashes, lava flow), because the methods often require prior knowledge about when the change event occurred. Methods targeting temporal changes, e.g. for monitoring continuous changes on the surface (construction, open-pit mine), infer multiple changes which may be unrelated to the coherent lifetime of a TCS pixel. However, only the change between a coherent and incoherent period is of relevance for InSAR time series analysis of TCS pixels. The change detection methods differ primarily by the characteristics of the SAR signal that are targeted by each method. So far, predominantly incoherent change detection, i.e. detection of changes in amplitude time series, was used to identify TCS pixels in the context of InSAR time series analysis. More recent studies also applied coherent change detection methods that directly exploit the interferometric phase to identify the coherent lifetime from the phase noise level. Coherent change detection methods are more sensitive to changes compared to incoherent methods due to the sensitivity of the phase (Monti-Guarnieri et al., 2018). Another set of coherent change detection methods can be found in the literature. These change detection methods rely on the coherence matrix instead of the phase noise. Coherence-matrix-based approaches were not yet studied in the context of TCS pixels for displacement analysis.

Monti-Guarnieri et al. (2018) assumed a model for the structure of the coherence matrix. This model includes two coherent blocks which are uncorrelated with each other as expected for a PS pixel under change. The observed coherence matrix was evaluated against the modelled coherence matrix using a LRT (for details see Section 4.3.1.2). The sensitivity of the methodology was studied using simulations and the applicability for damage mapping after an earthquake was demonstrated using Sentinel-1 images of the village Amatrice, Italy. The goal of the case study was to detect damages at buildings. The validation showed that most of the changes appeared after the earthquake. The method from Monti-Guarnieri et al. (2018) was extended for multiple changes in the time series by Manzoni et al. (2021). Similar approaches include the method by Costa et al. (2024) which detects block structures in the coherence matrix, and an extension of this method, which limits the bandwidth along the diagonal of the coherence matrix to improve the change detection for multiple rapid changes (Costa et al., 2025a).

3.2.5 Discussion

The methods for TCS analysis proposed in literature were predominantly developed for urban infrastructure and have not been evaluated for transport infrastructure. Buildings are bright scatterers for which the assumption of a significant change in the amplitude distribution is reasonable. Nevertheless, the coherent lifetime might start earlier or later than the detected change in the amplitude as shown by Dörr et al. (2022). However, in the context of transport infrastructure, the backscattering differs from that of buildings. While railway tracks yield a high amplitude in Sentinel-1 images, the road surface of highways reflects most of the signal away from the sensor, resulting in low amplitudes (Figure 1.3). In contrast, bridges can lead to a high amplitude signal, e.g. due to double bounce scattering. In the context of transport infrastructure, appearing TCS pixels are assumed to be more common compared to disappearing TCS pixels due to the construction of new infrastructure. During the construction of transport infrastructure, construction vehicles might lead to a higher amplitude signal and potentially also to coherent backscattering. This demonstrates that the assumptions about TCS pixels made for buildings are not directly transferable to transport infrastructure. TCS pixels have not yet been analysed for transport infrastructure monitoring and more research is required to understand the characteristics of TCS pixels at railway tracks, highways and bridges in Sentinel-1 images.

The method proposed by Dörr et al. (2022) is currently the most promising approach to TCS analysis as it overcomes the limitations of amplitude-based change detection and targets the coherent lifetime of the scatterers through the phase-based change point refinement. However, the phase noise estimation, which was developed within the framework of the MSBAS approach, was tailored to urban infrastructure monitoring, which poses different challenges compared to transport infrastructure. A predefined temporal displacement model was applied which includes temperature correlated displacements and a mean displacement velocity. This formulation is suitable if the displacement signal is assumed to be independent for each scatterer (see review on PSI methods in Section 2.3.5). The quality of the phase noise estimation is pivotal for the accuracy of the change detection. A major limitation of the method proposed by Dörr et al. (2022) is the anticipated temporal displacement model which yields wrong phase noise estimates for TCS pixels deviating from the model. Especially non-linear displacements may pose challenges during change detection. Another limitation is that the estimation quality of the phase contributions depends on the location of the change date within the time series. The parameters for the phase contributions are estimated from the interferograms in each subset defined by the change date. While longer time series are favourable for the estimation of the phase contributions, reliable estimation might not be possible from short time spans. Moreover, a sufficiently good initialisation of the change date is required to remove the phase contributions and facilitate convergence of the parameter estimation strategy in MSBAS.
For transport infrastructure monitoring using Sentinel-1 images, a spatially correlated displacement signal is anticipated (see discussion in Section 1.2). The spatial correlation of the displacement signal was not exploited by the method proposed by Dörr et al. (2022). In this thesis, an extension of the phase-based change point refinement is proposed that harnesses the spatial correlation of the signal and does not impose temporal assumptions for the phase noise estimation during change detection. The proposed method estimates the phase noise for each interferogram separately by ex-

ploiting the signal in the spatial neighbourhood. In this way, the phase noise level is not dependent on the change date. Moreover, in contrast to the phase-based change point refinement, the change date can directly be inferred from the phase noise and does not require an initialisation.

The literature review reveals that TCS analysis approaches focused predominantly on PS pixels. Consequently, TCS pixels were incorporated into existing PSI methods. DS pixels in single-look resolution, have not received any attention. This can be attributed to the complexity of the decorrelation mechanisms present at DS pixels which are difficult to differentiate from the abrupt decorrelation which characterises a TCS pixel.
The method based on the coherence matrix proposed by Monti-Guarnieri et al. (2018) is supposed to target DS pixels. However, the modelled block structure in the coherence matrix does not reflect the variety of decorrelation mechanisms inherent to DS pixels. Instead, it corresponds to the long-term coherent signal of an ideal PS pixel. Whether a PS or a DS pixel is addressed also depends on the neighbourhood used for the coherence matrix estimation in order to preserve the spatial details in the filtered phase. For DS pixels, an adaptive spatial neighbourhood facilitates the estimation of the coherence matrix by excluding neighbouring PS pixels. A non-adaptive spatial neighbourhood can be used to detect changes at PS pixels from the coherence matrix. A PS pixel may exhibit a significantly different backscattering compared to its neighbourhood. However, the coherence matrix cannot be estimated from a single PS pixel because several pixels are required to correlate the SAR observations. This means, the change detection based on the coherence matrix is only applicable for PS pixels if neighbouring pixels show a similar scattering behaviour, which is reasonable if the pixels belong to the same object e.g. to the same railway track. In this thesis, the coherence-matrix-based change detection from Monti-Guarnieri et al. (2018) is applied to PS pixels using a non-adaptive spatial neighbourhood because a spatially correlated displacement signal is assumed for transport infrastructure in Sentinel-1.
In this thesis, the applicability of three change detection methods in the context of TCS analysis is evaluated for transport infrastructure monitoring. The change detection methods comprise the phase-based change detection extending the work of Dörr et al. (2022), the coherence-matrix-based change detection of Monti-Guarnieri et al. (2018), and the amplitude-based change detection of Hu et al. (2019b).

The literature review shows that the TCS methods were often validated on real data based on the location of the scatterers. A detected scatterer was assumed to be plausible if the location of the TCS pixel corresponded to a physical object. While this validated the results spatially, a temporal validation was often missing. The presence of that physical object during the coherent lifetime of the TCS pixel increased the plausibility of the result. In this thesis, a temporal validation strategy is proposed which assesses the plausibility of the coherent lifetime based on optical images for reference.

4 A New Approach for Monitoring of Temporarily Coherent Transport Infrastructure

The methodology tailored to transport infrastructure monitoring which is developed within this thesis is presented in this chapter and builds upon the work by Piter et al. (2024, 2025a). First, an overview on the components of the methodology is given in Section 4.1 followed by the prerequisites and assumptions in Section 4.2. The processing steps of the methodology are presented in Section 4.3 and 4.4. To conclude the chapter, a theoretical discussion of the proposed methodology is provided in Section 4.5.

4.1 Overview

The overall goal of the proposed method is to monitor displacements at transport infrastructure derived from a stack of Sentinel-1 SAR images. The proposed workflow (Figure 4.1) consists of two main steps: Coherent lifetime estimation (Section 4.3) and time series analysis (Section 4.4). The method takes the coregistered SLC images as input and produces a displacement map with the displacement time series of the selected scatterers.

Each scatterer has an individual coherent lifetime which refers to the period in which the scatterer has a coherent signal. The coherent lifetime can cover the whole study period (CCS pixel) or a part of it (TCS pixel). To identify the coherent lifetime of each pixel, an approach is proposed consisting of change detection (Section 4.3.1) and pixel selection (Section 4.3.2).
During change detection, it is tested whether any change has occurred in the pixel's scattering mechanism. In case the scattering mechanism of a scatterer has changed, the interferometric phase decorrelates between the two subsets and the pixels show a coherent signal within a part of the time span. Several change detection methods for urban infrastructure have been proposed in the literature. Three change detection approaches with different assumptions are integrated into the coherent lifetime estimation framework. An extension of one of the methods is proposed to suit transport infrastructure. All three methods are assumed to address temporarily coherent PS pixels.

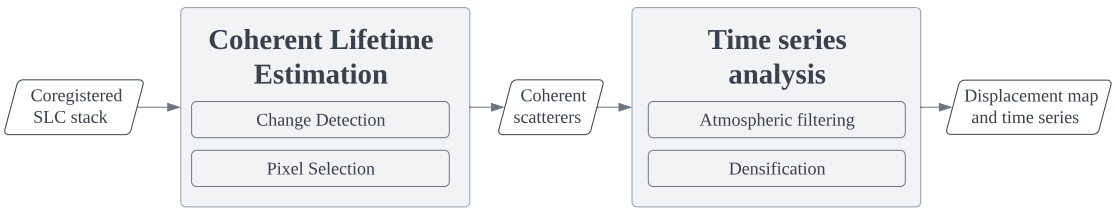


Figure 4.1: Flowchart of the proposed InSAR time series approach for transport infrastructure monitoring.

After change detection, pixels suitable for InSAR time series analysis are selected. This means, the quality of the interferometric phase is assessed through approximations and in case of high-quality, the pixel is selected. Depending on whether the pixel has exhibited a change, the coherent lifetime either spans the time before or after the change, or it covers the whole study period.

Finally, the displacement time series of the selected coherent scatterers are retrieved with a two-step approach consisting of an atmospheric filtering (Section 4.4.1) and a densification (Section 4.4.2). For this purpose, two sets of coherent pixels are used. The first set, called first-order points, comprises pixels of exceptionally high quality, which are used to estimate and remove the atmospheric phase contribution from the interferograms. The first-order points are selected among the CCS pixels.
During the densification, the displacement time series is estimated for a dense set of second-order points. In order to treat each scatterer according to its individual coherent lifetime, an approach is proposed which retrieves the displacement time series for the second-order points which consist of CCS and TCS pixels. In this way, the phases of all pixels are unwrapped according to each pixel's coherent lifetime.

4.2 Prerequisites and Assumptions

The InSAR time series analysis method requires a precisely coregistered stack of SAR images as input. Multilooking of the interferograms is avoided to maintain the highest possible spatial resolution. Moreover, the flat-earth and the topographic phase contribution are removed prior to the analysis. The phase contributions from orbital inaccuracies of the satellite mission and thermal noise of the sensor are assumed to be negligible which is reasonable for Sentinel-1.

Within the InSAR time series analysis, the displacement signal is sampled in time and space. While the temporal sampling is given by the temporal resolution of the sensor, here either 6 or 12 days, the spatial sampling is more heterogeneous. It depends on the spatial resolution and the distance between the coherent pixels. A spatially correlated displacement signal is expected to be present at the transport infrastructure and its vicinity (see discussion in Section 1.2). It is assumed that the spatial sampling given by the coherent pixels is sufficient to retrieve the displacement signal using spatial unwrapping. This requires that the phase difference between two neighbouring pixels does not exceed half the wavelength to avoid aliasing of the signal. Individual pixels which show a significantly different displacement signal from their surrounding are not considered, as their displacement signal is not confirmed by other pixels which reduces confidence in the interpretation of the displacement signal.

It is assumed that infrastructure are either present during the whole study period, or are constructed or demolished during the study period. Consequently, a maximum of one change is assumed to occur at a pixel (Figure 4.2a), thus multiple changes, such as temporal loss of coherence due to snow, are not relevant for the goal of this thesis. Scatterers whose signal decorrelates between every pair of image acquisitions can be considered as constantly changing and are treated as noise in the time series analysis. Three types of scatterers result from the assumption of a maximum of one

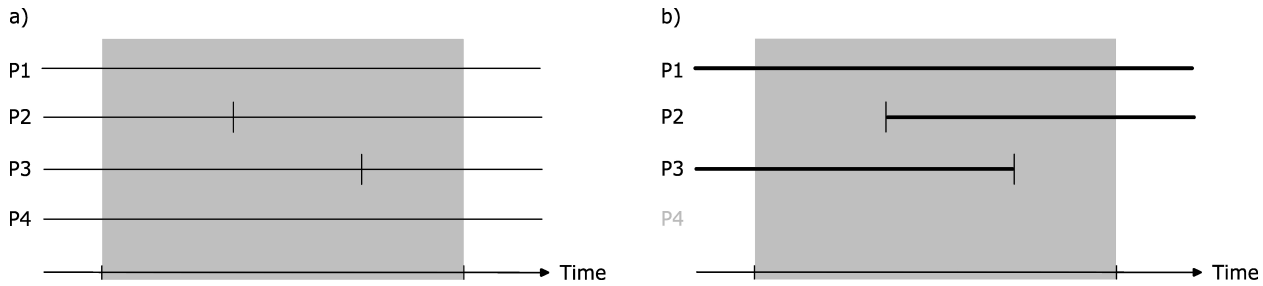


Figure 4.2: Examples for the coherent lifetime estimation for four pixels P1-P4, each depicted with a horizontal line. a) The change dates from the change detection are shown by a small vertical line. b) The selected pixels are depicted with their coherent lifetime indicated by the bold line. Gray area in the background depicts the study period. The pixels P1 and P4 do not exhibit a change in the scattering mechanism. P1 is coherent while P4 is not. Consequently, the displacement time series of P4 cannot be retrieved. P2 and P3 exhibit each a change but at different times. While the change of P2 marks the beginning of its coherent lifetime, the change of P3 ends the coherent lifetime.

change during the study period depending on their coherent lifetime (Figure 4.2b): The coherent lifetime of a CCS pixel covers the whole study period. The coherent lifetime of an appearing TCS pixel starts during the study period. The coherent lifetime of a disappearing TCS pixel ends during the study period. Decorrelated pixels, however, do not have a coherent lifetime as their signal is incoherent and are therefore not explicitly considered.

4.3 Coherent Lifetime Estimation

The goal of the coherent lifetime estimation is to identify pixels that maintain a coherent signal over a part or the whole study period. The flowchart for this estimation is depicted in Figure 4.3. First, changes in the scattering mechanism of a pixel are detected and second, the pixels with a coherent signal are selected. Multiple approaches for both, change detection and pixel selection, are presented as part of the methodology. The suitability of the approaches for transport infrastructure is evaluated in the experiments (Chapter 6).

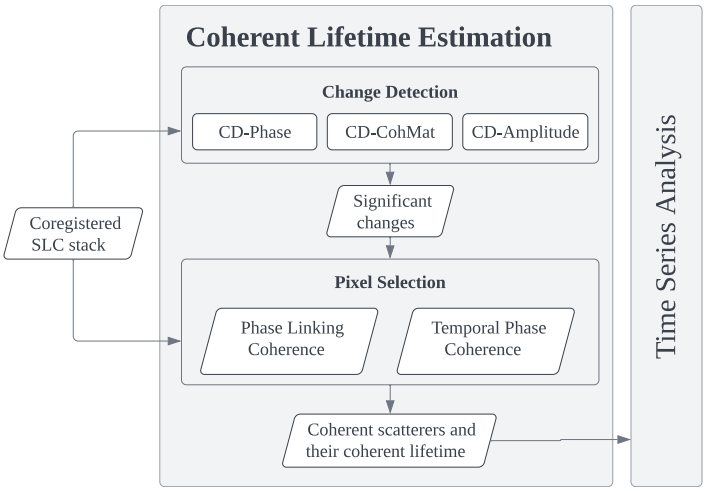


Figure 4.3: Flowchart of the proposed coherent lifetime estimation.

4.3.1 Change Detection

The aim of the change detection is to identify whether a pixel exhibits a change in its scattering mechanism and if so, to determine the image acquisition n after which this change happens. For this purpose, N temporally ordered SAR images with their indices $l_0 = \{1, \ldots, N\}$ are given. The change date divides the time series into two subsets with indices $l_1 = \{1, \ldots, n\}$ and $l_2 = \{n+1, \ldots, N\}$. As the time of the change is unknown prior to change detection and could happen between any consecutive acquisitions, the change date is searched by evaluating the likelihood of a change after each image. Finally, for each pixel the image is selected after which the change most likely occurred. The result of the change detection is the change map, which contains the change date n for each pixel and the score map indicating the significance of the detected changes. Whether the most likely change date actually is significant is subsequently determined by applying a threshold on the likelihood score related to the most likely change date.

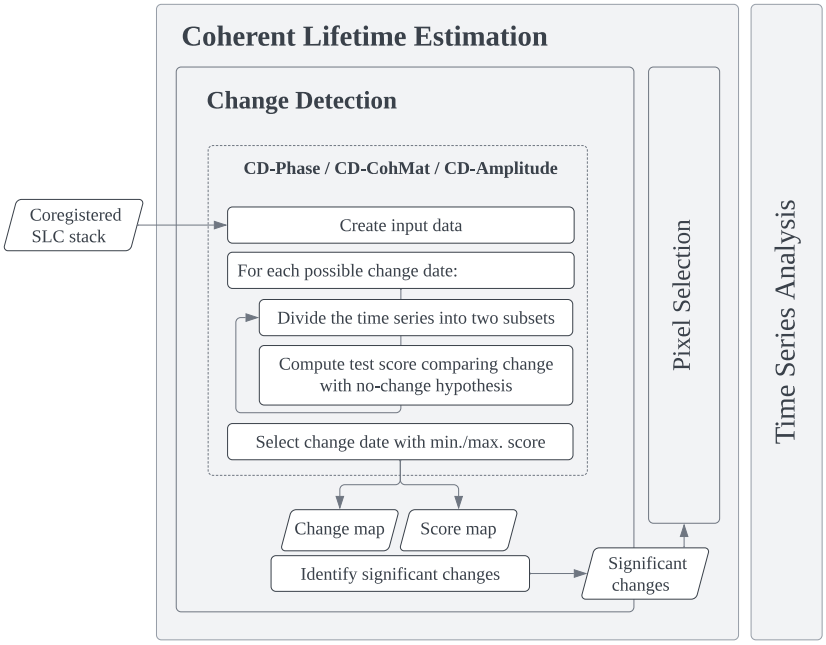


Figure 4.4: Flowchart of the proposed change detection. The three modularly usable change detection methods, CD-Phase, CD-CohMat, and CD-Amplitude, follow the same processing steps, but differ in the type of input data and the computation of the test scores.

The proposed InSAR time series method provides a framework to analyse and compare different change detection methods to evaluate their suitability for transport infrastructure monitoring. Three change detection methods are considered, two coherent and one incoherent change detection method. The first coherent change detection method is an extension of the previously proposed phase-based change detection of Dörr et al. (2022) and is presented in Section 4.3.1.1. The second coherent change detection method exploits the structure of the coherence matrix (Section 4.3.1.2, Monti-Guarnieri et al., 2018) to determine the change date. The incoherent change detection method analyses the amplitude time series (Section 4.3.1.3, Hu et al., 2019b). All three change detection methods follow the same aforementioned procedure and can be used interchangeably within the coherent lifetime estimation framework. The three change detection methods differ by the characteristics of the SAR

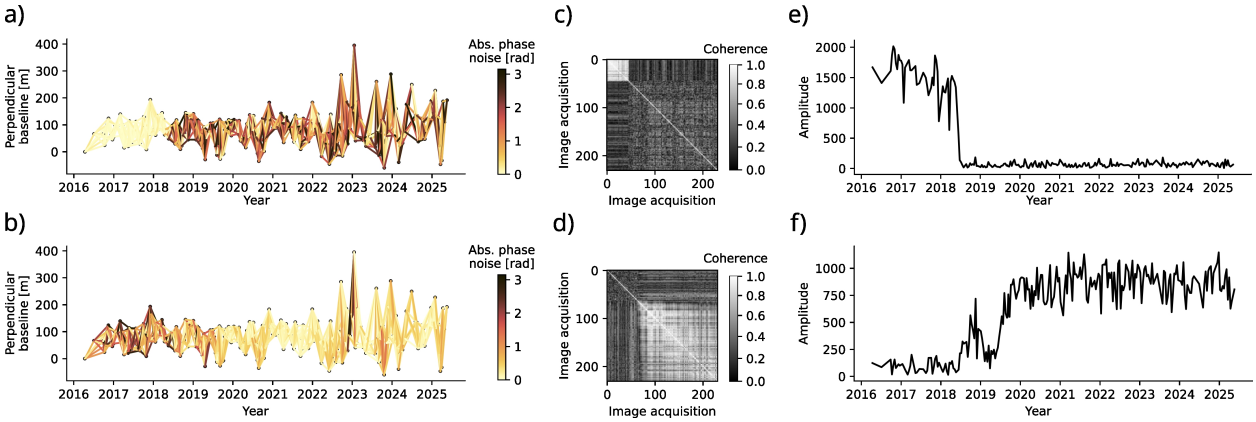


Figure 4.5: Examples of input for the three change detection methods: a) and b) phase noise in each interferogram of a small baseline interferogram network (Section 4.3.1.1), c) and d) coherence matrix (Section 4.3.1.2), e) and f) amplitude time series (Section 4.3.1.3) . The examples are taken from the study area in the Miami, USA analysed in Experiment 5 in Section 6.5. Top row panels (a, c and e) correspond to one scatterer on the temporary building, while the bottom row panels (b, d and f) correspond to one scatterer on the Eighty Seven Park Tower (see Figure 5.4 for SAR and optical view of the buildings and Figure 6.19 for the corresponding displacement time series). For the scatterer on the temporary building, the change is apparent and clear in the phase noises in the interferogram network, in the coherence matrix and in the amplitude time series. In contrast, while the change is noticeable at the scatterer on the Eighty Seven Park Tower, it cannot be clearly attributed to a specific date.

signal that they address and by the formulation of the likelihood of a change. The flowchart of the change detection is shown in Figure 4.4.

4.3.1.1 Changes in Phase Noise

The basic idea of the phase-based change detection method is to split the time series to a coherent part exhibiting low phase noise in the interferograms and an incoherent part with high phase noise (Figure 4.5a and b). This idea was originally proposed by Dörr et al. (2022) and is adapted here to use a spatial (Zhao and Mallorqui, 2019) instead of a temporal displacement model. Using the spatial displacement model, the phase noise is estimated per interferogram independently, i.e. the phase noise estimation does not depend on the length of the temporal subset. The method is referred to as CD-Phase in this thesis.

In the beginning, M_0 interferograms forming a redundant interferogram network are computed from the coregistered stack of SLC images. A change after image n divides the set of interferograms into two subsets with M_1 and M_2 interferograms before and after the change, respectively. The phase noise of a pixel p in the interferogram i is approximated by subtracting the complex sum of the phases in the immediate neighbourhood from the observed phase ϕ_p^i of the pixel p (Zhao and Mallorqui, 2019)

$$\phi_{p,\text{noise}}^i \simeq \angle \left(e^{j\phi_p^i} \sum_{q \in \text{neigh}(p)} e^{-j\phi_q^i} \right) \tag{4.1}$$

where $\angle(\cdot)$ denotes the phase of a complex number and neigh(p) denotes the set of pixels within a spatial window of size $W \times W$ centred at pixel p, excluding p itself. It is assumed that the phase contributions from atmosphere and displacement are spatially correlated over small distances. This assumption is reasonable when neighbouring pixels correspond to the same object on the surface, but it does not hold for isolated pixels showing a distinct displacement pattern. The approximation of the phase noise based on the given assumptions was shown to be reasonable using simulated and real data (Zhao and Mallorqui, 2019).

The LRT evaluates the null hypothesis that the pixel does not show any change, i.e., the phase noise in all interferograms follows the same distribution, against the alternative hypothesis that the pixel exhibits a change after acquisition n, i.e., the two subsets follow different distributions (Dörr et al., 2022). The test score Λ of the LRT is given by

$$\Lambda(n) = \frac{p_0}{p_1 \cdot p_2} \tag{4.2}$$

$$\log \Lambda(n) = \log p_0 - (\log p_1 + \log p_2) \tag{4.3}$$

using the logarithm to improve numerical stability. The score is computed from the likelihood p_k ($k \in \{0, 1, 2\}$ indicating the set of images and related interferograms)

$$p_k = p(\boldsymbol{\phi}_k \mid \gamma_k) = \prod_{i=1}^{M_k} f(\phi_k^i \mid \gamma_k) \tag{4.4}$$

that the phase noise of the interferograms follow the marginal distribution $f(\phi_k^i \mid \gamma_k)$ of the interferometric phase ϕ^i in interferogram i given by Equation (2.9) (Just and Bamler, 1994). The marginal distribution is described by the theoretical coherence γ and the expected phase value ϕ^0 around which the distribution is centred. Note, that the phase noise is expected to be zero, i.e. $\mathbb{E}[\phi^i] = 0$. Notably, the likelihood functions in the product in Equation (4.4) are statistically independent for non-redundant, but not for redundant interferogram networks. For the latter, the statistical dependence can reduce the accuracy of the change detection.

The phase noise $\boldsymbol{\phi}_{k,\text{noise}} = (\phi^1_{\text{noise}}, \ldots, \phi^{M_k}_{\text{noise}})^T$ is computed for the interferograms M_k resulting from the set of images given by the indices l_0 for the no-change hypothesis and from l_1 and l_2 for the change hypothesis. For each subset, first, the ensemble coherence (Ferretti et al., 2001) is estimated from the phase noise within each time span

$$\hat{\gamma}_k = \frac{1}{M_k} \left| \sum_{i=1}^{M_k} e^{j\phi^i_{\text{noise}}} \right| \tag{4.5}$$

and second the marginal distribution $f(\phi_k^i \mid \hat{\gamma}_k)$ is computed to evaluate the LRT. Note, that the estimation of the ensemble coherence (Equation 4.5) using the spatial displacement model (Equation 4.1) is equal to the Temporal Phase Coherence (TPC) proposed by Zhao and Mallorqui (2019) which is also used to select the coherent scatterers (Section 4.3.2.1).

The LRT is employed to compare the null hypothesis H_0, which states that there is no change in the time series, with the alternative hypothesis H_A, which states that there is a change. The likelihood p_0, that the phase noise from all images follows an identical phase distribution, is compared

to the likelihood product $p_1 \cdot p_2$ that the temporal subsets follow different phase distributions. To compensate for different numbers of samples used to compute the likelihoods p_0, p_1 and p_2, the log-likelihoods are normalised by the number of interferograms M_k

$$L(n) = \frac{\log p_0}{M_0} - \frac{\log p_1 + \log p_2}{M_1 + M_2} \underset{H_A}{\overset{H_0}{\gtrless}} T. \tag{4.6}$$

Notably, M_0 can be different from $M_1 + M_2$ because interferograms connecting the two subsets are considered in the null hypothesis, but not in the alternative hypothesis. Pixels showing a significant change are identified by applying a threshold T. The threshold should be chosen to minimise the number of false positive change detections and can be determined e.g. using simulations or bootstrapping. $L(n)$ is evaluated for all possible change points. If the null hypothesis is rejected for at least one n, the most likely change point is selected as

$$\hat{n} = \underset{n}{\operatorname{argmin}}\, L(n). \tag{4.7}$$

4.3.1.2 Changes in Coherence Matrix Structure

The main idea behind the coherence matrix change detection method proposed by Monti-Guarnieri et al. (2018) is that a change is reflected by the correlation structure in the coherence matrix. If there is no change, the coherence matrix of a PS pixel has one coherent block, whereas a change divides the matrix into two coherent blocks which are uncorrelated (Figure 4.5c and d). Originally, this method was developed for SAR change detection without application to interferometry, e.g. for the detection of damaged houses caused by an earthquake. The applicability of this method within the coherent lifetime estimation for transport infrastructure monitoring is evaluated in this thesis. The method is referred to as CD-CohMat.

The coherence matrix is estimated from pixels within the spatial neighbourhood assuming that the pixels exhibit the same scattering mechanism. A scatterer which is coherent over the whole study period (e.g. covering five acquisitions) can be described by

$$\boldsymbol{C}_0 = \sigma^2 \begin{bmatrix} 1 & \gamma & \gamma & \gamma & \gamma \\ \gamma^* & 1 & \gamma & \gamma & \gamma \\ \gamma^* & \gamma^* & 1 & \gamma & \gamma \\ \gamma^* & \gamma^* & \gamma^* & 1 & \gamma \\ \gamma^* & \gamma^* & \gamma^* & \gamma^* & 1 \end{bmatrix} = \sigma^2 \boldsymbol{\Gamma}_0 \tag{4.8}$$

with the covariance matrix $\boldsymbol{C}_0$, the coherence matrix $\boldsymbol{\Gamma}_0$, the coherence γ and its complex conjugate γ^*, and the signal variance σ^2. A change in the scattering mechanism after acquisition n is assumed to result in two distinct coherent blocks which are not correlated with each other

$$\boldsymbol{C}_n = \sigma^2 \begin{bmatrix} 1 & \gamma & \gamma & 0 & 0 \\ \gamma^* & 1 & \gamma & 0 & 0 \\ \gamma^* & \gamma^* & 1 & 0 & 0 \\ 0 & 0 & 0 & 1 & \gamma \\ 0 & 0 & 0 & \gamma^* & 1 \end{bmatrix} = \sigma^2 \boldsymbol{\Gamma}_n. \tag{4.9}$$

Following Monti-Guarnieri et al. (2018), it is assumed for simplicity that the signal variance σ^2 and the coherence γ are the same before and after the change. The likelihood $f(\boldsymbol{y} \mid \boldsymbol{C}_n)$ of a change after acquisition n is compared to the likelihood of no change $f(\boldsymbol{y} \mid \boldsymbol{C}_0)$ through the LRT in its logarithmic form

$$D(n) = \log \frac{f(\boldsymbol{y} \mid \boldsymbol{C}_0)}{f(\boldsymbol{y} \mid \boldsymbol{C}_n)} = S \cdot \log \left(\frac{|\boldsymbol{\Gamma}_n|}{|\boldsymbol{\Gamma}_0|} \right) + S \cdot Tr \left(\left(\boldsymbol{\Gamma}_0^{-1} - \boldsymbol{\Gamma}_n^{-1} \right) \hat{\boldsymbol{\Gamma}}_y \right) \underset{H_A}{\overset{H_0}{\gtrless}} T. \tag{4.10}$$

with the vector of complex-valued observations $\boldsymbol{y}$, the modelled coherence matrices for no-change $\boldsymbol{\Gamma}_0$ and change $\boldsymbol{\Gamma}_n$, the coherence matrix $\hat{\boldsymbol{\Gamma}}_y$ estimated from the complex-valued vectors of S samples in the spatial neighbourhood of the scatterer, the matrix determinant $|\cdot|$, and the trace operator $Tr(\cdot)$. A threshold T is applied to identify a significant change. The LRT is evaluated for each potential change date and if the null hypothesis is rejected for at least one n, the most likely change point is selected as

$$\hat{n} = \underset{n}{\operatorname{argmin}} D(n). \tag{4.11}$$

4.3.1.3 Changes in Amplitude Time Series

The basic idea of the amplitude change detection method proposed by Hu et al. (2019b) is that a change on the Earth surface is reflected by a significant change of the amplitude signal, e.g. the amplitude is significantly lower after a building is demolished (Figure 4.5e). The method compares the distribution of the amplitude time series before and after the change. The method is referred to as CD-Amplitude in this thesis.

The amplitude of a PS pixel follows a Rice distribution, while incoherent pixels follow a Rayleigh distribution (Hanssen, 2001). Estimating the parameters of the Rice distribution is time-consuming. Instead, this method uses the Rayleigh distribution as its parameter is easy and fast to compute. However, it comes at the cost of more false positive detections. The Rayleigh PDF of the amplitude A is given by

$$f(A \mid \sigma) = \frac{A}{\sigma^2} \exp \left(-\frac{A^2}{2\sigma^2} \right). \tag{4.12}$$

The scale parameter σ_k^2 is estimated from S_k independent samples of the amplitude time series

$$\hat{\sigma_k}^2 = \frac{1}{2S_k} \sum_{i=1}^{S_k} A_i^2 \tag{4.13}$$

with $k \in \{1, 2\}$ indicating the set of images before and after the change. A hypothesis test evaluates whether the two amplitude time series stem from the same Rayleigh distribution (null hypothesis H_0), which is the case if the scale parameter σ^2 is the same. Then, a potential change after acquisition n is validated through the test statistic K

$$K(n) = \frac{\hat{\sigma}_1^2}{\hat{\sigma}_2^2} \underset{H_0}{\overset{H_A}{\lessgtr}} F_{\alpha,\, 2n,\, 2(N-n)} \tag{4.14}$$

with the scale parameters $\hat{\sigma}_1^2$ and $\hat{\sigma}_2^2$ corresponding to the amplitude time series of the image sets with indices l_1 and l_2. The test statistic follows the Fisher distribution with $2n$ and $2(N-n)$ degrees of freedom, and with significance level α. Among the significant changes, the most likely change is selected with

$$\hat{n} = \underset{n}{\operatorname{argmax}} K(n). \tag{4.15}$$

4.3.2 Pixel Selection

InSAR time series analysis relies on pixels that maintain a coherent signal over time, which can be the whole or part of the time span, depending on whether a change was detected in the previous step. Selecting coherent pixels is, however, challenging due to the wrapped nature of the interferometric phase (see Section 2.3.2). Two pixel selection methods are applied to select PS and DS pixels. The corresponding flowchart of the pixel selection is shown in Figure 4.6.

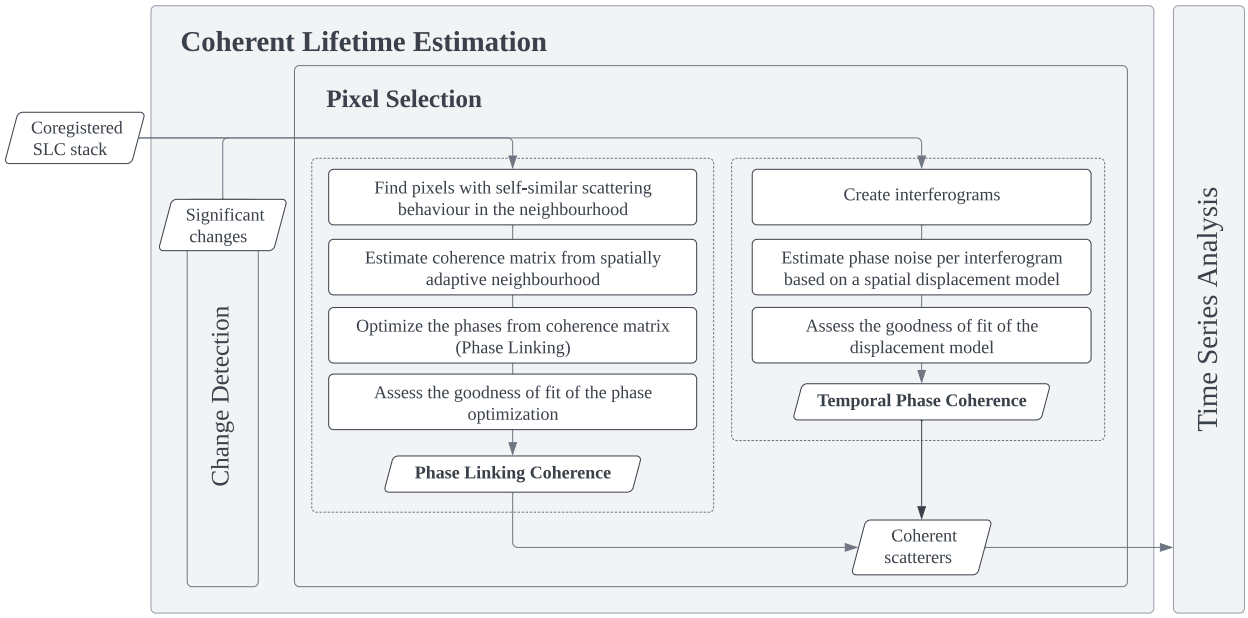


Figure 4.6: Flowchart of the proposed pixel selection.

4.3.2.1 Temporal Phase Coherence

A pixel is considered coherent if it exhibits a low phase noise, which can be evaluated after accounting for the phase contributions from atmosphere, displacement and DEM error. The Temporal Phase Coherence (TPC) proposed by Zhao and Mallorqui (2019) is chosen for the selection of PS pixels due to its computational efficiency and the underlying spatial displacement model. The phase noise estimation approach of the TPC is also used in the phase-based change detection approach discussed in Section 4.3.1.1. The displacement signal is assumed to be correlated in space in order to estimate the phase noise. The complex averaged phase of the neighbourhood is subtracted from the central pixel (see Equation 4.1). Afterwards, the coherence $\hat{\gamma}_{\mathrm{TPC}}$ is computed using Equation 4.5. The phase noise estimation strategy does not explicitly target PS or DS characteristics, but as no phase filtering is applied it is assumed that pixels with a high SNR, typically PS pixels, are targeted.

4.3.2.2 Phase Linking Coherence

DS pixels exhibit lower SNR and benefit from phase filtering before the estimation of their displacement time series (see Section 2.3.2). An adaptive spatial window is utilised to avoid loss of spatial resolution. The set of sibling pixels in the spatial neighbourhood of the targeted pixel are identified using statistical tests (Figure 4.7a). The Kolmogorov-Smirnov (KS)-test (Massey Jr, 1951) is used

which is a non-parametric test to measure the similarity of two distributions, here used to measure the similarity of the amplitude time series of the central pixel and a potential sibling pixel in the neighbourhood. Detected sibling pixels which are not spatially connected to the central pixel are discarded. Subsequently, the sample covariance matrix $\hat{\boldsymbol{C}}_y$ is estimated from N complex-valued observations $\boldsymbol{y} = [y_1, \ldots, y_N]^T$ of each of the N_S sibling pixels in the neighbourhood

$$\hat{\boldsymbol{C}}_y = \mathbb{E}[\boldsymbol{y}\boldsymbol{y}^H] = \frac{1}{N_S} \sum_{i=1}^{N_S} \boldsymbol{y}_i \boldsymbol{y}_i^* \tag{4.16}$$

with the Hermitian transposition denoted by ^{H}. The coherence matrix $\hat{\boldsymbol{\Gamma}}_y$ is obtained by normalisation of the covariance matrix (Ferretti et al., 2011). An example of the coherence matrix and the sibling pixels used for the estimation is shown in Figure 4.7. The optimised phase time series of the DS pixel is retrieved from the sample coherence matrix through phase linking. Here, the Combined Eigenvalue maximum likelihood Phase Linking (CPL) from Mirzaee et al. (2023) is selected which builds upon Eigenvalue decomposition-based Maximum likelihood of Interferometric phase (EMI) (Ansari et al., 2018). EMI estimates the phase time series from the sample coherence matrix $\hat{\boldsymbol{\Gamma}}_y$ using eigenvalue decomposition

$$(|\hat{\boldsymbol{\Gamma}}_y|^{-1} \circ \hat{\boldsymbol{\Gamma}}_y)\hat{\boldsymbol{\nu}} = \lambda \hat{\boldsymbol{\nu}} \tag{4.17}$$

with $\circ$ being the Hadamard product and the absolute values of the matrix entries denoted by $|\cdot|$. The solution is given by the Eigenvector $\hat{\boldsymbol{\nu}}$ corresponding to the smallest Eigenvalue λ. EMI requires a positive definite sample coherence matrix. If this requirement is not fulfilled, the CPL uses the approach from Fornaro et al. (2014), which is also based on eigenvalue decomposition. The computational complexity is reduced using sequential phase linking (Ansari et al., 2017) which splits the sample coherence matrix into several mini-stacks (Figure 4.7c). Phase linking is applied on each mini-stack separately, followed by a datum connection to combine the filtered phase time series from each mini-stack. Finally, the signal quality of a DS pixel is assessed with the PLC estimated from N SAR images

$$\hat{\gamma}_{PLC} = \frac{1}{N^2 - N} \sum_{n=1}^{N} \sum_{k \neq n}^{N} e^{j\phi_{nk}} e^{-j(\bar{\psi}_n - \bar{\psi}_k)} \tag{4.18}$$

with the observed interferometric phase ϕ and the filtered phase $\bar{\psi}$ of the SAR observations (Ferretti et al., 2011). The PLC describes the goodness-of-fit of the phase filtering.

4.4 Time Series Analysis

The time series method retrieves the displacement time series for the coherent pixels based on interferograms created from a coregistered stack of single-look SAR images. A categorisation of the proposed time series method based on the key characteristics of the method is given in Table 2.1 and the flowchart is presented in Figure 4.8. A spatial phase unwrapping strategy is selected to target local and regional displacements which are assumed to be spatially correlated (see Section 1.2). The spatial phase unwrapping strategy in combination with a redundant interferogram network (Berardino et al., 2002; Mora et al., 2003; Manunta et al., 2008; Devanthéry et al., 2014) allows to retrieve displacements without a prior temporal displacement model. Thus, it enables to derive

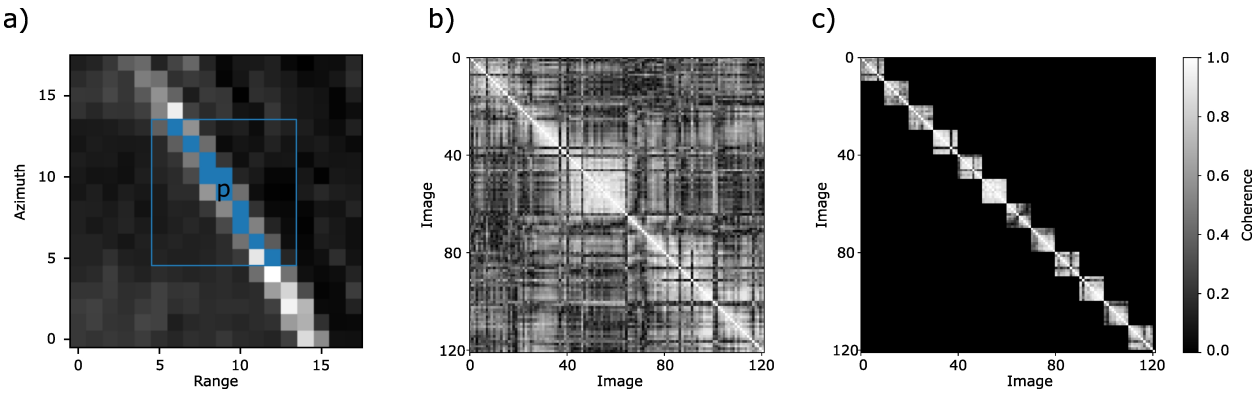


Figure 4.7: Example for the estimation of the coherence matrix from a spatially adaptive neighbourhood for a pixel on a highway in the study area Villena, Spain (Section 5.2). a) Temporally averaged amplitude image with a neighbourhood window of size 9×9 pixels^2 (blue rectangle) around the center pixel p. Blue pixels mark the sibling pixels of p detected with the KS-test. Notably, the sibling pixels coincide with the shape of the highway. b) Estimated coherence matrix $\hat{\Gamma}$ for pixel p. c) The same coherence matrix as in b) but restricted to mini-stacks along the diagonal containing 10 images each to reduce the computational burden of phase linking (Ansari et al., 2017).

non-linear displacements without temporal modelling which is a major limitation among common InSAR time series methods (Ferretti et al., 2001; Kampes, 2006; Van Leijen, 2014; Schenk, 2015). The separation of the displacement from other phase contributions is carried out in a two-step approach: atmospheric filtering based on high quality first-order points and densification with the second-order points. In the following, the atmospheric filtering and densification step are explained in detail.

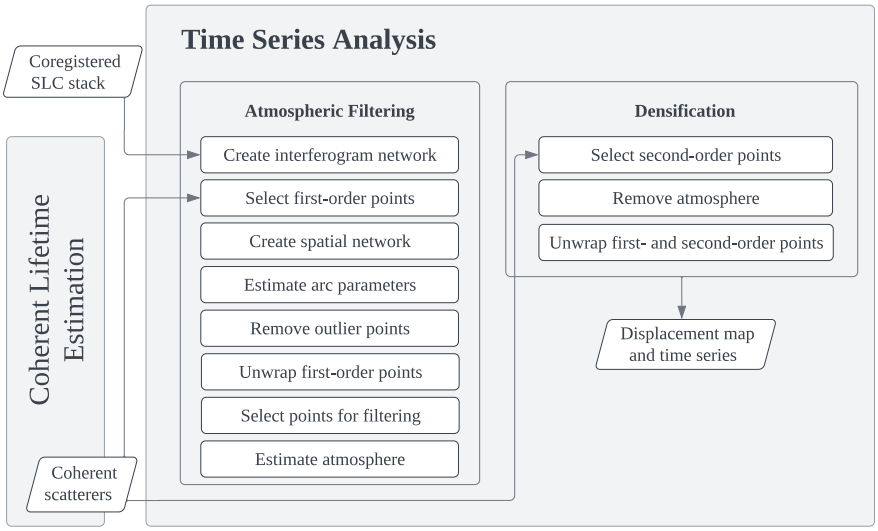


Figure 4.8: Flowchart of the proposed time series analysis.

4.4.1 Atmospheric Filtering

4.4.1.1 First-Order Points

The atmospheric phase contribution is estimated from a set of pixels homogeneously distributed in space. High quality pixels, called first-order points, are selected which enables a reliable spatial phase unwrapping. Only CCS pixels are used as first-order points to ensure that all images are covered by coherent pixels to estimate the atmospheric phase contribution. Without loss of generality, the TPC (Section 4.3.2.1) is chosen for selecting first-order points as the pixels selected with TPC require minimal outlier checking due to the good approximation of the phase noise compared to e.g. the ADI for pixel selection.

4.4.1.2 Outlier Removal

To achieve a reliable estimate of the atmospheric effect, outliers are removed from the first-order points. For this purpose, the first-order points are connected by a spatial network using a Delaunay triangulation and k-nearest neighbours to achieve a connected and highly redundant spatial network. The two parameters, DEM error difference Δh and velocity difference v are estimated from the double-differenced phases of an arc. For this, the ensemble coherence of the arc is maximised from M interferograms

$$\underset{v,\Delta h}{\operatorname{argmax}}\ \hat{\gamma}_{\text{arc}} = \frac{1}{M} \cdot \left| \sum_{i=1}^{M} e^{j \cdot \phi^i_{\text{noise}}(v,\Delta h)} \right| \tag{4.19}$$

with the phase noise ϕ^i_{noise} approximated by

$$\phi^i_{\text{noise}}\,(v, \Delta h) = \Delta\phi^i - \frac{4\pi}{\lambda} \left(B^i_t \cdot v + \frac{B^i_\perp}{r \sin\theta} \cdot \Delta h \right) \tag{4.20}$$

where $\Delta\phi$ is the wrapped double-differenced phase of the arc, λ is the radar wavelength, $B^i_\perp$ is the perpendicular baseline, r is the average distance between the sensor and the point, θ is the average local incidence angle of the arc, and B^i_t is the temporal baseline (Ferretti et al., 2000).

Outliers among the first-order points shall be removed before phase unwrapping. A point is considered an outlier, if it exhibits a high phase noise. The ensemble coherence characterises the goodness-of-fit of the estimated velocity difference and DEM error difference for the phase observations of the arc and is used as quality criterion to detect low-quality arcs related to individual points. To do so, the average ensemble coherence $\bar{\gamma}_{\text{arc}}$ per first-order point is assessed

$$\bar{\gamma}_{\text{arc}} = \frac{1}{n_a} \sum_{i=0}^{n_a} \hat{\gamma}_{\text{arc},i} \tag{4.21}$$

with the number of arcs n_a connected to the first-order point. The underlying assumption is that an incoherent point will lead to a low ensemble coherence in all of the connected arcs, independent of the coherence of the second point of that arc. First-order points with an average ensemble coherence $\bar{\gamma}_{\text{arc}}$ below a threshold are removed.

4.4.1.3 Phase Unwrapping

Once all outliers are removed, the interferometric phases are inverted and the displacement time series retrieved. The parameters estimated from the arcs serve only to identify outlier pixels w.r.t. the temporal displacement model. The wrapped phases $\boldsymbol{\phi}$ are spatially unwrapped with PUMA (Bioucas-Dias and Valadao, 2007) for each interferogram independently (Section 2.3.4) to obtain the unwrapped phases $\boldsymbol{\varphi}$; the needed spatial neighbourhood of the first-order points is defined by a Delaunay triangulation.

The interferogram network inversion connects the interferogram domain with the time domain. For each point, the M unwrapped interferometric phases φ are inverted to retrieve the N unambiguous phases ϑ in each image resulting in a redundancy of $r = M - N$ with $M > N$. The least-squares problem has a rank deficiency of $d = 1$ because all observations are relative temporal phase changes between two acquisitions. To remove the rank deficiency, the first image acquisition is introduced as a temporal reference by assuming zero displacement, i.e. $\vartheta_1 = 0$ and by removing the related entries in the design matrix and in the vector of unknowns (Niemeier, 2008). The functional model is given by

$$\varphi_i = \vartheta_l - \vartheta_j \tag{4.22}$$

for the i-th interferogram and two images l and j. The Gauss-Markov Model for the phase inversion consists of

$$\mathbf{l} = \mathbf{A}\mathbf{x} - \mathbf{v} \tag{4.23}$$

$$\begin{bmatrix} \varphi_1 \\ \vdots \\ \varphi_M \end{bmatrix} = \begin{bmatrix} -1 & 1 & 0 & \dots & 0 & \dots \\ -1 & 0 & 1 & \dots & 0 & \dots \\ 0 & -1 & 1 & \dots & 0 & \dots \\ 0 & 0 & -1 & \dots & 1 & \dots \\ \vdots & \vdots & \vdots & & \vdots & \end{bmatrix} \begin{bmatrix} \vartheta_1 \\ \vdots \\ \vartheta_N \end{bmatrix} - \begin{bmatrix} \mathrm{v}_1 \\ \vdots \\ \mathrm{v}_N \end{bmatrix} \tag{4.24}$$

with the observation vector $\mathbf{l}$ containing the unwrapped phases, the design matrix $\mathbf{A}$ representing the interferogram network, the vector of unknown parameters $\mathbf{x}$ and the vector of residuals $\mathbf{v}$.

The phase observations are correlated due to several factors including mathematical correlations due to the redundancy in the interferogram network, correlations from sensor characteristics and atmosphere (Hanssen, 2001; Kampes, 2006; Van Leijen, 2014; Agram and Simons, 2015). Phase unwrapping has a major impact on the uncertainty of the unwrapped phase observations. A simplified stochastic model is selected as a result of the unknown uncertainty arising from the process of spatial phase unwrapping. Thus, the stochastic model

$$\boldsymbol{\Sigma}_{\mathbf{ll}} = \sigma_0^2 \mathbf{Q}_{\mathbf{ll}} = \sigma_0^2 \mathbf{P}^{-1} = \sigma_0^2 \mathbf{I} \tag{4.25}$$

consists of equally weighted and uncorrelated observations. The solution of the network inversion is derived using least-squares

$$\hat{\mathbf{x}} = (\mathbf{A}^T \mathbf{P} \mathbf{A})^{-1} \mathbf{A}^T \mathbf{P} \mathbf{l} \tag{4.26}$$

with the cofactor matrix of the estimated parameters

$$\mathbf{Q}_{\hat{\mathbf{x}}\hat{\mathbf{x}}} = (\mathbf{A}^T \mathbf{P} \mathbf{A})^{-1}. \tag{4.27}$$

Finally, the unambiguous phases are converted into the displacement time series.

4.4.1.4 Estimation of Atmospheric Effects

The spatio-temporal behaviour of the atmosphere is exploited to estimate the atmospheric phase contribution. The atmosphere is correlated in space, but uncorrelated in time (Hanssen, 2001). Notably, in the following, the inverted phase time series $\boldsymbol{\vartheta}$ is used instead of the unwrapped interferometric phases $\boldsymbol{\varphi}$ which reduces the computational time and exploits the redundancy in the interferogram network. The goal is to separate the temporally uncorrelated atmosphere and noise from the temporally correlated displacement signal. To do so, the analysis is restricted to first-order points which exhibit a linear temporal displacement signal, which can be easily estimated; the approach follows the idea of Crosetto et al. (2018). To ensure that a point shows a linear displacement signal, it is tested whether the phase residuals contain a temporally correlated signal in addition to the linear displacement. First, the mean velocity and DEM error are estimated from the inverted phases of each image and are removed to obtain the phase residuals $\tilde{\boldsymbol{\vartheta}} = (\tilde{\vartheta}_i, \ldots, \tilde{\vartheta}_N)^T$. Pixels whose phase residuals do not contain any temporally correlated signal are detected using the temporal auto-correlation function $R(k)$ of the phase residual time series

$$R(k) = \frac{1}{(N-k)\sigma^2} \sum_{t=1}^{N-k} (\tilde{\vartheta}_t - \mu)(\tilde{\vartheta}_{t+k} - \mu) \tag{4.28}$$

with the lag k being a positive integer, $k < N$. A temporal autocorrelation at lag one, $R(1)$, below a threshold is classified as a temporally non-correlated signal, i.e. the residual phase does not contain any further temporally correlated displacement signal but instead only atmosphere and noise.

Afterwards, the spatially correlated atmospheric effect is separated from the spatially uncorrelated noise of the selected points. Simple Kriging (Wackernagel, 2003) is applied to estimate the atmospheric effect ϑ_{atmo} from the location of n_p first-order points at locations $\mathbf{s} = \left(s_1, \cdots, s_{n_p}\right)^T$. The atmospheric effect at location s_0 is the weighted average of all considered first-order points

$$\vartheta_{\text{atmo}}(s_0) = \mu + \sum_{i=1}^{n_p} w_i(\vartheta_{\text{atmo}}(s_i) - \mu) \tag{4.29}$$

with the weights w and the mean value μ of the atmospheric effect which is assumed to be zero. Assuming second-order stationarity, the weights w are derived from the variogram. The covariance $C(\vartheta_{\text{atmo}}(s_i), \vartheta_{\text{atmo}}(s_j))$ is assumed to depend only on the distance Δ between the points

$$C(\vartheta_{\text{atmo}}(s_i), \vartheta_{\text{atmo}}(s_j)) = C(\vartheta_{\text{atmo}}(s_i), \vartheta_{\text{atmo}}(s_i + \Delta)) = C(\Delta). \tag{4.30}$$

The atmospheric effect is interpolated to the location of the second-order points.

4.4.2 Densification

4.4.2.1 Second-Order Points

The dense displacement map is estimated from the first- and second-order points during the densification. Second-order points comprise both, CCS and TCS pixels and are selected using the TPC and the PLC. TCS pixels whose coherent lifetime covers less than a minimum number of images are discarded, because the pixel selection results are not reliable from few images only. The second-order points exhibit a higher phase noise compared to the first-order points. To facilitate the phase

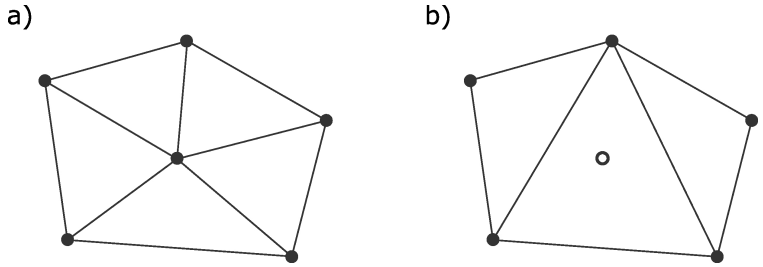


Figure 4.9: Scheme of the triangulation for the spatial phase unwrapping of CCS and TCS pixels during their coherent lifetimes. a) The six pixels marked with dots are coherent in the interferogram. b) One pixel marked by a hollow circle is not coherent in the interferogram. Thus, this pixel is excluded from the Delaunay triangulation.

unwrapping, the atmospheric effect is removed before. The interpolated atmospheric phase contribution is back-transformed to the interferogram-domain and removed from the wrapped phases of the first- and second-order points.

4.4.2.2 Phase Unwrapping

The retrieval of the displacement time series follows the same procedure as for the first-order points including spatial phase unwrapping and interferogram network inversion, but is adapted to accommodate for the different coherent lifetimes of TCS pixels.

The first- and second-order points are jointly connected by a Delaunay triangulation to define the spatial neighbourhood for the spatial phase unwrapping. The triangulation can be different in each interferogram because it depends on the coherent lifetime of the individual TCS pixels among the second-order points (Figure 4.9). While the interferogram network is identical for all CCS pixels, each TCS pixel has a different interferogram network. The interferogram network of TCS pixels contains a subset of the interferogram network of CCS pixels but is restricted to the TCS pixels' individual coherent lifetime. The phases of a TCS pixel are only unwrapped for interferograms within their coherent lifetime which can lead to different sets of coherent points in each interferogram and, thus a different triangulation.

The phase contribution resulting from the DEM error is estimated for each pixel from the unwrapped interferometric phases. Afterwards, the network of interferograms is inverted for each pixel to retrieve the displacement time series. The first image within the coherent lifetime of the pixel is chosen as the temporal reference for that pixel to remove the rank deficiency of the matrix of normal equations in the interferogram network inversion. Finally, the estimated unambiguous phases $\boldsymbol{\vartheta}$ are converted into displacement $\boldsymbol{d}$

$$\boldsymbol{d} = -\frac{\lambda}{4\pi}\boldsymbol{\vartheta}. \tag{4.31}$$

4.5 Discussion

The presented methodology is tailored to the characteristics of transport infrastructure depicted in Sentinel-1 images. Three main challenges were identified in the problem statement of the thesis

(Section 1.2) which are addressed by the proposed methodology: 1) The shape and size of the transport infrastructure in relation to the size of the Sentinel-1 image and its spatial resolution, 2) the backscattering at the transport infrastructure, and 3) the expected displacement signal to be monitored. The shape, size and backscattering predominantly affect the coherent lifetime estimation, while the displacement signal is primarily addressed in the time series analysis. In the following, the design choices of the proposed methodology for transport infrastructure monitoring are discussed considering the advantages, the underlying assumptions and the corresponding limitations.

4.5.1 Discussion on the Coherent Lifetime Estimation

Pixel Selection

The challenge is to select coherent pixels among the small set of pixels covering a transport infrastructure due to its narrow shape compared to the spatial resolution of the Sentinel-1 pixels. The backscattering at transport infrastructure impacts the choice of appropriate pixel selection methods. For highways, mostly DS pixels are anticipated due to the low backscattering signal of the mirror-like surface. More PS pixels are expected at railway tracks which show a brighter backscattering. The backscattering of bridges is even brighter and thus more PS pixels are expected. The selection of DS pixels requires phase filtering using a spatial window. An adaptive window and phase linking are chosen to preserve the spatial resolution (see Section 2.3.2), although phase linking comes with a considerable increase in computational time. For the selection of PS pixels, a spatial neighbourhood is considered as well. The spatial displacement model is prioritised over a temporal displacement model which would require to anticipate the temporal behaviour beforehand. The TPC assumes a spatially correlated displacement signal and requires coherent pixels in its neighbourhood to enable the estimation of the phase noise. The chosen pixel selection criteria, TPC for PS pixels and PLC from phase linking for DS pixels, are supposed to provide coherent pixels at the transport infrastructure.

Spatial Neighbourhood

The dependence on the temporal dimension is reduced when considering the spatial neighbourhood for pixel selection and change detection instead of the temporal evolution of the signal. However, it requires that the underlying process is stationary in space over at least the estimation window. For PLC estimation, the stationarity condition means that the sibling pixels should exhibit the same scattering behaviour over the whole study period. Siblings should therefore be carefully selected among the pixels in the neighbourhood as deviations from the stationarity assumption can lead to biased phases after phase linking. Therefore, an adaptive spatial window is applied in the context of phase linking.
For TPC, the stationarity condition means that the pixels within the estimation window should exhibit the same displacement signal as the central pixel. Here, a non-adaptive spatial window is applied. A larger estimation window provides more samples for averaging, while it comes with an increased likelihood of including pixels with a different displacement behaviour that could distort the phase noise estimation. It is more likely that the stationarity is fulfilled in a smaller estimation window, but a too small window size can also bias the estimation, as it gives more weight to each

sample during phase averaging. Comparing PLC and TPC shows that although both criteria are computed from a spatial window, the requirements on the spatial neighbourhood are different.
Two out of the three considered change detection methods also consider a spatial neighbourhood. For CD-Phase, the phase noise is estimated in the same way as for the TPC. For CD-CohMat, the coherence matrix is estimated from the SAR observations within the spatial neighbourhood. Here, either an adaptive spatial neighbourhood could be used to target DS pixels or a non-adaptive neighbourhood to address PS pixels (see discussion on TCS in Section 3.2.5). In this thesis, a non-adaptive window is selected for CD-CohMat to target PS pixels. Thus, all three change detection methods are targeting PS pixels. Nevertheless, the proposed InSAR time series method and in particular the proposed coherent lifetime estimation framework is not limited to PS pixels. A change detection method targeting the characteristics of DS pixels could also be employed in combination with phase linking for selecting the coherent DS pixels within their coherent lifetime.

Significant Changes

A limitation of CD-Phase and CD-CohMat is that a distribution underlying the LRT is missing. Thus, a threshold for identifying significant changes has to be manually selected, e.g. to reduce the number of false-positive detections. Another drawback of each of the considered change detection methods is that the uncertainty in the input data is not explicitly incorporated in the method. Nevertheless, it is expected that the LRT score reflects the uncertainty of the input data. The LRT score is supposed to yield a clear minimum for scatterers with a high SNR in contrast to scatterers with a low SNR. CD-Phase and CD-CohMat have the advantage that the connections, i.e. interferograms, between the image acquisitions are considered. The observations are redundant, but highly correlated as the same images were used in the computation of the interferograms. In contrast, CD-Amplitude considers each image independently.

One-Change Hypothesis

For the transport infrastructure monitoring task, only one change is assumed during the time span. However, the change detection methodology is not limited to one change, but instead could be easily adapted into a hierarchical form in which each subset is further tested for changes as also proposed in the literature (Hu et al., 2019b; Manzoni et al., 2021; Dörr et al., 2022). Nevertheless, assuming only one change is favourable for several practical reasons. From the perspective of the object, assuming only one change seems appropriate as the transport infrastructure usually does not change frequently. The transport infrastructure shall be monitored during its lifetime for which longer time series are more favourable. Long observation periods facilitate the interpretation of short-term anomalies in relation to long-term trends. From an estimation point of view, allowing several changes could lead to an over-segmentation of the time series. This is particularly problematic, because the observations are non-redundant which makes the change detection methods sensitive to noise in the input. Ensuring a low number of changes, in this case only one change, the estimation of the coherence of the period benefits from assuming temporal stationarity which allows to average the phase noise values and thereby reduces the impact of outliers in the time series.

4.5.2 Discussion on the Time Series Analysis

Two-Step Approach

The goal of the time series analysis is to retrieve the displacement at the transport infrastructure pixels. Though selecting and processing only pixels directly at the transport infrastructure may appear to be a straightforward concept, it is essential to also process pixels outside the transport infrastructure for three reasons. First, the assessment of the regional displacement signal is aided by processing pixels in the surrounding to obtain the overall picture even if the pixel density at the transport infrastructure is not high enough. Second, to avoid aliasing the displacement signal, a sufficient spatial sampling is required for spatial phase unwrapping which might not be achieved with pixels on the transport infrastructure only. Third, the shape and extent of the transport infrastructure within the image extent is insufficient to estimate the atmospheric phase contribution reliably, because a regular sampling of the atmospheric signal is required over the whole area. The densification approach chosen for the proposed time series analysis methodology has the advantage that the atmosphere is estimated from high-quality pixels with a homogeneous distribution over the study area. Moreover, the two-step approach is computationally efficient compared to the one-step approach which might require several iterations to identify and remove incoherent pixels.

Displacement Retrieval

The expected displacement is spatially correlated and appears on either a regional scale, i.e. also beyond the transport infrastructure, or on a local scale, i.e. affecting an area on the transport infrastructure which is covered by several pixels. Moreover, it is vital for the hazard assessment to detect temporally non-linear displacements, which can indicate accelerated displacements. The design of the time series analysis components allows to address both, spatially correlated and temporally non-linear displacement signals. A small baseline interferogram network is chosen to exploit the redundancy in the network. Moreover, non-ideal PS and DS pixels which decorrelate over time benefit from a small baseline interferogram network in which the interferograms exhibit a coherent signal. The redundant interferogram network is also favourable for TCS analysis, because a connected subset of the interferograms exists within the coherent lifetime of each TCS pixel. A spatial phase unwrapping scheme using PUMA is chosen which exploits the spatial correlation of the displacement signal and to avoid having to use a temporal displacement model. Spatial phase unwrapping, however, requires a sufficient spatial sampling of the signal. In areas with insufficient spatial sampling, PUMA preserves phase discontinuities in space if a path exists between the two parts separated by the discontinuity.

Atmospheric Filtering

The filtering of the atmosphere separates the phase contributions based on the correlation properties. The atmospheric phase contribution can only be accurately separated from noise if the displacement signal is correctly removed beforehand. This requires to model the displacement signal either explicitly by assuming a temporal model or implicitly by applying a temporal low-pass filter. The approach used in the presented methodology restricts the analysis to pixels with a linear

displacement signal and avoids non-linear displacements. Non-linear displacements have more degrees of freedom so that modelling both, explicit and implicit, is more error-prone. It was previously discussed that the presented phase unwrapping scheme does not impose a temporal displacement model. However, the first-order points are an exception because they are restricted to points exhibiting a temporally linear displacement signal. Consequently, this atmospheric filtering approach is only applicable if pixels with a temporally linear displacement signal are present all over the study area.

Pixel Selection and Thresholding

The selection of coherent pixels requires the choice of a coherence threshold for both TPC and PLC. Relaxing the threshold is a trade-off between gaining a higher number of pixels and the risk of including incoherent pixels for which the coherence estimate was incorrect. The coherence threshold should be adapted according to the characteristics of the study area or can be empirically estimated using simulations (Hooper et al., 2007). If the location of the transport infrastructure in the SAR image is known, the threshold can be relaxed at transport infrastructure pixels only (Macchiarulo et al., 2022a). This allows to increase the point density at the transport infrastructure without introducing incoherent pixels in the surrounding.

The proposed time series method selects both, first- and second-order points a priori, i.e. before phase unwrapping. The additional outlier check is applied for first-order points to ensure that they comprise highly coherent pixels. Spatial unwrapping of incoherent pixels could propagate errors to neighbouring pixels in the spatial network of points. A posteriori pixel selection after phase unwrapping is avoided due to two reasons. First, the phase noise of a pixel cannot be attributed purely to that specific pixel due to phase unwrapping errors resulting from the global optimisation. Second, a temporal displacement model has to be anticipated to extract the phase noise, which introduces additional assumptions.

CCS and TCS Pixels

It is proposed to select the first-order points only among the CCS pixels. This has the advantage that first-order points are present in all images for filtering the atmospheric effects, which would not be ensured if TCS pixels were used.
The proposed spatial unwrapping scheme for both, CCS and TCS pixels, leads to a different definition of the spatial neighbourhood in the spatial network, as there are different sets of points in each of the interferograms. This is not problematic as long as the spatial sampling of the displacement signal is dense enough to avoid aliasing of the signal.
The temporal reference is set to the first image in which a scatterer shows a coherent signal which can be different for each TCS pixel. The varying temporal reference is irrelevant, provided that the interpretation of the displacement results focuses on the mean displacement velocity. The mean displacement velocity as well as the visual analysis of the time series are independent of the temporal reference. A common temporal reference for all pixels in the study area might however be required for some applications. For instance, the analysis of the cumulative displacement yields

different results for pixels affected by the same spatial displacement pattern, if their time series have different length and are not adjusted for the same temporal reference. The time series of a TCS pixel could be adjusted by an offset which aligns it with the time series of a close-by CCS pixel, assuming that both, the TCS and CCS pixel belong to the same object (Dörr et al., 2022).

5 Experimental Setup

In this chapter, the experimental setup is presented which is used to investigate the proposed methodology and to answer the research questions. The objectives of each experiment are specified in Section 5.1. Then, the study areas together with the datasets are shown in Section 5.2 and the processing parameters are listed in Section 5.3. Finally, the evaluation strategy for the experiments is presented in Section 5.4.

5.1 Objectives

The overall goal of this thesis is to develop an InSAR time series method that enables to monitor transport infrastructure with Sentinel-1 data. The experiments are designed to underline the potential and limitations of this method. The proposed methodology exploits the characteristics of transport infrastructure. It further addresses the challenges identified in the problem statement of this thesis (see Section 1.2). The prerequisite for any displacement analysis is the availability and selection of coherent pixels at the transport infrastructure in Sentinel-1 images. The experiments focus on the coherent lifetime estimation of the scatterers to validate the change detection and pixel selection of the proposed methodology. Further, the displacement results obtained by the proposed InSAR time series method are validated. The following sets of experiments are conducted to answer the associated research questions.

1) **Pixel Selection at Transport Infrastructure**
   What is the potential of the proposed pixel selection methods for transport infrastructure depicted in Sentinel-1 images? How does the potential for transport infrastructure monitoring differ among railway tracks, highways and related bridges? Which scattering mechanism is most prevalent at transport infrastructure? How does the surrounding of the transport infrastructure impact the phase filtering, and is the filtering for DS pixel selection successful at railway tracks and highways?

The first experiment solely focuses on the pixel selection at transport infrastructure, i.e. only CCS pixels are considered. To ensure no confusion with TCS pixels exists, change detection is not applied and the utilised datasets cover merely three years in which no changes are known to exist at the transport infrastructure. Two study areas with similar spatial extent and the same number of images are examined. The study areas Villena and Neumünster are chosen to analyse both extremes of the potential of the new method due to a different degree of vegetation in the areas.

Validating the pixel selection results is challenging as the coherence of the interferometric phase in an interferogram depends on the backscattering and is a property of the signal. It cannot be

validated by independent reference data. Nevertheless, insights on the performance of the two pixel selection criteria are gained through a pixel-wise comparison of their coherence. The final displacement map could also serve as a criterion for the correctness of the pixel selection. If the pixel selection is correct, the displacement map should show reasonable displacement results which are consistent in the spatial neighbourhood. Nevertheless, the displacement map is not considered as criterion here, because it can only serve as implicit quality criterion due to the effect of the intermediate processing steps, in particular the phase unwrapping.

At the end, pixel selection requires the choice of a threshold to distinguish coherent from incoherent pixels which depends on the study area. The coherence distributions are compared to draw conclusions about the potential of Sentinel-1 images for transport infrastructure monitoring in the two study areas.

2) **Observability of Local and Regional Displacements**
Does the InSAR time series method provide meaningful displacement results for transport infrastructure? To which degree can local and regional displacements be observed and differentiated at transport infrastructure using Sentinel-1 images?

The second experiment extends the first by analysing the displacement maps for the same study areas resulting from the CCS pixels selected with a conservative coherence threshold. This experiment demonstrates the whole InSAR time series method for retrieving the displacement information for PS and DS pixels. A qualitative analysis of the displacement maps for the study areas Villena and Neumünster provides insights on the observability of regional and local displacements and is complemented by displacement profiles along selected transport infrastructure.

The assessment of regional and local displacements is essential for the transport infrastructure monitoring task. Regional displacements are defined as displacements that affect transport infrastructure, i.e. cover at least a part of it, but also affect the neighbourhood around the transport infrastructure. The fact, that the displacement exceeds the extent of the transport infrastructure allows to interpolate the displacement signal to the transport infrastructure in case the latter cannot be directly observed due to missing coherent pixels.

Local displacements, however, cannot be inferred from coherent pixels in the neighbourhood. Here, local displacements are defined as displacements only present at the transport infrastructure and its immediate surrounding, e.g. embankments. Consequently, coherent pixels have to be present directly at the transport infrastructure in order to observe the local displacement. While a regular sampling of coherent pixels along the transport infrastructure is favourable, this can often not be achieved. Instead, there a smaller and larger distances between the coherent pixels which are decisive for the magnitude of the spatial displacement gradients that can be observed. For hazard assessment, the observability of spatial displacement gradients, also called angular distortion, is important (Ma et al., 2022). The observability of local displacements is governed by the maximum distance between the points at the transport infrastructure which is assessed in Experiment 2.

3) **Coherent Lifetime Estimation at Transport Infrastructure**
How do the change detection methods for transport infrastructure perform? How plausible is the coherent lifetime estimated from the three change detection methods?

The proposed InSAR time series method for TCS analysis is validated in two subsequent experiments. The coherent lifetime estimation is validated in this experiment, while in the next experiment, the retrieval of the displacement time series is assessed. Although PS and DS pixels could be analysed within the coherent lifetime framework, the methodology is here demonstrated and validated for temporarily coherent PS pixels only. Hence, the suitability of CD-Phase, CD-CohMat and CD-Amplitude for the coherent lifetime estimation of PS pixels is investigated.

The plausibility of the coherent lifetime results are validated with respect to optical images used as a reference. New metrics are proposed to quantify the plausibility of the results instead of using classification error metrics due to the limited explanatory power of the reference data. Two study areas, Figuera and Sande, are examined with their datasets covering 10 and 11 years. Again, the study areas are selected to represent different conditions for change detection due to the different amount of vegetation.

4) **Displacement Analysis of Temporarily Coherent Pixels**
Does the InSAR time series method provide meaningful displacement results jointly for CCS and TCS pixels? What is the contribution of the identified TCS pixels to the observation of displacements at infrastructure in long time series?

In this experiment, the retrieval of the displacement time series for TCS analysis is investigated and exemplarily demonstrated for the results of the coherent lifetime estimation with CD-Phase and TPC. This experiment extends the previous experiment using the datasets from the same study areas. For each study area, two displacement maps are compared, one estimated from CCS pixels selected with TPC, the other one estimated from CCS and TCS pixels using CD-Phase and TPC. The displacement maps are qualitatively analysed to study the observability of newly constructed infrastructure through the integration of TCS pixels.

5) **Transferability to Urban Infrastructure**
To which degree can the proposed InSAR time series method be transferred to urban infrastructure monitoring? How plausible is the coherent lifetime estimated from the three change detection methods at urban infrastructure?

The last experiment investigates the transferability of the proposed methodology for transport to urban infrastructure monitoring. The study area Miami is used which has six buildings under change. The setting in this experiment is the same as in Experiment 3 and 4, i.e. the plausibility of the coherent lifetime estimated with CD-Phase, CD-CohMat and CD-Amplitude are compared. Moreover, the displacement maps from CCS pixels only and from CCS and TCS pixels are compared.

5.2 Study Areas and Datasets

Five study areas are selected to conduct the experiments. Four study areas focus on transport infrastructure while one covers an urban environment to study the transferability of the methodology to urban infrastructure. An overview on the study areas, datasets and related experiments is given in Table 5.1 and in Figure 5.1.

Table 5.1: Description of the study areas, datasets and their usage in the experiments.

	Villena	Figuera	Neumünster	Sande	Miami
Country	ESP	ESP	GER	GER	USA
Begin	02-01-2021	30-10-2014	05-01-2021	20-10-2014	12-04-2016
End	23-01-2024	09-07-2024	20-01-2024	16-09-2025	19-05-2025
Years	3	10	3	11	9
No. images	121	435	121	467	231
Orbit & track	Desc 8	Desc 8	Desc 139	Desc 37	Asc 48
Width	20.8 km	0.5 km	43.9 km	7.8 km	0.35 km
Length	55.8 km	1.7 km	27.9 km	8.3 km	0.84 km
Coregistration	Gamma	Gamma	Gamma	Gamma	ISCE
DEM	SRTM	Copernicus	SRTM	Copernicus	None
DEM resolution	30 m	90 m	30 m	30 m	-
Experiment	1, 2	3, 4	1, 2	3, 4	5

Villena and Figuera, Spain

The study area is located in Spain in the region of the city Villena (Figure 5.1a) and is characterised by sparse vegetation and semi-arid climate. This area covers several highways and railway tracks and is used in Experiment 1 and 2 to analyse the capabilities of the method under favourable conditions with little or no vegetation. Several transport infrastructure in the study area have been built during the past decade. Therefore, a subset of the Villena study area (Figure 5.1b) is additionally used which is here called Figuera due to its location close to the municipality La Font de la Figuera. The study area Figuera covers railway tracks, highways and corresponding bridges whose construction is shown in Figure 5.2 and is used in Experiment 3 and 4 to compare the performance of the change detection methods and to analyse the displacement time series retrieved for both, TCS and CCS pixels. At the highway, both, the embankments leading to the highway bridge and the bridge itself, have been constructed. Moreover, three railway tracks are present. For simplicity, these tracks are numbered as railway 1, railway 2, and railway 3. Two tracks are oriented in east-west direction among which the southern track (railway 1) did not change during the study period and the northern track (railway 2) was newly build. Also the track oriented in north-south (railway 3) was newly build.

One dataset for Villena and one for Figuera are used which stem from the same Sentinel-1 descending orbit track 8, but cover different time spans. For Villena, the dataset covers three years,

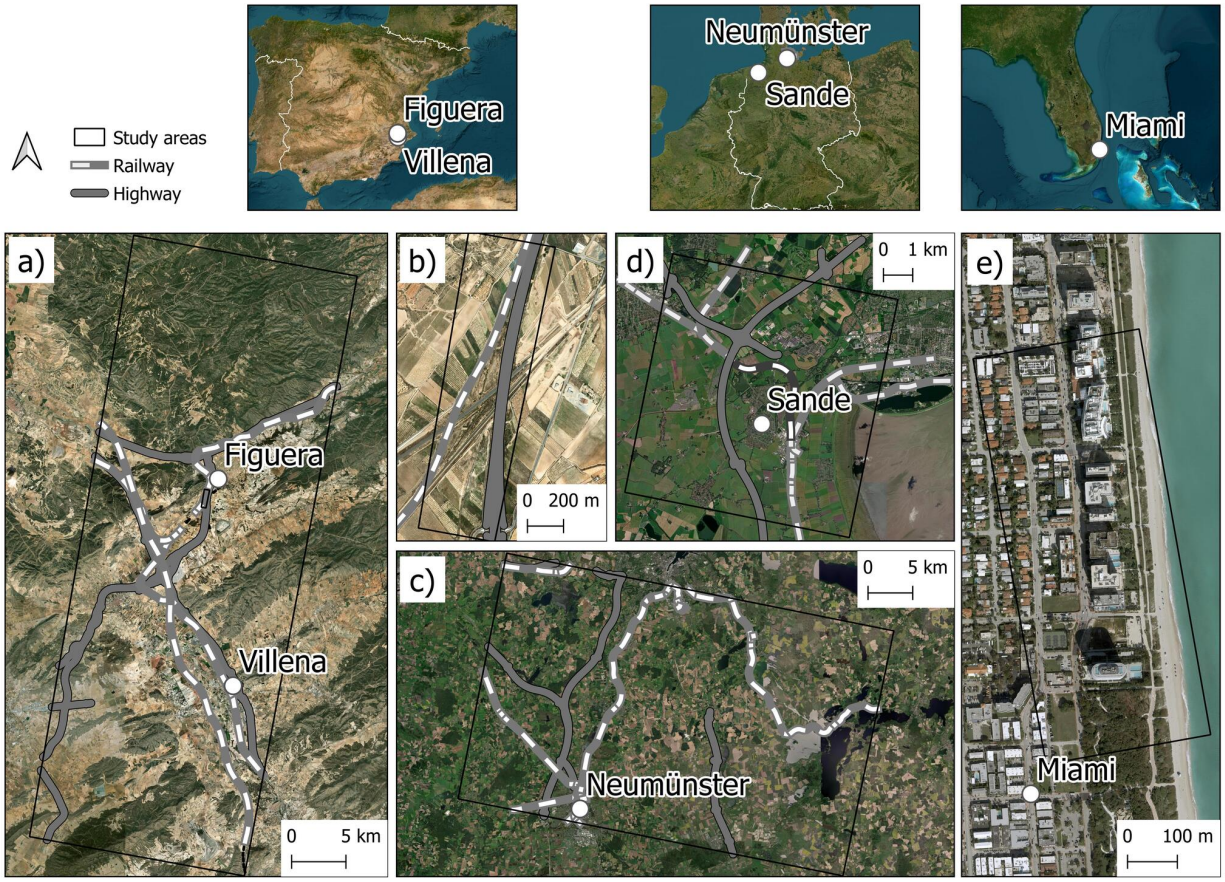


Figure 5.1: Overview on the study areas including two areas in Spain, a) Villena and b) Figuera, two study areas in Germany, c) Neumünster and d) Sande, and one area in the United States, e) Miami. Background image: ©ESRI.

02-01-2021 to 23-01-2024 with 121 images, in a time span with no changes at the transport infrastructure. The same time span and number of images are used in the dataset of the study area Neumünster. This time span is used to analyse the pixel selection methods in Experiment 1 and 2 without considering TCS pixels. For Figuera, a longer time span of 10 years is used, from 30-10-2014 to 09-07-2024 with 435 images. The longer time span is selected to cover the construction works in order to assess the performance of the coherent lifetime estimation in Experiments 3 and 4. The datasets are both coregistered using the commercial software package Gamma (Wegmüller et al., 2016) using a 30 m resolution Shuttle Radar Topography Mission (SRTM) DEM for Villena and a 90 m resolution Copernicus DEM[3] for Figuera.

Neumünster, Germany

The study area is located in Germany and covers the area of the city Neumünster in the south, to the city Kiel in the north, featuring a rural landscape with small cities, a few villages and extensive vegetation surrounding the transport infrastructure (Figure 5.1c). For this study area and time span,

[3] ©DLR e.V. 2010-2014 and ©Airbus Defence and Space GmbH 2014-2018 provided under COPERNICUS by the European Union and ESA; all rights reserved.

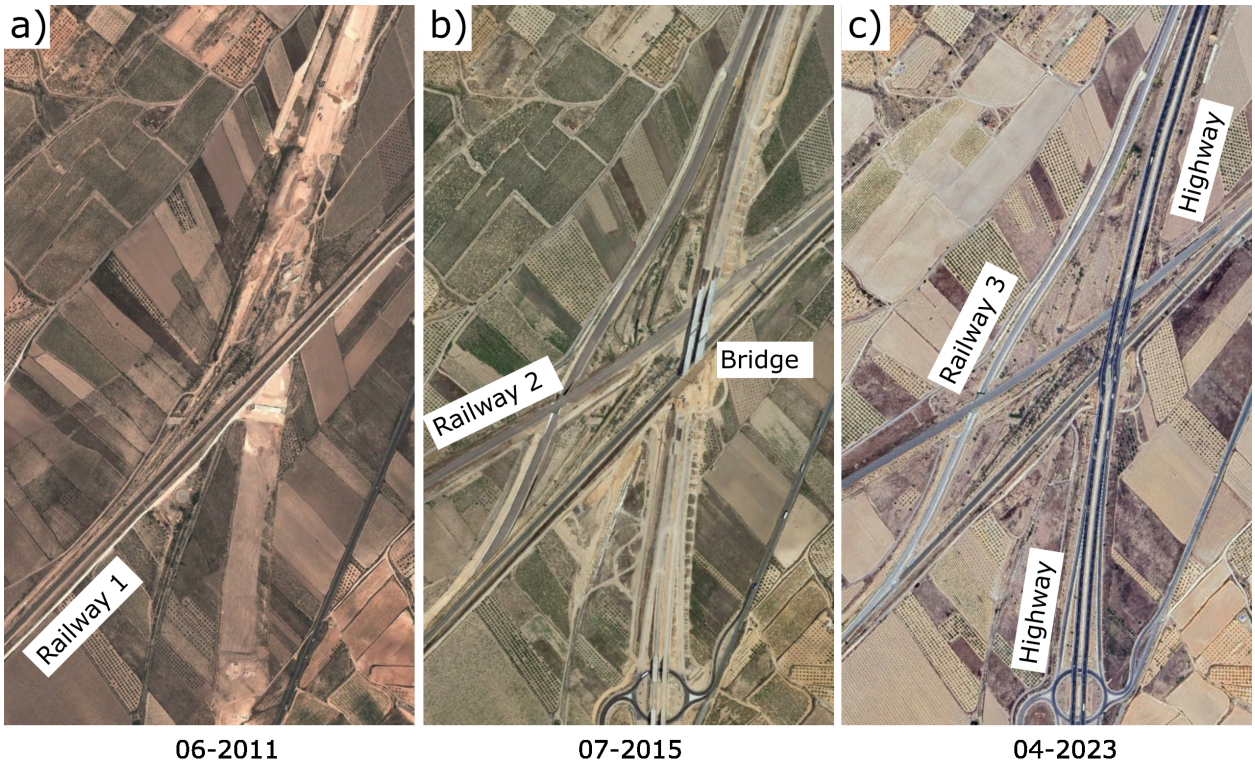


Figure 5.2: Study area Figuera for which a larger dataset is analysed with three railway tracks, a highway and a highway bridge. This study area is a subset of the Villena study area shown in Figure 5.1a. a)-c) Optical satellite images showing the different stages of the construction before and during the study period (Google Earth, Image ©2025 Airbus).

no changes at the transport infrastructure are known. Hence, the study area is used in Experiments 1 and 2 to examine the pixel selection methods without considering TCS pixels. The study area is selected due to its predominantly vegetated areas in the vicinity of the transport infrastructure in order to analyse the performance of the proposed method under challenging conditions.

The dataset covers three years from 05-01-2021 to 20-01-2024 with 121 SAR images. The SAR images are acquired in descending orbit direction from track 139. The same three years time span and number of images are used in the smaller dataset of the study area Villena. The dataset is coregistered using Gamma (Wegmüller et al., 2016) with a 30 m resolution SRTM DEM.

Sande, Germany

The study is located in Germany centred around the municipality Sande near the city Wilhelmshaven featuring a railway track which was constructed from mid 2017 to mid 2022 (Figure 5.1d). The surrounding of the transport infrastructure is characterised by dense vegetation. The area is used to study the performance of the coherent lifetime estimation in Experiments 3 and 4.

The dataset includes 467 images from Sentinel-1 descending orbit track 37 covering the study period from 20-10-2014 to 16-09-2025. The images are co-registered with Gamma (Wegmüller et al., 2016) with a 30 m resolution Copernicus DEM.



Figure 5.3: Study area Sande which shows the new railway track. According to the railway provider (Deutsche Bahn, 2025), the preliminary construction work has started 01-07-2017, while the main construction work started one year later in 10-08-2018. The railway track was put into operation in 30-06-2022, meaning that the construction must have finished before that date. a)-c) Optical airborne images showing the different stages of the construction before and during the study period (LGLN (2024) CC BY 4.0).

Miami, United States

The study area is located in the United States and covers the urban environment of Miami (Figure 5.1e). Along the coastline of Miami Surfside (Figure 5.4), several changes to high-rise buildings are known among which some show a subsidence signal (Aziz Zanjani et al., 2024). This study area is used to analyse the transferability of the proposed coherent lifetime and time series estimation to an urban environment in Experiment 5. Six buildings are analysed in detail which either were constructed, demolished or collapsed. The Champlain Tower collapsed on 24th of June 2021 claiming the lives of 98 people. The Eighty Seven Park Tower, Arte building, and 8926 Collins Ave have been constructed during the study period. Two buildings were demolished including the Surf House Condominiums north of the Arte building and a small building (called temporary building in Figure 5.4, probably a hut related to the construction of the neighbouring Eighty Seven Park Tower).

The dataset includes 231 images from Sentinel-1 ascending orbit track 48 in the time span from 12-04-2016 to 19-05-2025. The images are coregistered using the InSAR Scientific Computing Environment (ISCE) (Rosen et al., 2012) without a DEM to avoid inaccurate or misregistration as the available DEMs do not contain the high-rise buildings.

5.3 Processing Parameters

The processing parameters for change detection, pixel selection and time series analysis are presented in the following and listed in Table 5.2. Variations of the parameters for individual experiments are specified.

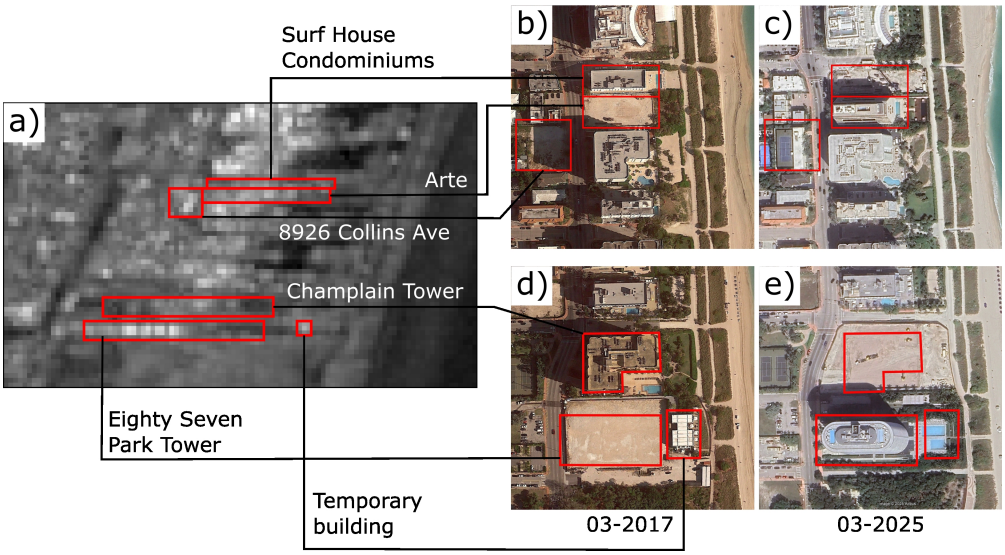


Figure 5.4: Study area in Miami with the location of the six analysed buildings shown with red masks. a) Mean SAR amplitude image. Optical satellite images b) and d) from the beginning (2017), and c) and e) from the end (2025) of the study period (Google Earth, Image ©2025 Airbus). The building masks in the SAR image appear elongated compared to those in optical images because the resolution is higher in the range direction than in the azimuth direction. Moreover, several scatterers are located along different heights of the building, but appear in different pixels in the range direction due to the SAR imaging geometry (see Figure 2.1).

Change Detection

Change detection is applied for the study areas Sande, Figuera and Miami. For Figuera and Miami, change detection is applied on the whole study area, while for Sande, change detection is restricted to the location of the railway tracks given by a mask for the infrastructure derived from OSM (see Section 5.4.1). Change detection is not applied for Villena and Neumünster as these datasets are used to study the suitability of the pixel selection.

The open-source research software SPAtioTemporal Selection of Scatterers (SpaTZ), developed within the scope of this thesis, is used for change detection with CD-Phase, CD-CohMat, and CD-Amplitude. For CD-Phase (Section 4.3.1.1), a redundant small baseline interferogram network is used with each image connected to the consecutive five images, i.e. a bandwidth of five. The phase noise is estimated for each pixel from a $3\times9\,\text{pixels}^2$ neighbourhood (azimuth×range). To identify significant changes in a pixel's time series, a threshold of -0.08 is applied on the score for Miami and -0.1 for Sande and Figuera. CD-CohMat (Section 4.3.1.2) is applied using a coherence-level of $\gamma = 0.8$ to model the coherence matrix. The coherence matrix is estimated from a non-adaptive $3\times9\,\text{pixels}^2$ neighbourhood (azimuth×range), which is the same as for CD-Phase. A threshold of -1600 is applied on the score estimated from the CD-CohMat to identify significant changes for Sande, Figuera and Miami. The thresholds for the LRT of CD-Phase and CD-CohMat were experimentally derived, according to the most accurate results. CD-Amplitude (Section 4.3.1.3) is applied with a particularly low significance level $\alpha = 0.0001$ to avoid wrong detections as recommended by Dörr et al. (2022). All pixels passing the hypothesis test are considered to exhibit a statistically significant change.

Pixel Selection

The pixels are selected based on their phase quality with either the TPC targeting PS pixels or the PLC targeting DS pixels. The open-source research software SARvey (Piter et al., 2025b), developed within the scope of this thesis, is used to compute the TPC. The TPC (Section 4.3.2.1) is computed from the whole time span in case no change was found during change detection. If a change was detected, the TPC is computed from the period before and after the change separately, and the period with the higher TPC is selected. The TPC is estimated from a redundant small baseline interferogram network which is the same network as used for the displacement retrieval during the time series analysis. Again, a neighbourhood given by a $3\times9\,\text{pixels}^2$ window is used, corresponding to an area of $60\,\text{m}\times45\,\text{m}$ for Sentinel-1 images. According to Zhao and Mallorqui (2019), the TPC depends on the type of interferogram network, with slightly higher coherence values for a star network compared to a small baseline network, which is mainly due to the different number of interferograms used to compute the TPC. In Experiment 1, the performance of the pixel selection is assessed using the TPC estimated from a single-reference network of interferograms instead of a small baseline network to examine the upper bound of the performance.

The open-source research software MIAmi Phase Linking in PYthon (MiaplPy) (Mirzaee et al., 2023) is used to perform phase linking and to compute the PLC. First, the coherence matrix is computed from the siblings of the central pixel which are identified with the KS test from a $19\times19\,\text{pixels}^2$ window corresponding to an area of $380\,\text{m}\times95\,\text{m}$. PS candidates ($\leq$10 siblings) are distinguished from DS candidates (>10 siblings). For this purpose, the central pixel is counted as one of the sibling pixels. For DS candidates, phase linking is performed with sequential CPL and a mini-stack size of 10 images. Finally, the phase quality of the filtered phases of the DS candidates is evaluated with the PLC. In Experiments 3 to 5, DS pixels are not included.

Time Series Analysis

The open-source research software SARvey (Piter et al., 2025b), developed within the scope of this thesis, is used to perform the time series analysis. A small baseline interferogram network is created and first-order points are selected with a TPC threshold of 0.9. The second-order points are selected with a TPC and PLC threshold of 0.8. The applied coherence thresholds were chosen conservatively in order to reduce the number of false-positive selections and to ensure the derivation of correct displacement results. For the second-order pixels, phase linking is applied to pixels within the ten-pixel buffer around the transport infrastructure to limit the computational costs, as the primary interest is in the displacement signal at the object and its immediate neighbourhood. The analysis is restricted to TCS pixels with a TPC higher than 0.8 during their coherent lifetime. Furthermore, pixels are removed from the analysis if their coherent lifetime is shorter than 30 images as the estimation of the coherence is biased with few samples only. Pixels not showing a significant change are considered as CCS pixels if their TPC exceeds 0.8 for the study period. The atmospheric filtering is skipped for Miami and Figuera as the study areas are small and the atmospheric effect is negligible when using a local reference point.

Table 5.2: Processing parameters for each study area.

	Villena	Figuera	Neumünster	Sande	Miami
Change Detection					
CD-Phase:					
LRT Threshold	-	-0.1	-	-0.1	-0.08
Window size in pixel^2	-	3×9	-	3×9	3×9
Interferogram network bandwidth	-	5	-	5	5
CD-CohMat:					
LRT Threshold	-	-1600	-	-1600	-1600
Window size in pixel^2	-	3×9	-	3×9	3×9
Model coherence	-	0.8	-	0.8	0.8
CD-Amplitude:					
Significance Level	-	0.0001	-	0.0001	0.0001
Pixel Selection					
Temporal Phase Coherence:					
Window size in pixel^2	3×9	3×9	3×9	3×9	3×9
Phase Linking Coherence:					
Window size in pixel^2	19×19	-	19×19	-	-
Min. no. of siblings for DS candidates	>10	-	>10	-	-
Time Series Analysis					
First-order points:					
Coherence threshold	0.9	0.9	0.9	0.9	0.9
Atmospheric filtering	✓	-	✓	✓	-
Second-order points:					
Coherence threshold	0.8	0.8	0.8	0.8	0.8
Min. length of coherent lifetime (no. images)	-	30	-	30	30

5.4 Evaluation Strategy

5.4.1 Masking of Infrastructure

The systematic analysis of transport infrastructure requires that the corresponding pixels in the SAR image are known. This is achieved by transferring the location of the transport infrastructure derived from the OSM dataset (OpenStreetMap contributors, 2025) to the radar coordinates of the Sentinel-1 images by finding pixels in the radar image whose map coordinates are close to the map coordinates of the infrastructure line. The assumption is that the geolocation of the coregistered image stack is accurate enough and the terrain is flat at the transport infrastructure such that shadow, layover or foreshortening resulting from the radar imaging geometry do not play a role. A buffer of ten pixels is created along the transport infrastructure line in the radar image to mask the pixels potentially belonging to the transport infrastructure. In the analysis, a pixel is considered to belong to a railway track or highway if it lies within the respective mask. For bridge analysis, the same masking approach is applied, without differentiating between railway and highway bridges.

The analysis of the buildings in Miami in Experiment 5 also requires masking. The buildings were masked manually in the geocoded amplitude image considering the radar imaging geometry (see Section 2.1). The validity of the masks was checked by visual comparison with the mean amplitude images of the study areas. Masking of infrastructure is used in all experiments.

5.4.2 Plausibility Metrics for the Coherent Lifetime

The estimated coherent lifetime is validated on the level of individual infrastructure objects. The period in which a change of the scattering mechanism is expected for that object is derived from high-resolution optical satellite images (Figure 5.2, 5.3, and 5.4) and for Sande, additionally from the information of the railway provider (Deutsche Bahn, 2025). A reference period is determined from multi-temporal high-resolution optical satellite images with irregular temporal spacing. Two cases are distinguished: Construction and demolition of infrastructure. For the construction case, the change from an incoherent signal to a coherent signal is supposed to happen when the construction is finished and, hence, the backscattering no longer changes such that the scatterer maintains a coherent signal over time. The exact time, when the construction is finished, is not visible in the optical image due to the irregular temporal spacing between the acquisitions. Therefore, the reference period is defined to start with the last image in which the construction was still visible and is defined to end with the first image in which the construction is no longer visible. For the demolition case, a scatterer is supposed to lose coherence once the infrastructure is demolished. Accordingly, the reference period starts with the last image in which the infrastructure is still visible and ends with the first image in which the infrastructure is no longer visible.

The reference period derived from optical images, however, cannot be treated as ground-truth due to several uncertainties, including the geolocation of the pixel, the exact location of the scatterer within the pixel, and geometric distortions resulting from the side-looking SAR sensor. However, it is assumed that scatterers within a provided object mask belong to that infrastructure object. The multi-temporal images cover the time span irregularly and provide only sparse temporal information. Moreover, backscattering of a microwave is a property of the object that cannot be inferred from

optical images. The actual change of the scattering mechanism within a pixel is not visible in optical images. Despite these uncertainties, the reference period is used to validate the coherent lifetime estimation. In the following, metrics are proposed which describe the plausibility of the estimated coherent lifetime of the TCS pixels. The presented metrics are termed plausibility metrics. The first two metrics use the information from the optical images, while the last two metrics exploit the similarity of the change dates for pixels within an infrastructure mask and the ambiguity of the change detection resulting from the coherence level of the pixels before and after the change.

Interval Deviation Rate and Number of Correct Pixels

The change detection results are plausible if they are located within the reference period, hence, if they correspond to the construction or demolition period. Allowing the change dates to be outside the reference period up to an acceptable deviation enables to study how close the change dates are to the reference. The percentage of correct pixels is assessed given a maximum acceptable deviation represented by the Interval Deviation Rate (IDR) (Wittich et al., 2022). The acceptable deviation is considered in both temporal directions, i.e. either the change date is before or after the reference period. Beside the relative metric IDR, the absolute number of correct pixels within an acceptable deviation is analysed.

Congruency

The coherent lifetime of a pixel should correspond to the lifetime of the infrastructure it is related to, i.e. if the infrastructure is constructed, the TCS pixel should appear, and for demolished objects, the TCS pixels should disappear. This requires the assumption that the coherence of the pixel's signal is lower during periods when the infrastructure is not present than during the lifetime of the infrastructure. The plausibility of the coherent lifetime estimation is therefore described by the number of TCS pixels which are congruent, i.e. whose coherent lifetime matches the lifetime of the infrastructure.

Similarity Among Infrastructure Pixels

All pixels within an infrastructure mask are assumed to belong to the same object, i.e. to the same railway track, highway, bridge, or building. The scattering mechanism of pixels which belong to the same object, should, as a consequence, also change at the same time. The similarity between the change dates of all pixels within a mask should be high, i.e. the difference between all change dates should be small. The Mean Absolute Temporal Difference (MATD) is computed from P pixels

$$MATD = \frac{1}{P^2/2} \sum_{i}^{P^2/2} |\Delta t_i| \tag{5.1}$$

with the time difference Δt in days between the change dates of two pixels on the same infrastructure and the number of pixel combinations $P^2/2$ within the mask.

Mean Absolute Coherence Difference

The estimated coherent lifetime is assumed to be plausible if the coherence is high during the TCS pixel's lifetime, but low in the other period. This is represented by the Mean Absolute Coherence Difference (MACD) which is computed from P pixels

$$MACD = \frac{1}{P} \sum_{i}^{P} |\hat{\gamma}_{i,\text{before}} - \hat{\gamma}_{i,\text{after}}| \tag{5.2}$$

with the TPC from the period before $\hat{\gamma}_{\text{before}}$ and after $\hat{\gamma}_{\text{after}}$ the change. A high value for MACD is favourable because the higher the values, the better the distinction between a low coherent and high coherent period of the signal.

6 Results and Discussion

In this chapter, the results of the five experiments are presented. The experiments are conducted to answer the research questions discussed in Section 5.1. The first two experiments focus on the selection of CCS pixels at transport infrastructure and the observability of regional and local displacement using the proposed InSAR time series method. With the Experiments 3 and 4, the coherent lifetime estimation with focus on change detection is investigated and the estimation of displacements for TCS pixels is demonstrated. The last experiment investigates whether the methodology can also be applied to urban infrastructure monitoring.

6.1 Experiment 1: Pixel Selection at Transport Infrastructure

In this first experiment, the focus is set on the selection of coherent CCS pixels at transport infrastructure. The two pixel selection criteria, TPC and PLC, are analysed to identify the potential of Sentinel-1 for different transport infrastructure types. First, the spatial neighbourhood utilised during the estimation of the TPC and PLC is analysed. Second, it is investigated which scattering type, point or distributed scattering, is more prevalent. Finally, the characteristics and the performance of the selection criteria are analysed.

Spatial Neighbourhood

The pixel selection criteria TPC and PLC are computed under consideration of the spatial neighbourhood in terms of a spatial window to estimate the phase quality. The choice of the window size for the estimation involves a trade-off: selecting a too small window may lead to an insufficient number of samples for an unbiased estimation, while opting for a too large window may include pixels unrelated to the object, thus, having different backscattering properties.

The cumulative distribution of the TPC is shown in Figure 6.1 for varying window sizes for the transport infrastructure in Villena and Neumünster. The Figure shows that the smaller the window size, the higher the TPC values. The biggest differences, however, appear at low coherent pixels, while the differences are minor for a coherence above 0.7. A window size of $3\times3\,\text{pixels}^2$ seems to overestimate the coherence. The difference between the number of pixels with a coherence above 0.6 is below 1 % for larger window sizes. Based on this analysis, a window size of $3\times9\,\text{pixels}^2$ is chosen for the PS selection with TPC because the coherence differences to larger window sizes are negligible. Moreover, it considers a local neighbourhood around the PS pixels considering the different spatial resolutions of the SAR images in azimuth and range.

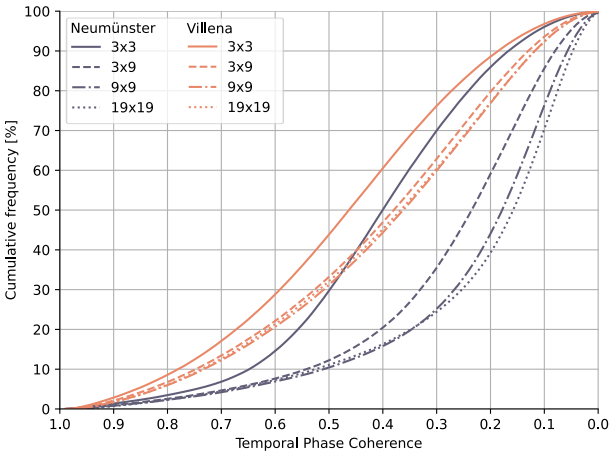


Figure 6.1: Cumulative distribution of TPC for pixels at the transport infrastructure estimated from different window sizes for Villena and Neumünster.

The selection of sibling pixels for the estimation of the coherence matrix is shown by qualitative examples in Figure 6.2. Three different window sizes, including 3×3 pixels^2, 9×9 pixels^2 and 19×19 pixels^2, are examined for exemplary pixels on highways and railway tracks in Villena and Neumünster. The example pixels include DS candidates with more than 10 siblings (Figure 6.2a, b, d, f) and PS candidates with less or equal to 10 siblings (Figure 6.2c, e). For the PS candidates, the number of siblings stays almost the same with increasing window size. This is due to the unique scattering behaviour of the PS pixels which differs from its surrounding. In contrast, for DS candidates, the larger the window size, the more siblings are found. In case of vegetation surrounding the transport infrastructure, the siblings are expected to be found among the transport infrastructure pixels because the signal from the vegetation is decorrelated and, thus, only provides noise. This can be seen for the DS candidates from Neumünster (Figure 6.2a, b). The spatial pattern of the siblings corresponds to the shape of the transport infrastructure visible in the mean amplitude image in the background. In Villena, the transport infrastructure is not surrounded by vegetation. Nevertheless a similar effect is observed. For the railway track pixel (Figure 6.2f), the siblings also correspond to the shape of the railway track and cover parts of two neighbouring tracks. The highway pixels in Figure 6.2d and e are located close to each other. While the pixel in Figure 6.2e is located on the side of the highway embankment oriented towards the sensor and thus shows a bright backscattering, the pixel in Figure 6.2d is located on the highway surface and shows a lower backscattering. As a consequence of the different backscattering, the pixel on the highway has several siblings in its neighbourhood which corresponds to the surface and other low backscattering parts. In contrast, the pixel on the embankment has only siblings which also show a high backscattering signal.

The required number of 11 siblings to classify a pixel as DS candidate for phase linking cannot be achieved from a window size of 3×3 pixels^2. However, the coherence matrices estimated from siblings within a 3×3 pixels^2 window are shown to highlight the bias in the coherence matrix resulting from too few samples. Increasing the window size from 9×9 pixels^2 to 19×19 pixels^2 results in the PLC staying on a similar level or increasing. It also increases the contrast and smoothness of the values in the coherence matrix, meaning that the decorrelation mechanism of the scatterer becomes clearer. The pixels shown in Figure 6.2a and b would not be selected as DS pixels as their PLC

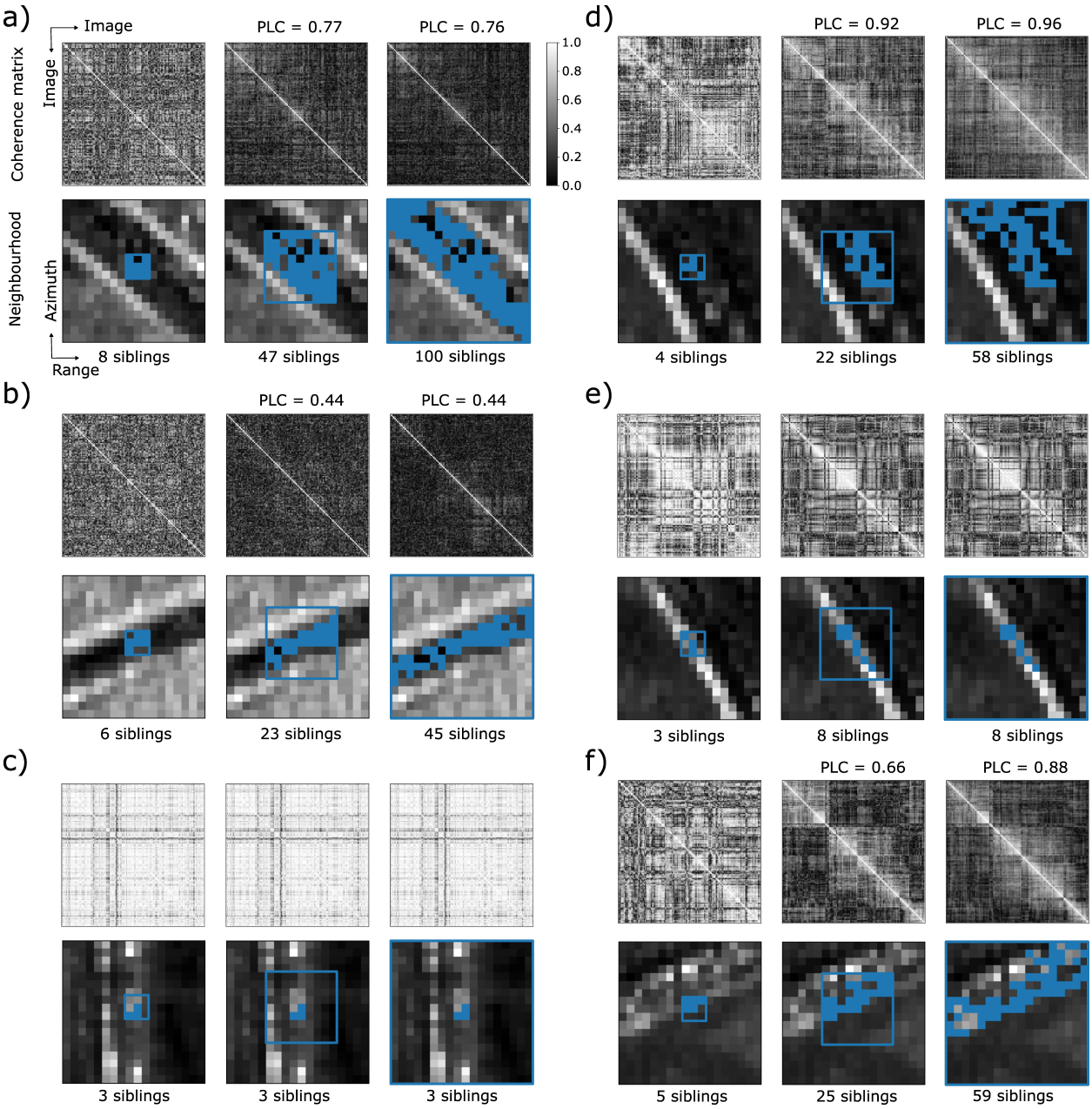


Figure 6.2: Examples for the detection of sibling pixels at transport infrastructure. In each subfigure, the upper row shows the coherence matrix estimated from the set of siblings shown in the bottom row. The sibling pixels are coloured blue and are depicted on top of the temporally averaged amplitude image. The spatial neighbourhood among which the siblings are searched is framed by a blue window. Three different window sizes are exemplarily shown: 3×3 pixels^2, 9×9 pixels^2 and 19×19 pixels^2. For each window size, the number of selected siblings and the corresponding PLC are listed. If the number of siblings is below 10, phase linking is not applied and the PLC cannot be estimated. The pixels in a)-c) are taken from Neumünster, while d)-f) are taken from Villena. The pixels in a)-e) correspond to highways and f) corresponds to a railway track.

does not exceed 0.8. As a conclusion from this analysis, a window size of 19×19 pixels^2 is used in the estimation of the coherence matrix for phase linking.

Point and Distributed Scattering

The scattering mechanisms are differentiated based on the number of siblings and are analysed first regardless of the quality of the pixels. The cumulative distribution of the siblings at transport infrastructure in Villena and Neumünster are shown in Figure 6.3a. The distributions differ depending on the transport infrastructure type. Bridges have the highest percentage of pixels with few siblings (e.g. <30 siblings) followed by railway tracks and the lowest at highways. This is observed in both study areas and corresponds to the observation that bridges show the brightest backscattering followed by railway tracks and highways (compare Figure 1.3). A strong and unique backscattering is related to a PS pixel which has only few siblings.

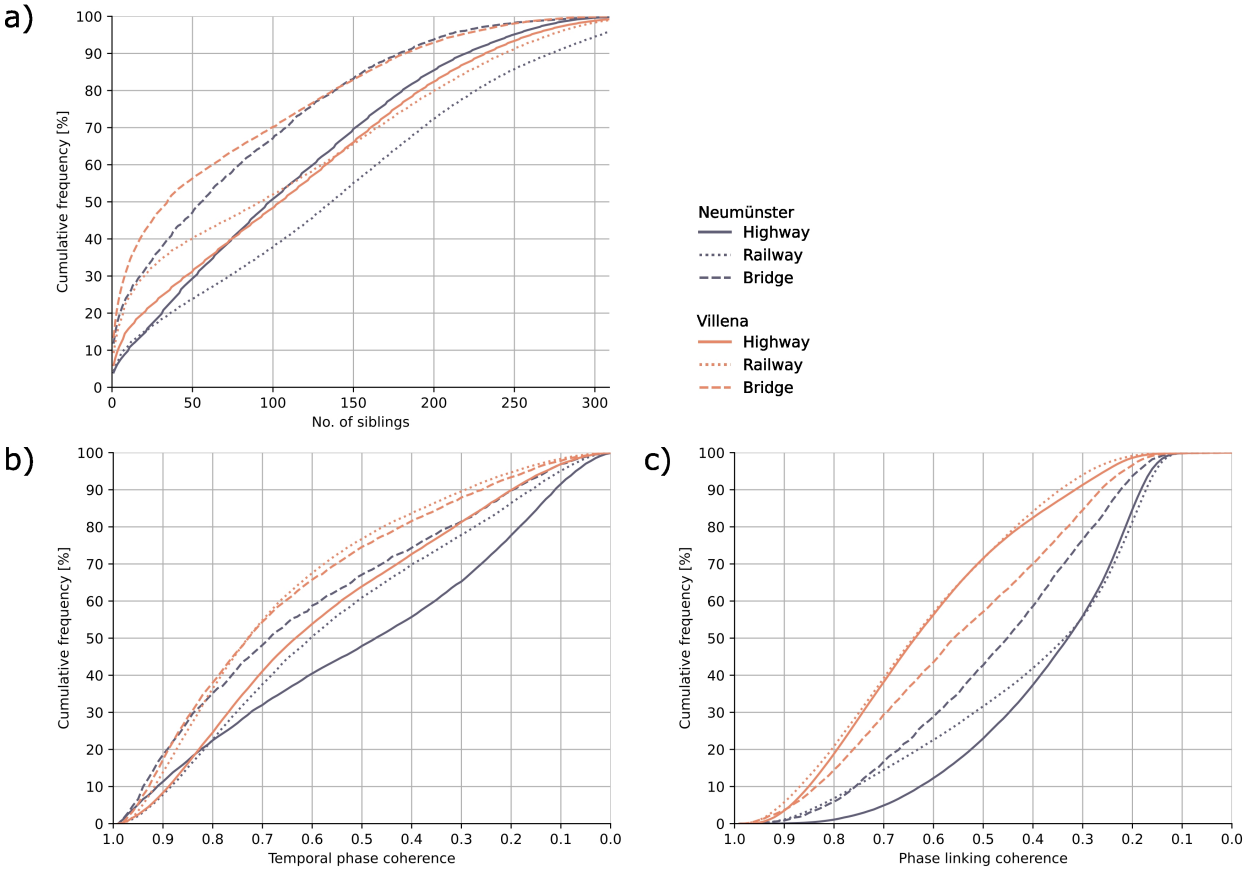


Figure 6.3: Cumulative distributions of a) the number of siblings, b) the TPC, and c) the PLC for highways, railway tracks and bridges in Neumünster and Villena.

The curves of the three infrastructure types differ between the study areas. In general, there is a higher percentage of pixels with a small number of siblings at all transport infrastructure in Villena compared to Neumünster. As a consequence, there are more PS candidates in Villena, ranging from 16 % to 33 %, and more DS candidates in Neumünster, ranging from 75 % to 90 %, as listed in Table 6.1. This demonstrates that there is a higher potential of finding coherent pixels among the DS candidates which cover the majority of the pixels on the transport infrastructure. Nevertheless,

Table 6.1: Percentage of pixels corresponding to PS and DS pixels or to their candidates. The PS and DS candidates are derived from the sibling analysis, while the coherent PS and DS pixels are selected using the TPC and PLC, respectively, among their candidates. The percentages are given for the study areas Villena (V) and Neumünster (N).

	Highway		Railway		Bridge	
	V	N	V	N	V	N
PS candidates	16 %	10 %	24 %	11 %	33 %	25 %
DS candidates	84 %	90 %	76 %	89 %	67 %	75 %
PS pixels	25 %	22 %	36 %	23 %	38 %	35 %
DS pixels	19 %	1 %	21 %	7 %	15 %	6 %

for Neumünster, a lower potential resulting from the DS candidates is anticipated. The analysis of the spatial neighbourhood of the transport infrastructure in the previous section showed, that a high number of siblings, for instance about more than 100 siblings (compare Figure 6.2a) can be reached in Neumünster only if the siblings include pixels outside the transport infrastructure. However, the surrounding is mostly covered by vegetation which yields a decorrelated signal. DS candidates, whose siblings include vegetation, most likely have a decorrelated signal itself. Consequently, DS candidates with a high number of siblings are assumed to be incoherent. Keeping the example of more than 100 siblings, 32 % of the pixels at bridges, 48 % at highways, and 62 % at railway tracks are assumed to be incoherent. This relation between number of siblings and signal correlation, however, does not hold for Villena where the surrounding of the transport infrastructure includes land cover that might show a correlated signal such as bare soil.

In conclusion, the analysis of the number of siblings reveals three effects. First, there is a much higher number of DS candidates compared to number of PS candidates. Second, this effect varies between the transport infrastructure types. While bridges exhibit a stronger backscattering and show the highest percentage of PS candidates, the highway has a lower backscattering and shows the most DS candidates. The number of siblings at railway track pixels lies in between the other two infrastructure types. Third, the number of sibling pixels varies significantly between the two study areas Villena and Neumünster. More PS candidates are found for the less vegetated study area Villena.
The classification of the pixels to the two scattering types based on the number of siblings is a straightforward approach. It considers the spatial stationarity assumption for DS pixels and limits PS candidates to pixels with a distinct scattering behaviour compared to its neighbourhood. However, this approach is limited due to the selection of a threshold on the number of siblings. Although a threshold of ten siblings is applied for further processing, the given analysis is based on the distribution which yields an overview on the potential of both PS and DS pixels. Notably, the threshold selection should ensure that enough samples are available to estimate the coherence matrix for DS candidates. In general, the more samples are considered, i.e. the more looks are applied, the higher the SNR of the filtered phases of the DS pixel (Hanssen, 2001).

Temporal Phase Coherence

The percentages of PS pixels among the PS candidates are listed for Villena and Neumünster in Table 6.1. The comparison of the transport infrastructure types shows that bridges have the highest percentage of PS pixels. While in Neumünster the percentages of PS pixels at railway tracks and highways are about the same, in Villena the railway tracks have 11 percentage points more PS pixels compared to highways. In Villena, higher roughness of the railway tracks compared to the highways could be a reason. The difference between the study areas could be the vegetation in the surrounding of the narrow railway tracks in Neumünster which might cause shadow in the SAR image at the location of the railway tracks.

The cumulative distributions of the TPC, shown in Figure 6.3b, reflect the monitoring potential depending on the selection of the threshold. Lowering the threshold of 0.8 which was selected for the experiments to, for instance, 0.7, yields more pixels for all transport infrastructure types, but a higher increase in Villena than in Neumünster. This shows that the backscattered signal is in general more coherent in Villena.

The TPC is assumed to address PS pixels and was previously only analysed for PS candidates. The relationship between TPC and the number of siblings is exemplarily shown for all pixels, i.e. both, PS and DS candidates, on the highways in Villena in Figure 6.4. Even though the majority of the PS pixels selected with a coherence threshold of 0.8 have equal or less than 10 siblings, PS pixels can have significantly more siblings. This shows that while TPC favours the selection of PS pixels over DS pixels, it is not exclusive to PS pixels.

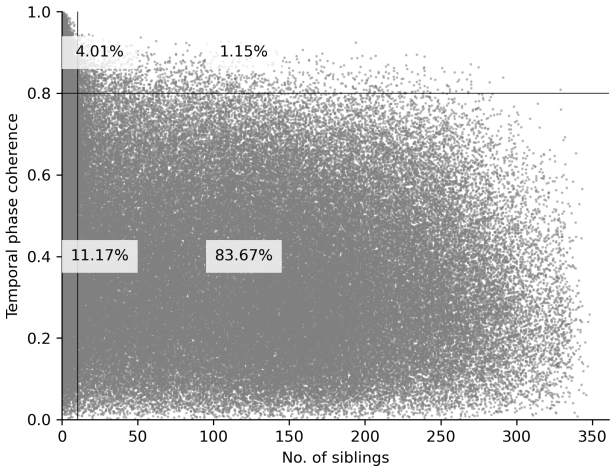


Figure 6.4: Comparison of TPC with the number of siblings found for pixels associated with highways in Villena. The black lines mark the applied thresholds on the number of siblings (10) to identify DS candidate pixels and on the coherence (0.8) for pixel selection. Note that the location of each point on the x-axis is shifted by a random value sampled from a uniform distribution in the interval [-0.25, 0.25] to better visualise points with the same location.

Phase Linking for Distributed Scatterer Selection

The selection of DS pixels is performed through phase linking from the coherence matrix. For this purpose, a subset of the coherence matrix, a ministack with 10 images, was used. The phase quality

can subsequently be assessed with the PLC to measure the fit of the phase filtering w.r.t. the whole coherence matrix or to the ministack which was used during phase linking. Figure 6.5 depicts the histograms of the PLC for DS candidates in Villena (Figure 6.5a) and Neumünster (Figure 6.5b) for three variants: 1) Phase linking is applied on the full coherence matrix and the PLC is also evaluated on the full coherence matrix. 2) Phase linking is applied on the ministack and is also evaluated on the same ministack. 3) Phase linking is applied on the ministack, but the PLC is evaluated on the full coherence matrix. The results show that variant 2 is strongly biased towards high coherence values, while variant 3 agrees well with variant 1 for high coherence values. Variant 1 is assumed to better reflect the phase filtering quality compared to variant 2, because the full coherence matrix has been considered. Consequently, variant 3 is chosen for the experiments because the ministack reduces the computational time compared to variant 1 while yielding a reliable estimate of the PLC.

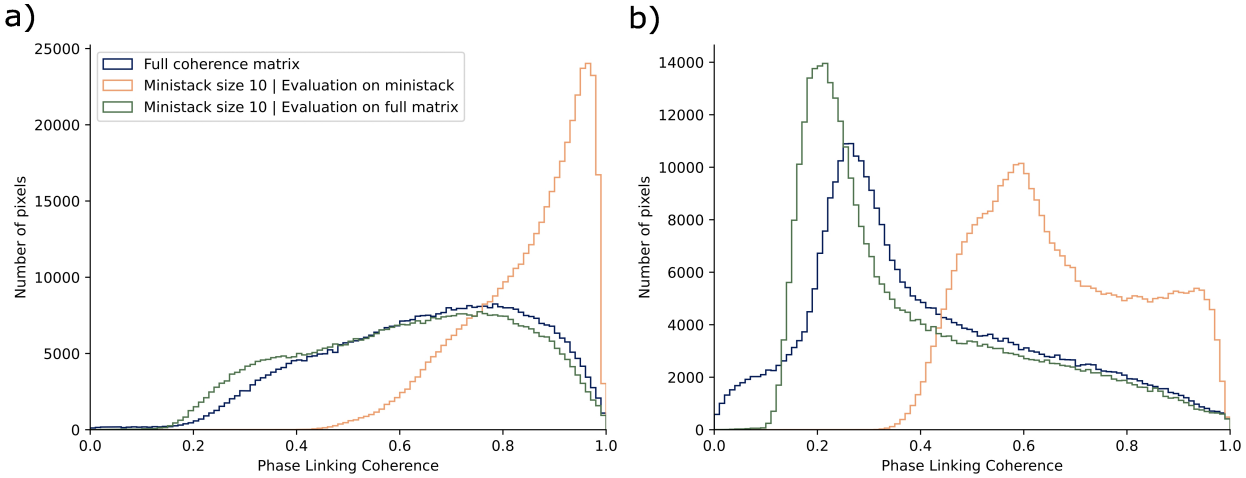


Figure 6.5: Histograms of the PLC evaluated on three phase linking variants considering the full or part of the coherence matrix for all DS candidate pixels on transport infrastructure in a) Villena and b) Neumünster. Pixels on railway tracks, highways or bridges are not differentiated.

The cumulative distribution of the PLC for DS candidates is depicted in Figure 6.3c and the percentages of selected DS pixels are listed in Table 6.1. More DS pixels are selected in Villena than in Neumünster for each of the transport infrastructure types. Moreover, the general coherence level is higher in Villena because a lower coherence threshold would increase the number of DS pixels more in Villena than in Neumünster. The percentage of DS pixels ranges from 15 % to 21 % in Villena, while only 1 % to 7 % of the pixels are selected in Neumünster.

The relationship between PLC and TPC is depicted for DS candidates in Figure 6.6 for both study areas and for railway tracks and highways. The majority of the pixels, between 77 % and 99 %, are rejected by both criteria, whereas less than 1.5 % of the pixels are selected by both methods. This means that the two pixel selection methods appear to provide complementary sets of pixels. The improvement through phase filtering, which increases the SNR of the pixels' signal, is apparent from the pixels which exhibit a higher PLC than TPC. For the coherence threshold of 0.8, it comprises about 7 % at railway tracks in Neumünster and up to 21 % at railway tracks and highways in Villena. In contrast, the set of pixels that are only selected with TPC contains less than 1 % for each of the infrastructure types in both study areas. It is worth noting that the TPC and PLC are not describing the same model fit. While TPC describes the fit of the phases w.r.t.

the phase contribution model, the PLC measures the fit of the phase filtering. Consequently, the scatter plot in Figure 6.6 shows almost no correlation between TPC and PLC.

Figure 6.6 also shows the pixels coloured with their number of siblings. Although pixels which are selected by both selection criteria predominantly have less than 50 siblings, no clear correlation between the number of siblings and the coherence is observed in neither TPC nor PLC. In Neumünster, pixels with low coherence tend to have a high number of siblings (>200 siblings), while highly-coherent pixels mostly exhibit lower number of siblings (<200 siblings). This confirms the hypothesis, that a higher number of siblings includes vegetated pixels and, hence, corresponds to a pixel with a decorrelated signal. In Villena, pixels with a high number of siblings are also found among the selected DS pixels. This suggests that the surrounding of the transport infrastructure in Villena contributes coherent information to the phase filtering, leading to an enhanced SNR for the infrastructure.

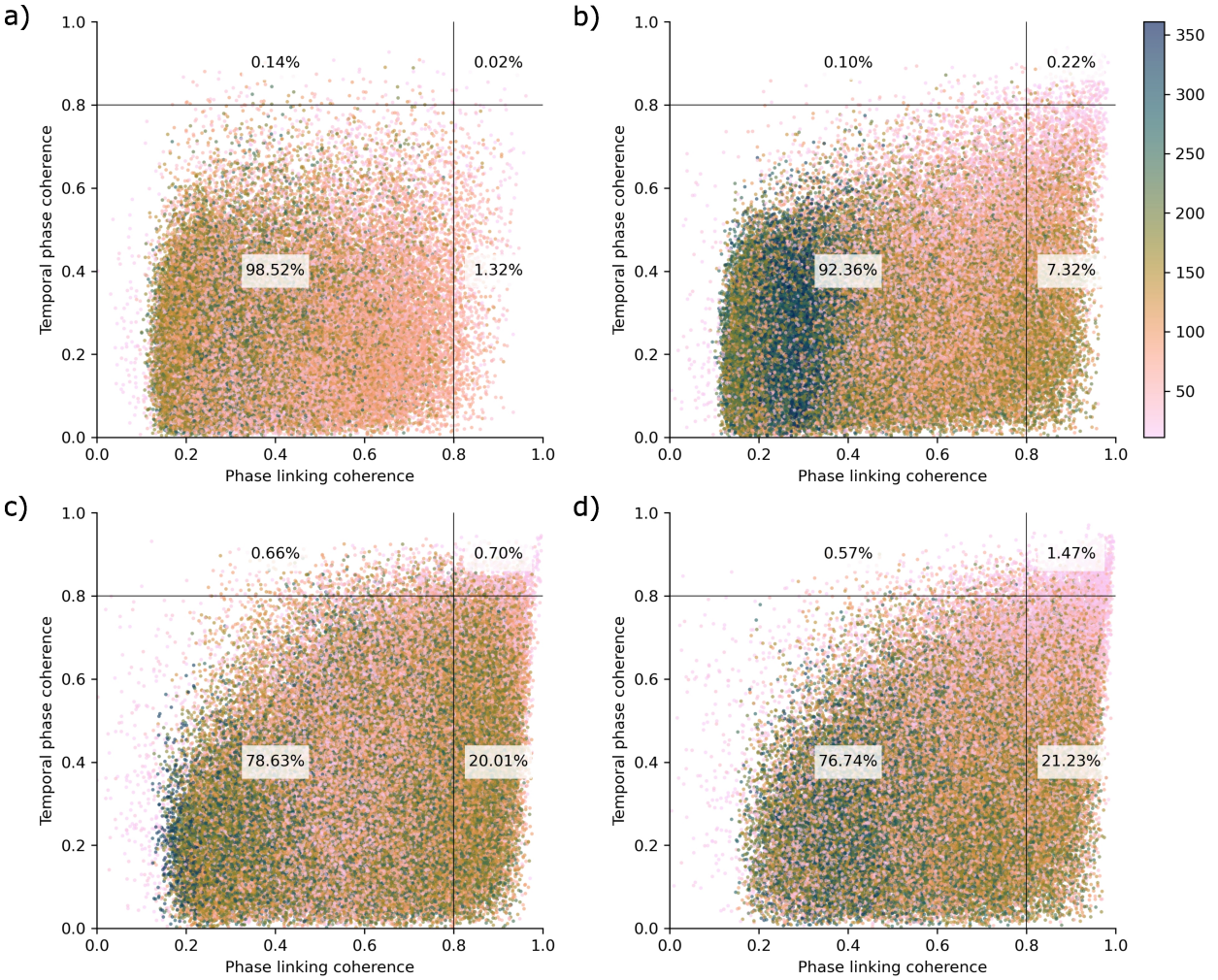


Figure 6.6: Pixel-wise comparison of TPC and PLC for DS candidate pixels for highways (a, c) and railway tracks (b, d) from Neumünster (a, b) and Villena (c, d). The black lines mark the applied thresholds on the coherence (0.8) for pixel selection. The colour represents the number of siblings found for each pixel.

The results in this experiment were derived by exploiting a mask for the transport infrastructure in the radar image. By using a fixed buffer size for the mask, which is larger than the transport

infrastructure itself, it is ensured that all pixels potentially related to the transport infrastructure were included in the analysis. However, this approach also includes pixels in the immediate surrounding, which could be related to other objects, such as buildings, rocky surfaces, vegetation or embankments introducing uncertainties to the interpretation of the results.

The analysis of the scattering types based on the number of siblings revealed that most of the pixels on the transport infrastructure are DS candidates, suggesting significant potential for pixel selection methods that target DS pixels, such as phase linking. The percentage of PS pixels is significantly lower compared to that of DS pixels, but the set of pixels from TPC and PLC are complementary. As anticipated, the coherence of the DS pixels is affected by the neighbourhood of the transport infrastructure, which, in case of Neumünster, is mainly characterised by vegetation which quickly decorrelates over time. The vegetation significantly limits the potential of DS candidates in Neumünster, while a high percentage of DS pixels can be exploited in Villena. The DS pixels thereby constitute the majority of the coherent pixels in Villena and is inevitable for monitoring transport infrastructure. In Neumünster, this is also the case for monitoring railway tracks, but DS pixels contribute marginally to highway monitoring.

6.2 Experiment 2: Observability of Local and Regional Displacements

Monitoring of transport infrastructure requires a dense spatial sampling of the displacement signal. While the potential and limitations of coherent pixels at transport infrastructure in Sentinel-1 images was assessed in Experiment 1 independent of the spatial distribution of the pixels, the location of the coherent pixels and the observability of a displacement signal is analysed in this experiment. Two types of displacement signals relevant for transport infrastructure monitoring are considered: regional and local displacements. Local displacements only affect the transport infrastructure and cover small areas, i.e. correspond to spatially high frequent displacement. In contrast, regional displacements affect both, the transport infrastructure and its surrounding. Regional displacements cover larger areas and correspond to spatially low frequent displacement. Of course, regional and local displacement signals can also be superimposed. Being able to measure local displacements is of higher importance for the goals of this thesis, because spatially high frequent displacement signals can result in larger gradients compared to low frequent signals. At the same time, a higher spatial sampling of the displacement signal is required to correctly retrieve the local displacement signal which sets higher requirements for monitoring local displacement signals. Regional displacement signals can also be observed from coherent pixels in the surrounding and then be interpolated to the transport infrastructure to assess the related hazard. However, measuring regional displacement directly at the transport infrastructure is of course more favourable. The observability of regional and local displacements is analysed in this experiment in the study areas Villena and Neumünster.

The displacement maps are shown in Figure 6.7 depicting the mean LOS velocity for Villena (Figure 6.7a) and Neumünster (Figure 6.7b). The study area Villena is characterised by two large areas showing displacement away from the satellite. One area is located around and in the vicinity of the city Villena. Here, the velocity reaches a maximum of 26 mm/year away from the satellite and

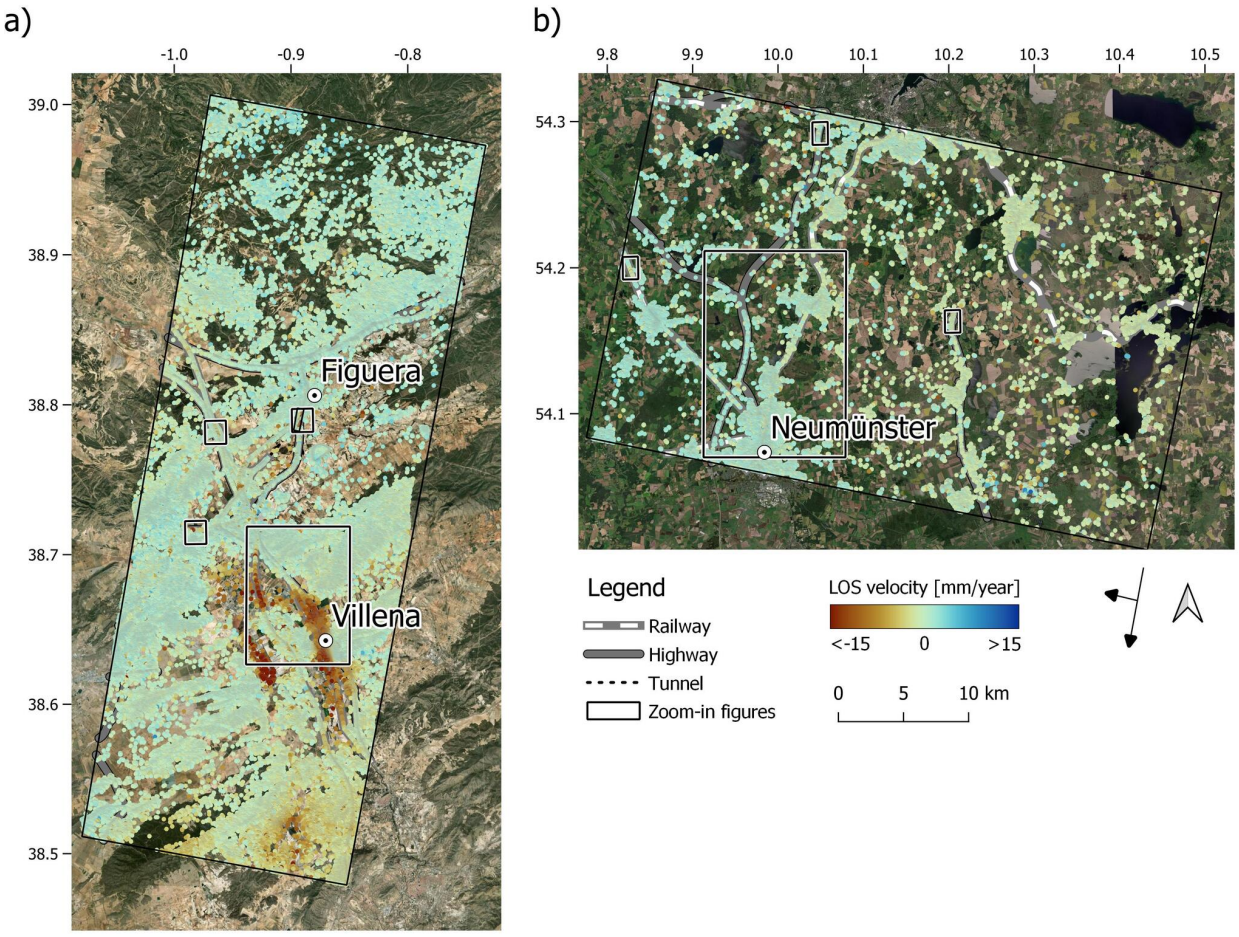


Figure 6.7: Velocity maps of a) Villena and b) Neumünster showing the LOS displacement. Zoom-in figures with regional displacements are shown in Figure 6.8. Zoom-in figures with local displacements are depicted in Figure 6.9 for Villena and in Figure 6.10 for Neumünster. Background image: ©ESRI.

the size of the corresponding area is approximately 44 km^2. The other area is located in the south of the study area showing a bowl-formed displacement with a maximum velocity of 12 mm/year away from the satellite affecting an area of approximately 16 km^2. Intensive groundwater exploitation (Molina et al., 2009) is anticipated to be the reason for the displacement in the two areas, which probably results in land subsidence. The study area Neumünster shows a homogeneous displacement map with no larger displacement areas. Only individual scatterers exhibit a displacement of more than 10 mm/year away or towards the sensor.

The comparison of the two study areas shows that Villena has significantly more coherent scatterers with 314 scatterers per km^2 compared to 80 scatterers per km^2 in Neumünster. The higher number of coherent scatterers at the transport infrastructure in Villena was anticipated as discussed in Section 6.1. The overall higher scatterer density results from PS pixels which were included in the analysis to aid the spatial phase unwrapping of the transport infrastructure pixels. DS pixels were not selected outside the transport infrastructure, because phase linking comes with high computational costs, without the pixels in the neighbourhood providing information for monitoring local displacements at transport infrastructure.

Regional displacements

Figure 6.8 shows the mean LOS velocity maps for regional displacements in Villena and Neumünster. Additionally, velocity profiles along selected railway tracks and highways are depicted. In general, higher scatterer densities are prevalent in cities because scatterers corresponding to buildings are probably included in the transport infrastructure mask.

In Villena (Figure 6.8a), regional displacement away from the sensor is visible and the displacement is also prevalent at the transport infrastructure. The velocity profile (Figure 6.8b) reflects the displacement clearly at the highway segment due to the high scatterer density in this area with small gaps of 277 m. The velocity profile is smooth with variations in a range of 1.5 mm/year indicating that the proposed method allows to retrieve the mean velocity from spatially low frequent displacement signals precisely. The railway segment (Figure 6.8c) shows larger velocity variations of 4 mm/year along the profile. The high variations could correspond to a higher spatial variability of the displacement signal or non-linear temporal displacement which is insufficiently represented by the mean displacement velocity. The railway tracks lie in the vicinity of the salt meadows called Laguna y Saleros de Villena which could affect the stability of the ground. Alternatively, as a regional low frequent displacement signal is expected, the higher variation in the mean velocity could arise from scatterers with a lower SNR. A sparser coverage with a larger gradient is visible between section distance 1.8 km and 2.1 km. The largest gap between the scatterers is 303 m. The velocity profiles at both transport infrastructure in Villena allow to estimate the spatial gradients to assess the hazard at the infrastructure.

In Neumünster (Figure 6.8d), a stable area is observed, i.e., no regional displacement. The irregularly spaced scatterers and the sparse scatterer coverage are major limitations in this study area. However, regional displacements with a spatially low frequent displacement and a larger spatial extent are not visible. The selected highway and railway segments are chosen due to their

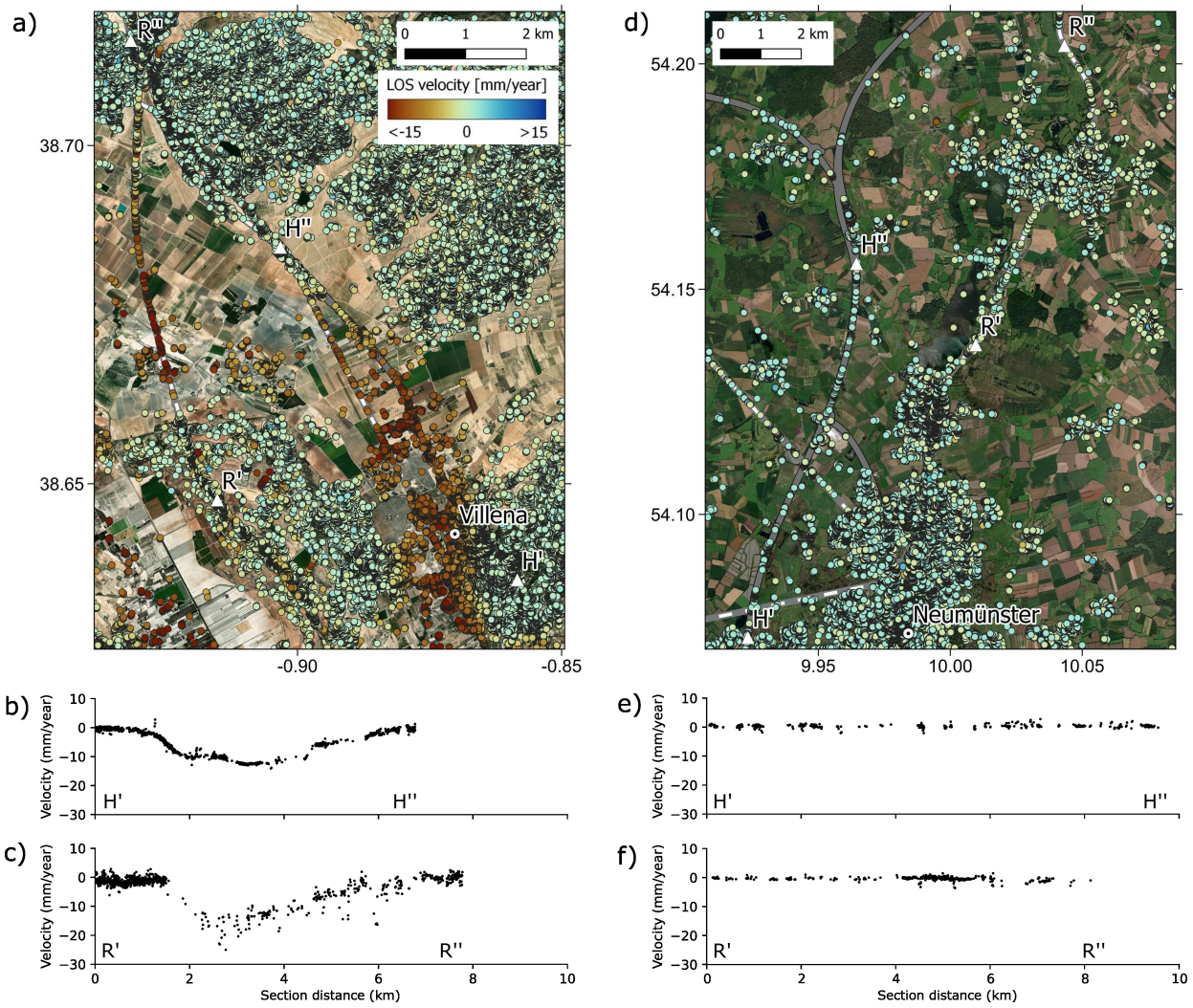


Figure 6.8: Velocity maps showing the LOS displacements for the zoom-ins in a) Villena and d) Neumünster. The mean velocity profiles along a highway (b and e) and a railway (c and f) segment are shown for each study area. The legend is the same as in Figure 6.7. The start and end points of the velocity profiles are marked with a white triangle.

high spatial coverage and serve as examples of the upper limit of what is achievable in this area. Their velocity profiles are shown in Figures 6.8e and f. Along the highway, the spatial sampling of the points is governed by the location of bridges and traffic signs to which the scatterers correspond. The part of the railway segment which shows a dense coverage is within an urban area. The mean velocity variations are small with a range of 1 mm/year and fluctuate around zero. The gaps in the profile have a length of 509 m and 566 m at the railway and the highway, respectively. While the given examples show the upper bound of the scatterer distribution, most highway and railway segments suffer from lower sampling of the displacement signal to be able to monitor regional displacements. In general, the study area lacks extensive point coverage due to the presence of agricultural fields and grasslands, which tend to quickly decorrelate over time. The vegetation surrounding both infrastructure types casts shadows on the infrastructure and reduces its visibility.

In conclusion, regional displacements could be observed in both study areas. Regional displacements are clearly visible in several cases in Villena due to the regular coverage of coherent pixels. However, a regular spatial distribution and scatterer density is the exception in Neumünster, such that regional displacements cannot be reliably retrieved for large parts of this study area. The agricultural fields and grassland in the surrounding of the transport infrastructure in Neumünster limit the observation of regional displacements to the pixels on the object, while in Villena, scatterers are available in the vicinity of the transport infrastructure and can aid the assessment and interpretation of regional displacements.

Local displacements

Three areas with railway and highway segments are selected for both study areas and are shown with the velocity profiles at the segments in Figure 6.9 and 6.10. The capability of the proposed InSAR time series method to retrieve local displacement signals from Sentinel-1 images at transport infrastructure is analysed based on several segments, which are approximately 2 km long.

Local displacements are visible in several areas in Villena as depicted in Figure 6.9. All transport infrastructure segments have a dense scatterer coverage. Only the segment in Figure 6.9b shows a gap between neighbouring points with a length of 233 m, while the other segments have a dense scatterer coverage and smaller gaps with a length of up to 81 m. The mean velocity of the highway segment (H'-H") and the railway 2 segment (R2'-R2") in Figure 6.9a show no displacement signal, whereas railway 1 (R1'-R1") shows a localised displacement around section distance 0.7 km. The displacement shows a maximum velocity of up to 10 mm/year away from the satellite and affects a 300 m long section of the track. The displacement signal is local as it can neither be seen in the velocity profiles of the railway 2 nor of the highway which are merely about 200 m apart. Another clear displacement signal is depicted in Figure 6.9b for a highway segment with up to 20 mm/year away from the satellite and a high spatial gradient around section distance 0.6 km. Neighbouring pixels at the displacement gradient have a velocity difference of 10 mm/year to 15 mm/year. Starting from section distance 0.8 km, the profile has a 233 m wide gap for which the hazard cannot be assessed. Also here, the displacement signal is local and is not visible in the surrounding of the transport infrastructure. The most complex displacement pattern is depicted in Figure 6.9c for a highway segment. Three parts can be differentiated in the velocity profile. A 200 m long part with

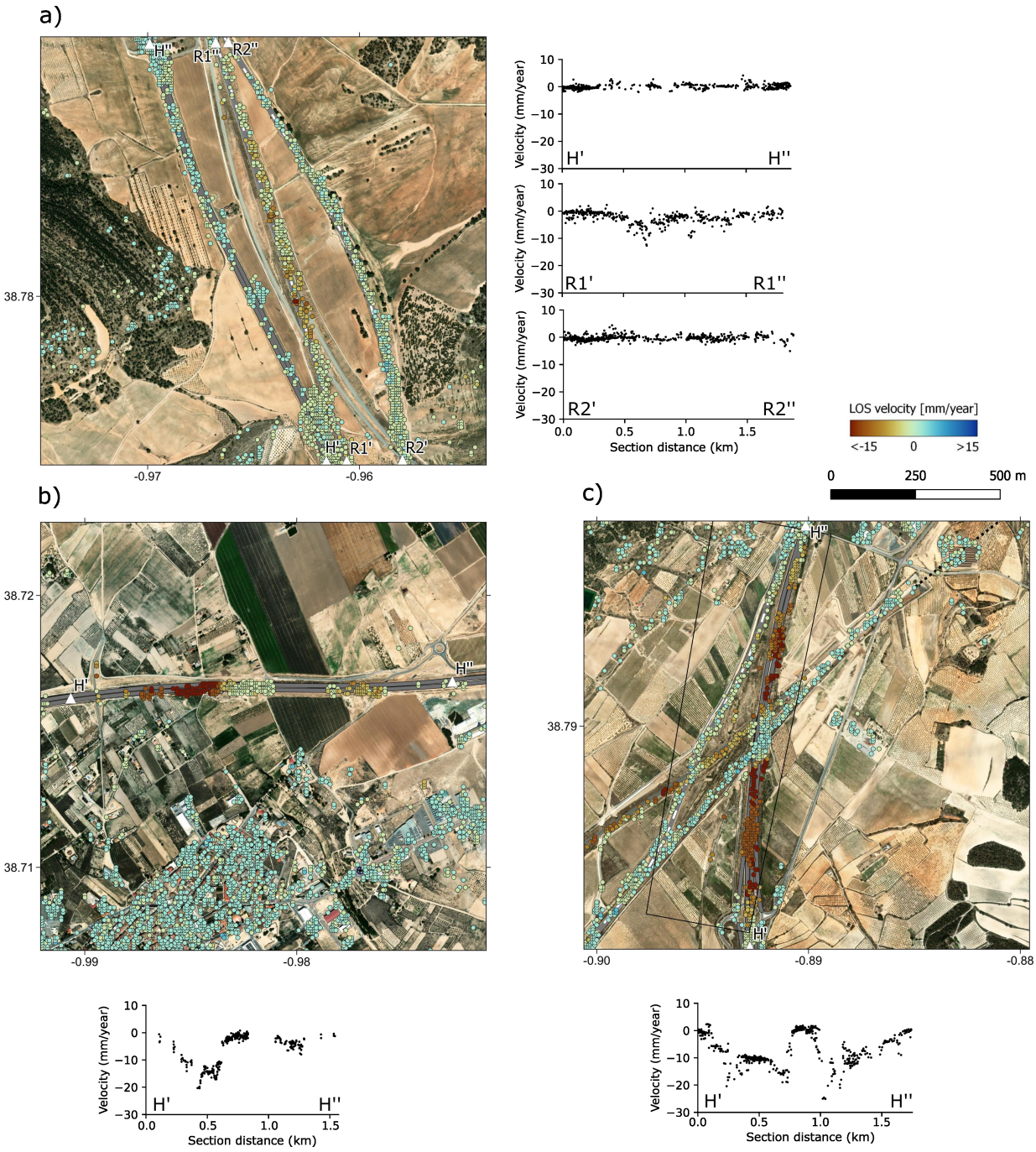


Figure 6.9: Velocity maps showing the LOS displacement for the zoom-ins in Villena (Figure 6.7a) for two railway and three highway segments. The legend is the same as in Figure 6.7. For each segment, the mean velocity profile is shown along the transport infrastructure. Start and end points of the profiles are depicted by the white triangles. The extent of the study area Figuera used in other experiments is depicted in c) by the black rectangle. Background image: ©ESRI.

no displacement corresponding to the bridge over the railway tracks and two parts, one north and one south of the bridge corresponding to the highway embankments leading towards the bridge. The highway embankments show a gradually increasing velocity the closer the scatterers are to the bridge. The displacement gradient approaches the bridge from both sides. The velocity is zero at both ends of the segment while it is the highest with 25 mm/year away from the satellite directly next to the bridge. The bridge itself does not show a displacement velocity different from 0 mm/year. Both embankments of the highway are moving away from the sensor, while the bridge appears stable. The displacement could be due to the post-construction settlement of the highway embankment. Perhaps the foundation of the bridge prevents settlement.

In the study area Neumünster, a significantly lower scatterer density and larger distances between the scatterers are common compared to Villena. For instance, a representative scatterer density is shown north of the white triangle H' in the northern part of the velocity map in Figure 6.7d. There are transport infrastructure with long gaps between neighbouring scatterers, e.g., a 3 km gap at the highway and several gaps of up to 7.5 km at a railway track resulting from individual trees along the railway track. It is obvious, that a local displacement signal cannot be monitored with such a sparse coverage. However, the upper limit of the opportunities for transport infrastructure monitoring in a vegetated study area, such as Neumünster, is demonstrated by the three selected areas shown in Figure 6.10 with comparably high scatterer density and coverage. The density and coverage are similar at the railway segment in Figure 6.10a and the highway segments in Figure 6.10c. At the railway segment, the mean velocities vary in a range of 3 mm/year along the profile, while the highway segment appears stable. Larger gaps of 234 m in the profile limit the observability to spatially low frequent displacements and hinders the assessment of higher spatial frequencies. The highway segment in Figure 6.10b shows a homogeneous point distribution comparable to the spatial distributions in Villena as no gaps are visible. The velocity profile shows that the highway segment is mostly stable, but also covers a localised displacement of up to 8 mm/year away from the sensor over a length of 130 m starting around section distance 1.4 km. At the same section distance, there are other pixels with no displacement indicating that only one highway lane could be affected.

The analysis shows that local displacement signals are observable at transport infrastructure with Sentinel-1 images in both study areas. However, for most of the transport infrastructure in Neumünster the point density is not sufficient. In contrast, the high coherence of the scatterers in Villena allowed to observe local displacements at several locations.

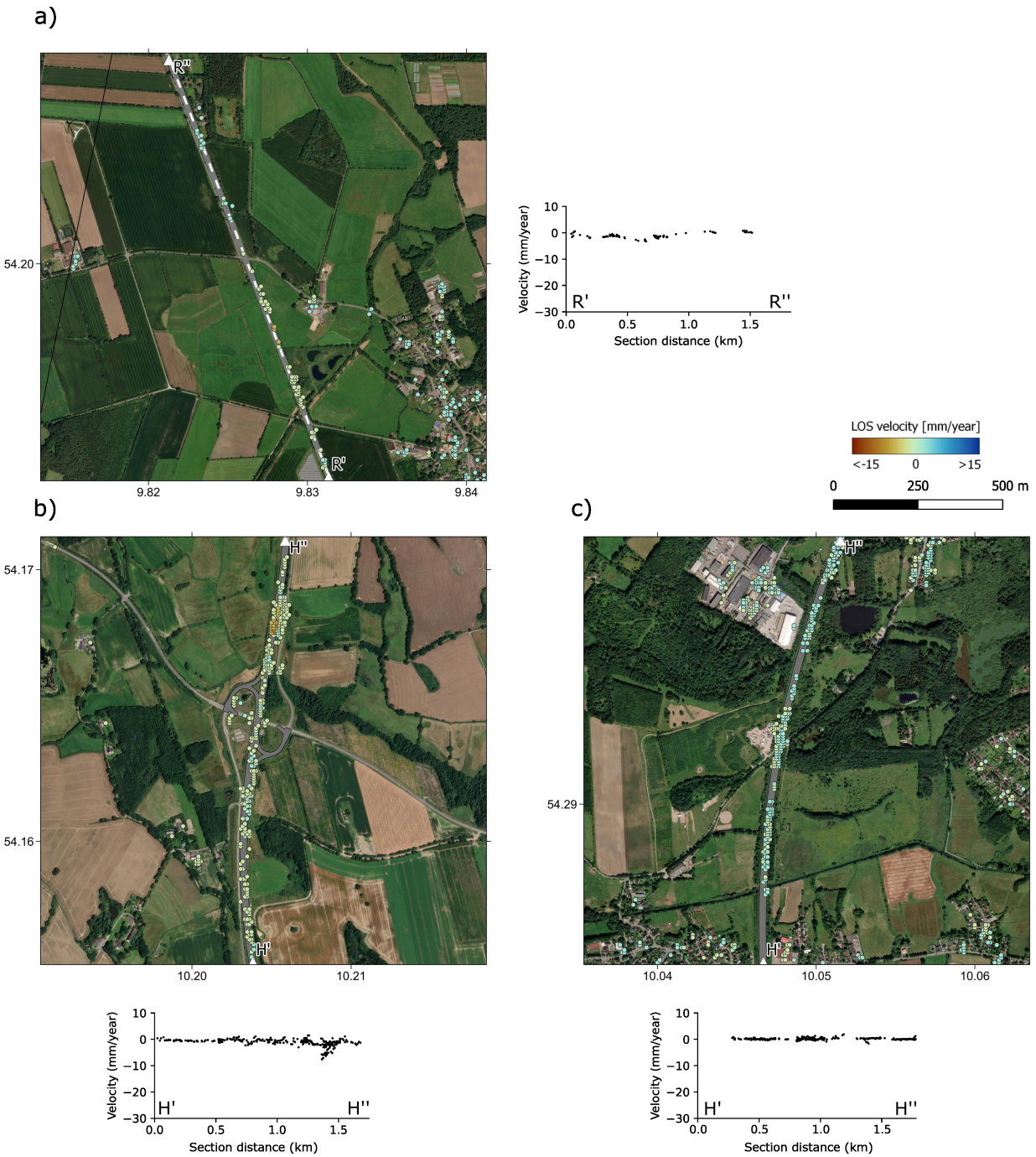


Figure 6.10: Velocity maps showing the LOS displacement for the zoom-ins in Neumünster (Figure 6.7b) for one railway and two highway segments. The legend is the same as in Figure 6.7. For each segment, the mean velocity profile is shown along the transport infrastructure. Start and end points of the profiles are depicted by the white triangles. Background image: ©ESRI.

6.3 Experiment 3: Coherent Lifetime Estimation at Transport Infrastructure

In this experiment, the change detection methods are applied in two study areas, Sande and Figuera. The different characteristics of the change detection methods are analysed and compared. First, the change maps resulting from change detection are analysed for all three change detection methods. Second, the coherent lifetime is derived based on the results from each change detection method and its plausibility is assessed in comparison to the reference data from optical images.

Change Maps

The characteristics of the change detection methods are analysed based on the resulting change maps. The change maps shown in Figure 6.11 represent for each pixel the index of the image after which the change happened. The change maps appear noisy and are difficult to interpret without additional information about the significance of the computed change date. The corresponding score maps indicate the certainty for the change (Figure 6.11e-g). Changes are computed also for noisy pixels, but their change is irrelevant for deriving displacement time series. Therefore, TCS pixels are selected after assessing both, the significance of the change and the coherence of the scatterers' phase.

The change maps illustrate a spatially homogeneous change index along some of the transport infrastructure whose location can be seen in the amplitude image in Figure 6.11a. Neighbouring pixels showing the same change index are assumed to belong to the same object. The change detection methods provide different change dates along the transport infrastructure. The change dates from CD-Phase and CD-CohMat agree better with each other, compared to the change dates derived from CD-Amplitude. Interestingly, although both the CD-Phase and CD-CohMat include the spatial neighbourhood of the pixel in their computation, CD-Phase preserves the spatial information, whereas CD-CohMat does not, leading to a spatially low-pass filtered effect in Figure 6.11c. Strong scatterers in the neighbourhood of the central pixel dominate the signal in the coherence matrix and prevent finding the change date belonging to the central pixel. Even though the phase noise estimation is also affected by strong scatterers in the neighbourhood, the spatial information is preserved if the displacement signal is spatially correlated. The change map resulting from CD-Amplitude also preserves the spatial information because the spatial neighbourhood is not considered during the change detection. The analysis of the change maps highlights the spatial characteristics of the three methods, however, a more detailed comparison of the change maps on a pixel level is non-informative because the certainty of the change estimation and the coherence of the scatterer should be considered.

The score maps (Figure 6.11e and f) of CD-Phase and CD-CohMat show spatial patterns similar to their respective change maps. The pixels with lower scores predominantly correspond to the transport infrastructure. The score map of CD-CohMat does not preserve the spatial information either, but instead the score map shows rectangular shapes. The score maps from both, CD-Phase and CD-CohMat, show low score values in the same areas of the map corresponding to significant changes. This means that both methods respond to the same characteristics of the

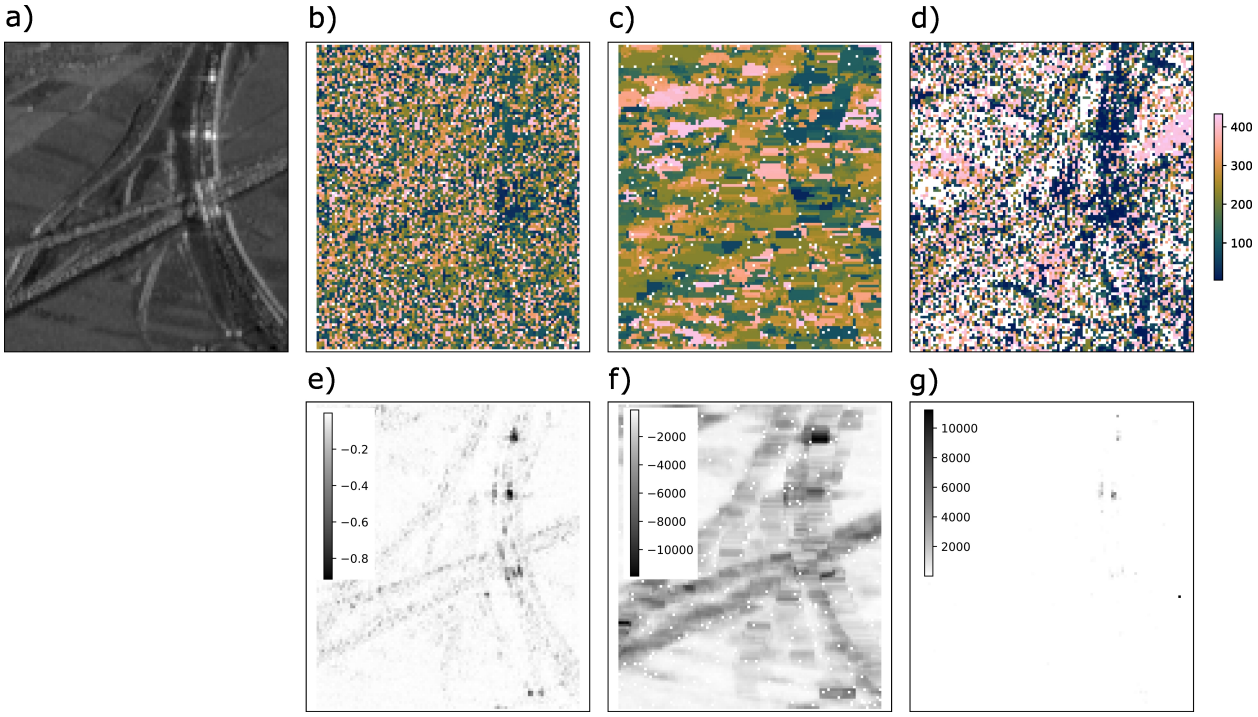


Figure 6.11: Change detection results for the study area Figuera with a) mean amplitude image, b)-d) change maps indicating the image acquisition for each pixel after which the change has occurred, and e)-g) change scores for each pixel belonging to the change dates in the change maps. The corresponding change maps and score maps from the change detection methods are presented column-wise with CD-Phase (b, e), CD-CohMat (c, f), and CD-Amplitude (d, g). The change cannot be estimated for pixels at the border of the maps from CD-Phase and CD-CohMat due to the estimation window and are depicted in white. Changes which are classified as insignificant based on the F-test in CD-Amplitude are also depicted in white.

signal. Only the very high peaks are visible on the score map of CD-Amplitude, which correspond to the brightest pixels in the mean amplitude image. However, the majority of the pixels in the study area were found to be significant with CD-Amplitude, as revealed by all non-white pixels in the change map (Figure 6.11d). Probably the reason for the high number of significant changes found with CD-Amplitude is the underlying assumption that the amplitude time series could be described by a Rayleigh distribution for all types of scatterers. The CD-Amplitude method is sensitive to outliers in the amplitude time series, which could e.g. stem from vehicles. Construction vehicles are reflecting the signal stronger than the transport infrastructure. As a consequence, many false positive detections are included by the amplitude change detection method despite the particularly low significance level chosen for the experiment.

The computational time of the three change detection methods differs by several magnitudes and is evaluated for a relatively small image extent consisting of 120×110 pixels^2. The change detection methods are parallelised and optimised for computational efficiency. The computational time is the shortest for CD-Amplitude (three seconds). In comparison, CD-Phase takes 100 times longer (five minutes) compared to CD-Amplitude. CD-CohMat has the longest computation time (four hours) which is 4800 times longer than CD-Amplitude and 48 times longer than CD-Phase. The high computational demand of CD-CohMat arises from the inversion of the coherence matrix. The

size of the coherence matrix is determined by the number of images in the stack, hence, resulting in longer computational with increasing stack size. The long computational time of CD-CohMat is unfavourable for large images and increasingly large image stacks as provided by the Sentinel-1 mission.

Plausibility of the Coherent Lifetime

The quality of the change detection is validated for pixels which exhibit a coherent signal, i.e. the plausibility of the coherent lifetime of these pixels is assessed with respect to the reference period derived from the optical images. For this purpose, the pixels selected from each method are shown in coherent lifetime plots for both study areas, Sande and Figuera. The coherent lifetime plots depict the change date and the coherence before and after the change (Figure 6.12 and 6.14). The plausibility metrics are computed to analyse the performance of the change detection methods (Figure 6.13 and 6.15).

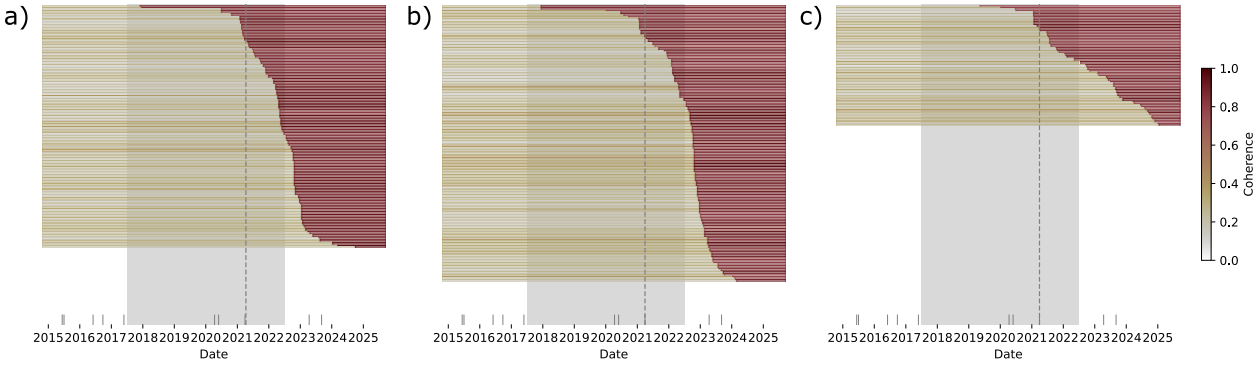


Figure 6.12: Coherent lifetime of TCS pixels at the railway track in Sande derived from a) CD-Phase, b) CD-CohMat, and c) CD-Amplitude. Each line represents one scatterer at the railway track. Only TCS pixels that were selected during the coherent lifetime estimation are depicted. The lines are coloured by the coherence of the scattering within the time span before and after the estimated change and are sorted by the change date in ascending order. The grey areas show the period in which the construction has happened according to optical satellite images (from Google Earth and LGLN, compare Figure 5.3). The short vertical gray lines along the x-axis indicate the dates of available optical images. The vertical dashed lines highlight the last optical image in which the construction was still visible.

The coherent lifetime of pixels at the new railway track in the study area Sande are shown in Figure 6.12 for the three change detection methods. A higher number of pixels indicates that the change dates correspond to the coherent period of the signal, while wrong change dates would decrease the coherence of the temporal subsets leading to less coherent pixels. Most TCS pixels are detected by CD-CohMat, followed by CD-Phase with slightly less pixels and only half of the pixels detected by CD-Amplitude. The coherence is low for all pixels before the change and high after the change independent of the method. This shows that the change from an incoherent landcover, here vegetation, to construction site and finally to the coherent railway track unambiguously yields appearing scatterers. This is also shown by the number of congruent pixels in Figure 6.13c. All TCS pixels detected by each of the three change detection methods are congruent. The MACD shown in Figure 6.13e reveals that each change detection method yields on average the same coherence

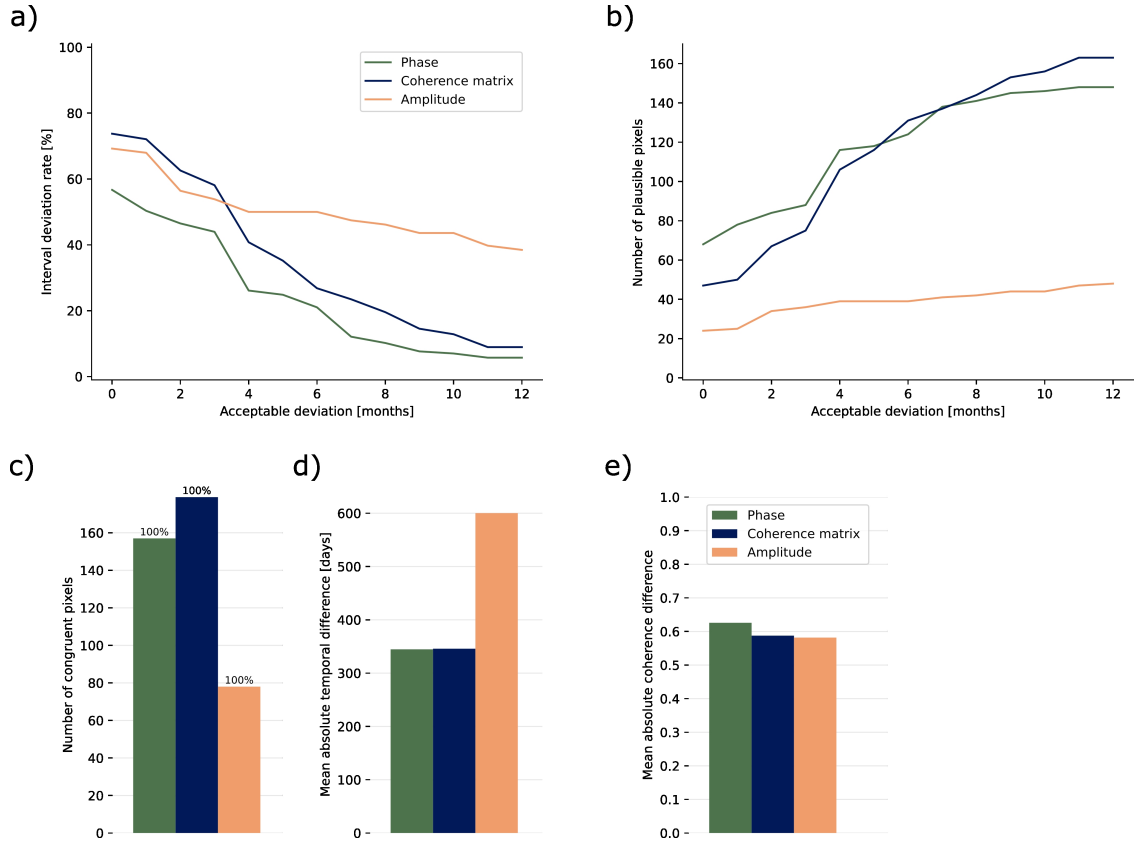


Figure 6.13: Comparison of the plausibility metrics for the three change detection methods at the railway track in the study area Sande. a) Interval deviation rate, b) number of plausible pixels, c) number of congruent pixels as well as the percentage of the congruent pixels among all pixels, d) similarity of the change dates in terms of MATD, and e) mean absolute coherence difference.

increase at the TCS pixels of around 0.6. The methods differ, however, in the IDR (Figure 6.13a). The CD-Phase method agrees best with the reference period as less than 60 % of the pixels are outside the reference period. The IDR decreases to about 10 % for an acceptable deviation of 12 months. While the IDR of CD-CohMat decreases in a similar way as for CD-Phase, the change dates of CD-Amplitude do not fit to the reference period. The IDR of CD-Amplitude decreases from around 70 % to roughly 50 % meaning that half of the pixels have a change date that differs more than a year from the reference period. The same behaviour is also reflected by the number of plausible pixels shown in Figure 6.13b. However, in absolute numbers, CD-Phase yields the most plausible pixels within the reference period, while CD-CohMat provides the most plausible pixels for an acceptable deviation of 12 month. Comparing the number of pixels of CD-CohMat and CD-Amplitude, the latter yields only a fourth of the plausible pixels for an acceptable deviation of 12 month. The results from CD-Phase and CD-CohMat are more plausible than the results from CD-Amplitude. This is also reflected by the similarity of the change dates expressed by the MATD shown in Figure 6.13d. The MATD is the same for CD-Phase and CD-CohMat with around 350 days, but almost double with 600 days for the CD-Amplitude.

Five transport infrastructure are analysed in the study area Figuera. In Figure 6.14, the coherent lifetime of the pixels resulting from CD-Phase are exemplarily shown (The same plots derived from CD-CohMat and CD-Amplitude are presented in the Appendix in Figure A.1 and A.2, respectively).

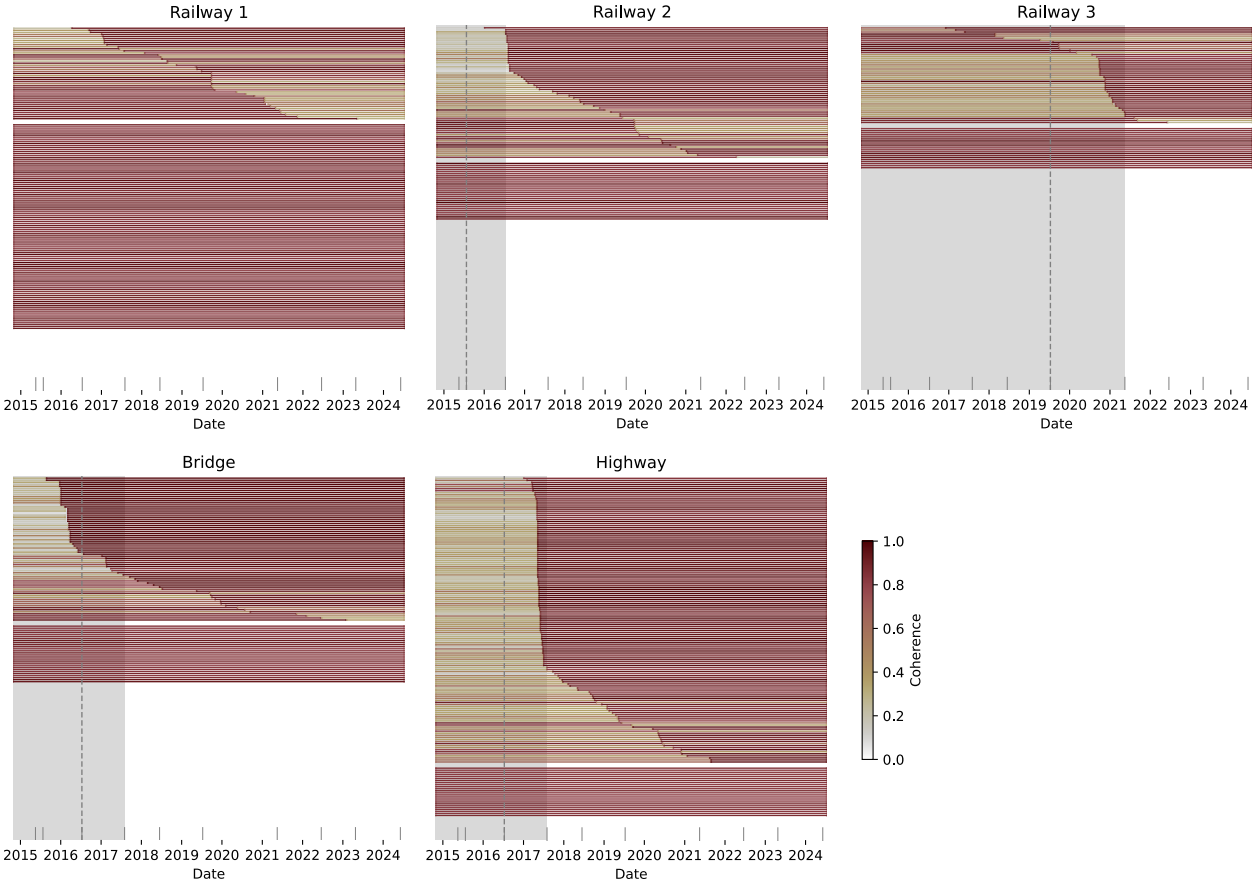


Figure 6.14: Coherent lifetime of TCS pixels at five transport infrastructure in Figuera derived from CD-Phase. Each line represents one scatterer within the mask of a transport infrastructure. Only TCS pixels that were selected during the coherent lifetime estimation are depicted. The lines are coloured by the coherence of the scattering within the time span before and after the estimated change and sorted by the change date in ascending order. The grey areas show the period in which the construction has happened according to optical satellite images (from Google Earth and National Air Orthophotography Plan (PNOA)). The short vertical gray lines along the x-axis indicate the dates of available optical images. The vertical dashed lines highlight the last optical image in which the construction was still visible.

Four out of five transport infrastructure are constructed during the study period and, consequently, appearing TCS pixels are expected. Nevertheless, in the coherent lifetime results derived from CD-Phase, also disappearing pixels are present. At railway 3 for instance, the coherent lifetime of the disappearing pixels covers the construction period. The disappearing TCS pixels could be coherent objects that are related to the landcover present before or during the construction of the railway track. Railway 2 is also covered by disappearing pixels whose change dates are, however, after the reference period.

Railway 1 has not undergone any change during the study period according to the optical images. Hence, only CCS pixels are expected within the infrastructure mask. In the results from CD-Phase, two thirds of all pixels at railway 1 are CCS pixels (Figure 6.14). However, one third of the coherent pixels are TCS pixels. Their change dates vary over a time span of around 7 years, suggesting that the changes are not associated with a particular event. The transport infrastructure that were constructed, also have CCS pixels within the mask. These pixels do not exhibit a significant

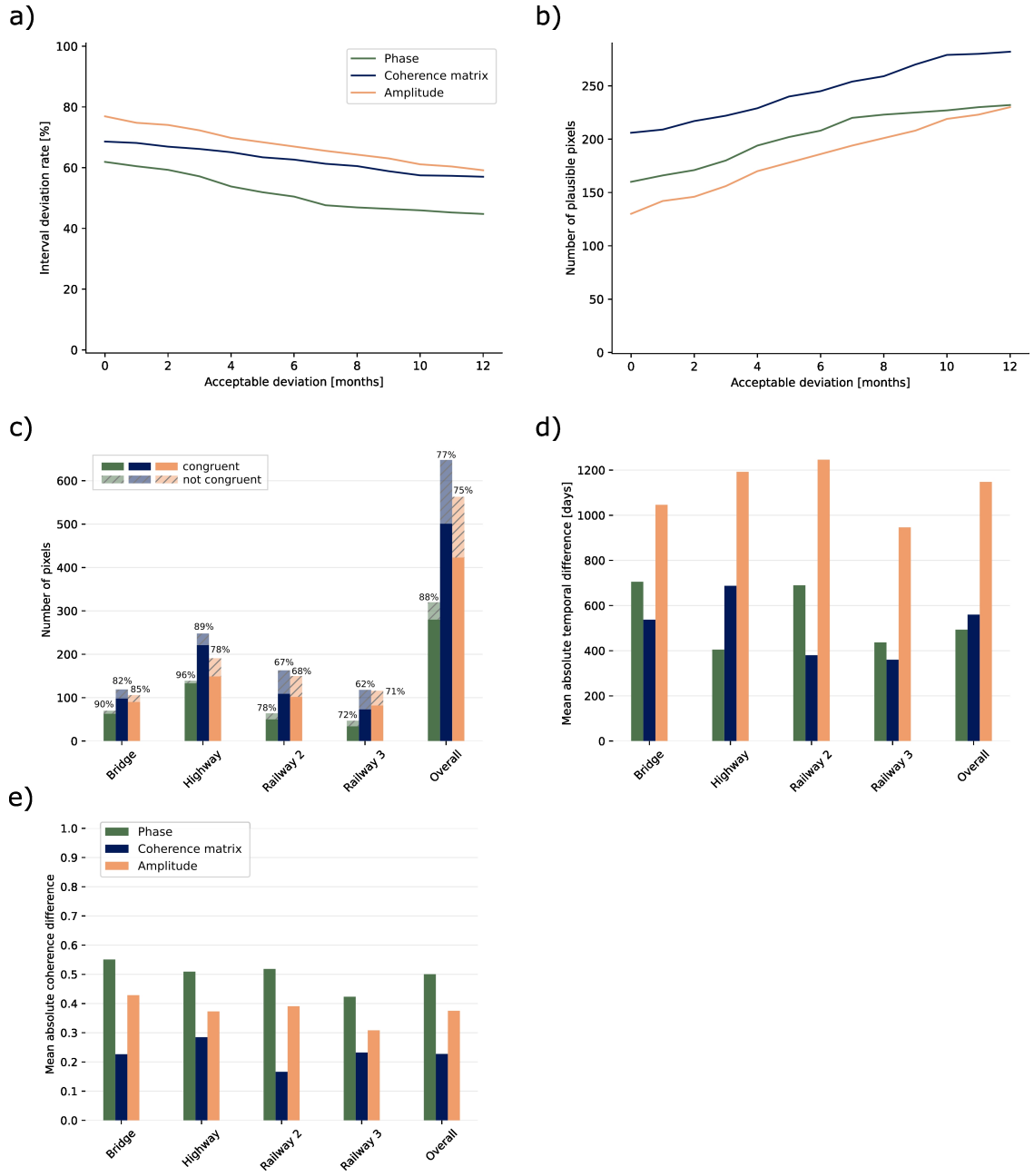


Figure 6.15: Comparison of the plausibility metrics for the three change detection methods at the transport infrastructure types in the study area Figuera. Results are not shown for Railway 1 as no change is expected for this infrastructure. a) Interval deviation rate, b) number of plausible pixels, c) number of congruent pixels as well as the percentage of the congruent pixels among all pixels, d) similarity of the change dates in terms of MATD, and e) mean absolute coherence difference.

change, but have a coherent signal during the study period. The CCS pixels might not belong to the transport infrastructure itself.
The example of the highway clearly shows a good match between the change dates with the reference for two-thirds of the TCS pixels for the results of CD-Phase. In contrast, the changes at the bridge pixels are not at the end of the reference period for half of the TCS pixels. Instead, their change dates are before the last optical image that still shows the construction site (07-2016, dashed line in Figure 6.14). This observation contradicts the assumption that scatterers appear at the end of the construction time. A visual analysis of the optical images indicates that the bridge structure including the deck was already constructed before 07-2016, while the asphalt layer was added afterwards which is visible in the optical image from 07-2016. It suggests that the TCS pixels with the early change dates could correspond to parts of the bridge structure which are not affected by the added asphalt layer.
Across all transport infrastructure in this study area, five pixels were found in the results of CD-Phase whose signal is coherent both, before and after the change. However, it is not clear from the coherent lifetime whether these scatterers are CCS pixels without a change or TCS pixels with two coherent periods.

For Figuera, the plausibility metrics of the three change detection methods are shown in Figure 6.15. Most TCS pixels were found from CD-CohMat with more than 600 pixels, followed by CD-Amplitude with around 550 pixels and the least with more than 300 pixels from CD-Phase (Figure 6.15c). While for the study area Sande, which shows a change from vegetation to railway track, a higher number of TCS pixels was argued to be an indicator for correct change dates, the opposite might hold true for Figuera. In Figuera, the changes occur in an area whose landcover is coherent already before the change. The surface changes from bare soil, or at least hardly vegetated area, to transport infrastructure. A pixel might be coherent even though its change date was wrongly estimated. This seems to be the case for the CD-Amplitude results which provides many TCS pixels, but more than 60 % of the pixels deviate from the reference even for an acceptable error of 12 month. The high MATD for the CD-Amplitude of around 1150 days (i.e. 3 years) shows that the change dates have a high variability. Despite providing the lowest number of TCS pixels, CD-Phase yields the highest overall percentage of congruent pixels (88 %, i.e. 11-13 percentage points more than CD-CohMat and CD-Amplitude) and has the lowest IDR (Figure 6.15a). The lowest number of TCS pixels are provided by CD-Phase for the railway 2 and railway 3. Importantly, pixels which are identified as CCS pixels are not counted here. CCS pixels were mainly found using CD-Phase and rarely by the other two methods which is partly the reason for the low number of pixels. The percentage of TCS pixels which have a change date within the reference period, i.e. IDR for zero month deviation, is between 60 % and 80 % for Figuera (Figure 6.15a) which is similar to the level in Sande with 58 % to 76 % (Figure 6.13a) for all change detection methods. The rate at which the IDR decreases with increasing acceptable deviation is, however, different. In Figuera, the IDR decreases only by about 10 to 15 percentage points for all three methods within one year deviation, while in Sande, it decreases between 30 to 60 percentage points depending on the method and decreases even down to an IDR of around 10 % for CD-Phase and CD-CohMat. This difference between the study areas suggests that the change from vegetation to infrastructure is more accurately assessed particularly by CD-Phase and CD-CohMat. The performance difference between CD-Phase and

CD-Amplitude becomes more clear from absolute numbers in terms of the number of plausible pixels (Figure 6.15b) which is higher for CD-Phase although almost twice the number of TCS pixels were detected with CD-Amplitude.
The change dates are similar to each other for CD-Phase and CD-CohMat (Figure 6.15d). While the MATD differs among the infrastructure, the overall MATD of CD-Phase and CD-CohMat is similar with around 500 and 550 days, respectively. The MATD is twice as high for CD-Amplitude with around 1150 days. These differences between the change detection methods match the observation from Sande.
The highest MACD is observed for CD-Phase with 0.5, while it is around 0.4 for CD-Amplitude and less than 0.25 for CD-CohMat. It means that CD-CohMat splits the time series into two subsets which differ on average less than 0.25 in coherence. It suggests that the coherent part is most clearly distinguished from the incoherent part by CD-Phase. Interestingly, for Sande, the MACD was similar for all three methods. This indicates that the coherence gain depends on the coherence level of the landcover before the change. For Figuera, it is anticipated that CD-Phase provides the highest MACD as the method is tailored to find the change date that maximises the TPC in one of the temporal subsets, while for instance, CD-CohMat find the change date which is related to the largest decorrelation between two temporal subsets.

This experiment has shown that coherent change detection is more effective for estimating the coherent lifetime than incoherent change detection, which was primarily used in previous studies, as discussed in the literature review in Section 3.2.5. The two coherent change detection methods, CD-CohMat and CD-Phase provided similar change detection results. However, CD-Phase has two advantageous compared to CD-CohMat: it preserves spatial details and it comes with significantly lower computational demand. The plausibility analysis revealed different performance of the change detection methods depending on the type of landcover before the change. The change from vegetation to railway track in the study area Sande was unambiguously detected by both coherent change detection methods, while in Figuera, the high overall coherence level of the scatterers caused difficulties for the proposed coherent lifetime estimation. Even though only appearing TCS pixels were expected due to the constructed infrastructure, also disappearing scatterers were detected. The least number of TCS pixels was derived from the CD-Phase results, but instead, several CCS pixels were detected at the changing infrastructure. Also several false positive detections were identified at railway 1 for which no changes during the study period are known. Determining the significance of the detected change is essential for the correct treatment of TCS pixels and for the interpretation of their displacement time series. Possibly, the detected change dates might not have been significant, but were incorrectly classified as significant based on the threshold on the test score. To improve the detection of significant changes, the characteristics of the whole score series could be leveraged to base the decision on multiple features, e.g. the magnitude of local minima, or the gradients of the score series in the vicinity of the global minimum (Mehltretter and Heipke, 2019). Moreover, the proposed coherent lifetime method needs to be adapted for TCS pixels with several independent coherent lifetimes.

6.4 Experiment 4: Displacement Analysis of Temporarily Coherent Pixels

In this experiment, displacement time series are derived jointly from CCS and TCS pixels using exemplarily the change detection results from CD-Phase. The applicability of the proposed InSAR time series method is demonstrated for Sande and Figuera. Moreover, the observability of displacements at newly constructed transport infrastructure is investigated. The LOS displacement maps for Sande and Figuera are depicted in Figure 6.16 and 6.17, respectively.

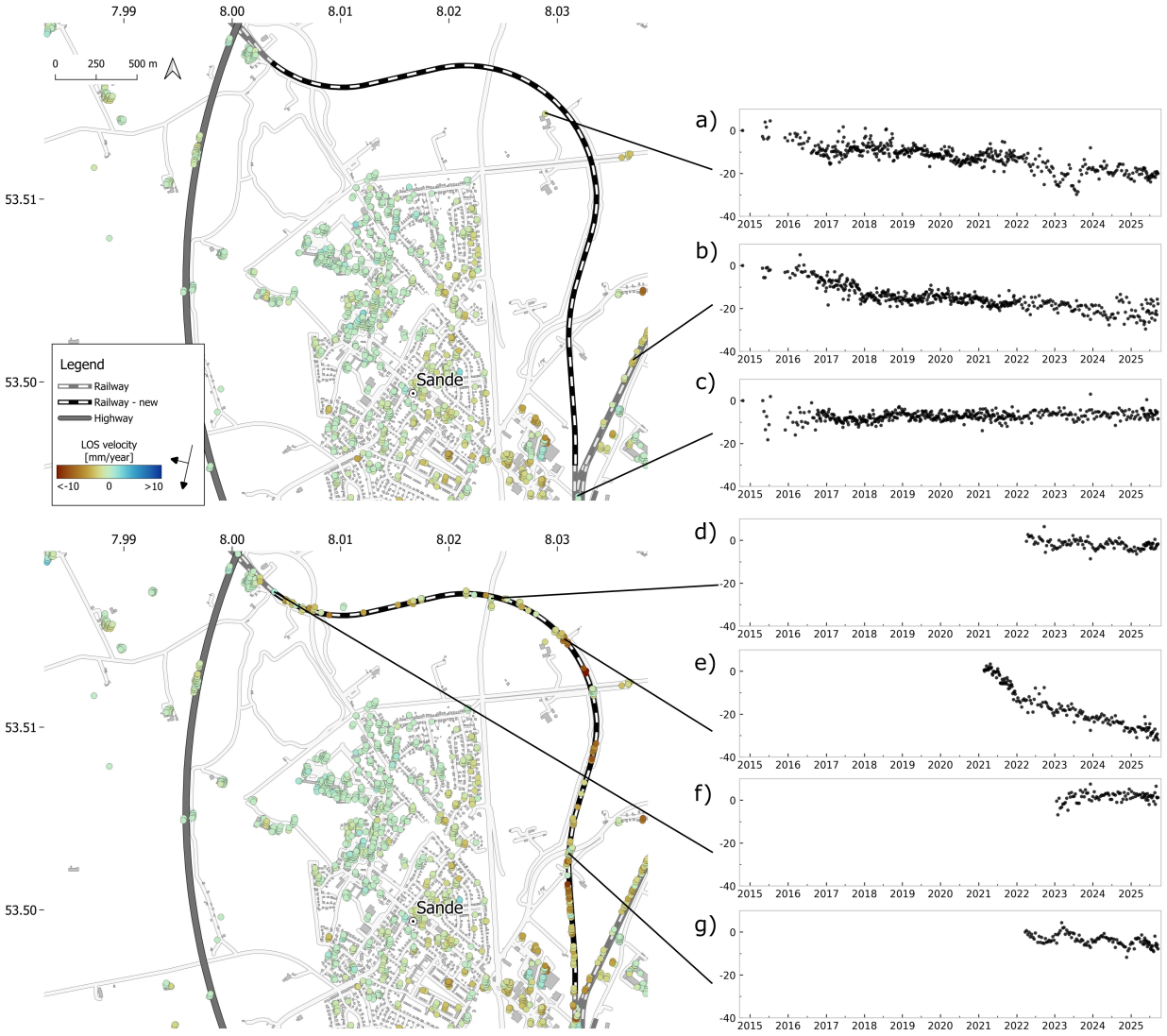


Figure 6.16: Velocity maps of Sande showing LOS displacement derived from CCS pixels only (top), and jointly from CCS and TCS pixels (bottom). Displacement time series (in mm) are shown for selected scatterers on the transport infrastructure (b-g) and on a building close to the new railway track (a). The geolocation of the scatterers were corrected based on the estimated DEM error. Background map is created from OSM data (OpenStreetMap contributors, 2025).

The displacement map of Sande estimated from CCS pixels (Figure 6.16, top map) shows that the new railway track cannot be observed from the whole time span, as none of the CCS pixels are located on the new railway track. The displacement time series (Figure 6.16a-c) show examples of CCS

pixels in this area for a farm close to the new railway track and for two railway pixels at the existing railway tracks. Considering TCS pixels in the InSAR time series analysis (Figure 6.16, bottom map) allows to derive the displacement time series also for the new railway from 156 additional TCS pixels. Several railway pixels show a displacement away from the sensor of up to 10 mm/year, for instance shown by the displacement time series in Figure 6.16e. The displacement time series of two pixels located at bridges along the railway track (Figure 6.16d and g) exhibit a seasonal displacement signal. The joint analysis of CCS and TCS pixels yields reasonable time series results and improves the observability of the railway track in Sande.

The displacement map of Figuera derived from merely CCS pixels (Figure 6.17, top map) contains 294 CCS pixels. The highway bridge is stable but shows a seasonal displacement pattern (Figure 6.17d) associated with thermal expansion. At the northern highway embankment, high displacement rates with a decaying time series are present (Figure 6.17a-c), which could correspond to post-construction settlement. Railway 1, located in the south, is covered by several CCS pixels, which is reasonable as it has neither been constructed nor been demolished during the study period. Some parts of the infrastructure are hardly observable with CCS pixels only, such as the southern part of the highway embankment or the railway 3 which is oriented in north-south direction. The depicted time series (Figure 6.17a-f) show a slightly higher noise level in the beginning of the time span.

The displacement map derived from both CCS and TCS pixels (Figure 6.17, bottom map) shows an increase in measurement points by 193 % with 413 TCS pixels out of 567 selected pixels in total. It means that several pixels which were originally classified as CCS pixels are here selected as TCS pixels, thus, being inconsistent with the displacement results from CCS pixels only. Consequently, pixels with only a partially coherent signal might be selected as CCS pixels if the InSAR time series analysis method disregards TCS pixels. This problem is more likely to arise if the incoherent part is short. The reason is that the TPC, which is used to select coherent pixels, averages the phase noise level from the whole time span and represents it by one coherence value. Thus, the TPC treats a pixel with a slightly higher noise level over the whole time span in the same way as a pixel with a generally low phase noise level but a short incoherent period.

The displacement map of Figuera estimated from only CCS pixels shows an overestimation of the displacement signal along the highway compared to the results from TCS pixels. Moreover, the displacement time series of the TCS pixels are smoother and the time series consistently start around mid of 2017 for pixels at the highway. For instance, the time series of the TCS pixels on the northern part of the highway (Figure 6.17g-i) are shortened by about three years in the beginning of the time span which aligns with the noisy observations in the time series of the corresponding CCS pixels (Figure 6.17a-c). Similarly, the time series of the TCS pixel at the bridge is shortened by about two years (Figure 6.17d and j).

For other parts of the highway, the displacement time series are shown for several TCS pixels jointly (e.g. Figure 6.17k and l) to show the spatial context of the displacement signal. Neighbouring TCS pixels show the same displacement pattern as they presumably belong to the same object. For

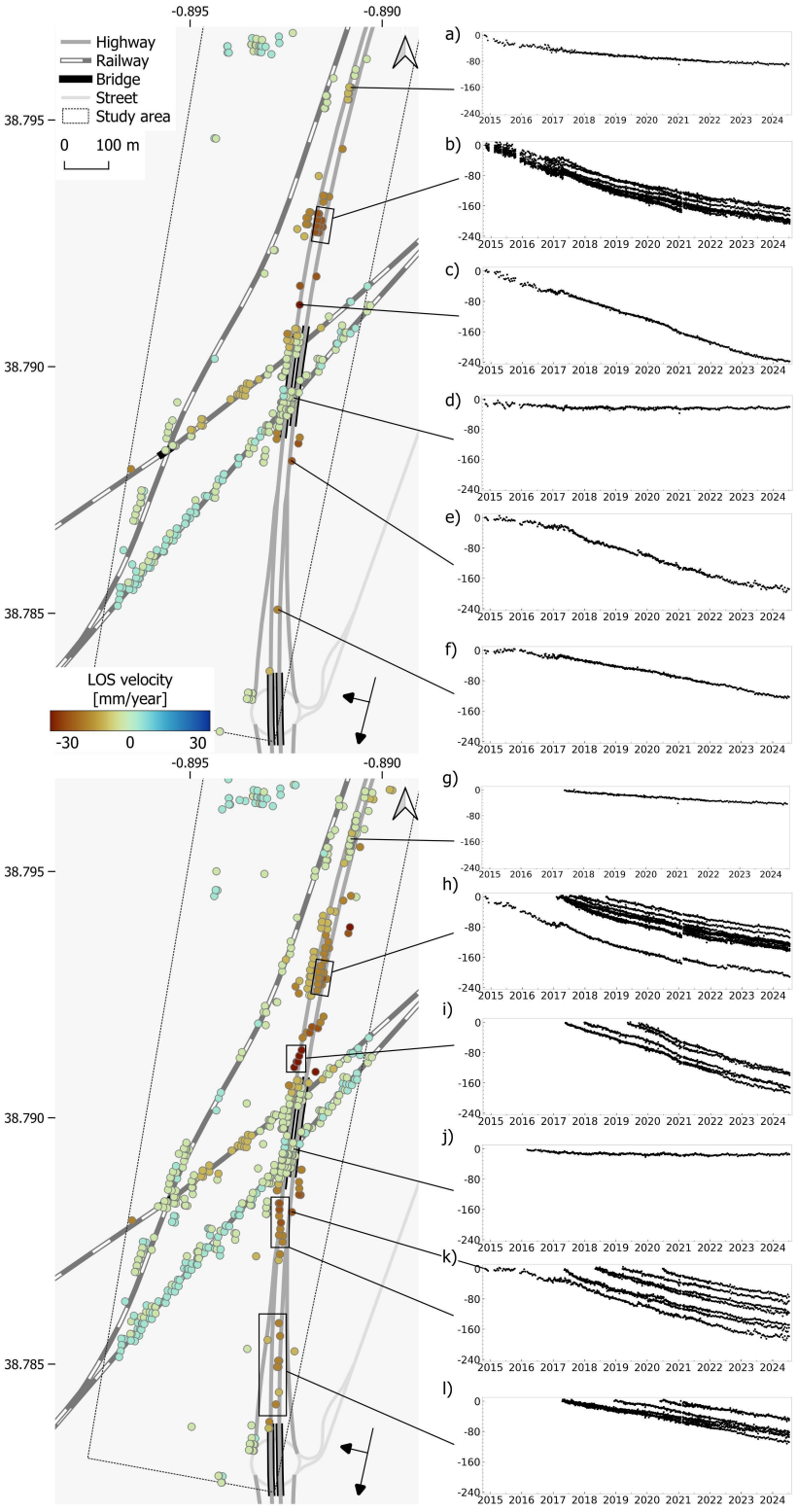


Figure 6.17: Velocity maps of Figuera showing LOS displacement derived from CCS pixels only (top), and jointly from CCS and TCS pixels (bottom). The displacement time series are derived using the InSAR time series for joint phase unwrapping of CCS and TCS pixels. Displacement time series (in mm) are shown for selected scatterers on the transport infrastructure (a-l). The geolocation of the scatterers are corrected based on the estimated DEM error. Background map is created from OSM data (OpenStreetMap contributors, 2025).

each scatterer, the first date within the coherent lifetime is used as a temporal reference leading to an offset between the time series of neighbouring pixels which here is merely a question of visualisation.

Beside railway tracks and highways for which the time series methodology is tailored to, also the displacement time series of bridges is retrieved in the two study areas. The displacement maps in Experiment 1 and 2 also covered bridges. However, the proposed time series analysis method for railway tracks and highways is not tailored to bridges in general. Particularly long-span bridges, e.g. over water, can pose different challenges and could require a phase unwrapping strategy relying on a temporal displacement model considering the thermal expansion of the bridge material as discussed in the literature review in Section 3.1. Nevertheless, for the small bridges in the study areas, the InSAR time series method also shows reasonable displacement time series reflecting the expected thermal expansion of the bridges. In the next experiment, the applicability of the proposed methodology is tested also for urban infrastructure which can pose similar challenges as bridges.

This experiment, demonstrated the performance of the proposed time series method for CCS and TCS. Including TCS pixels in the InSAR time series analysis did not only increase the measurement point density and led to a better spatial coverage of the infrastructure, but also improved the quality of the displacement results particularly for the study area Figuera. The incoherent parts of the time series of the highway pixels which is associated with the construction period, are removed. Thus, an overestimation of the velocity is avoided and error propagation to neighbouring pixels during spatial phase unwrapping is reduced.

6.5 Experiment 5: Transferability to Urban Infrastructure

The development of TCS analysis methods originated from urban infrastructure monitoring due to frequent changes in the built environment (see Section 3.2). In this experiment, the proposed InSAR time series method which is tailored to transport infrastructure, is tested for urban infrastructure in the study area Miami. In particular, the applicability of CD-Phase which relies on a spatial displacement model is evaluated. The coherent lifetime of scatterers at the six buildings under change and the resulting displacement maps are analysed to assess the transferability of the proposed methodology for transport infrastructure to an application for which usually a temporal displacement model is anticipated.

Coherent Lifetime

The coherent lifetime of the pixels at the six buildings of interest are shown with the reference period derived from optical images in Figure 6.18 for the three change detection methods. Due to the low number of pixels covering each of the buildings, the plausibility metrics MACD, MATD and IDR are not assessed as few samples distort their interpretation. Instead, the focus is set on absolute numbers derived from the coherent lifetime plots in Figure 6.18 and listed in Table 6.2.

For most of the buildings, CD-Phase yields the most selected TCS pixels and shows the most plausible TCS pixels with a change date within the reference period. The performance of the CD-CohMat is slightly worse, while the results from CD-Amplitude show the least TCS pixels for

most of the buildings and two buildings are without selected TCS pixels. The results suggest that CD-Amplitude is also unsuitable in the context of urban infrastructure. The TCS pixels detected from CD-Phase and CD-CohMat show similar change dates and comparable coherence values for the temporal subsets. However, for the Surf House Condominiums, TCS pixels are detected merely with CD-Phase. This suggests that CD-CohMat may have either estimated the wrong change date or the test scores were classified as insignificant based on the user defined threshold.

Table 6.2: Number of plausible TCS pixels from the three change detection methods: Number of TCS pixels with change date within reference period out of total selected TCS pixels per building. Best selections are indicated in bold.

	CD-Phase	CD-CohMat	CD-Amplitude
Champlain Tower	3 / 4	**5 / 5**	0 / 0
Temporary building	0 / 6	0 / 5	0 / **7**
Surf House Condo.	**3 / 4**	0 / 0	0 / 0
87 Park Tower	**17 / 21**	16 / 20	3 / 7
Arte building	**11 / 18**	10 / 13	2 / 5
8926 Collins Ave	**10 / 14**	8 / **14**	0 / 4

The coherent lifetime of the detected TCS pixels is aligned with the lifetime of the buildings, i.e. disappearing scatterers are found at buildings that were removed or collapsed (Figure 6.18, top row), while appearing scatterers are found at buildings that were constructed during the study period (Figure 6.18, bottom row). An exception are two disappearing TCS pixels at the Arte building: One from CD-Amplitude and the other from CD-Phase. These two pixels could, however, belong to the neighbouring Surf House Condominiums which better fits the change date.

The detected changes from all three methods yield a coherent and an incoherent period for the pixels. An exception are two scatterers in the results from the coherence matrix change detection (one at Arte, one at 8926 Collins Ave) showing a high coherence both, before and after the change. These two scatterers could be misclassified CCS pixels. Alternatively, the scattering mechanisms before and after the significant change are both coherent.

The estimated change dates agree well with the reference period for the demolition of the buildings as shown in the optical images. The coherent lifetimes of three out of four TCS pixels from CD-Phase and all four TCS pixels from CD-CohMat end at the collapse of the Champlain Tower. For the Surf House Condominiums, only CD-Phase yields TCS of which three out of four coincide with the reference period for the demolition. For the temporary building, all methods yield the same change date. However, the coherent lifetimes of all scatterers end even before the building is visible for the last time in the optical image. This inconsistency is assumed to arise from a wrong date associated to the optical image in Google Earth. An inaccurate date associated to an image in Google Earth is not unlikely, because a clear inconsistency has been found for another image in the same study area. Moreover, the visual inspection of the SAR images and input data to each of the change detection methods (top row panels in Figure 4.5) support the change detection result.



Figure 6.18: Coherent lifetime of TCS pixels at six buildings (Figure 5.4) of which three disappeared (top row) and three were constructed during the study period (bottom row). Each line represents one scatterer within the mask of a building. Only TCS pixels that were selected during the coherent lifetime estimation are depicted for each of the change detection methods. The lines are coloured by the coherence of the scattering within the time span before and after the estimated change and sorted by the change date in ascending order. The grey areas show the period in which the demolition or construction has happened according to optical satellite images (from Google Earth). The date of the collapse of the Champlain Tower is indicated by a vertical dotted line. The short vertical gray lines along the x-axis indicate the dates of available optical images. The vertical dashed lines highlight the last optical image in which the construction was still visible.

The change dates are more diverse at the newly constructed buildings. While the change dates from the CD-Phase and CD-CohMat are either at the end or after the end of the construction period, CD-Amplitude often detects changes at the beginning of the construction period. The amplitude signal already changes at the beginning of the construction period due to brighter backscattering, e.g. from construction vehicles as it is also observed at the transport infrastructure. During the construction period both the amplitude and the phase signal continuously change. A correlated phase signal is first maintained after the construction has finished. The building-level analysis hereby confirms the temporal offset between the change date from amplitude and the start of the coherent lifetime of the TCS pixel that was found and discussed by Dörr et al. (2022).

The CD-Phase is an extension of the phase-based change point refinement proposed for urban infrastructure monitoring by Dörr et al. (2022). CD-Phase is adapted to suit transport infrastructure monitoring and is based on a spatial displacement model which is uncommon for urban infrastructure monitoring. The results in this experiments, however, show that CD-Phase is also applicable for monitoring urban infrastructure in Sentinel-1 images. Beside the spatial displacement model, the CD-Phase approximates the phase noise by assuming that the phase contribution from DEM error is negligible. While this assumption holds true for flat terrain, the simplification could pose problems at high-rise buildings in Miami where the central pixel corresponds to a scatterer on the top of the building, while pixels in the $3{\times}9\,\text{pixels}^2$ neighbourhood could correspond to either other pixels

at different heights along the building or to the ground. Particularly pixels on the ground would introduce a DEM error phase contribution that is treated as noise during the phase noise estimation. This can be observed for the pixel on the top of the Eighty Seven Park Tower, which, with a height of 67 m, is the highest building in the study area. During the period from 2023 to mid of 2024, higher phase noise values are observed at this TCS pixel in interferograms with larger perpendicular baselines (Figure 4.5b). The higher phase noise probably arises from the neglected DEM error as it appears during the coherent lifetime of the scatterer. Using a larger neighbourhood could increase the effect because it might include even more pixels from different heights. On the other hand, reducing the neighbourhood size can also negatively impact the estimation of the phase noise, as there would be too few pixels available to reliably eliminate the phase contributions. The selected window size of $3{\times}9\,\text{pixels}^2$ is a trade-off between the described effects and corresponds to a neighbourhood size of $60\,m \times 45\,m$. As the coherent lifetime of the TCS at the Eighty Seven Park Tower was accurately estimated (Figure 6.18), it is argued that the approach is suitable even in urban areas with images from the Sentinel-1 mission which has shorter perpendicular baselines compared to other missions due to the narrow orbital tube.

The validation quality of the estimated coherent lifetime depends not only on the quality of the reference data, but also on the accuracy of the object masks. The pixels are assigned to a building based on a mask in the SAR image coordinate system which were created manually. The location of the masks was visually validated after geocoding. Slightly larger masks were created to cover all pixels belonging to the object. Hence, the masks might also cover non-object pixels. Also layover and shadow effects complicate the interpretation of the SAR signal, particularly at the high-rise buildings due to their high elevation and the side-looking SAR sensor geometry (Figure 2.1).

The results of this experiment are in-line with the previous experiments which showed that the coherent change detection methods, CD-Phase and CD-CohMat, provide comparable results, while the results from the incoherent change detection, CD-Amplitude, is unsuitable for the task. Similar to the scatterers in the study area Sande, the coherent lifetime can be clearly differentiated from the non-coherent period which shows a lower coherence level, indicating that the one-change hypothesis is appropriate for this study area. Moreover, the CD-Phase method was argued to be suitable even for urban infrastructure monitoring despite its spatial displacement model and the neglected DEM error phase contribution.

Displacement Results

The displacement maps derived from CCS pixels only, and jointly from CCS and TCS pixels are shown in Figure 6.19. Exemplarily, the results from the coherent lifetime estimation with CD-Phase are used for the further displacement retrieval. The displacement maps show displacements at several high-rise buildings which were previously reported by Aziz Zanjani et al. (2024) who found displacement associated with post-construction settlement of up to 2 cm/year. The displacement map derived from merely CCS pixels (Figure 6.19, top map) contains 184 scatterers. The high-rise buildings in the northern part of the study area exhibit a post-construction settlement, while the high-rise buildings in the southern part appear to be stable. The six buildings, marked with hatch-

crossed area in the map, are not observable with CCS pixels which is expected as changes happened at these buildings during the study period.

In contrast, the displacement map derived from both CCS and TCS pixels (Figure 6.19, bottom map) also covers the six buildings under change and contains 394 scatterers, corresponding to an increase of the measurement points by 214 % compared to CCS pixels only. The displacement map contains 254 TCS pixels, i.e. some of the previously detected CCS pixels were classified as TCS pixels. A denser displacement map is obtained through the integration of TCS pixels into the InSAR time series analysis. The displacement of the six buildings could only be observed in the results obtained from both CCS and TCS pixels.

The displacement results agree with the displacement time series from Aziz Zanjani et al. (2024) showing the same displacement rates and decaying time series for the high-rise buildings (cf. Figure 5 from Aziz Zanjani et al., 2024, The Surf Club: 5b, k, l and m; Eighty Seven Park Tower: 5c, n and o). However, the joined processing of CCS and TCS pixels allows to consider the individual coherent lifetimes of the TCS pixels which was not possible by the approach taken by Aziz Zanjani et al. (2024) in which the study period was split according to the expected lifetime of the infrastructure.

Correcting the geolocation of scatterers is important for the interpretation of the displacements at infrastructure due to the geometric distortions appearing for high-rise building in SAR images. In the proposed methodology, the geolocation correction is computed based on the DEM error estimate from the unwrapped phases of the scatterers. The displacement map of the urban area shows the scatterers located on the west side of the buildings after the geolocation correction was applied which aligns with the viewing direction of the satellite in the ascending orbit. That means, the geolocation of the scatterers fits to the location of the buildings although the DEM error component is not explicitly estimated during the spatial unwrapping approach chosen in the methodology. Still, a small shift between the location of the CCS pixels in the two displacement maps is visible. The shift arises from slightly different DEM error estimates with a maximum difference of 6 m. The DEM error estimate should be the same, independent of whether TCS pixels are included in the phase unwrapping. Although the difference is negligible for the sake of this experiment, an InSAR time series method tailored to urban infrastructure monitoring should include an explicit estimation of the DEM error from the wrapped phases (e.g. Schenk, 2015).

In summary, this experiment demonstrated that the coherent lifetime method provides plausible results also for urban infrastructure. It was also shown that disappearing TCS pixels can be accurately detected. Urban infrastructure monitoring usually requires a temporal displacement model for correctly retrieving localised displacement signals due to spatial discontinuities of displacement and height of the scatterers. Although not optimal, the proposed InSAR time series analysis method based on a spatial displacement model retrieved comparable displacement time series as in previously published results from literature. While the methodology seems applicable for medium spatial resolution Sentinel-1 images, adaptations are likely required to monitor urban infrastructure in high-resolution imagery.

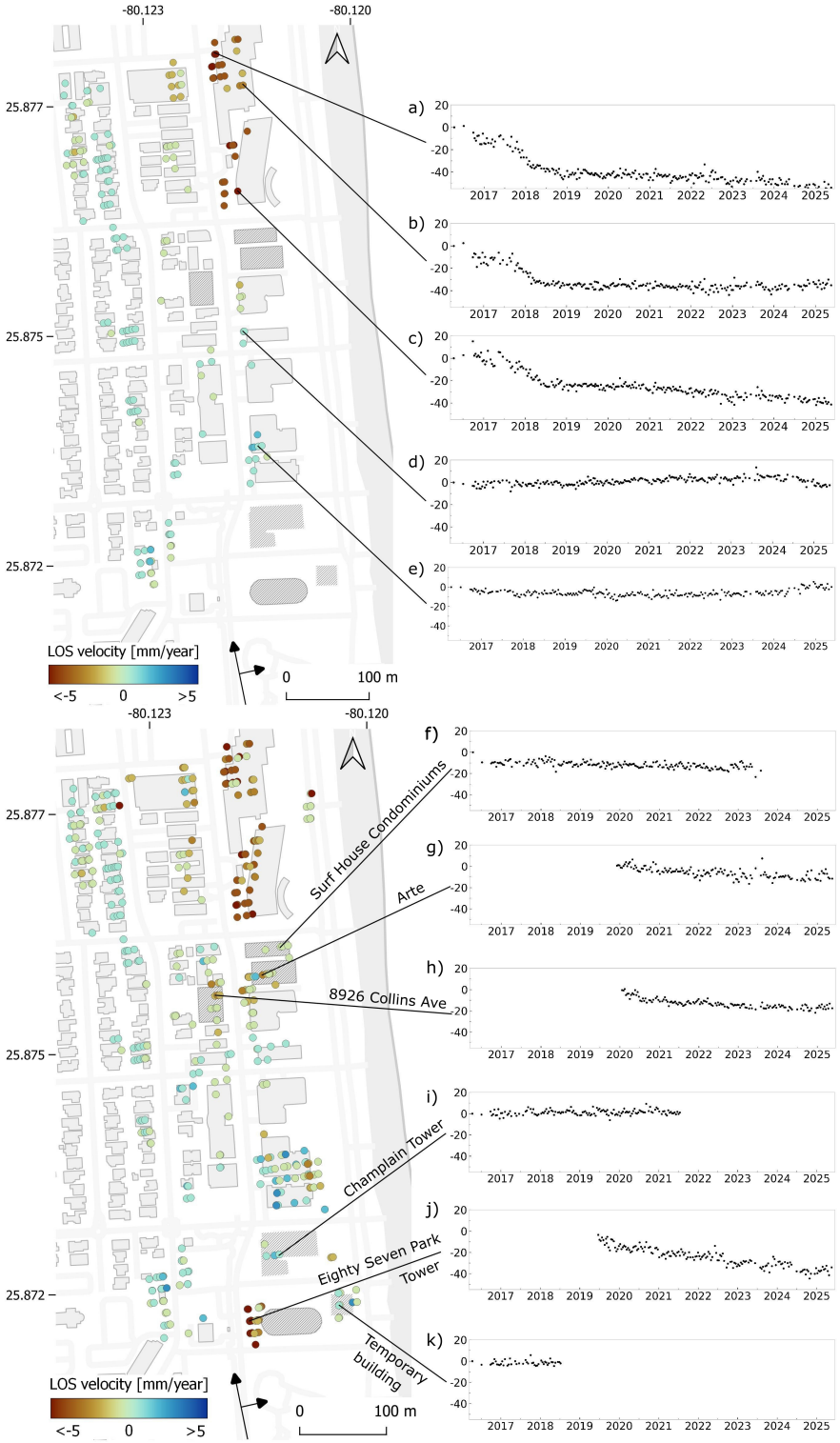


Figure 6.19: Velocity maps of the study area in Miami showing the LOS displacement derived from CCS pixels only (top), and jointly from CCS and TCS pixels (bottom). The changes are detected with CD-Phase. Displacement time series (in mm) are shown for selected scatterers on the high-rise buildings. The geolocation of the scatterers were corrected based on the estimated DEM error. Buildings with cross-hatched area are analysed in more detail in Figure 6.18. Background map is created from OSM data (OpenStreetMap contributors, 2025).

7 Conclusions and Outlook

This thesis introduces a new Interferometric Synthetic Aperture Radar (InSAR) time series analysis method tailored to transport infrastructure monitoring with Sentinel-1 images to leverage the potential of this long-term satellite mission with regular revisits and freely available data. The approach combines a small-baseline interferogram network with spatial phase unwrapping and a spatially correlated displacement model. It avoids a predefined temporal displacement model while preserving single-look resolution by selecting both, Point Scatterer (PS) and Distributed Scatterer (DS) pixels, based on the signal in their spatial neighbourhood. The atmospheric phase is estimated from reliable PS pixels across the scene and removed prior to phase unwrapping, enabling to retrieve local displacement signals at transport infrastructure.

The experimental results from two study areas show that using both PS and DS pixels provides a coverage of transport infrastructure that allows the observation of regional displacement signals. Moreover, the results show that resolving localised displacement signals at bridges, highway embankments, and railway tracks is possible with the method despite the medium spatial resolution of the Sentinel-1 sensor. This demonstrates a clear monitoring potential of Sentinel-1 for transport infrastructure, which relies on combining PS and DS pixels. Relying on PS alone, as found in the literature, would miss relevant features and reduce coverage. The performance was found to vary with the surrounding vegetation and with the type of infrastructure. The findings indicate that the presence of vegetation in the vicinity of transport infrastructure has a substantial impact on the number of coherent pixels, thereby significantly reducing the potential for monitoring. Railway tracks and bridges offer more coherent scatterers, whereas highways provide fewer useful pixels due to the low reflectivity of the smooth road surface. The findings were obtained over a three-year period, hence, the monitoring potential with Sentinel-1 with the proposed methodology may differ for shorter or longer time spans. While the findings cannot necessarily be generalised across countries because design, surface materials, and surroundings differ, they contribute to understanding the prevalent scattering mechanisms on transport infrastructure and help to set realistic expectations for the development of a transport infrastructure monitoring service.

This thesis also advances the analysis of Temporarily Coherent Scatterer (TCS) pixels at transport infrastructure which are caused by construction or demolition resulting in an abrupt change of the scattering. An InSAR time series framework is introduced that estimates and uses each pixel's individual coherent lifetime. The method first detects changes in scattering over time for each pixel and then selects its coherent lifetime. The framework is modular and accommodates different change detection methods. To retrieve the displacement time series, the phases of Continuously Coherent Scatterer (CCS) and TCS pixels are unwrapped jointly per interferogram within each

pixel's coherent lifetime and thereby biases are avoided that would arise when incoherent intervals are included.

In the experiments, three change detection methods were evaluated which target different characteristics of the Synthetic Aperture Radar (SAR) signal. The evaluation covered three study areas: two with transport infrastructure and one urban area to test the transferability of the method due to the focus of prior TCS studies on urban infrastructure monitoring. It was consistently found across all sites that the incoherent change detection based on the amplitude signal only, was less suitable for the coherent lifetime estimation of TCS pixels than the two coherent change detection methods which also consider the phase of the SAR signal. Incoherent change detection was predominantly used for TCS analysis in literature, however, the poor performance observed in the experiment is consistent with more recent studies. The two coherent change detection methods produced comparable results. However, the coherence-matrix-based approach required much longer computation time than the phase-noise-based method. The former also reduced spatial detail during coherence-matrix estimation, whereas the latter preserved these details during phase noise estimation. Therefore, the phase-noise-based change detection appears more suitable for large areas and large Sentinel-1 image stacks. Further, the experiments showed that including TCS pixels improves the displacement analysis. It increased coverage where CCS pixels alone are insufficient and improved quality by excluding incoherent intervals. The current method is not optimal for monitoring of high-rise buildings. Although the displacement results agree with published studies, the geolocation correction remains below its full potential and requires adaptations for fitting to urban environments.

Despite the convincing results of the InSAR time series method for TCS analysis, limitations remain. False positive detections of TCS pixels were observed at infrastructure for which a change is not expected. The method also struggles in areas with generally high coherence, which can produce ambiguous coherent lifetimes for pixels on the same infrastructure. Further investigations must be conducted utilising simulations and sensitivity analysis for the selection of thresholds for the change detection methods. Future work should improve the robustness of the coherent lifetime estimation and investigate the effect of the study period length on the estimation quality. One approach could be to include prior knowledge about the object's location and extent to exploit the signal of neighbouring pixels for regularisation during the coherent lifetime estimation. Another possible direction for future research could be to formulate the coherent lifetime estimation as a segmentation instead of an edge-detection problem. Optimizing the length of multiple segments by minimizing the decorrelation within each segment, while maximizing the decorrelation between the segments seems to be closer to the nature of the coherent lifetime estimation problem.

The framework for coherent lifetime estimation was demonstrated for temporarily coherent PS pixels, but may also be extended to temporarily coherent DS pixels, if both, change detection and pixel selection target DS pixels' signal properties. So far, the analysis of temporarily coherent DS pixels has received limited attention from researchers. However, the extension of the framework to DS pixels is advantageous, as these pixels are essential for monitoring transport infrastructure. While the definition of temporarily coherent PS pixels is straightforward because the signal is assumed to be either coherent or incoherent, DS pixels are affected by various sources of decorrelation

and a lower Signal-to-Noise Ratio (SNR). Therefore, the challenge is to distinguish the abrupt decorrelation resulting from scattering change from other decorrelation sources.

It can be concluded that the proposed methodology allows monitoring of transport infrastructure with Sentinel-1 images even in the context of construction works. Thereby, this thesis also contributes to expanding the applicability of InSAR time series analysis to changing environments.

A Appendix

A.1 Literature Overview on Transport Infrastructure Monitoring

The studies considered during the literature review in Section 3.1 are listed in Table A.1 for completeness. These studies used SAR data from different satellite missions which are listed with their specifications in Table A.2.

Table A.1: Quantitative literature review on transport infrastructure monitoring with InSAR time series analysis. Abbreviations: Sentinel-1 (S1), TerraSAR-X (TSX), COSMO-SkyMed (CSK), Radarsat (RS), ERS or Envisat (ERS/ENV), Advanced Land Observing Satellite (ALOS). Point Scatterer (PS), Distributed Scatterer (DS), in multilooked (ml) or in single-look interferograms (sl).

	Bridge	Railway	Highway	S1	TSX	CSK	RS	ERS/ENV	ALOS	PS	DS (ml)	DS (sl)
Perissin et al. (2012)			✓			✓				✓		
Fornaro et al. (2012)	✓				✓					✓		
Sousa and Bastos (2013)	✓							✓		✓		
Chang and Hanssen (2015)		✓						✓		✓		
Chang et al. (2016)		✓					✓			✓		
Poreh et al. (2016)	✓					✓				✓		
North et al. (2017)		✓	✓	✓						✓		
Qin et al. (2017b)		✓			✓					✓		
Huang et al. (2017)	✓			✓						✓		
Qin et al. (2017a)	✓				✓					✓		
Lazecky et al. (2017)	✓				✓					✓		
Kang et al. (2017)	✓				✓					✓		
Chang et al. (2018)		✓					✓	✓		✓		
Wang et al. (2018)		✓			✓					✓		
Huang et al. (2018)	✓			✓						✓		
Zhang et al. (2018)	✓								✓	✓		
Selvakumaran et al. (2018)	✓				✓						✓	
Cusson et al. (2018)	✓						✓			✓		
Peduto et al. (2018)	✓				✓					✓		
Fárová et al. (2019)			✓	✓						✓	✓	
Delgado Blasco et al. (2019)			✓	✓						✓		

Table A.1: (Continued.)

	Bridge	Railway	Highway	S1	TSX	CSK	RS	ERS/ENV	ALOS	PS	DS (ml)	DS (sl)
Wang et al. (2019)			✓		✓					✓		
Ma et al. (2019)	✓	✓				✓				✓		✓
Hu et al. (2019a)	✓	✓					✓			✓		
Zhang et al. (2019)		✓			✓			✓		✓		
Qin et al. (2019)	✓			✓	✓	✓				✓		
Milillo et al. (2019)	✓			✓		✓				✓		
Orellana et al. (2020)			✓	✓		✓				✓	✓	
Chang et al. (2020)		✓		✓						✓		
Selvakumaran et al. (2020)	✓				✓					✓		
Haghighi and Motagh (2021)		✓	✓	✓							✓	
Zhu et al. (2021)			✓		✓					✓		
Wang et al. (2021a)		✓		✓	✓					✓		
Chen et al. (2021)		✓			✓			✓		✓		
Jia et al. (2021)		✓					✓			✓		
Schlögl et al. (2021)	✓			✓						✓		
Qin et al. (2021)	✓			✓	✓	✓				✓		
Cusson et al. (2021)	✓						✓			✓		
Talledo et al. (2022)	✓		✓			✓				✓		
Macchiarulo et al. (2022a)			✓	✓		✓		✓		✓		
Shi et al. (2022)			✓	✓							✓	
Xing et al. (2022)			✓		✓						✓	
Shami et al. (2022)		✓		✓							✓	
Schlögl et al. (2022)	✓			✓						✓		
Markogiannaki et al. (2022)	✓			✓						✓		
Orellana et al. (2023)			✓			✓		✓		✓	✓	
Nettis et al. (2023)	✓			✓		✓				✓		✓
Wang et al. (2023a)	✓			✓						✓		
Lasri et al. (2023)	✓			✓						✓		
Song et al. (2023)	✓				✓					✓		
Farneti et al. (2023)	✓					✓				✓		
Tonelli et al. (2023)	✓					✓				✓		
Niu et al. (2024)			✓	✓							✓	
Bernhard et al. (2024)		✓			✓					✓		
Xue et al. (2024)		✓		✓						✓		
Miano et al. (2024)	✓					✓				✓		
Zhou et al. (2024)	✓			✓							✓	
Calò et al. (2024b)	✓					✓				✓		✓

Table A.1: (Continued.)

	Bridge	Railway	Highway	S1	TSX	CSK	RS	ERS/ENV	ALOS	PS	DS (ml)	DS (sl)
Cusson and Stewart (2024)	✓						✓			✓		
Lorenz et al. (2024)	✓				✓					✓		
Sadeghi et al. (2024)	✓				✓					✓		
Long et al. (2025)	✓		✓		✓					✓		
Monti et al. (2025)			✓	✓						✓		
Giordano et al. (2025)	✓			✓						✓		
Talledo and Saetta (2025)	✓			✓						✓		
Zhou et al. (2025)	✓					✓				✓		✓
Caspani et al. (2026)	✓					✓				✓		

Table A.2: Specifications of the satellite missions used for transport infrastructure monitoring in the literature (Section 3). Notably, the sensors of the listed satellite missions offer several SAR imaging modes with different spatial resolutions. Only the spatial resolutions which were most commonly used in the studied literature are listed here. Unfortunately, the imaging mode and spatial resolutions are not always explicitly mentioned by the study authors. Abbreviations: European Space Agency (ESA), Deutsches Zentrum für Luft- und Raumfahrt (DLR), Agenzia Spaziale Italiana (ASI), Canadian Space Agency (CSA), Japan Aerospace Exploration Agency (JAXA).

	Sentinel-1	TerraSAR-X	COSMO-SkyMed	Radarsat-2	ERS/ENV	ALOS-2
Wavelength	C-band	X-band	X-band	C-band	C-band	L-band
Revisit time	6-12 days	11 days	16 days	24 days	35 days	14 days
Spatial resolution	5 m×20 m	1-3 m	1-3 m	5 m	30 m	3-10 m
Operator	ESA	DLR	ASI	CSA	ESA	JAXA

A.2 Coherent Lifetime Plots for Figuera

The results of the coherent lifetime estimation for the study area Figuera derived from CD-CohMat and CD-Amplitude are shown in Figure A.1 and A.2, respectively. The coherent lifetime estimation results derived from CD-Phase is shown in Figure 6.14 and discussed in Section 6.3.

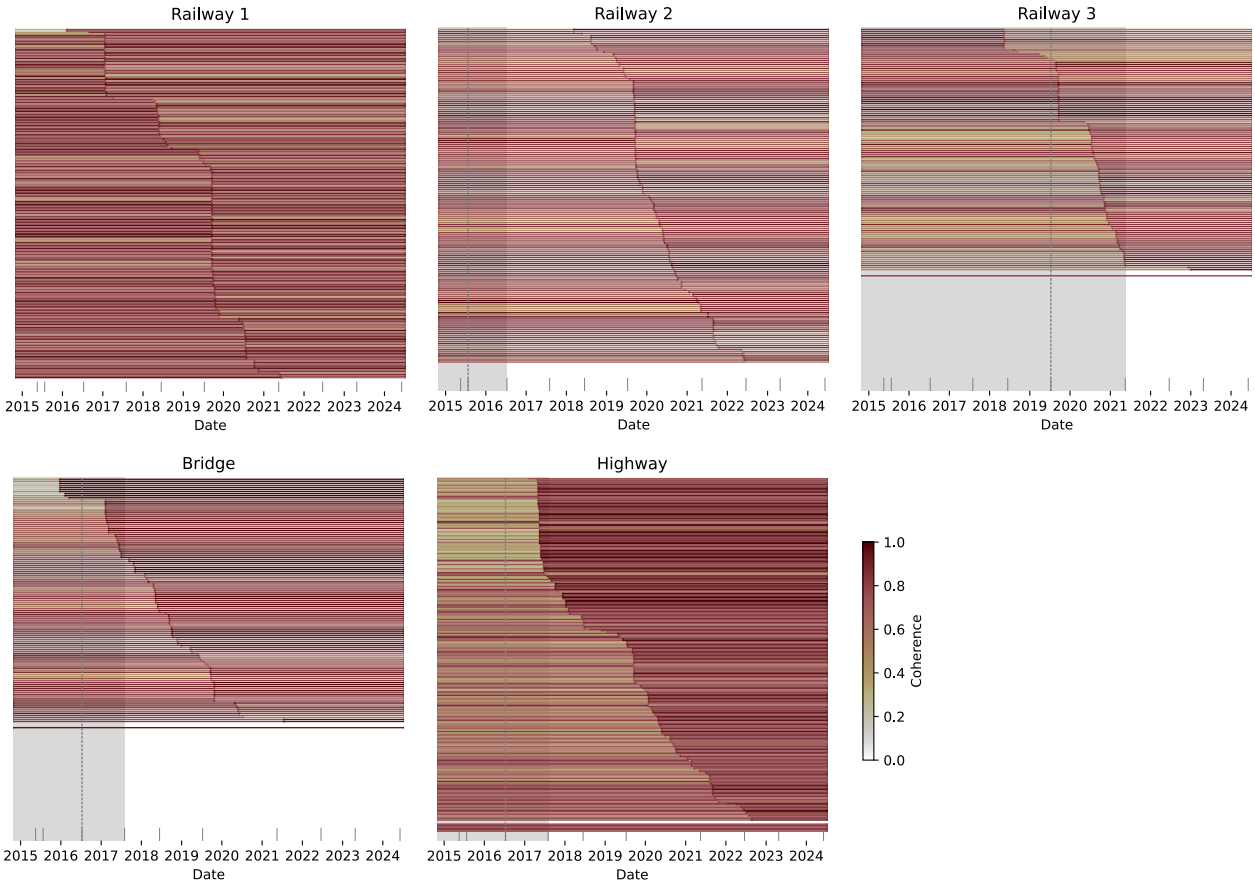


Figure A.1: Coherent lifetime of TCS pixels at five transport infrastructure in Figuera derived from CD-CohMat. Each line represents one scatterer within the mask of a transport infrastructure. Only TCS pixels that were selected during the coherent lifetime estimation are depicted. The lines are coloured by the coherence of the scattering within the time span before and after the estimated change and sorted by the change date in ascending order. The grey areas show the period in which the construction has happened according to optical satellite images (from Google Earth and National Air Orthophotography Plan (PNOA)). The short vertical gray lines along the x-axis indicate the dates of available optical images. The vertical dashed lines highlight the last optical image in which the construction was still visible.

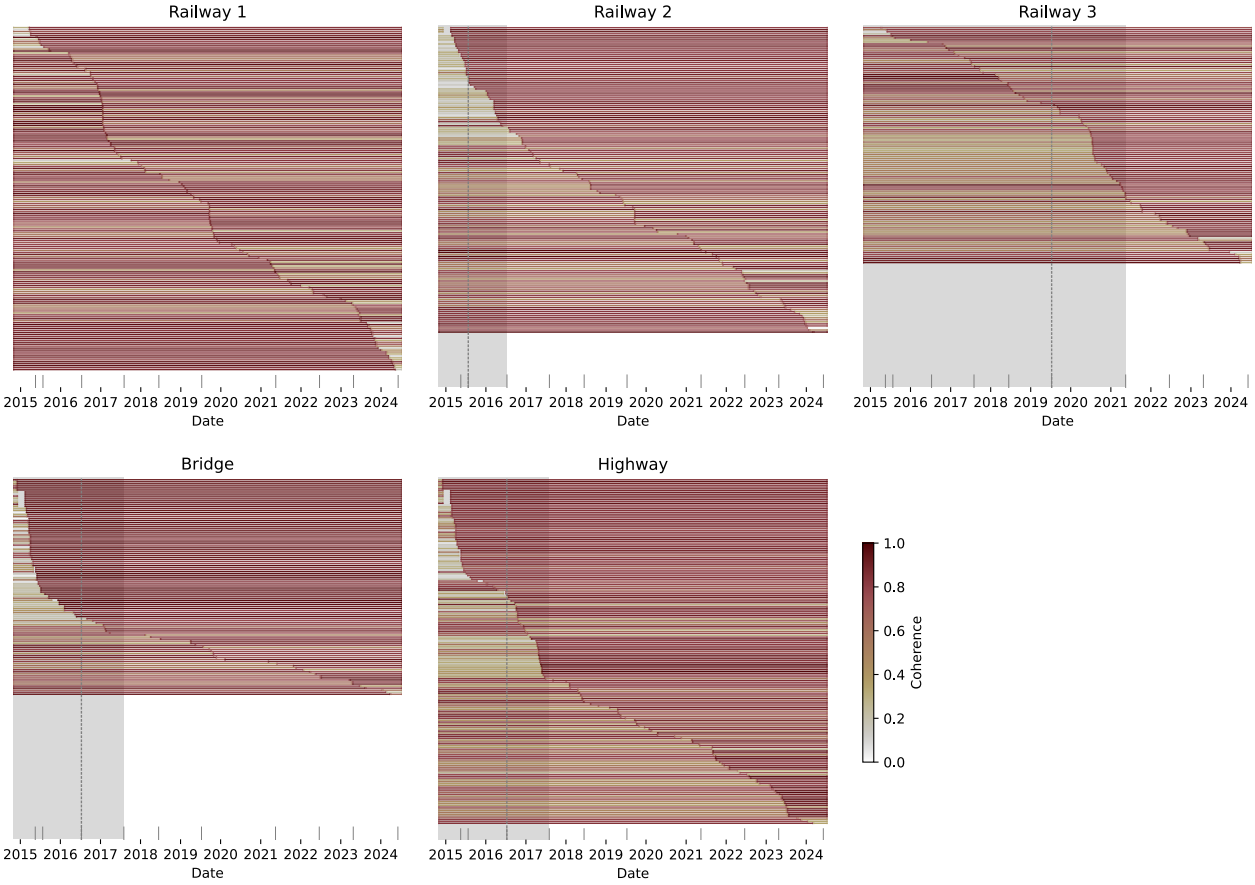


Figure A.2: Coherent lifetime of TCS pixels at five transport infrastructure in Figuera derived from CD-Amplitude. See Figure A.1 for description.

A.3 Implementation in Open-Source Software

The methodology developed in this thesis is implemented in two open-source software packages: SPAtioTemporal Selection of Scatterers (SpaTZ) for change detection and SARvey for InSAR time series analysis (Haghighi et al., 2025; Piter et al., 2025b). Both packages are implemented in Python and provide a main command-line interface which steers the processing, while the parameters are stored in a configuration file. The components of the software packages are designed in a user-friendly way with interactive visualisation and data exploration tools. A screenshot of the interactive change detection tool implemented in SpaTZ is shown in Figure A.3. The processing steps are parallelised and optimised in speed and memory handling. The datasets are compatible with the data formats of two well-established open-source InSAR time series analysis software packages: MIAmi Phase Linking in PYthon (MiaplPy) (Mirzaee et al., 2023) and Miami INsar Time-series software in PYthon (MintPy) (Yunjun et al., 2019). Thus, existing command-line tools from these two software packages can be used in combination with SARvey and SpaTZ. The output of SARvey is provided in common Geographic Information System (GIS) data formats such as shapefile or geopackage. SARvey is accessible for all researchers without licensing costs due to its open-source implementation in Python and thereby contributes to reducing the lack of reproducibility in InSAR time series analysis research reported by Balz and Rocca (2020).

The software SARvey is an integral part of the transport infrastructure monitoring service for

Schleswig-Holstein developed during the project SAR4Infra (2020-2024) financed by the German Federal Ministry of Digital and Transport. The project was conducted in coorporation with the surveying authority of Schleswig-Holstein (LVermGeo.SH), the road construction and transport authority Schleswig-Holstein (LBV.SH), and the Helmholtz Innovation Lab (FERN.Lab) at the Helmholtz Centre for Geosciences (GFZ). Within this project, a processing chain was developed, starting from the co-registration of the SAR images, followed by the retrieval of displacement time series with SARvey and ending with a post-processing step for the statistical analysis of the displacement at transport infrastructure. The processing chain is deployed on the cloud computing server COpernicus Data and Exploitation platform – DEutschland (CODE-DE)[4] financed by the German Federal Ministry of Digital and Transport to provide access to remote sensing data and derived remote sensing products for German authorities. The final displacement products are provided to the authorities involved in the project.

[4] https://code-de.org/en/

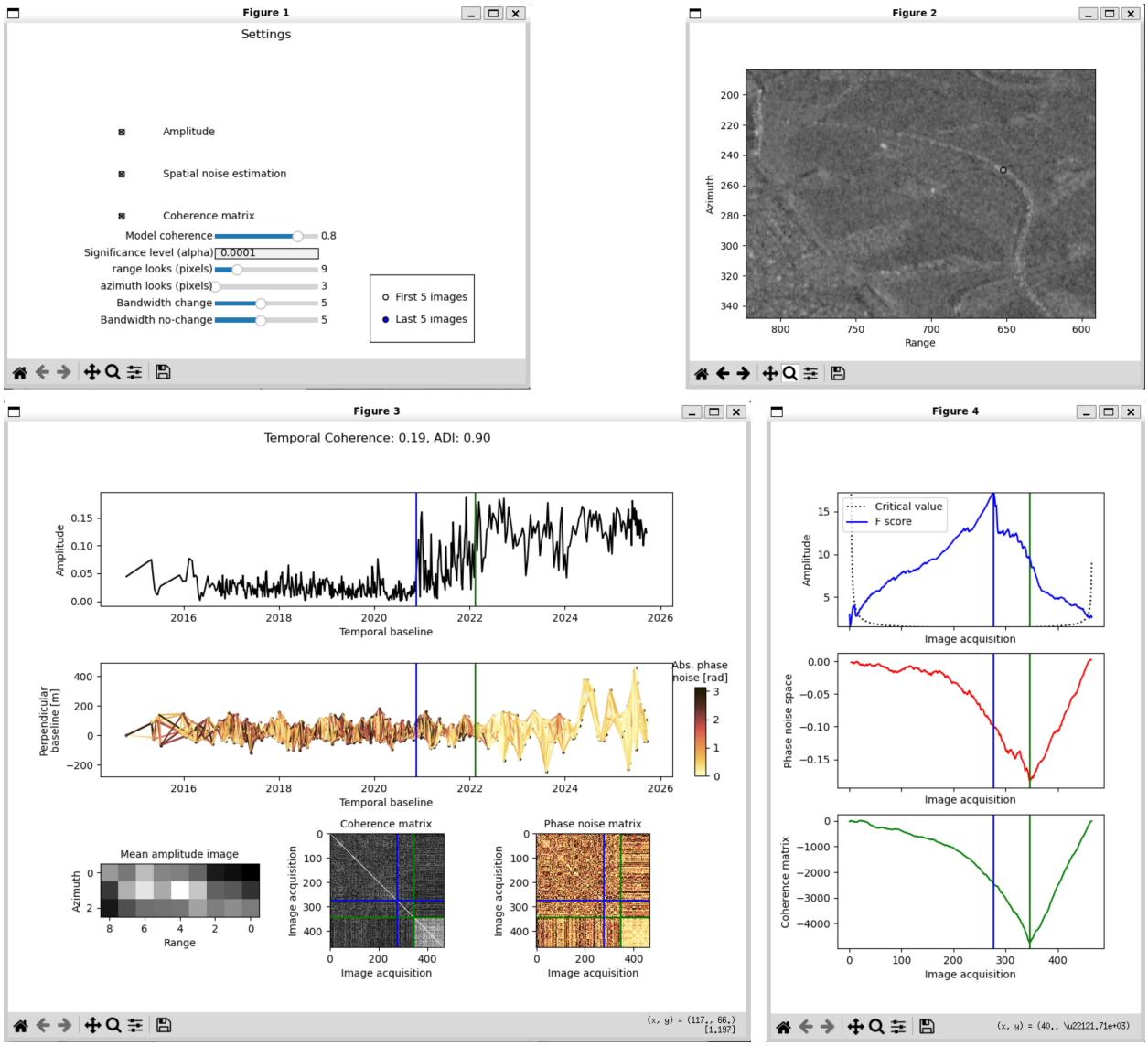


Figure A.3: Interactive change detection tool implemented in the software SpaTZ, developed within the scope of this thesis, for analysing the temporal behaviour of individual scatterers and for comparing the change detection methods. The example shows a TCS pixel in the study area Sande (see Section 5.2) at the new railway track marked with a black circle in the top right window (*Figure 2*). *Figure 1*: Settings for controlling the three change detection methods CD-Amplitude, CD-Phase and CD-CohMat. *Figure 2*: Amplitude image averaged over the last five images of the SAR stack. *Figure 3*: Input to each of the change detection methods including the amplitude time series, the absolute phase noise in a small baseline interferogram network, the mean amplitude image within the spatial neighbourhood considered during estimation (here $3\times9\,\text{pixels}^2$), the coherence matrix and the phase noise matrix. *Figure 4*: Score time series for each change detection method and the detected changes. The vertical lines in *Figure 3* and *Figure 4* highlight the location of the detected changes. These changes are also marked by horizontal lines in the coherence matrix and the phase noise matrix due to the symmetry of the matrices. The vertical and horizontal lines correspond to the change detection methods as shown by the colours: blue for CD-Amplitude, red for CD-Phase, and green for CD-CohMat. The lines are depicted in each of the graphs to enable the direct comparison of the detected changes. Notably, CD-Phase and CD-CohMat detected the same change date and, thus, the red line is not visible because it is overlayed by the green line.

Acknowledgements

The research in this doctoral thesis was financed by the German Federal Ministry of Digital and Transport through the project SAR4Infra. The presented results contain modified Sentinel-1 data from the Copernicus program of the European Space Agency. The figures in this thesis were created using Python, QGIS (QGIS Development Team, 2025) and InSAR-Explorer (Haghighi et al., 2025). Moreover, figures were created using the Scientific Colour Maps (Crameri, 2023) to prevent visual distortion of the data and exclusion of readers with colour-vision deficiencies (Crameri et al., 2020).

I would like to express my gratitude to my supervisor Prof. Dr.-Ing. Mahdi Motagh for guiding me during the doctoral studies and for giving me the chance to dive into the fascinating topic of radar remote sensing. Further, I would like to thank the reviewers Prof. Dr. Andy Hooper and Prof. Dr.-Ing. Hamza Alkhatib for their meticulous reading of my thesis, their insightful comments and the discussions during the doctoral exam. I would like to thank my supervisor Dr.-Ing. Mahmud Haghshenas Haghighi for sharing his inexhaustible passion for InSAR time series analysis and Earth observation. The controversial discussions, the opportunity for growth and the hours spent sitting together in front of a computer are all greatly appreciated. I would like to express my warmest thanks to Prof. Dr.-Ing. habil. Christian Heipke for his appreciative leadership of the institute and his support in overcoming all kinds of scientific and non-scientific challenges. Further, I would like to thank all current and former members of our institute and of our radar remote sensing group at IPI and GFZ who created an inspiring and supportive working environment. During my stay at the Institut Cartogràfic i Geològic de Catalunya in Barcelona, Dr. Oscar Mora guided me in the development of a state-of-the-art InSAR time series method. I am thankful for all the fruitful discussions with him about different approaches to InSAR time series analysis. I would like to thank Prof. Dr. Falk Amelung for the exciting and insightful collaboration on the Miami coastal subsidence at high-rise buildings, and for all the suggestions and feedback that helped to improve the methodology implemented in SARvey. Further, I would like to thank all SAR4Infra project partners at LVermGeo.SH, LBV.SH, and Fern.Lab for the productive collaboration. For me, working with Daniela Rabe, Johannes Knoch, and Dr. Romulo Goncalves from Fern.Lab, particularly during the software development sprints, was enriching and very much enjoyable. Without their support, my research code would not have been turned into the software package SARvey.

Finally, I would like to express my gratitude to my family and friends for the constant support and for encouraging me to follow my curiosity. A special word of thanks goes to Wiebke for believing in me, for all her support throughout my doctoral journey, and for the inspiring discussions about science and life.

Bibliography

Agram, P. and Simons, M., 2015. A noise model for InSAR time series. *Journal of Geophysical Research: Solid Earth* 120(4), pp. 2752–2771.

Amelung, F., Galloway, D. L., Bell, J. W., Zebker, H. A. and Laczniak, R. J., 1999. Sensing the ups and downs of Las Vegas: InSAR reveals structural control of land subsidence and aquifer-system deformation. *Geology* 27(6), pp. 483–486.

Ansari, H., Adam, N. and Brcic, R., 2014. Amplitude time series analysis in detection of persistent and temporal coherent scatterers. In: *2014 IEEE Geoscience and Remote Sensing Symposium*, pp. 2213–2216. ISSN: 2153-7003.

Ansari, H., De Zan, F. and Bamler, R., 2017. Sequential Estimator: Toward Efficient InSAR Time Series Analysis. *IEEE Transactions on Geoscience and Remote Sensing* 55(10), pp. 5637–5652.

Ansari, H., De Zan, F. and Bamler, R., 2018. Efficient phase estimation for interferogram stacks. *IEEE Transactions on Geoscience and Remote Sensing* 56(7), pp. 4109–4125.

Aziz Zanjani, F., Amelung, F., Piter, A., Sobhan, K., Tavakkoliestahbanati, A., Eberli, G. P., Haghighi, M. H., Motagh, M., Milillo, P., Mirzaee, S., Nanni, A. and Andiroglu, E., 2024. InSAR Observations of Construction-Induced Coastal Subsidence on Miami's Barrier Islands, Florida. *Earth and Space Science* 11(12), pp. e2024EA003852.

Balz, T. and Rocca, F., 2020. Reproducibility and Replicability in SAR Remote Sensing. *IEEE Journal of Selected Topics in Applied Earth Observations and Remote Sensing* 13, pp. 3834–3843.

Barra, A., Reyes-Carmona, C., Herrera, G., Galve, J. P., Solari, L., Mateos, R. M., Azañón, J. M., Béjar-Pizarro, M., López-Vinielles, J., Palamà, R., Crosetto, M., Sarro, R., Cuervas-Mons, J. and Monserrat, O., 2022. From satellite interferometry displacements to potential damage maps: A tool for risk reduction and urban planning. *Remote Sensing of Environment* 282, pp. 113294.

Bekaert, D., Hooper, A. and Wright, T., 2015a. A spatially variable power law tropospheric correction technique for InSAR data. *Journal of Geophysical Research: Solid Earth* 120(2), pp. 1345–1356.

Bekaert, D., Walters, R., Wright, T., Hooper, A. and Parker, D., 2015b. Statistical comparison of InSAR tropospheric correction techniques. *Remote Sensing of Environment* 170, pp. 40–47.

Berardino, P., Fornaro, G., Lanari, R. and Sansosti, E., 2002. A new algorithm for surface deformation monitoring based on small baseline differential SAR interferograms. *IEEE Transactions on Geoscience and Remote Sensing* 40(11), pp. 2375–2383.

Bernhard, P., Haener, D. and Frey, O., 2024. Detection of Railway Track Anomalies Using Interferometric Time Series of TerraSAR-X Satellite Radar Data. *IEEE Journal of Selected Topics in Applied Earth Observations and Remote Sensing* 17, pp. 11750–11760.

Bianchini, S., Raspini, F., Solari, L., Del Soldato, M., Ciampalini, A., Rosi, A. and Casagli, N., 2018. From Picture to Movie: Twenty Years of Ground Deformation Recording Over Tuscany Region (Italy) With Satellite InSAR. *Frontiers in Earth Science*.

Bioucas-Dias, J. M. and Valadao, G., 2007. Phase Unwrapping via Graph Cuts. *IEEE Transactions on Image Processing* 16(3), pp. 698–709.

Blanco-Sánchez, P., Mallorquí, J. J., Duque, S. and Monells, D., 2008. The Coherent Pixels Technique (CPT): An Advanced DInSAR Technique for Nonlinear Deformation Monitoring. *Pure and Applied Geophysics* 165(6), pp. 1167–1193.

Boykov, Y. and Kolmogorov, V., 2004. An experimental comparison of min-cut/max-flow algorithms for energy minimization in vision. *IEEE Transactions on Pattern Analysis and Machine Intelligence* 26(9), pp. 1124–1137.

Brcic, R. and Adam, N., 2013. Detecting changes in persistent scatterers. In: *2013 IEEE International Geoscience and Remote Sensing Symposium - IGARSS*, pp. 117–120. ISSN: 2153-7003.

Calò, M., Ruggieri, S., Nettis, A. and Uva, G., 2024a. A GIS Plugin for the Assessment of Deformations in Existing Bridge Portfolios via MTInSAR Data. *Remote Sensing* 16(22), pp. 4293.

Calò, M., Ruggieri, S., Nettis, A. and Uva, G., 2024b. A MTInSAR-Based Early Warning System to Appraise Deformations in Simply Supported Concrete Girder Bridges. *Structural Control and Health Monitoring* 2024(1), pp. 8978782.

Cao, Y., Jónsson, S. and Li, Z., 2021. Advanced InSAR tropospheric corrections from global atmospheric models that incorporate spatial stochastic properties of the troposphere. *Journal of Geophysical Research: Solid Earth* p. e2020JB020952.

Carnec, C. and Delacourt, C., 2000. Three years of mining subsidence monitored by SAR interferometry, near Gardanne, France. *Journal of Applied Geophysics* 43(1), pp. 43–54.

Caro Cuenca, M., Hooper, A. J. and Hanssen, R. F., 2011. A New Method for Temporal Phase Unwrapping of Persistent Scatterers InSAR Time Series. *IEEE Transactions on Geoscience and Remote Sensing* 49(11), pp. 4606–4615.

Caspani, V. F., Tonelli, D., Bado, M. F., Rocca, A., Perissin, D. and Zonta, D., 2026. Bridge monitoring with satellite InSAR technology and clustering algorithm. *Measurement* 258, pp. 118939.

Chang, L. and Hanssen, R., 2015. Detection of permafrost sensitivity of the Qinghai–Tibet railway using satellite radar interferometry. *International Journal of Remote Sensing* 36(3), pp. 691–700.

Chang, L., Dollevoet, R. P. and Hanssen, R. F., 2016. Nationwide railway monitoring using satellite SAR interferometry. *IEEE Journal of Selected Topics in Applied Earth Observations and Remote Sensing* 10(2), pp. 596–604.

Chang, L., Dollevoet, R. P. and Hanssen, R. F., 2018. Monitoring line-infrastructure with multisensor SAR interferometry: Products and performance assessment metrics. *IEEE Journal of Selected Topics in Applied Earth Observations and Remote Sensing* 11(5), pp. 1593–1605.

Chang, L., Ku, O. and Hanssen, R. F., 2019. Identification of deformation pattern changes caused by enhanced oil recovery (EOR) using InSAR. *International Journal of Remote Sensing* 40(4), pp. 1495–1505.

Chang, L., Sakpal, N. P., Elberink, S. O. and Wang, H., 2020. Railway infrastructure classification and instability identification using Sentinel-1 SAR and laser scanning data. *Sensors* 20(24), pp. 7108.

Chen, B., Gong, H., Chen, Y., Lei, K., Zhou, C., Si, Y., Li, X., Pan, Y. and Gao, M., 2021. Investigating land subsidence and its causes along Beijing high-speed railway using multi-platform InSAR and a maximum entropy model. *International Journal of Applied Earth Observation and Geoinformation* 96, pp. 102284.

Chen, C. W., 2001. Statistical-cost network-flow approaches to two-dimensional phase unwrapping for radar interferometry. PhD thesis, Stanford University.

Costa, G., Monti Guarnieri, A. V., Manzoni, M. and Parizzi, A., 2025a. BUD: Band-limited uncalibrated detector of environmental changes for InSAR monitoring framework. *ISPRS Journal of Photogrammetry and Remote Sensing* 230, pp. 55–72.

Costa, G., Monti-Guarnieri, A. V., Manzoni, M. and Rucci, A., 2024. A non-parametric estimator for Coherent Change Detection: The Permutational Change Detection. *IEEE Transactions on Geoscience and Remote Sensing* pp. 1–1.

Costa, G., Virgilio Monti Guarnieri, A., Parizzi, A. and Rizzoli, P., 2025b. DANI-NET: A Physics-Aware Deep Learning Framework for Change Detection Using Repeat-Pass InSAR. *IEEE Transactions on Geoscience and Remote Sensing* 63, pp. 1–27.

Costantini, M., 1998. A novel phase unwrapping method based on network programming. *IEEE Transactions on Geoscience and Remote Sensing* 36(3), pp. 813–821.

Crameri, F., 2023. Scientific colour maps.

Crameri, F., Shephard, G. E. and Heron, P. J., 2020. The misuse of colour in science communication. *Nature Communications* 11(1), pp. 5444.

Crosetto, M., Devanthéry, N., Monserrat, O., Barra, A., Cuevas-González, M., Mróz, M., Botey-Bassols, J., Vázquez-Suñé, E. and Crippa, B., 2018. A persistent scatterer interferometry procedure based on stable areas to filter the atmospheric component. *Remote Sensing* 10(11), pp. 1780.

Crosetto, M., Monserrat, O., Cuevas-González, M., Devanthéry, N. and Crippa, B., 2016. Persistent scatterer interferometry: A review. *ISPRS Journal of Photogrammetry and Remote Sensing* 115, pp. 78–89.

Crosetto, M., Monserrat, O., Cuevas, M. and Crippa, B., 2011. Spaceborne differential SAR interferometry: Data analysis tools for deformation measurement. *Remote Sensing* 3(2), pp. 305–318.

Crosetto, M., Solari, L., Mróz, M., Balasis-Levinsen, J., Casagli, N., Frei, M., Oyen, A., Moldestad, D. A., Bateson, L., Guerrieri, L., Comerci, V. and Andersen, H. S., 2020. The Evolution of Wide-Area DInSAR: From Regional and National Services to the European Ground Motion Service. *Remote Sensing* 12(12), pp. 2043.

Cusson, D. and Stewart, H., 2024. Satellite Synthetic Aperture Radar, Multispectral, and Infrared Imagery for Assessing Bridge Deformation and Structural Health—A Case Study at the Samuel de Champlain Bridge. *Remote Sensing* 16(4), pp. 614.

Cusson, D., Rossi, C. and Ozkan, I. F., 2021. Early warning system for the detection of unexpected bridge displacements from radar satellite data. *Journal of Civil Structural Health Monitoring* 11(1), pp. 189–204.

Cusson, D., Trischuk, K., Hébert, D., Hewus, G., Gara, M. and Ghuman, P., 2018. Satellite-Based InSAR Monitoring of Highway Bridges: Validation Case Study on the North Channel Bridge in Ontario, Canada. *Transportation Research Record* 2672(45), pp. 76–86.

Czikhardt, R., van der Marel, H., van Leijen, F. J. and Hanssen, R. F., 2022. Estimating Signal-to-Clutter Ratio of InSAR Corner Reflectors From SAR Time Series. *IEEE Geoscience and Remote Sensing Letters* 19, pp. 1–5.

Dalaison, M. and Jolivet, R., 2020. A Kalman Filter Time Series Analysis Method for InSAR. *Journal of Geophysical Research: Solid Earth* 125(7), pp. e2019JB019150.

Dehls, J. F., Larsen, Y., Marinkovic, P., Lauknes, T. R., Stødle, D. and Moldestad, D. A., 2019. INSAR.No: A National InSAR Deformation Mapping/Monitoring Service In Norway – From Concept To Operations. In: *IGARSS 2019 - 2019 IEEE International Geoscience and Remote Sensing Symposium*, pp. 5461–5464. ISSN: 2153-7003.

Delgado Blasco, J. M., Foumelis, M., Stewart, C. and Hooper, A., 2019. Measuring Urban Subsidence in the Rome Metropolitan Area (Italy) with Sentinel-1 SNAP-StaMPS Persistent Scatterer Interferometry. *Remote Sensing* 11(2), pp. 129.

Deutsche Bahn, 2025. Bahnverlegung Sande. https://www.oldenburg-wilhelmshaven.de/bahnverlegung-sande.html. Accessed: 2025-10-14.

Devanthéry, N., Crosetto, M., Monserrat, O., Cuevas-González, M. and Crippa, B., 2014. An approach to persistent scatterer interferometry. *Remote Sensing* 6(7), pp. 6662–6679.

Die Autobahn GmbH des Bundes, 2025. Sanierung der A20 bei Tribsees. https://www.autobahn.de/planen-bauen/projekt/sanierung-der-a20-bei-tribsees-damm-abtragung. Accessed: 2025-09-08.

Dörr, N., Schenk, A. and Hinz, S., 2022. Fully Integrated Temporary Persistent Scatterer Interferometry. *IEEE Transactions on Geoscience and Remote Sensing* 60, pp. 1–15.

Emadali, L., Motagh, M. and Haghshenas Haghighi, M., 2017. Characterizing post-construction settlement of the Masjed-Soleyman embankment dam, Southwest Iran, using TerraSAR-X SpotLight radar imagery. *Engineering Structures* 143, pp. 261–273.

Esch, C., 2020. Development of a one-step three dimensional approach for the phase unwrapping process in a differential InSAR stack based on Small BAseline Subset (SBAS) interferograms. PhD thesis, Universitäts- und Landesbibliothek Bonn.

Farneti, E., Cavalagli, N., Costantini, M., Trillo, F., Minati, F., Venanzi, I. and Ubertini, F., 2023. A method for structural monitoring of multispan bridges using satellite InSAR data with uncertainty quantification and its pre-collapse application to the Albiano-Magra Bridge in Italy. *Structural Health Monitoring* 22(1), pp. 353–371.

Fárová, K., Jelének, J., Kopačková-Strnadová, V. and Kycl, P., 2019. Comparing DInSAR and PSI techniques employed to Sentinel-1 data to monitor highway stability: A case study of a massive Dobkovičky landslide, Czech Republic. *Remote Sensing* 11(22), pp. 2670.

Fattahi, H., Agram, P. and Simons, M., 2017. A network-based enhanced spectral diversity approach for TOPS time-series analysis. *IEEE Transactions on Geoscience and Remote Sensing* 55(2), pp. 777–786.

Fattahi, H. and Amelung, F., 2013. DEM error correction in InSAR time series. *IEEE Transactions on Geoscience and Remote Sensing* 51(7), pp. 4249–4259.

Fattahi, H. and Amelung, F., 2015. InSAR bias and uncertainty due to the systematic and stochastic tropospheric delay. *Journal of Geophysical Research: Solid Earth* 120(12), pp. 8758–8773.

Ferretti, A., Colesanti, C., Perissin, D., Prati, C. and Rocca, F., 2004. Evaluating the effect of the observation time on the distribution of SAR permanent scatterers. In: *Proc. of FRINGE 2003 Workshop, Frascati, Italy.*

Ferretti, A., Fumagalli, A., Novali, F., Prati, C., Rocca, F. and Rucci, A., 2011. A new algorithm for processing interferometric data-stacks: SqueeSAR. *IEEE Transactions on Geoscience and Remote Sensing* 49(9), pp. 3460–3470.

Ferretti, A., Prati, C. and Rocca, F., 2000. Nonlinear subsidence rate estimation using permanent scatterers in differential SAR interferometry. *IEEE Transactions on Geoscience and Remote Sensing* 38(5), pp. 2202–2212.

Ferretti, A., Prati, C. and Rocca, F., 2001. Permanent scatterers in SAR interferometry. *IEEE Transactions on Geoscience and Remote Sensing* 39(1), pp. 8–20.

Fornaro, G., Reale, D. and Verde, S., 2012. Bridge thermal dilation monitoring with millimeter sensitivity via multidimensional SAR imaging. *IEEE Geoscience and Remote Sensing Letters* 10(4), pp. 677–681.

Fornaro, G., Verde, S., Reale, D. and Pauciullo, A., 2014. CAESAR: An approach based on covariance matrix decomposition to improve multibaseline–multitemporal interferometric SAR processing. *IEEE Transactions on Geoscience and Remote Sensing* 53(4), pp. 2050–2065.

Giordano, P. F., Kwapisz, M., Miano, A., Liuzzo, R., Vorwagner, A., Limongelli, M. P., Prota, A. and Ralbovsky, M., 2025. Monitoring of a multi-span prestressed concrete bridge using satellite interferometric data and comparison with on-site sensor results. *Structural Concrete.*

Goel, K. and Adam, N., 2012. An advanced algorithm for deformation estimation in non-urban areas. *ISPRS Journal of Photogrammetry and Remote Sensing* 73, pp. 100–110.

Guarnieri, A. M. and Tebaldini, S., 2008. On the exploitation of target statistics for SAR interferometry applications. *IEEE Transactions on Geoscience and Remote Sensing* 46(11), pp. 3436–3443.

Haghighi, M. H., 2019. Local and large scale InSAR measurement of ground surface deformation. PhD thesis, Leibniz Universität Hannover.

Haghighi, M. H. and Motagh, M., 2021. Land Subsidence Hazard in Iran Revealed by Country-Scale Analysis of Sentinel-1 InSAR. *The International Archives of Photogrammetry, Remote Sensing and Spatial Information Sciences* XLIII-B3-2021, pp. 155–161.

Haghighi, M. H. and Motagh, M., 2024. Uncovering the impacts of depleting aquifers: A remote sensing analysis of land subsidence in Iran. *Science Advances* 10(19), pp. eadk3039.

Haghighi, M. H., Piter, A. and Motagh, M., 2025. SARvey and InSAR Explorer: Open-source tools for InSAR data processing and visualization. In: *2025 IEEE Geoscience and Remote Sensing Symposium*, p. 9414–9417.

Hanssen, R. F., 2001. *Radar Interferometry: Data Interpretation and Error Analysis*. Vol. 2, Springer Science & Business Media.

Hooper, A., 2008. A multi-temporal InSAR method incorporating both persistent scatterer and small baseline approaches. *Geophysical Research Letters*.

Hooper, A. and Zebker, H. A., 2007. Phase unwrapping in three dimensions with application to InSAR time series. *JOSA A* 24(9), pp. 2737–2747.

Hooper, A., Segall, P. and Zebker, H., 2007. Persistent scatterer interferometric synthetic aperture radar for crustal deformation analysis, with application to Volcán Alcedo, Galápagos. *Journal of Geophysical Research: Solid Earth*.

Hooper, A., Zebker, H., Segall, P. and Kampes, B., 2004. A new method for measuring deformation on volcanoes and other natural terrains using InSAR persistent scatterers. *Geophysical Research Letters*.

Hu, F., Gong, Y., Cheng, S. and Xu, F., 2024. Amplitude-Aided 3-D Phase Unwrapping for Temporary Coherent Scatterers Interferometry. *IEEE Transactions on Geoscience and Remote Sensing* 62, pp. 1–15.

Hu, F., Leijen, F. J. v., Chang, L., Wu, J. and Hanssen, R. F., 2019a. Monitoring Deformation along Railway Systems Combining Multi-Temporal InSAR and LiDAR Data. *Remote Sensing* 11(19), pp. 2298.

Hu, F., Wu, J., Chang, L. and Hanssen, R. F., 2019b. Incorporating Temporary Coherent Scatterers in Multi-Temporal InSAR Using Adaptive Temporal Subsets. *IEEE Transactions on Geoscience and Remote Sensing* 57(10), pp. 7658–7670.

Huang, Q., Crosetto, M., Monserrat, O. and Crippa, B., 2017. Displacement monitoring and modelling of a high-speed railway bridge using C-band Sentinel-1 data. *ISPRS Journal of Photogrammetry and Remote Sensing* 128, pp. 204–211.

Huang, Q., Monserrat, O., Crosetto, M., Crippa, B., Wang, Y., Jiang, J. and Ding, Y., 2018. Displacement monitoring and health evaluation of two bridges using Sentinel-1 SAR images. *Remote Sensing* 10(11), pp. 1714.

Hussain, S., Pan, B., Afzal, Z., Ali, M., Zhang, X., Shi, X. and Ali, M., 2023. Landslide detection and inventory updating using the time-series InSAR approach along the Karakoram Highway, Northern Pakistan. *Scientific Reports* 13(1), pp. 7485.

Izumi, Y., Takeuchi, W., Widodo, J., Sulaiman, A., Awaluddin, A., Aditiya, A., Razi, P., Anggono, T. and Sumantyo, J. T. S., 2022. Temporal Subset SBAS InSAR Approach for Tropical Peatland Surface Deformation Monitoring Using Sentinel-1 Data. *Remote Sensing* 14(22), pp. 5825.

Jia, C., Yang, X., Wu, J., Ding, P. and Bian, C., 2021. Monitoring Analysis and Numerical Simulation of the Land Subsidence in Linear Engineering Areas. *KSCE Journal of Civil Engineering* 25(7), pp. 2674–2689.

Jolivet, R. and Simons, M., 2018. A Multipixel Time Series Analysis Method Accounting for Ground Motion, Atmospheric Noise, and Orbital Errors. *Geophysical Research Letters* 45(4), pp. 1814–1824.

Jolivet, R., Grandin, R., Lasserre, C., Doin, M.-P. and Peltzer, G., 2011. Systematic InSAR tropospheric phase delay corrections from global meteorological reanalysis data. *Geophysical Research Letters*.

Jung, J., Kim, D.-j., Lavalle, M. and Yun, S.-H., 2016. Coherent Change Detection Using InSAR Temporal Decorrelation Model: A Case Study for Volcanic Ash Detection. *IEEE Transactions on Geoscience and Remote Sensing* 54(10), pp. 5765–5775.

Just, D. and Bamler, R., 1994. Phase statistics of interferograms with applications to synthetic aperture radar. *Appl. Opt.* 33(20), pp. 4361–4368.

Kalia, A. C., Frei, M. and Lege, T., 2017. A Copernicus downstream-service for the nationwide monitoring of surface displacements in Germany. *Remote Sensing of Environment* 202, pp. 234–249.

Kampes, B. M., 2006. *Radar interferometry.* Vol. 12, Springer.

Kang, J., Wang, Y., Körner, M. and Zhu, X. X., 2017. Robust Object-Based Multipass InSAR Deformation Reconstruction. *IEEE Transactions on Geoscience and Remote Sensing* 55(8), pp. 4239–4251.

Kelch, S., 2024. Warum die Carolabrücke in Dresden einstürzte. https://www.zdfheute.de/politik/deutschland/carolabrueke-in-dresden-bruecke-einsturz-100.html. Accessed: 2025-09-08.

Kircher, M., Roth, A., Adam, N., Kampes, B. and Neugebauer, H., 2003. Remote sensing observation of mining induced subsidence by means of differential SAR-interferometry. In: *2003 IEEE International Geoscience and Remote Sensing Symposium*, Vol. 1, pp. 209–211 vol.1.

Koohmishi, M., Kaewunruen, S., Chang, L. and Guo, Y., 2024. Advancing railway track health monitoring: Integrating GPR, InSAR and machine learning for enhanced asset management. *Automation in Construction* 162, pp. 105378.

Lanari, R., Mora, O., Manunta, M., Mallorqui, J., Berardino, P. and Sansosti, E., 2004. A small-baseline approach for investigating deformations on full-resolution differential SAR interferograms. *IEEE Transactions on Geoscience and Remote Sensing* 42(7), pp. 1377–1386.

Lanari, R., Reale, D., Bonano, M., Verde, S., Muhammad, Y., Fornaro, G., Casu, F. and Manunta, M., 2020. Comment on "Pre-Collapse Space Geodetic Observations of Critical Infrastructure: The Morandi Bridge, Genoa, Italy" by Milillo et al. (2019). *Remote Sensing* 12(24), pp. 4011.

Lasri, O., Giordano, P. F., Limongelli, M. P. and Previtali, M., 2023. Remote monitoring of a concrete bridge using PSInSAR. *ce/papers* 6(5), pp. 893–899.

Lazecky, M., Hlavacova, I., Bakon, M., Sousa, J. J., Perissin, D. and Patricio, G., 2017. Bridge Displacements Monitoring Using Space-Borne X-Band SAR Interferometry. *IEEE Journal of Selected Topics in Applied Earth Observations and Remote Sensing* 10(1), pp. 205–210.

Lee, J.-S., Hoppel, K., Mango, S. and Miller, A., 1994. Intensity and phase statistics of multilook polarimetric and interferometric SAR imagery. *IEEE Transactions on Geoscience and Remote Sensing* 32(5), pp. 1017–1028.

Li, G., Zhao, C., Yan, M., Wang, B. and Liu, X., 2025. Estimation of Surface Height Changes and Deformation Time Series With Improved SBAS-InSAR Technique. *IEEE Transactions on Geoscience and Remote Sensing* 63, pp. 1–13.

Long, J., Xing, X., Zheng, G., Wang, L., Yao, X. and Yang, X., 2025. InSAR Joint Modeling and Deformation Estimation for Highway Network in Soft Soil Areas. *IEEE Journal on Miniaturization for Air and Space Systems* 6(3), pp. 274–285.

Lorenz, R., Petryna, Y., Lubitz, C., Lang, O. and Wegener, V., 2024. Thermal deformation monitoring of a highway bridge: Combined analysis of geodetic and satellite-based InSAR measurements with structural simulations. *Journal of Civil Structural Health Monitoring* 14(5), pp. 1237–1255.

Luo, Q., Li, J. and Zhang, Y., 2022. Monitoring Subsidence over the Planned Jakarta–Bandung (Indonesia) High-Speed Railway Using Sentinel-1 Multi-Temporal InSAR Data. *Remote Sensing* 14(17), pp. 4138.

Ma, P., Li, T., Fang, C. and Lin, H., 2019. A tentative test for measuring the sub-millimeter settlement and uplift of a high-speed railway bridge using COSMO-SkyMed images. *ISPRS Journal of Photogrammetry and Remote Sensing* 155, pp. 1–12.

Ma, P., Zheng, Y., Zhang, Z., Wu, Z. and Yu, C., 2022. Building risk monitoring and prediction using integrated multi-temporal InSAR and numerical modeling techniques. *International Journal of Applied Earth Observation and Geoinformation* 114, pp. 103076.

Macchiarulo, V., Milillo, P., Blenkinsopp, C. and Giardina, G., 2022a. Monitoring deformations of infrastructure networks: A fully automated GIS integration and analysis of InSAR time-series. *Structural Health Monitoring* p. 14759217211045912.

Macchiarulo, V., Milillo, P., Blenkinsopp, C., Reale, C. and Giardina, G., 2022b. Multi-temporal InSAR for transport infrastructure monitoring: Recent trends and challenges. *Proceedings of the Institution of Civil Engineers - Bridge Engineering* pp. 1–26.

Manunta, M., De Luca, C., Zinno, I., Casu, F., Manzo, M., Bonano, M., Fusco, A., Pepe, A., Onorato, G., Berardino, P., De Martino, P. and Lanari, R., 2019. The Parallel SBAS Approach for Sentinel-1 Interferometric Wide Swath Deformation Time-Series Generation: Algorithm Description and Products Quality Assessment. *IEEE Transactions on Geoscience and Remote Sensing* 57(9), pp. 6259–6281.

Manunta, M., Marsella, M., Zeni, G., Sciotti, M., Atzori, S. and Lanari, R., 2008. Two-scale surface deformation analysis using the SBAS-DInSAR technique: a case study of the city of Rome, Italy. *International Journal of Remote Sensing* 29(6), pp. 1665–1684.

Manzoni, M., Monti-Guarnieri, A. and Molinari, M. E., 2021. Joint exploitation of spaceborne SAR images and GIS techniques for urban coherent change detection. *Remote Sensing of Environment* 253, pp. 112152.

Markogiannaki, O., Xu, H., Chen, F., Mitoulis, S. A. and Parcharidis, I., 2022. Monitoring of a landmark bridge using SAR interferometry coupled with engineering data and forensics. *International Journal of Remote Sensing* 43(1), pp. 95–119.

Massey Jr, F. J., 1951. The Kolmogorov-Smirnov test for goodness of fit. *Journal of the American statistical Association* 46(253), pp. 68–78.

Mehltretter, M. and Heipke, C., 2019. CNN-based cost volume analysis as confidence measure for dense matching. In: *Proceedings of the IEEE International Conference on Computer Vision Workshops*, p. 2070–2079.

Meyer, F., 2010. A review of ionospheric effects in low-frequency SAR — Signals, correction methods, and performance requirements. In: *2010 IEEE Iinternational Geoscience and Remote Sensing Symposium*, IEEE, pp. 29–32. ISSN: 2153-7003.

Miano, A., Mele, A., Silla, M., Bonano, M., Striano, P., Lanari, R., Di Ludovico, M. and Prota, A., 2024. Space-borne DInSAR measurements exploitation for risk classification of bridge networks. *Journal of Civil Structural Health Monitoring*.

Milillo, P., Giardina, G., Perissin, D., Milillo, G., Coletta, A. and Terranova, C., 2019. Pre-collapse space geodetic observations of critical infrastructure: the Morandi bridge, Genoa, Italy. *Remote Sensing* 11(12), pp. 1403.

Minh, D. H. T., Hanssen, R. and Rocca, F., 2020. Radar interferometry: 20 years of development in time series techniques and future perspectives. *Remote Sensing* 12(9), pp. 1364.

Mirzaee, S., Amelung, F. and Fattahi, H., 2023. Non-linear phase linking using joined distributed and persistent scatterers. *Computers & Geosciences* 171, pp. 105291.

Molina, J. L., García Aróstegui, J. L., Benavente, J., Varela, C., de la Hera, A. and López Geta, J. A., 2009. Aquifers Overexploitation in SE Spain: A Proposal for the Integrated Analysis of Water Management. *Water Resources Management* 23(13), pp. 2737–2760.

Monserrat, O., Crosetto, M., Iglesias, R., Rossi, G., Calcagni, L. and Crippa, B., 2009. A tool for 2+ 1D phase unwrapping: Application examples. In: *Proc. Fringe 2009 Workshop*.

Monti-Guarnieri, A. V., Brovelli, M. A., Manzoni, M., Mariotti d'Alessandro, M., Molinari, M. E. and Oxoli, D., 2018. Coherent Change Detection for Multipass SAR. *IEEE Transactions on Geoscience and Remote Sensing* 56(11), pp. 6811–6822.

Monti, R., Reguzzoni, M. and Aponte, O., 2025. Sentinel-1 SAR modeling of a highway in a landslide-susceptible area. *Engineering Research Express* 7(2), pp. 025127.

Mora, O., Mallorqui, J. and Broquetas, A., 2003. Linear and nonlinear terrain deformation maps from a reduced set of interferometric SAR images. *IEEE Transactions on Geoscience and Remote Sensing* 41(10), pp. 2243–2253.

Morishita, Y., 2021. Nationwide urban ground deformation monitoring in Japan using Sentinel-1 LiCSAR products and LiCSBAS. *Progress in Earth and Planetary Science* 8(1), pp. 6.

Morishita, Y., Lazecky, M., Wright, T. J., Weiss, J. R., Elliott, J. R. and Hooper, A., 2020. LiCSBAS: An Open-Source InSAR Time Series Analysis Package Integrated with the LiCSAR Automated Sentinel-1 InSAR Processor. *Remote Sensing* 12(3), pp. 424.

Nettis, A., Massimi, V., Nutricato, R., Nitti, D. O., Samarelli, S. and Uva, G., 2023. Satellite-based interferometry for monitoring structural deformations of bridge portfolios. *Automation in Construction* 147, pp. 104707.

Niemeier, W., 2008. *Ausgleichungsrechnung: Statistische Auswertemethoden.* Walter de Gruyter.

Niu, Y., Xu, Y., Guo, C., Liu, J., Zhang, J., Liu, Q., Yang, Z. and Zhang, J., 2024. Research on geological hazard characteristics and susceptibility of the Duku Highway based on SBAS-InSAR and improved spatiotemporal clustering. *Scientific Reports* 14(1), pp. 29323.

North, M., Farewell, T., Hallett, S. and Bertelle, A., 2017. Monitoring the response of roads and railways to seasonal soil movement with persistent scatterers interferometry over six UK sites. *Remote Sensing* 9(9), pp. 922.

OpenStreetMap contributors, 2025. OpenStreetMap.

Orellana, F., Delgado Blasco, J. M., Foumelis, M., D'Aranno, P. J., Marsella, M. A. and Di Mascio, P., 2020. DInSAR for road infrastructure monitoring: Case study highway network of Rome metropolitan (Italy). *Remote Sensing* 12(22), pp. 3697.

Orellana, F., D'Aranno, P. J. V., Scifoni, S. and Marsella, M., 2023. SAR Interferometry Data Exploitation for Infrastructure Monitoring Using GIS Application. *Infrastructures* 8(5), pp. 94.

Osmanoğlu, B., Sunar, F., Wdowinski, S. and Cabral-Cano, E., 2016. Time series analysis of InSAR data: Methods and trends. *ISPRS Journal of Photogrammetry and Remote Sensing* 115, pp. 90–102.

Oxford English Dictionary, 2025. monitor, v., sense 2.c. Oxford University Press. Accessed: 2025-09-08.

Papoutsis, I., Kontoes, C., Alatza, S., Apostolakis, A. and Loupasakis, C., 2020. InSAR Greece with parallelized persistent scatterer interferometry: A national ground motion service for big Copernicus Sentinel-1 data. *Remote Sensing* 12(19), pp. 3207.

Parizzi, A. and Brcic, R., 2011. Adaptive InSAR stack multilooking exploiting amplitude statistics: A comparison between different techniques and practical results. *IEEE Geoscience and Remote Sensing Letters* 8(3), pp. 441–445.

Peduto, D., Elia, F. and Montuori, R., 2018. Probabilistic analysis of settlement-induced damage to bridges in the city of Amsterdam (The Netherlands). *Transportation Geotechnics* 14, pp. 169–182.

Pepe, A. and Lanari, R., 2006. On the Extension of the Minimum Cost Flow Algorithm for Phase Unwrapping of Multitemporal Differential SAR Interferograms. *IEEE Transactions on Geoscience and Remote Sensing* 44(9), pp. 2374–2383.

Perissin, D. and Wang, T., 2012. Repeat-Pass SAR Interferometry With Partially Coherent Targets. *IEEE Transactions on Geoscience and Remote Sensing* 50(1), pp. 271–280.

Perissin, D., Wang, Z. and Lin, H., 2012. Shanghai subway tunnels and highways monitoring through Cosmo-SkyMed Persistent Scatterers. *ISPRS Journal of Photogrammetry and Remote Sensing* 73, pp. 58–67.

Piter, A., Haghighi, M. H. and Motagh, M., 2024. Challenges and Opportunities of Sentinel-1 InSAR for Transport Infrastructure Monitoring. *PFG – Journal of Photogrammetry, Remote Sensing and Geoinformation Science* 92(5), pp. 609–627.

Piter, A., Haghighi, M. H. and Motagh, M., 2025a. Temporarily Coherent Scatterer Selection for Transport Infrastructure Monitoring with Sentinel-1 InSAR. In: *6th Joint International Symposium on Deformation Monitoring (JISDM)*.

Piter, A., Haghighi, M. H., FERN.Lab and Motagh, M., 2025b. SARvey - survey with SAR v1.2.0.

Poreh, D., Iodice, A., Riccio, D. and Ruello, G., 2016. Railways' stability observed in Campania (Italy) by InSAR data. *European Journal of Remote Sensing* 49(1), pp. 417–431.

QGIS Development Team, 2025. QGIS Geographic Information System. QGIS Association.

Qin, X., Ding, X., Liao, M., Zhang, L. and Wang, C., 2019. A bridge-tailored multi-temporal DInSAR approach for remote exploration of deformation characteristics and mechanisms of complexly structured bridges. *ISPRS Journal of Photogrammetry and Remote Sensing* 156, pp. 27–50.

Qin, X., Li, Q., Ding, X., Xie, L., Wang, C., Liao, M., Zhang, L., Zhang, B. and Xiong, S., 2021. A structure knowledge-synthetic aperture radar interferometry integration method for high-precision deformation monitoring and risk identification of sea-crossing bridges. *International Journal of Applied Earth Observation and Geoinformation* 103, pp. 102476.

Qin, X., Liao, M., Yang, M. and Zhang, L., 2017a. Monitoring structure health of urban bridges with advanced multi-temporal InSAR analysis. *Annals of GIS* 23(4), pp. 293–302.

Qin, X., Liao, M., Zhang, L. and Yang, M., 2017b. Structural Health and Stability Assessment of High-Speed Railways via Thermal Dilation Mapping With Time-Series InSAR Analysis. *IEEE Journal of Selected Topics in Applied Earth Observations and Remote Sensing* 10(6), pp. 2999–3010.

Raspini, F., Bianchini, S., Ciampalini, A., Del Soldato, M., Montalti, R., Solari, L., Tofani, V. and Casagli, N., 2019. Persistent Scatterers continuous streaming for landslide monitoring and mapping: the case of the Tuscany region (Italy). *Landslides* 16(10), pp. 2033–2044.

Raspini, F., Bianchini, S., Ciampalini, A., Del Soldato, M., Solari, L., Novali, F., Del Conte, S., Rucci, A., Ferretti, A. and Casagli, N., 2018. Continuous, semi-automatic monitoring of ground deformation using Sentinel-1 satellites. *Scientific Reports* 8(1), pp. 1–11.

Rocca, F., 2007. Modeling interferogram stacks. *IEEE Transactions on Geoscience and Remote Sensing* 45(10), pp. 3289–3299.

Rosen, P. A., Gurrola, E., Sacco, G. F. and Zebker, H., 2012. The InSAR scientific computing environment. In: *EUSAR 2012; 9th European Conference on Synthetic Aperture Radar*, VDE, pp. 730–733.

Sadeghi, Z., Wright, T., Hooper, A. and Selvakumaran, S., 2024. Using Ray Tracing to Improve Bridge Monitoring With High-Resolution SAR Satellite Imagery. *IEEE Journal of Selected Topics in Applied Earth Observations and Remote Sensing* 17, pp. 1155–1166.

Samiei-Esfahany, S., Martins, J. E., van Leijen, F. and Hanssen, R. F., 2016. Phase Estimation for Distributed Scatterers in InSAR Stacks Using Integer Least Squares Estimation. *IEEE Transactions on Geoscience and Remote Sensing* 54(10), pp. 5671–5687.

Sandwell, D., Mellors, R., Tong, X., Wei, M. and Wessel, P., 2011. Open radar interferometry software for mapping surface deformation.

Schenk, A., 2015. PS-Interferometrie in urbanen Räumen - Optimierte Schätzung von Oberflächenbewegungen mittels Multi-SBAS Verfahren. PhD thesis, Karlsruher Institut für Technologie (KIT).

Schlögl, M., Dorninger, P., Kwapisz, M., Ralbovsky, M. and Spielhofer, R., 2022. Remote Sensing Techniques for Bridge Deformation Monitoring at Millimetric Scale: Investigating the Potential of Satellite Radar Interferometry, Airborne Laser Scanning and Ground-Based Mobile Laser Scanning. *PFG – Journal of Photogrammetry, Remote Sensing and Geoinformation Science* 90(4), pp. 391–411.

Schlögl, M., Widhalm, B. and Avian, M., 2021. Comprehensive time-series analysis of bridge deformation using differential satellite radar interferometry based on Sentinel-1. *ISPRS Journal of Photogrammetry and Remote Sensing* 172, pp. 132–146.

Selvakumaran, S., Plank, S., Geiß, C., Rossi, C. and Middleton, C., 2018. Remote monitoring to predict bridge scour failure using Interferometric Synthetic Aperture Radar (InSAR) stacking techniques. *International Journal of Applied Earth Observation and Geoinformation* 73, pp. 463–470.

Selvakumaran, S., Rossi, C., Marinoni, A., Webb, G., Bennetts, J., Barton, E., Plank, S. and Middleton, C., 2020. Combined InSAR and Terrestrial Structural Monitoring of Bridges. *IEEE Transactions on Geoscience and Remote Sensing* 58(10), pp. 7141–7153.

Shami, S., Azar, M. K., Nilfouroushan, F., Salimi, M. and Reshadi, M. A. M., 2022. Assessments of ground subsidence along the railway in the Kashan plain, Iran, using Sentinel-1 data and NSBAS algorithm. *International Journal of Applied Earth Observation and Geoinformation* 112, pp. 102898.

Shamshiri, R., Motagh, M., Nahavandchi, H., Haghighi, M. H. and Hoseini, M., 2020. Improving tropospheric corrections on large-scale Sentinel-1 interferograms using a machine learning approach for integration with GNSS-derived zenith total delay (ZTD). *Remote Sensing of Environment* 239, pp. 111608.

Shamshiri, R., Nahavandchi, H., Motagh, M. and Hooper, A., 2018. Efficient ground surface displacement monitoring using Sentinel-1 data: Integrating distributed scatterers (DS) identified using two-sample t-test with persistent scatterers (PS). *Remote Sensing* 10(5), pp. 794.

Shi, X., Niu, F., Qu, T., Zhang, H., Jiang, M., Jiang, H., Zhang, Z. and Wang, X., 2022. Stability analysis of Shiwei-Labudalin Highway in Inner Mongolia, Northeastern China using Sentinel-1 InSAR. *Cold Regions Science and Technology* 202, pp. 103647.

Song, X., Zhang, L., Lu, Z., Wu, J., Song, R., Liang, H. and Bian, W., 2023. Towards Retrieving Discontinuous Deformation of Bridges by MTInSAR with Adaptive Segmentation. *IEEE Transactions on Geoscience and Remote Sensing* pp. 1–1.

Sousa, J. J. and Bastos, L., 2013. Multi-temporal SAR interferometry reveals acceleration of bridge sinking before collapse. *Natural Hazards and Earth System Sciences* 13(3), pp. 659–667.

Spaans, K. and Hooper, A., 2016. InSAR processing for volcano monitoring and other near-real time applications. *Journal of Geophysical Research: Solid Earth* 121(4), pp. 2947–2960.

Talledo, D. A. and Saetta, A., 2025. A Multi-Level Semi-Automatic Procedure for the Monitoring of Bridges in Road Infrastructure Using MT-DInSAR Data. *Remote Sensing* 17(14), pp. 2377.

Talledo, D. A., Miano, A., Bonano, M., Di Carlo, F., Lanari, R., Manunta, M., Meda, A., Mele, A., Prota, A., Saetta, A. and Stella, A., 2022. Satellite radar interferometry: Potential and limitations for structural assessment and monitoring. *Journal of Building Engineering* 46, pp. 103756.

Tang, W., Motagh, M. and Zhan, W., 2020. Monitoring active open-pit mine stability in the Rhenish coalfields of Germany using a coherence-based SBAS method. *International Journal of Applied Earth Observation and Geoinformation* 93, pp. 102217.

Tonelli, D., Caspani, V. F., Valentini, A., Rocca, A., Torboli, R., Vitti, A., Perissin, D. and Zonta, D., 2023. Interpretation of Bridge Health Monitoring Data from Satellite InSAR Technology. *Remote Sensing* 15(21), pp. 5242.

Torres, R., Snoeij, P., Geudtner, D., Bibby, D., Davidson, M., Attema, E., Potin, P., Rommen, B., Floury, N., Brown, M., Traver, I. N., Deghaye, P., Duesmann, B., Rosich, B., Miranda, N., Bruno, C., L'Abbate, M., Croci, R., Pietropaolo, A., Huchler, M. and Rostan, F., 2012. GMES Sentinel-1 mission. *Remote Sensing of Environment* 120, pp. 9–24.

Van Leijen, F. J., 2014. Persistent scatterer interferometry based on geodetic estimation theory. PhD thesis, Technical University Delft.

Villamil Lopez, C. and Stilla, U., 2022. Monitoring of Construction Activity by Change Detection on SAR Time Series Using Coherent Scatterers. *IEEE Journal of Selected Topics in Applied Earth Observations and Remote Sensing* 15, pp. 7499–7514.

Wackernagel, H., 2003. *Multivariate geostatistics: an introduction with applications*. Springer Science & Business Media.

Wang, B., Zhao, C., Zhang, Q., Yang, C., Li, W., Li, G., Kang, Y. and Zheng, S., 2023a. SAR Interferometry Infrastructure Deformation Monitoring by the Number of Redundant Observations Optimizes Phase Unwrapping Networks. *IEEE Journal of Selected Topics in Applied Earth Observations and Remote Sensing* pp. 1–11.

Wang, H., Chang, L. and Markine, V., 2018. Structural Health Monitoring of Railway Transition Zones Using Satellite Radar Data. *Sensors* 18(2), pp. 413.

Wang, R., Yang, T., Yang, M., Liao, M. and Lin, J., 2019. A safety analysis of elevated highways in Shanghai linked to dynamic load using long-term time-series of InSAR stacks. *Remote Sensing Letters* 10(12), pp. 1133–1142.

Wang, W., Motagh, M., Mirzaee, S., Li, T., Zhou, C., Tang, H. and Roessner, S., 2023b. The 21 July 2020 Shaziba landslide in China: Results from multi-source satellite remote sensing. *Remote Sensing of Environment* 295, pp. 113669.

Wang, Y., Bai, Z., Zhang, Y., Qin, Y., Lin, Y., Li, Y. and Shen, W., 2021a. Using TerraSAR X-Band and Sentinel-1 C-Band SAR Interferometry for Deformation Along Beijing-Tianjin Intercity Railway Analysis. *IEEE Journal of Selected Topics in Applied Earth Observations and Remote Sensing* 14, pp. 4832–4841.

Wang, Y., Liu, D., Dong, J., Zhang, L., Guo, J., Liao, M. and Gong, J., 2021b. On the applicability of satellite SAR interferometry to landslide hazards detection in hilly areas: a case study of Shuicheng, Guizhou in Southwest China. *Landslides* 18(7), pp. 2609–2619.

Wegmüller, U., Werner, C., Strozzi, T. and Wiesmann, A., 2004. Monitoring mining induced surface deformation. In: *2004 IEEE International Geoscience and Remote Sensing Symposium*, Vol. 3, pp. 1933–1935 vol.3.

Wegmüller, U., Werner, C., Strozzi, T., Wiesmann, A., Frey, O. and Santoro, M., 2016. Sentinel-1 Support in the GAMMA Software. *Procedia Computer Science* 100, pp. 1305–1312.

Werner, C., Wegmuller, U., Strozzi, T. and Wiesmann, A., 2003. Interferometric point target analysis for deformation mapping. In: *2003 IEEE International Geoscience and Remote Sensing Symposium*, Vol. 7, pp. 4362–4364 vol.7.

Wittich, D., Rottensteiner, F., Voelsen, M., Heipke, C. and Müller, S., 2022. Deep learning for the detection of early signs for forest damage based on satellite imagery. *ISPRS Annals of the Photogrammetry, Remote Sensing and Spatial Information Sciences* V-2-2022, pp. 307–315.

Xing, X., Zhu, Y., Xu, W., Peng, W. and Yuan, Z., 2022. Measuring Subsidence Over Soft Clay Highways Using a Novel Time-Series InSAR Deformation Model With an Emphasis on Rheological Properties and Environmental Factors (NREM). *IEEE Transactions on Geoscience and Remote Sensing* 60, pp. 1–19.

Xue, Y.-A., Zou, Y.-F., Li, H.-Y. and Zhang, W.-Z., 2024. Regional subsidence monitoring and prediction along high-speed railways based on PS-InSAR and LSTM. *Scientific Reports* 14(1), pp. 24622.

Yu, C., Li, Z., Penna, N. T. and Crippa, P., 2018. Generic atmospheric correction model for interferometric synthetic aperture radar observations. *Journal of Geophysical Research: Solid Earth* 123(10), pp. 9202–9222.

Yunjun, Z., Fattahi, H. and Amelung, F., 2019. Small baseline InSAR time series analysis: Unwrapping error correction and noise reduction. *Computers & Geosciences* 133, pp. 104331.

Zacher, T., 2025. Neue Bilder zeigen: So schlecht stand es um die Rahmedetalbrücke. https://www.tagesschau.de/inland/regional/nordrheinwestfalen/wdr-neue-bilder-zeigen-so-schlecht-stand-es-um-die-rahmedetalbruecke-100.html. Accessed: 2025-09-08.

Zebker, H. and Villasenor, J., 1992. Decorrelation in interferometric radar echoes. *IEEE Transactions on Geoscience and Remote Sensing* 30(5), pp. 950–959.

Zhang, L., Ding, X. and Lu, Z., 2010. Modeling PSInSAR time series without phase unwrapping. *IEEE Transactions on Geoscience and Remote Sensing* 49(1), pp. 547–556.

Zhang, L., Ding, X. and Lu, Z., 2011. Ground settlement monitoring based on temporarily coherent points between two SAR acquisitions. *ISPRS Journal of Photogrammetry and Remote Sensing* 66(1), pp. 146–152.

Zhang, L., Sun, Q. and Hu, J., 2018. Potential of TCPInSAR in Monitoring Linear Infrastructure with a Small Dataset of SAR Images: Application of the Donghai Bridge, China. *Applied Sciences* 8(3), pp. 425.

Zhang, Q., Li, Y., Zhang, J. and Luo, Y., 2019. InSAR technique applied to the monitoring of the Qinghai–Tibet Railway. *Natural Hazards and Earth System Sciences* 19(10), pp. 2229–2240.

Zhao, F. and Mallorqui, J. J., 2019. A Temporal Phase Coherence Estimation Algorithm and Its Application on DInSAR Pixel Selection. *IEEE Transactions on Geoscience and Remote Sensing* 57(11), pp. 8350–8361.

Zhou, L., Li, X., Pan, Y., Ma, J., Wang, C., Shi, A. and Chen, Y., 2024. Deformation monitoring of long-span railway bridges based on SBAS-InSAR technology. *Geodesy and Geodynamics* 15(2), pp. 122–132.

Zhou, Y., Hao, G., Qin, X., Yi, F. and Tan, Z., 2025. A refined DS-InSAR technique for long-term deformation monitoring of low-coherence bridge groups. *Engineering Structures* 335, pp. 120335.

Zhu, L., Xing, X., Zhu, Y., Peng, W., Yuan, Z. and Xia, Q., 2021. An Advanced Time-Series InSAR Approach Based on Poisson Curve for Soft Clay Highway Deformation Monitoring. *IEEE Journal of Selected Topics in Applied Earth Observations and Remote Sensing* 14, pp. 7682–7698.